

NORTHWESTERN UNIVERSITY

Design of Tungsten-free, L₁₂-strengthened Cobalt-based Superalloys

A DISSERTATION

SUBMITTED TO THE GRADUATE SCHOOL

IN PARTIAL FULFILLMENT FOR THE REQUIREMENTS

for the Degree

DOCTOR OF PHILOSOPHY

Field of Materials Science and Engineering

By

Brandon C. Ohl

EVANSTON, IL

June 2023

© Copyright by Brandon C. Ohl 2023

All Rights Reserved

Abstract

Recent developments have enabled $L1_2$ -strengthened Co-based superalloys, which have the potential to surpass Ni-based superalloys as the material of choice for the hottest sections of turbine blades due to cobalt's 40 °C higher melting point. The most-studied branch of Co-based superalloys are based on the $L1_2$ phase $Co_3(Al,W)$; however, there is interest in replacing W with other γ' -formers to reduce alloy density. Here, mechanical properties and microstructural stability for twenty-one Co-based, W-free, $L1_2$ -strengthened superalloys are investigated.

Six $Co_xNi_{10-x}Al_5Cr_yV_3Ti_2Nb_{1.5}Ta_{1.5}B_{0.08}$, (where $x=10, 20, \text{ or } 30$ at.% and $y=4$ or 8 at.%) found that the $\gamma + \gamma'$ microstructure is stable for all alloys up to 1000 h at 850 °C, with γ' area fraction increasing from 32 to 49% with increasing Ni in the alloys with 4% Cr and remaining constant at 45% in alloys with 8% Cr; solvus temperatures increase by 15-20 °C per 10 at.% Ni addition and by 15-20 °C as Cr doubles from 4 to 8%; average lattice misfits are between 0.6 and 1%, slightly increasing with Cr and Ni content; oxidation resistance improves with Cr, and to a lesser extent, Ni; creep behavior follows the power law for all six alloys at 850 °C with a stress exponent of 10-12, with improved creep resistance at higher Ni content.

Seven quaternary Co-Ni-Ta-Al alloys along the tie line between Ni-12.5Al and Co-12.5Ta (at.%) found that a pure $\gamma + \gamma'$ region exists up to ~50% Co/(Co+Ni) fraction. At 69% Co/(Co+Ni) fraction a needlelike phase precipitates, and above 85% Co/(Co+Ni) fraction, λ_3 precipitates (13% in CoNi86, 36% in CoNi100). The γ phase still precipitates cuboidal γ' at low aging times, but this discontinuously precipitates at higher aging times. Increasing Co:Ni ratios results in decreasing solidus and liquidus temperatures and increased γ/γ' lattice misfit and γ phase tetragonal distortion.

Eight Co-(30-x)Ni-xFe-5Al-4/8Cr-3V-2Ti-1.5Nb-1.5Ta-0.08B (x= 10, 12, 14, 18, at.%) found that Fe substitutions for Ni decreases γ' volume fraction, and additionally decreases the total $\gamma + \gamma'$ region (due to non- γ' precipitates and associated depletion zones) with 18 at.% Fe; Ni \rightarrow Fe substitutions increase solvus temperature by an average of 3 °C per 1 at.% Fe, with negligible changes to solidus and liquidus temperatures, and doubling Cr from 4 to 8 at.% results in a consistent ~5 °C increase in solvus and 5-10 °C decrease in solidus and liquidus; Ni \rightarrow Fe substitutions reduce $a_{\gamma'}$ and increase a_{γ} , resulting in a decreasing lattice misfit of ~0.02% per 1 at.% Fe, but doubling Cr from 4 to 8 at.% reduces both $a_{\gamma'}$ and a_{γ} equally such that the lattice misfit is mostly constant; a marked yield strength anomaly is observed at 800 °C with yield strength of 530-590 MPa and only weak dependence on Fe and Cr content; Fe substitutions does not affect the stress exponent (n=12) but noticeably decreases creep resistance such that with stress-at-constant-strain-rate decreasing by 5-20 MPa per at.% Fe substitution, while Cr additions improve creep resistance except in the 18Fe case.

A machine-learning model was built to predict the strain rate in the steady-state regime of any Co-based superalloy at a particular temperature and stress, given inputs of alloy composition, heat treatment history, and microstructure (γ' precipitate volume fraction). The model is trained on nearly 1,000 distinct Co-based superalloys with γ/γ' microstructure reported in the recent literature. Instead of using CALPHAD-predicted inputs which have proven unreliable (especially in newer alloys systems such as these), we have developed additional intermediary machine-learning models for six materials properties. These models require only a compositional input to predict solvus-, solidus-, and liquidus temperatures, peak hardness, and lattice misfit and yield strength (at ambient and elevated temperature). These intermediate materials properties results are

fed back into the creep prediction ML model to improve its accuracy. Additionally, we validated results by predicting intermediate- and creep-properties for 16 new alloys, and experimentally determining those values.

Six multi-principal-element (“high-entropy”) CoFeNi-based superalloys were produced with (i) various ratios of Co, Fe, and Ni, (ii) a constant concentration (13 at%) of γ' formers (V, Al, Ti, Nb, and/or Ta, without W), and (iii) up to 8% Cr. The role of different ratios of γ' - to γ -formers on phase stability is investigated via calorimetry and microstructural studies after aging up to 1000 h at 850 °C, culminating in a novel W-free γ' -strengthened superalloy with equiatomic γ - and γ' -forming elements, $(\text{Co,Fe,Ni})_{87}(\text{V,Ti,Al})_{13}$. We find a stable, continuous $\gamma+\gamma'$ phase field when transitioning from W-free Co-based superalloys to the equiatomic $(\text{CoFeNi})_{87}(\text{V,Ti,Al})_{13}$ composition, which display a γ/γ' microstructure with γ' volume fraction of ~40% and without additional phases.

Acknowledgements

Personal

David, you are the best mentor a person could ever ask for. They say that PhD students need to “pick two” out of liking their PI, their research group, or their research project—I never had this dilemma. I’m so grateful for that day as a 1st year student when we discussed how you could move the research funds around to let me take this project with you. You’ve pushed me when I lagged, supported me when I needed guidance, and accommodated my personal needs. I could not have succeeded without your attention to detail, lightning-fast turnarounds, and contagious enthusiasm for science. Spencer and Prof. Young, you’ll get your own acknowledgement later, but you deserve an extra thanks for telling me I needed to work for David!

Thank you to my committee members: Dr. Carrie Campbell, Prof. Howard Stone, Prof. Ian McCue, and Prof. Peter Voorhees. All of you have graciously offered time, energy, and guidance to ensure the success of my research. Carrie has provided mentorship since I first joined the Co-superalloy CHiMaD group and was especially critical in guiding me through the machine-learning portion of my research. Howard—I can’t thank you enough for agreeing to let me work at Cambridge during the pandemic. It was truly an invaluable experience to see another group’s research process—especially one with as much superalloy expertise as yours!

Thank you to the whole Dunand group for all the shared late nights, food scouting parties, and cross-brainstorming. Sam, Clement, John, Harrison, Ming—frisbee afternoons and game nights were the perfect break from the lab. Jennie—thanks for being a great role model and always making me feel welcome. I learned so much from different members of the Co-subgroup: Nando,

Tony, Whitney, Fei, Kuma, and Hyeji—it was always a pleasure to see your progress parallel to mine and learn from each other.

Many thanks to everyone who has provided me with experimental assistance, laboratory training, and advice over the course of my PhD. Northwestern (and Cambridge) have so many helpful folks that it would be impossible to list them all, but I will do my best. Thank you to Nando Reyes and Tony Chung, who were working on this project before I joined and passed me the torch. Thank you to Northwestern facility managers Carla Shute, Dieter Isheim, Tirzah Abbot, and Christos Malliakas, who trained or troubleshot many different equipment. Thank you to postdoc Hon-Tong Pang, facility manager Sue Gymer, and fellow student George Wise for training me at the Cambridge facilities even through the pandemic-induced red tape. Thank you to (now professor!) Lewis Owen, for the extensive help using GSAS-II, and other discussions. Thank you to Amir Farkoosh for helping with pretty much everything. Seriously, I emailed him a question at 2 AM on Saturday, and he responded, “I’ll be there in 15 minutes.” Thanks to my wonderful undergraduate assistants Jesse Ji and Davin “it’s-okay-if-you-mispronounce-my-name-for-a-whole-month” Yoo. Jesse coded the very first version of my machine learning program, and Davin helped a ton with sample preparation and SEM for my high entropy superalloys.

I dedicate this paragraph solely to those who helped me with coding. The machine-learning program was pretty much the first code I’d ever written, and a quick call or email with one of these people would usually save me several hours of bugfixing. Thanks to one of my roommates, Haroon Nawaz, who not only kept me up way too late with interesting conversation, but also provided a critical suggestion which helped my k-clustering integrate with the rest of the program. Thanks to Jesse Ji, Carrie Campbell, and Kamal Choudhary for writing the first seed of the ML code, which

gave me a starting point to begin my Google searches. Thanks to my dad, Marty Ohl, who also helped me get to the root cause of some of my bugs. By far the most tangible assistance came from Ren Lopez from NU's Research Computing Services.

Thank you to everyone who helped me get to the point where I was even ready to begin this PhD journey. I was supported by all my undergraduate faculty at the University of North Texas, but I want to especially acknowledge a few: Prof. Marcus Young, one of David's previous students, who allowed me to join his research lab as a freshman and mentored me on no less than 3 projects. Prof. Rick Reidy, unending fountain of advice—from research to class scheduling, to relationships, and even book recommendations. Prof. Sundeep Mukherjee, who made me really realize how interesting advanced metallurgy can be. Prof. Srinivasan Srivilliputhur, who would invite me to join his table when dining in the cafeteria and showing me that professors are people too. Prof. Jincheng Du, who not only supported us to our TMS Materials Bowl victory, but also advised me on my senior design project along with Spencer Taylor and Ty Thomas. Spencer and Ty (and the rest of my UNT cohort), thanks for keeping me sane through undergrad and continually stoking my passion for materials science. Thank you Prof. Yoko Yamabe-Mitarai, for accepting me into your research group at NIMS in Japan, giving me an important cultural exchange, and allowing me to meet my wife! I would be remiss if I didn't acknowledge at least one of my many amazing high school teachers: Mrs. Vicki Hermsdorf, thank you for first cultivating my appreciation for chemistry.

Thank you to my friends and family. Mom and Dad, you never stopped believing in me, and you raised me to be confident enough that I never stopped believing in myself either. Jonathan and Justin, my brothers, thanks for all the holiday Smash Bros. Josh and Jack, friends from way back,

it has been a privilege to start in school together and continue our med school and grad school journeys in parallel.

Ewelina, my wife, the person I'm most certain is reading this: I love you. I couldn't have survived grad school without your support. Unlike "normal" spouses who doze off when a grad student talks about their research, you actually understand me and excitedly await my results. You have sacrificed more than anyone else to ensure my success.

Research Support

This work was supported by the U.S. Department of Commerce, National Institute of Standards and Technology, as part of the Center for Hierarchical Materials Design (CHiMaD) at Northwestern University (NU) via award 70NANB14H012. This study was further supported by Rolls-Royce plc. and the Engineering and U.K. Physical Sciences Research Council (EPSRC) for provision of material and funding at the University of Cambridge. This work made use of the MatCI Facility which receives support from the MRSEC Program (NSF DMR- 1720139) of the Materials Research Center at Northwestern University; and the IMSERC X-RAY and the EPIC facility of Northwestern University's NUANCE Center, which received support from the Soft and Hybrid Nanotechnology Experimental (SHyNE) Resource (NSF ECCS-1542205). Synchrotron x-ray diffraction was performed at the DuPont-Northwestern-Dow Collaborative Access Team (DND-CAT) located at Sector 5 of the Advanced Photon Source (APS). DND-CAT is supported by Northwestern University, The Dow Chemical Company, and DuPont de Nemours, Inc. The Advanced Photon Source is a U.S. Department of Energy (DOE) Office of Science User Facility

operated for the DOE Office of Science by Argonne National Laboratory under Contract No. DE-AC02-06CH11357.

Table of Contents

Abstract.....	3
Acknowledgements.....	6
Personal.....	6
Research Support	9
Table of Contents.....	11
List of Figures.....	18
1. INTRODUCTION	31
2. BACKGROUND.....	34
2.1 Historical Development of Co-based Superalloys.....	34
2.1.1 Discovery and Rediscovery of L1 ₂ -strengthened Co-based Superalloys	34
2.1.2 Pedigree of Current Work.....	35
2.2 Mechanical Properties of High-Temperature Alloys.....	36
2.2.1 Theory of Ambient-temperature Deformation	36
2.2.2 Theory of High-temperature Deformation (Creep)	38
2.2.3 Lattice Misfit	41
2.2.4 Rafting in Superalloys	42
3. Effects of Ni and Cr additions on $\gamma + \gamma'$ Microstructure and Mechanical Properties of W-free Co-Al-V-Nb-Ta-based Superalloys	43

	12
3.1 Abstract.....	43
3.2 Introduction.....	43
3.3 Experimental Methods	45
3.4 Results and Discussion	49
3.4.1 Transformation Temperatures	49
3.4.2 $\gamma + \gamma'$ Microstructure	52
3.4.3 Lattice Misfit	59
3.4.4 Oxidation	62
3.4.5 Creep Properties	66
3.4.6 Hardness	70
3.5 Conclusions.....	73
3.6 Acknowledgements.....	74
3.7 Competing Interests Statement	75
3.8 Supplementary Information	75
3.8.1 Composition.....	75
3.8.2 DSC Curves	76
3.8.3 Microstructure	77
3.8.4 Effect of Quenching Rate	80
3.8.5 Lattice Misfit	84

	13
3.8.6 Oxidation	87
3.8.7 Post-Crept Microstructure	90
4. Lattice misfit and aging of quaternary (Co,Ni)-12.5 at.%(Ta,Al) alloys with $\gamma + \gamma'$ microstructure	94
4.1 Abstract	94
4.2 Introduction	94
4.3 Experimental Methods	97
4.4 Results and Discussion	100
4.4.1 Lattice Misfit	101
4.4.2 Transformation Temperatures	106
4.4.3 Aged Microstructure	109
4.4.4 Electron Backscatter Diffraction	116
4.5 Conclusions	118
4.6 Acknowledgements	119
4.7 Competing Interests Statement	119
4.8 Supplemental	119
4.8.1 Calculation of Interfacial Strain	120
4.8.2 CoNi69 Needlelike precipitates	122

5. Microstructure and Mechanical Properties of L1 ₂ -strengthened Co-Fe-Ni-based Superalloys	124
.....	124
5.1 Abstract.....	124
5.2 Introduction.....	124
5.3 Experimental Methods	129
5.4 Results and Discussion	132
5.4.1 Microstructure	132
5.4.2 Transformation Temperatures	141
5.4.3 Lattice Misfit	144
5.4.4 Oxidation behavior	146
5.4.5 Hardness	149
5.4.6 Temperature Dependence of Yield Strength	151
5.4.7 Creep Properties	154
5.5 Conclusions.....	158
5.6 Acknowledgements.....	159
5.7 Competing Interests Statement	160
5.8 Supplementary Information	160
5.8.1 Element Cost.....	160
5.8.2 Composition.....	161

		15
5.8.3	Microstructure	161
5.8.4	Transformation Temperatures	163
5.8.5	Lattice Misfit	164
5.8.6	Oxidation	165
5.8.7	Mechanical Tests	167
6.	Machine-Learning Prediction of Steady-State Creep Strain Rate in γ/γ' Cobalt-based Superalloys.....	169
6.1	Abstract.....	169
6.2	Introduction.....	169
6.3	Data Collection Methods	173
6.3.1	Experimental Errors.....	176
6.4	Computational Methods.....	179
6.5	Results and Discussion	185
6.5.1	ML Prediction of Lattice Misfit.....	186
6.5.2	ML Prediction of Solvus Temperature	189
6.5.3	ML Prediction of Solidus Temperature	192
6.5.4	ML Prediction of Liquidus Temperature.....	195
6.5.5	ML Prediction of Hardness.....	198
6.5.6	ML Prediction of Yield Strength (at Various Temperatures).....	204

	16
6.5.7	Effect of K-means Clustering 208
6.5.8	ML Prediction of Steady-State Creep Rate 210
6.5.9	Data Validation..... 211
6.6	Future Work 219
6.7	Conclusions..... 219
6.8	Acknowledgements..... 220
6.9	Competing Interests Statement 220
6.10	Supplementary Information 221
7.	Development of a W-free CoFeNi-based High-Entropy Superalloy with High γ' Volume Fraction 224
7.1	Abstract..... 224
7.2	Introduction..... 224
7.3	Experimental Methods 227
7.4	Results and Discussion 229
7.4.1	Transformation Temperatures 229
7.4.2	Microstructure 236
7.4.3	Volume Fraction of γ' phase..... 240
7.5	Conclusions..... 245
7.6	Acknowledgements..... 245

	17
7.7 Competing Interests Statement	246
8. References	247
9. Summary and Future Work.....	273
10. Appendix.....	276
10.1 Scanning Electron Microscopy	276

List of Figures

Figure 2-1. Dark-field transmission electron micrograph of Co-9Al-7.5W (at.%) aged at 900 °C for 3 days showing coherent, blocky γ' precipitates in γ matrix; selected area diffraction pattern in insert show $L1_2$ superlattice spots. Reproduced from [7]..... 35

Figure 2-2. Yield strength as a function of average precipitate radius $\langle R \rangle$, considering mechanisms of precipitate shearing and dislocations bowing through Orowan bypass. The antiphase boundary between two dislocations is also illustrated in the shearing example..... 38

Figure 2-3. The three creep regimes at constant stress and temperature. In the primary stage, strain rate starts fast but decreases to steady-state. In the steady-state stage, strain rate does not change with time. In the tertiary state, strain rate accelerates until fracture..... 40

Figure 3-1. Temperature ranges for two- and single-phase microstructures, with solvus, solidus, and liquidus temperatures marked for each alloy in °C) (standard deviation is shown in error bars). Also shown are “previous-generation” Co-Ta-V and Co-Nb-V alloys from Tirado Reyes et al. [26,34], as well as the (metastable) Co-based superalloy with the highest solvus temperature Co-30Ni-12Al-8Ta from Chen et al. [65], the highest-solvus stable alloy Co-30Ni-10Al-2Ti-4Ta-5V from Chen et al. [13], the original γ' Co-based superalloy Co-9.2Al-9W from Sato et al. [7], and the highest-solvus Co-Al-Mo alloy, Co-32Ni-9.9Al-1.4Ti-1.7Ta-4.6Mo from Makineni et al. [52]..... 50

Figure 3-2. SEM micrographs of $\gamma + \gamma'$ microstructure for alloys aged at 850°C for 72 and 1000 h. The γ' phase coalesces into plates, creating thin channels within the plates and thick

channels between plates (as highlighted in 20Ni-8Cr at 1000 h aging, with a red horizontal and vertical arrow, respectively)..... 55

Figure 3-3. SEM micrographs showing representative grain-boundary triple junctions (highlighted in red) for 20Ni-4Cr and 20Ni-8Cr at all aging times. Grain boundaries may exhibit coarse γ' precipitates which are not aligned in either grain (example circled in 20Ni-4Cr for 1000 h) or may show γ' merged across the grain boundary (example circled in 20Ni-8Cr for 1000 h). Occasionally, a γ' -depleted region is present next to a grain boundary (example circled in 20Ni-8Cr for 500h)..... 59

Figure 3-4. Plot of lattice misfit as a function of Ni content for the low- and high-Cr alloys. These data points are an average of all clear reflection pairs, regardless of whether they were collected from APS or lab XRD. 61

Figure 3-5. Oxidation behavior at 850 °C for all alloys, shown as plots of time dependence of: (left) mass gain normalized by initial surface area and (right) square of normalized mass gain, with line of best-fit according to Eq. (1) whose slopes (parabolic rate constant k) are given in units of $\text{mg}^2/(\text{cm}^4\text{h})$ 63

Figure 3-6. Backscattered SEM micrographs of cross-section of specimens oxidized in TGA instrument (850 °C / 20 h), showing top oxide surface scale (marked S), an intermediated mixed oxide scale (marked M) and the bulk alloy. The surface scale of 10Ni-4Cr is absent because of spalling prior to metallographic mounting..... 65

Figure 3-7. Double logarithmic plot of secondary strain rate vs compressive stress at 850 °C, with stress exponents given next to each curve. Color represents Ni content (red = 10%, blue =

20%, green = 30%) and symbol shape represents Cr content (triangle = 4%, square = 8%). Best-fit lines are shown, as solid lines for 4Cr alloys and dashed lines for 8Cr alloys..... 67

Figure 3-8. Double logarithmic plot of secondary strain rate vs compressive stress at 850 °C for the alloys in this study (red, green, blue, with data points shown in Fig. 3-7) compared to previous-generation alloys (gray), as well as W-containing alloys (black). Symbols which are fully filled are for alloys with 1.5Ta and 1.5Nb; symbols which are filled on the left half are for alloys with 3Ta-0Nb; symbols which are filled on the right half are for alloys with 0Ta-3Nb. Hollow symbols are for alloys with neither Ta nor Nb, and represent the Co-Al-W family [26,34,71]... 69

Figure 3-9. SEM micrograph of creep deformed alloys, with compressive stress applied in the vertical direction. (left) microstructure of γ' phase rafted horizontally for 30Ni-8Cr. (right) Grain boundary sliding in 30Ni-8Cr, highlighted in red..... 70

Figure 3-10. Plot of hardness as a function of aging time (on a logarithmic scale). Samples were tested in the as-homogenized state (0 h), and after aging at 850°C between 24 and 1000 h. 71

Figure 4-1 (Top) Ni-Al binary phase diagram with Ni-12.5Al composition highlighted, reproduced from[93]. (Middle) Co-Ta binary phase diagram with Co-12.5Al composition highlighted, reproduced from[97]. (Bottom) Partial quaternary isothermal section from the Co-Ni-Ti-Al system showing continuous $\gamma+\gamma'$ region, reproduced from [98]. 97

Figure 4-2. Schematic illustration showing how interfacial stress may result in a tetragonal distortion of the γ matrix. In an alloy with positive lattice misfit, the γ' lattice parameter is larger than that of the γ and hence experiences a hydrostatic compressive stress to maintain coherency.

The γ , which exists as thin films between the γ' experiences biaxial tensile stress, stretching two parameters (a) and leading to a Poisson contraction of the third parameter (c). The short parameter is aligned perpendicular to the γ/γ' interface and is oriented differently in the horizontal and vertical γ channels..... 100

Figure 4-3. Neutron data from alloy CoNi0 in Bank 2, with the highest resolution, in blue. The red line is the background, and the green line is the calculated Pawley peak fitting. Red and blue dashes at the bottom indicate the locations of γ' and tetragonal γ peaks. 101

Figure 4-4. Lattice parameters for the γ' phase (black), the tetragonally-distorted γ phase (labelled “a”(red) and “c”(blue)), and calculated unstrained γ phase (green, labelled “0”). 102

Figure 4-5. Lattice parameters for γ' (black triangles) and calculated cubic γ (black circles). Error bars for the lattice parameters are smaller than the markers used. Lattice misfit (%) is plotted in red (error bars smaller than markers), and interfacial stress (MPa) is in blue..... 105

Figure 4-6. DSC thermograms on heating for alloys CoNi14-CoNi100. Because DSC data were collected on homogenized and air-cooled samples, the γ' fraction formed on cooling (rather than aging) was low, and therefore the solvus peaks are small. An expanded view of the most-visible solvus peak, in CoNi31, is presented in the inset figure..... 107

Figure 4-7. Solvus, solidus, and liquidus temperatures for alloys CoNi14-CoNi100. DSC data were not collected for CoNi0..... 108

Figure 4-8. SEM images of $\gamma+\gamma'$ microstructure for alloys CoNi0-CoNi50, up to 1000 hrs. aging at 750 °C at 50,000x magnification..... 110

Figure 4-9. BS image showing microstructure of alloy CoNi100 after homogenization and aging for 1 hour.....	111
Figure 4-10. SE images of γ' and γ microstructure in alloys CoNi69 to CoNi100, aging up to 1000 hours. Cuboidal γ' was completely consumed by the lamellar discontinuous precipitate in alloys CoNi86 and CoNi100 at 1000 hours.	112
Figure 4-11. BSE image of a region with discontinuous precipitation in CoNi69 after 1000h aging at 750 °C.....	113
Figure 4-12. A region in alloy CoNi86 with lamellar λ_3 and cubic γ' phases, aged 10 h. As the alloy ages, the lamellar morphology consumes the cubic morphology, and completes consumption between 100 and 1000 h aging.....	114
Figure 4-13. Backscatter electron imaging of discontinuous precipitation in alloys CoNi69 to CoNi100, aging up to 1000 h at 1,000x magnification. CoNi100 aged for 1 h is shown with higher magnification.	115
Figure 4-14. EBSD results for CoNi100 aged 100h (right) phase map showing the 3 identified crystal structures. Lamellar precipitates which discontinuously form appear to have the same crystal structure as the globular precipitates previously labelled λ_3 (left) electron image captures synchronously. (bottom) crystal structure for the phase with R-3m symmetry.....	117
Figure 5-1. Secondary electron SEM micrographs of representative grain interiors showing γ + γ' microstructure in alloys aged at 850 °C between 24 and 1000 h.	135

Figure 5-2. Secondary electron SEM micrographs showing representative grain triple junctions in alloys aged at 850 °C between 24 and 1000 h. Some higher-magnification backscatter inserts are included, all with 2 μm scalebars, to illustrate triple junction precipitates..... 137

Figure 5-3. Secondary electron SEM micrographs showing 18Fe8Cr alloy aged 1000 h at 850 °C, with $\gamma + \gamma'$ matrix containing globular precipitates labelled with red arrows, needle-like precipitates with purple arrows, and depletion zones with blue arrows. 138

Figure 5-4. Plot of γ' volume fraction as a function of Fe concentration for our six Fe- and Cr-containing alloys aged for 1000 h at 850 °C. Reference 0Fe and 10Fe alloys from previous studies [152,153] are also connected to the red and blue lines. Literature data are shown for Co-9Al-7W-0/2Fe aged for 96 h at 850 °C [129], Co-7Al-7W-0/20Fe aged for 200 h at 765 °C[122], Co-9Al-9W-0.12B-0/16Fe aged for 200 h at 900 °C [61], and Co-30Ni-4Cr-10Al-6W-0.1B-xFe aged for 4096 h at 900 °C [132]. 140

Figure 5-5. Plot of solvus, solidus, and liquidus temperatures as a function of Fe concentration for all 6 alloys, as well as literature data [61,122,128,129,131,132,152]. 142

Figure 5-6. Plot of lattice parameter a for γ' phase (y-axis) vs. γ phase (x-axis) for 4Cr alloy series (solid symbols) and 8Cr alloys (hollow symbols). Dotted lines represent constant lattice misfit δ . Error bars correspond to esds values from GSAS-II. 145

Figure 5-7. Oxidation behavior in dry air at 850 °C for up to 20 h. (a) plot of mass gain per surface area as a function of time. (b) plot of parabolic oxidation rate constant vs Fe content. Also shown in both figures are results for 0Fe4Cr and 0Fe8Cr alloys, collected using the same instrument [152]...... 147

Figure 5-8. Secondary electron micrographs of cross-sections of specimens oxidized in TGA instrument (850 °C / 20 h), showing three distinct oxide layers: a top scale enriched in Co, a middle layer enriched in Fe, and a bottom layer enriched in Ni and other elements, as illustrated in EDS elemental maps..... 148

Figure 5-9. Time evolution of microhardness for all 6 alloys aged at 850 °C. Error bars represent the standard deviation of 10 indents. Small offsets are added in the x-axis to improve readability. 149

Figure 5-10. (a) Plot of yield strength vs temperature for experimental alloys, as well as literature alloys: Co-9Al-9W [157], CTC-1 with composition Co-11Ti-15Cr [10], MAR-M302 (non- γ' -strengthened commercial Co-based superalloy) [158], IN713C (γ' -strengthened commercial Ni-based superalloy with up to 2.5% Fe) [159], and IN718 (γ' - and γ'' -strengthened commercial Ni-based superalloy with 18 wt.% Fe) [116]. Gray and black symbols are from the literature; hollow symbols are Ni-based alloys.(b) Plot of yield strength vs temperature for our alloys, showing the first test of each alloy as solid symbols, and the second test as hollow symbols. 151

Figure 5-11. Plot of yield strength (peak value at 800 °C) vs γ' volume fraction, for our six Fe-containing alloys and reference Co-9Al-9W at 789 °C [157]. Our data contains two tests: one at 800 °C, and the other (labeled with “-2”) interpolated from results at 775 and 825 °C..... 153

Figure 5-12 Double logarithmic plot of compressive strain rate vs. stress at 850 °C for our experimental Fe-containing alloys with two Cr concentrations (4 and 8 at.%), as well as the

reference alloy (0Fe)[152], with 4 or 8 at.% Cr. Also shown is Co-9Al-9W with 0, 4, 8 at.% Cr[71].

..... 155

Figure 5-13. Secondary SEM images of specimens after compressive creep (stress was applied in the vertical direction) at 850 °C. Images were chosen to display the most pronounced examples of n-type rafting, the severity of which depends on grain orientation. 157

Figure 6-1. Early stage of the ML model, predicting solidus temperature. Blue dots are from our machine-learning model, and gray dots are from CALPHAD, using the most up-to-date TCNI-11 database (as of 2022). Predicted values which lie on the red line exactly match experimental results. 171

Figure 6-2. Schematic showing the model design. 184

Figure 6-3. Test fitting of the predicted lattice misfit value (%) vs the experimental misfit value. Error bars correspond to our estimated reproducibility of this experimental measurement, taken as $\pm 20\%$ of the misfit value. 187

Figure 6-4. Plots for (a) misfit feature importance, (b) histogram of database measurements, (c) standard deviation, and (d) average accuracy plot. 188

Figure 6-5. Test fitting of the predicted solvus temperature vs the experimental value. Error bars correspond to our estimated reproducibility of this experimental measurement, taken as ± 20 °C. 189

Figure 6-6. Plots for (a) solvus feature importance, (b) histogram of database measurements, (c) standard deviation plot, and (d) average accuracy plot. 192

Figure 6-7. Test fitting of the predicted solidus temperature vs the experimental value. Error bars correspond to our estimated reproducibility of this experimental measurement, taken as ± 20 °C.	192
Figure 6-8. Plots for (a) solidus feature importance, (b) histogram of database measurements, (c) standard deviation plot, and (d) average accuracy plot	194
Figure 6-9. Test fitting of the predicted liquidus temperature vs the experimental value. Error bars correspond to our estimated reproducibility of this experimental measurement, taken as ± 20 °C.	196
Figure 6-10. Plots for (a) liquidus feature importance, (b) histogram of database measurements, (c) standard deviation plot, and (d) average accuracy plot	198
Figure 6-11. Test fitting of the predicted peak hardness vs the experimental value. Error bars correspond to our estimated reproducibility of this experimental measurement, taken as ± 50 HV.	202
Figure 6-12. Plots for (a) hardness feature importance, (b) histogram of database measurements, (c) standard deviation plot, and (d) average accuracy plot	203
Figure 6-13. Test fitting of the predicted yield strength vs the experimental value. Error bars correspond to our estimated reproducibility of this experimental measurement on different nominally identical samples, taken as ± 100 MPa.	205
Figure 6-14. Plots for (a) creep feature importance, (b) and (c) histogram of database measurements, (d) standard deviation plot, and (e) average accuracy plot	208

Figure 6-15. Plots of cluster quality vs k value. (left) sum of squared distances (lower is better); (middle) Silhouette value (closer to 1 is better); (right) Calinski-Harabasz index (higher is better).
 209

Figure 6-16. Double logarithmic plot of time to 1% steady-state creep strain (which is inversely proportional to a strain rate) vs the experimental value. Error bars correspond to our estimated reproducibility of this experimental measurement, taken as $\pm 33\%$ of the value. 210

Figure 6-17. Plots of mean-squared error (MSE) vs seed number for 100 seeds randomly creating test/training data splits. 211

Figure 6-18. Double logarithmic plot of predicted time to 1% steady-state creep (which is inversely proportional to a strain rate) vs the experimental value. Error bars correspond to our estimated reproducibility of this experimental measurement, taken as $\pm 33\%$ of the value. Validation MSE = 1.06E10. Colors represent the family (green-yellow: W-free, Fe-free; blue-purple: W-free, Fe-containing; red-orange: W-containing, Fe-containing. Hollow symbols represent elements with Fe, and solid symbols represent Fe-free alloys. Squares indicate alloys with 4% Cr, and circles indicate alloys with 8%Cr. 214

Figure 6-19. Feature importance for predicting creep on the 16-alloy validation set..... 217

Figure 7-1. DSC measurements for solvus, solidus, and liquidus of all 6 alloys. Reported measurement averages heating and cooling cycles, and error bars correspond to the standard deviation..... 230

Figure 7-2. Plot of solvus vs Fe at.%. Hollow symbols represent Cr = 8 at.%, solid symbols have less Cr. Present work is shown in purple triangles. Prior work of related alloys is shown in

circles [152,175]. Additional literature data shows Co-9Al-7W-xFe (black)[129], Co-9Al-9W-0.12B-xFe (black)[61], Co-7Al-7W-xFe (green)[184], Co-20Ni-10Cr-10Al-7W-0.1B-xFe (mustard) [131] and Co-30Ni-4Cr-10Al-6W-0.1B-xFe (orange) [181]. 232

Figure 7-3. Plot of solvus vs Fe/(Co+Fe) at.%. Hollow symbols represent Cr = 8 at.%, solid symbols have less Cr. Present work is shown in purple triangles. Prior work of related alloys is shown in circles [152,175]. Additional literature data shows Co-9Al-7W-xFe (black)[129], Co-9Al-9W-0.12B-xFe (black)[61], Co-7Al-7W-xFe (green)[184], Co-20Ni-10Cr-10Al-7W-0.1B-xFe (mustard) [131] and Co-30Ni-4Cr-10Al-6W-0.1B-xFe (orange) [181]. 233

Figure 7-4. Plot of solvus vs Fe/(Ni+Fe) at.%. Hollow symbols represent Cr = 8 at.%, solid symbols have less Cr. Present work is shown in purple triangles. Prior work of related alloys is shown in circles [152,175]. Additional literature data shows Co-9Al-7W-xFe (black)[129], Co-9Al-9W-0.12B-xFe (black)[61], Co-7Al-7W-xFe (green)[184], Co-20Ni-10Cr-10Al-7W-0.1B-xFe (mustard) [131] and Co-30Ni-4Cr-10Al-6W-0.1B-xFe (orange) [181]. 234

Figure 7-5. Plot of solvus vs Ni/(Ni+Co) at.%. Hollow symbols represent Cr = 8 at.%, solid symbols have less Cr. Present work is shown in purple triangles. Prior work of related alloys is shown in circles [152,175]. Additional literature data shows Co-9Al-7W-xFe (black)[129], Co-9Al-9W-0.12B-xFe (black)[61], Co-7Al-7W-xFe (green)[184], Co-20Ni-10Cr-10Al-7W-0.1B-xFe (mustard) [131] and Co-30Ni-4Cr-10Al-6W-0.1B-xFe (orange) [181]. 235

Figure 7-6. SE micrograph of alloy HEA aged 850 °C for 1000h, (left) bulk $\gamma+\gamma'$ region, (right) grain boundaries at triple point, which are free of additional phases. 237

Figure 7-7. SE micrograph of alloy CCA aged 850 °C for 1000h, (left) bulk $\gamma+\gamma'$ region, (right) grain boundaries at triple point, both of which contain an additional intermetallic phase in moderate ~10% volume fraction..... 237

Figure 7-8. SE micrograph of alloy 30Ni aged 850 °C for 1000h, (left) bulk $\gamma+\gamma'$ region, (center) grain boundaries at triple point, which are free of additional phases, (right) grain boundary with needlelike precipitate, possibly due to oxygen diffusing through grain boundaries.. 238

Figure 7-9. SE micrograph of alloy HEA aged 850 °C for 1000h, (left) bulk $\gamma+\gamma'$ region, (right) grain boundaries at triple point, which are free of additional phases. 239

Figure 7-10. Plot of γ' volume fraction vs Fe concentration. Hollow symbols represent Cr = 8 at.%, solid symbols have less Cr. Present work is shown in purple triangles. Prior work of related alloys is shown in circles [152,175]. Additional literature data shows Co-9Al-7W-xFe (black)[129], Co-9Al-9W-0.12B-xFe (black)[61], and Co-30Ni-4Cr-10Al-6W-0.1B-xFe (orange) [181]. Additionally, we plot the high entropy alloy $(\text{CoFeNi})_{84}\text{V}_8\text{Ti}_8$ [195]..... 240

Figure 7-11. Plot of γ' volume fraction vs Fe/(Fe+Co) atomic ratio. Hollow symbols represent Cr = 8 at.%, solid symbols have less Cr. Present work is shown in purple triangles. Prior work of related alloys is shown in circles [152,175]. Additional literature data shows Co-9Al-7W-xFe (black)[129], Co-9Al-9W-0.12B-xFe (black)[61], and Co-30Ni-4Cr-10Al-6W-0.1B-xFe (orange) [181]. Additionally, we plot the high entropy alloy $(\text{CoFeNi})_{84}\text{V}_8\text{Ti}_8$ in maroon [195]. 242

Figure 7-12. Plot of γ' volume fraction vs Fe/(Fe+Ni) atomic ratio. Hollow symbols represent Cr = 8 at.%, solid symbols have less Cr. Present work is shown in purple triangles. Prior work of

related alloys is shown in circles [152,175]. Co-30Ni-4Cr-10Al-6W-0.1B-xFe (orange) [181] and the high entropy alloy (CoFeNi)₈₄V₈Ti₈ in maroon [195]. 243

Figure 7-13. Plot of γ' volume fraction vs Ni/(Ni+Co) atomic ratio. Hollow symbols represent Cr = 8 at.%, solid symbols have less Cr. Present work is shown in purple triangles. Prior work of related alloys is shown in circles [152,175]. Co-30Ni-4Cr-10Al-6W-0.1B-xFe (orange) [181] and the high entropy alloy (CoFeNi)₈₄V₈Ti₈ in maroon [195]. 244

Figure 9-1. Chart showing the completed (yellow) and proposed future (teal) W-free Co-based superalloy compositions, with design considerations for what effect each alloy would clarify. 273

Figure 9-2. Table of compositions, calculated density, solvus temperature, and γ' volume fraction for alloys studied in this work and proposed new alloys (1-10) with their short names (teal colors). Cells are color-coded such that green applies to the maximum value in a given range, and red applies to the minimum value. 275

1. INTRODUCTION

For the last seven decades, superalloys based on nickel, iron, and/or cobalt [1] have proven to be the optimal material for gas turbines blades and disks, which must maintain creep resistance at high temperatures for very long times under highly oxidative and corrosive environments. These three elements (Ni, Fe, Co) are highly soluble in each other, have very similar density and melting points, and excellent strength and toughness. Nickel-based superalloys have seen much wider use than Co- or Fe-based superalloys, because of their stable γ/γ' microstructure (fcc γ -matrix with coherent $L1_2$ γ' -precipitates) which impede dislocation motion—especially at high temperature—due to Kear-Wilsdorf locking [2–5].

However, recent developments have enabled γ' -strengthened Co-based superalloys [6,7]. The γ' phase is based on variations of the following $L1_2$ phases: $Co_3(Al,W)$, Co_3Ti , $Co_3(Nb,Mo)$, $Co_3(Al,V)$, $Co_3(Ti,V)$, $Co_3(Nb,V)$, or $Co_3(Ta,V)$ [8–14]. When fully alloyed—typically with Ni to widen the $\gamma + \gamma'$ phase field, with Al and Cr for oxidation resistance, and with combinations of γ' -formers (e.g., Ti, W, Ta, Nb, V, Mo), and grain boundary strengtheners (e.g., C, B, Zr)—these alloys show comparable creep-, coarsening- and corrosion-resistance as their Ni-based counterparts. Additionally, they typically show positive, rather than negative lattice misfit, which may improve their rafting behavior [15–23].

While these new $L1_2$ -strengthened Co-based superalloys show promising results, they are hampered by a few disadvantages:

- These alloys typically show a narrow $\gamma + \gamma'$ phase field, where small compositional changes may disrupt the microstructure and promote topologically close-packed phases (TCPs) or

other undesirable intermetallics. In other cases, γ' may appear at low aging times, but later prove to be metastable. One well-studied method of increasing the phase stability is to add Ni, which is especially prevalent in the so-called “CoNi” base superalloys and “high entropy superalloys” (HESAs) [24].

- These alloys are often undesirably dense, considering that one of their main applications would be as turbine blades on aircraft. The most-studied family of Co-based superalloys relies on a γ' composition of $\text{Co}_3(\text{Al,W})$, where Al and W fill the L_{12} corner sites. For example, the ternary Co-9Al-9W, at.% (Co-3.6Al-24.5W, wt%) has a theoretical density of 9.3 g/cm^3 , compared to most Ni-based superalloys which have a density near 8.9 g/cm^3 [25]. Several families of W-free or low-W alloys have been developed which may even reach density values below 8.0 g/cm^3 [26–28].
- The material cost for these alloys makes them unattractive for commercial applications since Co is approximately two to four times the cost of Ni; but more importantly, Co is a strategic mineral with extensive use in current Li-ion batteries, which is primarily mined from politically unstable locations, and thus its price may fluctuate volatily from year to year [29,30]. However, material cost is of reduced importance in turbine blade applications because the alloys usually undergo expensive processing steps to eliminate creep-prone grain boundaries [31] so that cost is driven by the processing steps; furthermore, turbine blades are easy to recycle. Alloy cost can be further reduced by substituting a large fraction of Co for Ni or—significantly better—Fe, although Fe additions have proven deleterious in all previously-studied Co-based superalloys.

This research explores the compositional $\gamma + \gamma'$ space of W-free, Co-based superalloys with the goal of developing alloys with comparable high-temperature performance to the denser Co-Al-W-based superalloys.

2. BACKGROUND

2.1 Historical Development of Co-based Superalloys

2.1.1 Discovery and Rediscovery of L₁₂-strengthened Co-based Superalloys

Although Co-based superalloys have been used without γ' , these have been relegated to low-stress, high-temperature applications where Co's melting point or corrosion resistance delivered better performance than Ni or Fe.

The first known discovery of an L₁₂-strengthened Co-based superalloy was in Lee's PhD thesis, in the Co-Al-W system [6]. Unfortunately, Lee never published his finding in a peer-reviewed journal, and his discovery was lost until the renewed interest in Co-based superalloys in recent years.

Sato et al. are credited with the discovery of L₁₂-strengthened Co-based superalloys, although we now know that this research was a rediscovery [7]. This monumental article (published in *Science* in April 2006), regarding Co-Al-W-based alloys with $\gamma + \gamma'$ microstructure, has sparked the current research field of Co-based superalloys. As of March 2023, his publication garnered slightly more than 1,000 citations. In particular, they highlighted the ternary Co-8.8Al-9.8W, Co-9.2Al-9W and Co-9Al-7.5W, the quaternary Co-8.8Al-9.8W-2Ta and Co-8.8Al-9.8W-2Mo, and the quinary Co-20Ni-10Al-10W-2Ta (at.%) compositions.

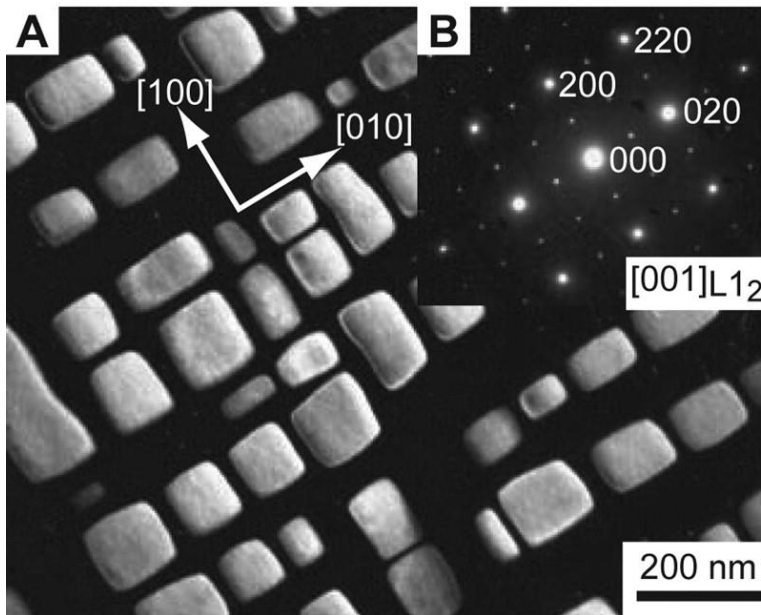


Figure 2-1. Dark-field transmission electron micrograph of Co-9Al-7.5W (at.%) aged at 900 °C for 3 days showing coherent, blocky γ' precipitates in γ matrix; selected area diffraction pattern in insert show $L1_2$ superlattice spots. Reproduced from [7]

2.1.2 Pedigree of Current Work

Two W- and Mo-free systems, Co-Nb-V and Co-Ta-V were computationally predicted by Nyshadham et al. [32], and were shown to exhibit $\gamma + \gamma'$ microstructure by Reyes et al. [11]. Complex Co-Nb-V and Co-Ta-V alloys with $\gamma + \gamma'$ microstructure were achieved via additions of Ni, Al, Ti, Cr and B [33,34]. These W- and Mo-free superalloys have density in the range 8.25-8.65 g/cm³, and they show excellent creep- and oxidation resistance.

My initial W-free superalloys are based on hybrid of the two above families to create complex, 9-element, Co-based compositions, which includes both Nb and Ta as γ' -formers (beside Al, Ti, and V), Cr to increase oxidation resistance, Ni to replace Co, and B to strengthen grain boundaries.

Upon realizing that these alloys contain some of the same γ' -formers as the $L1_2$ phase $(\text{Co,Fe})_3\text{V}$ [35], I attempted substituting Fe into these alloys, even though previous attempts to add Fe to Co-based superalloys lead to disappointing results. While these Fe-containing alloys had worse mechanical properties than the base version, they had significantly improved phase stability and mechanical properties compared to W-containing Co-based superalloys with comparable Fe levels. Further iterations of these alloys attempted to stabilize the microstructure with other γ' -formers, and also tap into the “high-entropy” effect by using equiatomic amounts of γ - and γ' -formers.

2.2 Mechanical Properties of High-Temperature Alloys

2.2.1 Theory of Ambient-temperature Deformation

Strength is mostly independent of temperature at low homologous temperature ($< 1/2 T_m$). At room temperature, cast $\gamma + \gamma'$ superalloys are primarily strengthened by (i) solid solution strengthening and (ii) dislocation interactions between the γ matrix (FCC crystal structure) and coherent γ' precipitates ($L1_2$ crystal structure).

When dislocations move through the γ matrix and encounter a γ' precipitate, they may bow to bypass the precipitates, or directly shear through them, depending on precipitate size. If dislocations can shear through the coherent γ' precipitates, the material may exhibit “ordered strengthening” because the dislocation creates an antiphase boundary (APB) which requires additional energy to expand through the sheared precipitate. To reduce APB energy, it is common for dislocations to pair up as so-called “super-dislocations,” where the leading dislocation creates

the APB and the trailing dislocation annihilates it, keeping the total APB area small. In general, particle-cutting stress is proportional to \sqrt{R} , where R is the particle radius [2,36]. For a dislocation pair strongly interacting with each other as they pass through an ordered phase, the cutting stress, τ_c , is

$$\tau_c = \sqrt{\frac{3}{2}} \cdot \left(\frac{Gb}{R}\right) \cdot \varphi^{\frac{1}{2}} \cdot \frac{w}{\pi^{\frac{3}{2}}} \cdot \left(\frac{2\pi\gamma_{APB} \cdot R}{wGb^2} - 1\right)^{\frac{1}{2}}$$

where G is the shear modulus, b is the burger's vector, R is the particle radius, φ is the volume fraction, $w \sim 1$ is a dimensionless constant (added to convey some uncertainty), and γ_{APB} is the antiphase boundary energy [2].

As illustrated in Fig. 2-2, the energy required to bypass precipitates by bowing increases with decreasing particle spacing or precipitate radius according to Orowan strengthening, $\tau_{Or} = \frac{Gb}{L} \propto \frac{1}{R}$, where τ_{Or} is the Orowan stress, G is the shear modulus, b is the burger's vector, L is the distance between non-shearable particles, and R is the precipitate radius [2,36]. Energy required to bypass precipitates decreases with precipitate spacing (which decreases with coarsening), so the path of least resistance for a dislocation can be graphed as a function of average precipitate radius $\langle R \rangle$.

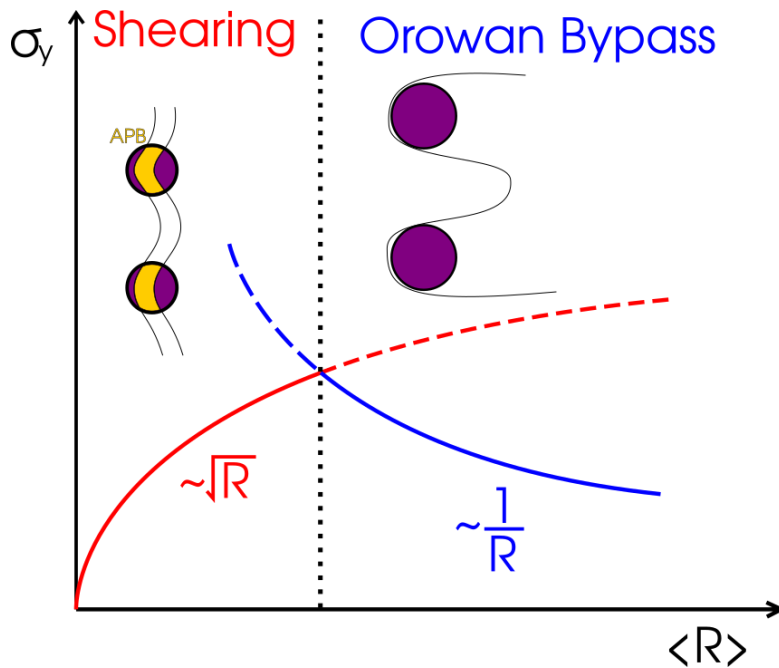


Figure 2-2. Yield strength as a function of average precipitate radius $\langle R \rangle$, considering mechanisms of precipitate shearing and dislocations bowing through Orowan bypass. The antiphase boundary between two dislocations is also illustrated in the shearing example.

Solid solution strengthening provides additional strength due to elastic interactions between dislocations and strain caused by solid solution atoms (size mismatch), and the different bonding between the various atoms (modulus mismatch).

2.2.2 Theory of High-temperature Deformation (Creep)

At high temperature ($> \frac{1}{2} T_m$), additional mechanisms may be thermally activated such that deformation may occur even at stresses below the yield point. This type of deformation at high temperatures over long periods of time is called “creep,” and is the primary failure mode for turbine blades.

Creep typically occurs in three stages as shown in Fig. 2-3 [37]:

1. In the **primary** stage, initial creep rate is fast but slows down. The material typically begins with a low dislocation density (allowing for fast creep rate) which rapidly increases as dislocations interact with each other and other obstacles.
2. In the **steady-state**, or secondary stage, dislocations are created and annihilated at equal rates, resulting in a constant strain rate for a given stress and temperature. Superalloys spend most of their lifetime in this regime, which is convenient to model for a wide stress range using a Norton plot; thus, improving steady-state creep resistance is usually the primary design goal.
3. In the **tertiary** stage, deformation rate increases due to microstructural changes such as crack and cavity formation, precipitate coarsening or dissolution, or detrimental phase precipitation. In this stage, materials should no longer be in service because failure may occur suddenly.

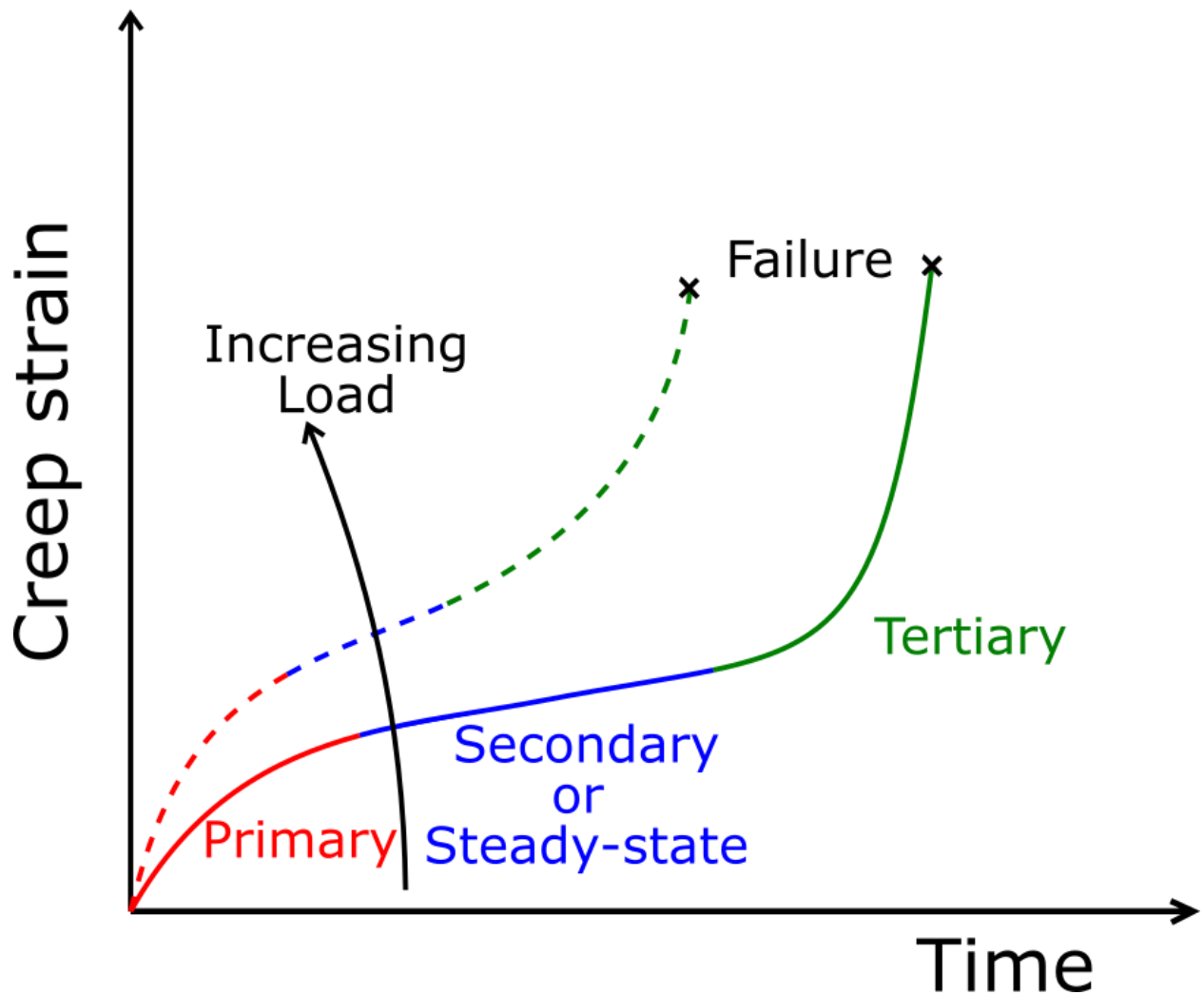


Figure 2-3. The three creep regimes at constant stress and temperature. In the primary stage, strain rate starts fast but decreases to steady-state. In the steady-state stage, strain rate does not change with time. In the tertiary state, strain rate accelerates until fracture.

The secondary creep strain rate $\dot{\epsilon}$ can be described by a power law equation [38]:

$$\dot{\epsilon} = A\sigma^n \exp\left(\frac{-Q}{RT}\right)$$

where A is a constant, σ is stress, n is the stress exponent, Q is the activation energy, R is the ideal gas constant, and T is the absolute temperature.

A common figure in superalloy research is the “Norton plot,” which graphs steady-state strain rate is against stress in a double-logarithmic axes according to the above equation. At a constant temperature, the best-fit line of these points reveals the stress exponent, n .

2.2.3 Lattice Misfit

Lattice misfit is the difference in lattice parameter between the γ and γ' phases, defined as $\delta = 2(a_{\gamma'} - a_{\gamma}) / (a_{\gamma'} + a_{\gamma})$ where $a_{\gamma'}$ and a_{γ} are the lattice constants of the two phases [39]. Cobalt-based superalloys typically have a positive lattice misfit, while Ni-based superalloys typically show negative lattice misfit.

Misfit affects dislocation motion and coarsening kinetics—however, there is not a clear “optimal” value of lattice misfit [40]. Low misfits ensure that γ' is shearable and coherent, and it lowers the driving force for coarsening. On the other hand, high misfit increases interfacial stress, which can inhibit dislocations as they shear through γ' . Misfit also plays an important role in “rafting,” which is the morphological change γ' undergoes when directionally coarsening under stress [41]. Thus, larger misfit tends to be better in low-temperature creep and higher misfit tends to be better at high temperature creep.

For this reason, and given that γ has a higher coefficient of thermal expansion than γ' , alloys with positive lattice misfit should have improved creep properties because the misfit decreases as a function of temperature. Unfortunately, it is difficult-to-impossible to experimentally isolate the effects of lattice misfit upon creep behavior because misfit strongly depends on elemental

composition, so that changing the elemental composition affects other factors which influence creep more directly, such as solid-solution strengthening or changes in γ' volume fraction [42,43].

2.2.4 Rafting in Superalloys

Rafting refers to the directional coarsening of the γ' phase under creep, which is largely influenced by lattice misfit and the elastic moduli of the two phases [39]. Rafting can be categorized as “p-type,” where γ' elongate parallel to the stress axis, and “n-type” where γ' elongate perpendicular to the stress axis.

If the lattice misfit is negative, tensile creep results in n-type rafting and compressive creep results in p-type rafting. If the lattice misfit is positive, tensile creep results in p-type rafting and compressive creep results in n-type rafting.

As my superalloys are Co-based and tested in compression, we expect to see n-type rafting when examining the post-creep microstructure. This n-type rafting is generally considered superior to p-type rafting, or even no rafting, because of the reduction in vertical γ channels [44].

3. Effects of Ni and Cr additions on $\gamma + \gamma'$ Microstructure and Mechanical Properties of W-free Co-Al-V-Nb-Ta-based Superalloys

3.1 Abstract

The effect of Ni and Cr additions on microstructure, lattice misfit, oxidation, and creep properties are investigated for six W- and Mo-free cobalt-based superalloys with compositions $\text{Co}_x\text{Ni}_{10-x}\text{Al}_y\text{Cr}_{8-y}\text{V}_3\text{Ti}_2\text{Nb}_{1.5}\text{Ta}_{1.5}\text{B}_{0.08}$ (at.%), where $x=10, 20, \text{ or } 30$ and $y=4 \text{ or } 8$. In all alloys, the $\gamma + \gamma'$ microstructure is stable for up to 1000 h upon aging at 850 °C. As Ni increases from 10 to 30 at.%, the γ' area fraction increases from 32 to 49% in the three low-Cr alloys, while remaining constant (45%) for the high-Cr alloys. All alloys show positive γ/γ' lattice misfits of 0.8 ± 0.2 %, consistent with γ' rafting observed after creep. Both Cr and Ni additions increase oxidation resistance, more so for 8% Cr than for 30% Ni, as expected from the high stability of chromium oxide. Increasing Cr from 4 to 8 at.% slightly increases creep resistance at 850 °C and increasing Ni from 10 to 30% has a similar effect.

3.2 Introduction

Nickel-based superalloys, have been the dominant high-temperature alloy system for over seven decades due to the high volume fraction of γ' -ordered L_{12} precipitates (based on the $\text{Ni}_3(\text{Al,Ti})$ phase composition) which impede dislocation motion in a fcc γ matrix; upon addition of various alloying elements, these alloys exhibit excellent deformation- and environmental resistance at temperatures as high as $\sim 1000^\circ\text{C}$ [2,4,5,45]. Recently, a similar γ/γ' microstructure (with a γ' composition based on the $\text{Co}_3(\text{Al,W})$ phase) was achieved in Co-Al-W-based alloys

[6,7], which upon further alloying additions with Ti, Cr, B, and refractory elements, display similar creep-, oxidation-, corrosion- and coarsening resistance as multicomponent Ni-based superalloys [15–21,46]. Cobalt-based superalloys show higher melting temperatures, and potentially higher wear resistance and hot corrosion resistance, than their Ni-base counterparts, but their density tends to be higher due to the high W content [47–50]. An improved operating temperature could be achieved if the solvus temperature of Co-based alloys can be raised, via alloying, to the same fraction of the liquidus temperature as for Ni-base superalloys (i.e., the same homologous solvus temperature).

In addition to γ' composition based on $\text{Co}_3(\text{Al,W})$, other γ' phases have been observed in Co-based γ matrices, based on Co_3Ti , $\text{Co}_3(\text{Nb,Mo})$, $\text{Co}_3(\text{Nb,V})$, and $\text{Co}_3(\text{Ta,V})$. This enables the creation of $\gamma + \gamma'$ microstructure in W-free, lower-density Co-based superalloys, as recently developed in the Co-Al-Mo-Nb system [9,51–53]. Another low-density, W-free Co-superalloy system is based on the Co-Ti system stabilized with Ni, Cr, Al, W, and/or V [8,10,21,54–58]. Two other W- and Mo-free systems, Co-Nb-V and Co-Ta-V, based on computational predictions by Nyshadham et al. [32], exhibit $\gamma + \gamma'$ microstructure [11]. Since this discovery, other V-based γ' compositions have also been obtained by other groups [14,59,60]. Complex Co-Nb-V and Co-Ta-V alloys with $\gamma + \gamma'$ microstructure were achieved via additions of Ni, Al, Ti, Cr and B [33,34]: two based on Co-Nb-V (Co-10Ni-5Al-4Cr-2Ti-3Nb-3V-0.04B and Co-10Ni-5Al-8Cr-2Ti-3Nb-3V-0.04B) and two based on Co-Ta-V (Co-10Ni-5Al-2Ti-3Ta-3V-0.04B, and Co-10Ni-5Al-4Cr-2Ti-3Ta-3V-0.04B). These W- and Mo-free superalloys have density in the range 8.25-8.65 g/cm³, and they show excellent creep- and oxidation resistance.

10Ni-0Cr(Ta) [34]	77 (75)	10 (9.6)	“	0	“	“	0	3 (8.9)	0.04 (0.007)
10Ni-4Cr(Ta) [34]	73 (71.4)	“	“	4 (3.5)	“	“	“	3 (9)	“
10Ni-4Cr(Nb) [26]	73 (74.7)	“	“	“	“	“	3 (4.8)	0	“
10Ni-8Cr(Nb) [26]	69 (70.9)	“	“	8 (7.3)	“	“	“	“	“

Table 3-1 Nominal compositions (at.%, and wt.% in parentheses) of investigated alloy (with both Nb and Ta), and four “previous generation” alloys (with either Nb or Ta).

These six experimental alloys are based on the previously-studied Co-Ta-V- and Co-Nb-V-based alloys [33,34], with: 3 at.% of either Nb or Ta; 0, 4 or 8 at.% Cr; and 10 at.% Ni [11,26,33,34]. Partial substitution of Co with Ni is known to stabilize the $\gamma + \gamma'$ microstructure [61,62], and it reduces alloy cost. Chromium and aluminum are added for corrosion resistance and density reduction. In Co-Al-W-based alloys, excessive Cr addition leads to precipitation of undesirable intermetallic or topologically close-packed (TCP) phases such as χ and μ [20,61], decreased solvus temperature, and reduced γ/γ' lattice misfit. Thus, in this work, Cr content is limited to 8 at.%. Finally, Al, V, Ti, Nb, and Ta are γ' -formers, while B is added for grain-boundary strengthening.

Alloys were prepared from pure elements: Co (99.9+%), Ni (99.95%), Al (99.5%), Cr (99.995%), V (99.7%), Ti (99.95%), Nb (99.8%), Ta (99.95%), and B (95-97%), purchased from Alfa Aesar (Tewksbury, MA) which were arc-melted under an Ar atmosphere six times, with a flip between each remelting. The resulting button-shaped ingots (~30 g) were encapsulated in fused silica tubes flushed with Ar, vacuum-sealed, and homogenized for 48 h at 1200 °C, followed by water quenching. Sections of the ingots were aged in evacuated fused silica tubes at 850°C for durations between 24 and 1000 h, followed by water quenching.

Alloy compositions (given in Table S3-1) were verified by Energy Dispersive Spectroscopy (EDS) using polished cross-sections of homogenized specimens in a FEI Quanta 65 Scanning Electron Microscope (SEM), with 10 mm working distance and 25 kV accelerating voltage. All aged specimens were investigated with secondary-electron- and backscatter-electron detectors using a 10 mm working distance and 30 kV accelerating voltage. Specimens for SEM were mounted in epoxy, polished down to 1 μ m diamond suspension, and etched with Carapella's reagent.

The γ' area fraction was determined in ImageJ, by a combination of thresholding and hand-tracing of precipitates, from at least five micrographs, each one with an area $>20 \mu\text{m}^2$. In many cases, the volume fraction can be assumed to be equal to the area fraction [20,63]. In an ordered cubic structure, this approximation may be an overestimate [16], but imageJ thresholding inherently underestimates area fraction by ignoring very small tertiary γ' precipitates. These very small, ~ 10 nm, tertiary γ' precipitates commonly occur in Ni- and Co-based superalloys at lower temperatures upon cooling from aging [5,64]. Vickers microhardness was measured with ten indents, spanning the full area of the sample, using a Struers Duramin-5 Micro-hardness Tester, with 300 g load and 5 s indent times.

Differential Scanning Calorimetry (DSC) was performed using a Mettler Toledo TGA/DSC 3+ instrument operating with an alumina pan and 40 mL/min N_2 cover gas, with heating and cooling rates of 5 $^\circ\text{C}/\text{min}$. Both homogenized samples and samples aged for 24 h at 850 $^\circ\text{C}$ were used to determine γ' solvus temperature, as well as solidus and liquidus temperatures, from the cooling curves. Samples were cycled at least three times above and below their solvus temperature.

On separate samples, an additional 2-cycle ramp at 10 °C/min and 60 mL/min N₂ cover gas was used to determine liquidus while minimizing composition change due to oxidation at high temperature.

Differential Thermal Analysis (DTA) was run on the same instrument over a 20 h time span, to determine oxidation behavior at 850 °C under laboratory air flowing at 40 mL/min, with 40-200 mg samples aged for 168 h in alumina pans. Oxidized samples were mounted metallographically and investigated with SEM and EDS, using the same conditions as described previously.

Synchrotron x-ray diffraction (XRD) was performed at the Advanced Photon Source (APS, at Argonne National Laboratory) on the 5-BM-C beamline with bending magnets (wavelength $\lambda = 0.6209 \text{ \AA}$, energy $E = 19.97 \text{ keV}$), to measure lattice parameters on samples aged for 168 h. Large grains made data acquisition inconsistent, so a laboratory x-ray source was used on other samples from the same alloys, which were first recrystallized (to achieve smaller grains) via the following procedure: (i) cold rolling to 50% thickness reduction in 5-10 passes, (ii) recrystallizing at 1200 °C for 5 min and (iii) aging at 850 °C for 72 h in evacuated capsules, followed by water quenching. XRD data were collected at room temperature on a STOE-STADI-MP powder diffractometer equipped with an asymmetric curved Ge monochromator (Mo-K α 1 radiation, $\lambda = 0.70930 \text{ \AA}$) and a one-dimensional Si strip detector (MYTHEN2 1K from DECTRIS). The line-focused X-ray tube was operated at 50 kV and 40 mA. The instrument was calibrated against a NIST Silicon standard (640d) prior the measurement.

Creep tests were performed on a dead-load creep frame in air at 850 °C. Cylindrical samples (10 mm height, 5 mm diameter) were prepared by electro-discharge machining from ingots which

had been homogenized, aged in vacuum-encapsulated tubes at 850 °C for 168 h, and water quenched. Creep samples were placed between boron-nitride-lubricated silicon carbide or alumina platens and deformed at monotonically increasing compressive stresses from 200-600 MPa, accumulating ~10% total strain. Minimum creep strain rate was determined at each stress level by the sample displacement rate after primary creep, measured by an extensometer and linear variable displacement transducer with a resolution of 10 μm . Deformed specimens were sectioned parallel to the applied load and imaged in SEM, using the conditions described previously.

3.4 Results and Discussion

3.4.1 Transformation Temperatures

The γ' solvus, solidus, and liquidus temperatures are shown in Fig. 3-1. One additional sample of 20Ni-4Cr was run under Ar cover gas to ensure no nitrides were being formed under N₂. The curve with Ar cover gas did not significantly differ from the curve with N₂ cover gas, so remaining tests were completed with N₂ cover gas. Raw DSC curves are shown in Figs. S3-1 and S3-2.

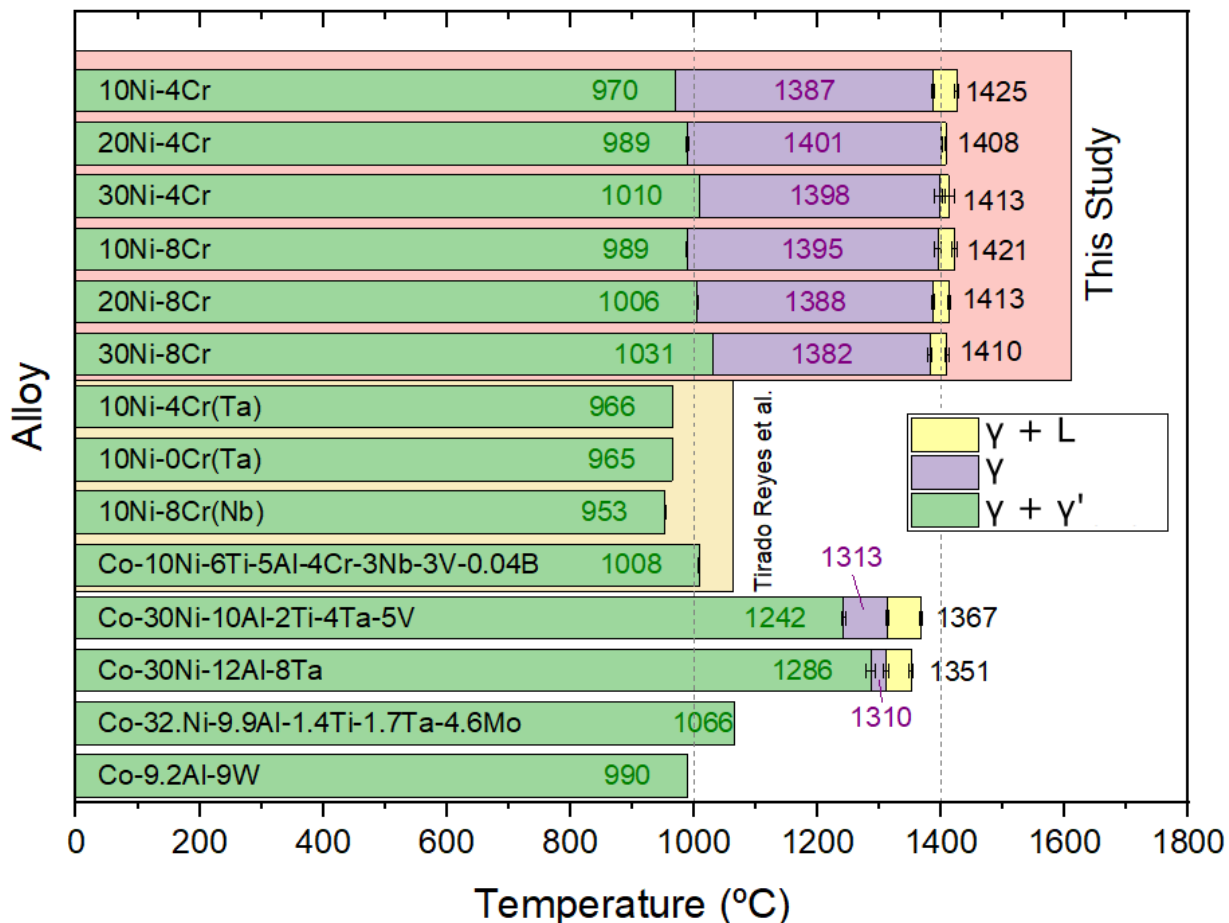


Figure 3-1. Temperature ranges for two- and single-phase microstructures, with solvus, solidus, and liquidus temperatures marked for each alloy in °C (standard deviation is shown in error bars). Also shown are “previous-generation” Co-Ta-V and Co-Nb-V alloys from Tirado Reyes et al. [26,34], as well as the (metastable) Co-based superalloy with the highest solvus temperature Co-30Ni-12Al-8Ta from Chen et al. [65], the highest-solvus stable alloy Co-30Ni-10Al-2Ti-4Ta-5V from Chen et al. [13], the original γ' Co-based superalloy Co-9.2Al-9W from Sato et al. [7], and the highest-solvus Co-Al-Mo alloy, Co-32Ni-9.9Al-1.4Ti-1.7Ta-4.6Mo from Makineni et al. [52].

Solvus temperatures increase by 15-20 °C per 10 at.% Ni addition, and 15-20 °C as Cr increases from 4 to 8 at.%, so that 30Ni-8Cr has the highest value: 1031°C. Solidus and liquidus temperatures show no clear trend with composition, and all alloys displaying similar solidus and liquidus values, i.e., 1394 ± 7 and 1416 ± 9 °C, respectively, with a narrow freezing range of ~10-40 °C.

The trend of Ni increasing solvus temperature confirms that Ni stabilizes the γ' phase, as expected because Ni-based superalloys have a much wider $\gamma + \gamma'$ phase field compared to Co-

based alloys. This is also supported from the literature in Co-Al-W alloys where Ni substitutions for Co increases the solvus temperature. For example, in Co-xNi-10Al-10W, the solvus temperature increases linearly, by an average of 24 °C per 10 at.% substitution of Ni for Co, from 0 to 80 at.% Ni. In Co-xNi-10Al-7.5W, it increases linearly, by an average of 26 °C per 10 at.% Ni [62]. Chen et al. also found that solvus in Co-xNi-12Al-2Ta increased from 949 to 1048 °C as Ni content increased from 0 to 30 at.% [65]. Zenk et al. reported that exchanging Co and Ni concentration in 44.5Co-32Ni-8Al-8Cr-5W-2.5Ti-1.5Ta-0.4Si-0.1Hf (at.%) raised the solvus from 1145 to 1195 °C [66]. However, there are alloys where Ni has been shown to decrease solvus temperature, such as Co-8Ti-11V, where up to 10 at.% Ni substitutions for Co reduced solvus from 1167 to 1108 °C[67].

Our W-free alloys have solvus values similar to Co-Al-W alloys, with 30Ni-8Cr having a solvus temperature 41 °C higher than a ternary Co-9Al-9W alloy [7] and 35 °C lower than Co-32Ni-9.9Al-1.4Ti-1.7Ta-4.6Mo, which is the Co-Al-Mo alloy with one of the highest solvus temperature in the literature [52]. The highest solvus temperature of any Co-based superalloy at the time of writing, Co-30Ni-12Al-8Ta, is 1286 °C, although its $\gamma + \gamma'$ microstructure is metastable, slowly decomposing to $\gamma + \text{CoAl} + \text{Co}_7\text{Ta}_2$ at 800 °C [65]. The highest solvus temperature of any Co-based superalloy reported as stable is 1242 °C in Co-30Ni-10Al-2Ti-4Ta-5V [13], which is stable after cold rolling and aging at 1100 °C for 360 h.

The earlier 10Ni-4Cr(Ta) alloy [34], which varies from our 10Ni-4Cr alloy by having 3 at.% Ta instead of 1.5Ta+1.5Nb (at.%), has a solvus temperature 5 °C lower than our 10Ni-4Cr, which is within experimental error. Thus, replacing 1.5% Ta with 1.5% Nb has no measurable effect on

solvus temperature, despite the much higher melting point of Ta as compared to Nb. By contrast, the earlier 10Ni-8Cr(Nb) alloy [34], which differs from our 10Ni-8Cr by having 3Nb instead of 1.5Ta-1.5Nb, has a solvus temperature 36 °C lower, indicating that replacing 1.5%Nb with 1.5%Ta increases markedly the solvus temperature.

Chromium increases solvus temperature in our alloys, unlike in Co-Al-W alloys [18]. In another example, for a series of Co-30Ni-12Al-4Ta-xCr alloys [65], the solvus temperature increases very little (by 5 and 3 °C) as Cr increases from 0 to 4 to 8 at.%, and decreases slightly for Cr=12 at.%, to a value 9 °C below the Cr-free alloy.

3.4.2 $\gamma + \gamma'$ Microstructure

a. Grains

All six experimental alloys displayed a two-phase $\gamma + \gamma'$ microstructure when aged up to 1000 h at 850 °C, as shown in Fig. 3-2. Representative micrographs for all alloys in all aging steps are given in Supplemental Information, Figs. S3-3 to S3-8. In some aging conditions, short (~1 μm long) needlelike precipitates were observed, which occupy much less than 1% of the total cross-sectional area and occur for various aging times and compositions. In one case, two different sections of the same alloy (10Ni-4Cr aged for 500 h) were prepared separately: one sample (which was quenched slowly due to difficulty breaking the evacuated tube in water) showed these precipitates while the other (normally fast quenched in water) did not. It is likely that these precipitates are due to compositional inhomogeneity within the solidified ingot and/or to slower quench rates. More details are provided in the Supplementary Information section, Figs. S3-9 to S3-11.

γ' precipitate morphology is largely influenced by lattice misfit and affects coarsening resistance. It is well-known that increased magnitude of misfit results in more cuboidal-shaped precipitates, while near-zero misfit results in more spherical-shaped precipitates [68,69]. Rafting—the directional coarsening of γ' precipitates under deviatoric stress—is also influenced by lattice misfit, and is discussed in greater detail in section 3.5[22,70].

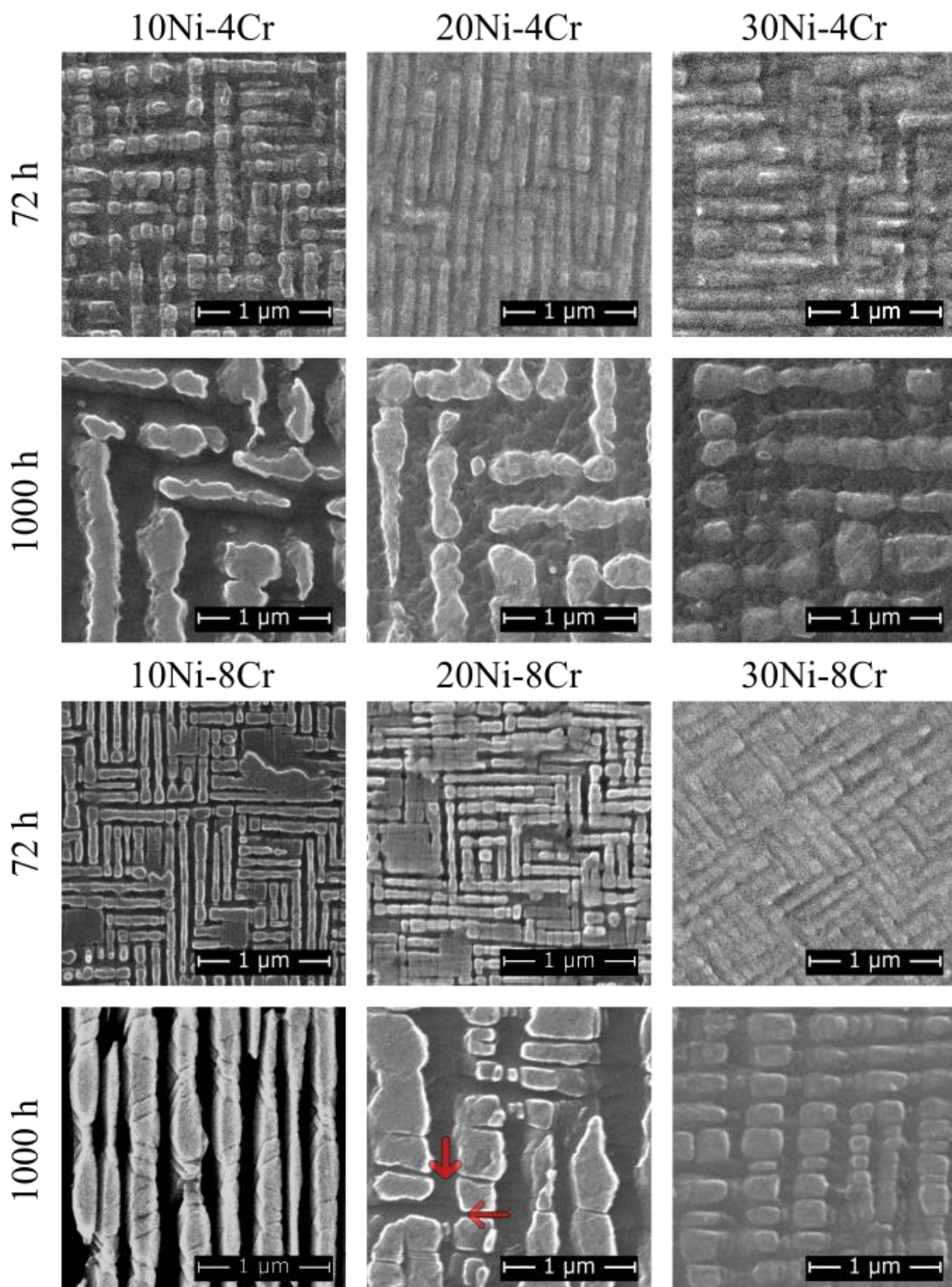


Figure 3-2. SEM micrographs of $\gamma + \gamma'$ microstructure for alloys aged at 850°C for 72 and 1000 h. The γ' phase coalesces into plates, creating thin channels within the plates and thick channels between plates (as highlighted in 20Ni-8Cr at 1000 h aging, with a red horizontal and vertical arrow, respectively).

In 10Ni-4Cr and 20Ni-4Cr, γ' precipitates coalesce between aging times of 168 and 500 h, transforming from smooth, rounded cuboids to ragged, plate-like precipitates, appearing as highly elongated precipitates in cross-sections. Both precipitate shape and area fraction of our 10Ni-4Cr alloy correspond closely to those of 10Ni-4Cr(Ta), suggesting that replacing half the original Ta content (3 at.%) with Nb does not affect phase morphology. The morphology reported for 10Ni-4Cr(Nb) also resembles 10Ni-4Cr and 10Ni-4Cr(Ta).

The γ' precipitates in 30Ni-4Cr remain mostly cuboidal after 500 h aging; even after 1000 h aging, they remain more distinct than those in 20Ni-4Cr and 10Ni-4Cr after 500 h aging. At every aging step, 30Ni-4Cr displays occasional Nb-rich precipitates, with a similar shape but slightly larger size than γ' precipitates, located at both grain boundaries and within grains. For the longest aging time of 1000 h, these precipitates have a diameter of 0.1-1 μm and an area fraction well below 0.1%.

The 8Cr series of alloys exhibits γ' precipitates with sharper corners than the 4Cr series. The 10Ni-8Cr alloy shows highly elongated γ' precipitates displaying thick and thin γ channels (highlighted in Fig. 3-2) after aging for 72 h. The thinner γ channels show the shape of the original γ' precipitates after partial merging. There is no merging between γ' precipitates across the thick γ channels. After aging for 500 and 1000 h, the γ' precipitates maintain a smooth outline, but the thick and thin γ' channels are no longer orthogonal to each other. Also, γ' precipitates in 20Ni-8Cr coalesce less than in 10Ni-8Cr, and, in 30Ni-8Cr, cuboidal γ' precipitates remain unmerged, up to 1000 h aging. However, like its lower Cr counterpart (30Ni-4Cr), 30Ni-8Cr contains rare Nb-rich

precipitates that intermittently decorate grain boundaries and occasionally appear in the bulk grain, in area fractions well below 0.1 %.

Overall, the 4Cr alloy series has precipitates with more irregular shapes which often coalesce in the thin γ' channels. While the shape does not change with increasing Ni content, γ' area fraction increases from $32 \pm 4\%$ in 10Ni-4Cr, to $37 \pm 3\%$ in 20Ni-4Cr, to $49 \pm 6\%$ in 30Ni-4Cr. The γ' area fraction is the same for our 10Ni-4Cr and the previous 10Ni-4Cr(Ta), further indicating that partial substitution of Nb for Ta does not impact the microstructure in these alloys.

The three alloys in the 8Cr series show very similar microstructures, regardless of Ni content. The area fraction of γ' precipitates is constant within error: $44 \pm 8\%$ in 10Ni-8Cr, $45 \pm 4\%$ in 20Ni-8Cr, and $45 \pm 2\%$ in 30Ni-8Cr. Although Atom Probe Tomography would be needed to verify partitioning behavior, the fact that Ni increases γ' volume fraction in the 4Cr series but not the 8Cr series suggests that Cr causes Ni and Co to partition more evenly to γ and γ' (rather than preferentially across γ' and γ , respectively). Although Ti content also changed, Tirado Reyes et al. showed that increasing Cr from 0 to 4 to 8 at.% in the alloys Co-10Ni-6Ti-5Al-0Cr-3Nb-3V-0.04B, Co-10Ni-6Ti-5Al-4Cr-3Nb-3V-0.04B, and Co-10Ni-8Cr-5Al-3Nb-3V-2Ti-0.04B reduced the Ni γ'/γ partitioning from 1.66 to 1.53 to 1.47 and increased the Co partitioning from 0.78 to 0.84 to 0.88.

In our 8Cr alloys, the γ' corners are sharper and the precipitates are more cube-like than in the 4Cr series, consistent with a higher γ - γ' lattice misfit, which agrees with results reported for W-free alloys by Tirado Reyes et al. [34], but disagrees with the observations in Co-Al-W and Co-Ti-based alloys [25,40–42] where increasing Cr results in more rounded γ' precipitates with

lower lattice misfit. It is also worth noting that Cr partitions in a wide range (below unity) in different alloys systems, such as $k_{Cr}^{\gamma'/\gamma} = 0.23$ in Co-30Ni-8Al-14Cr-1Ta-2W-4Ti[74] or $k_{Cr}^{\gamma'/\gamma} = 0.86$ in Co-30Ni-9.5Al-5.5W-6.5Cr-0.1C-4Ti-2Ta[75].

b. Grain boundaries

SEM micrographs of grain-boundary triple junctions are shown in Fig. 3-3 for 20Ni-4Cr and 20Ni-8Cr aged for 24 – 1000 h. Features on the grain boundaries include coarse precipitates (likely γ'), γ' depletion zone, and γ' fine precipitates coalescing between two different grain orientations. The grain boundary morphology shown in these two alloys are representative of the entire series, and images for other alloys are given in the Supplementary Information, Figs. S3-S8.

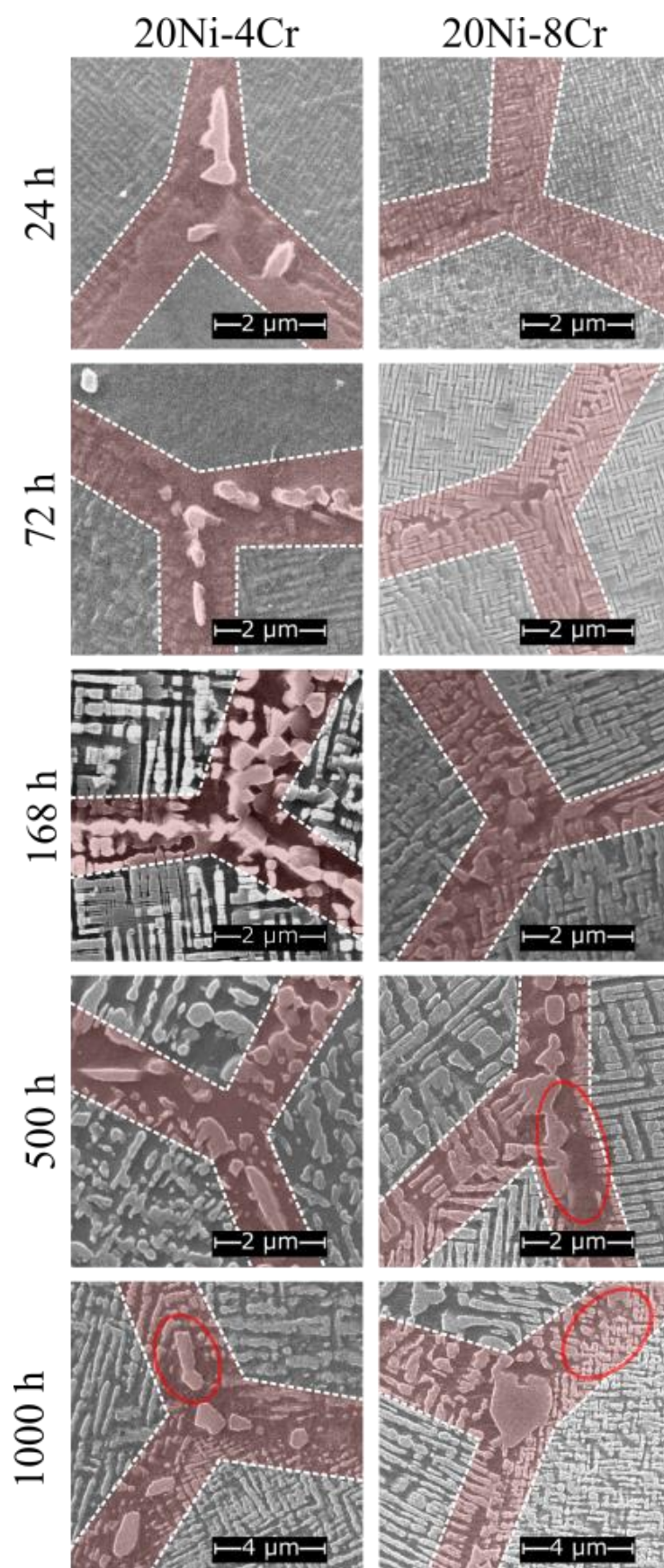


Figure 3-3. SEM micrographs showing representative grain-boundary triple junctions (highlighted in red) for 20Ni-4Cr and 20Ni-8Cr at all aging times. Grain boundaries may exhibit coarse γ' precipitates which are not aligned in either grain (example circled in 20Ni-4Cr for 1000 h) or may show γ' merged across the grain boundary (example circled in 20Ni-8Cr for 1000 h). Occasionally, a γ' -depleted region is present next to a grain boundary (example circled in 20Ni-8Cr for 500h).

Most grain boundaries are free from non- γ' precipitates. Depending on the grain orientations, the grain boundaries show a narrow γ' -free region (circled in Fig. 3-3 for 20Ni-8Cr aged 500 h) or coarse, coalesced γ' precipitates (circled in Fig. 3-3 for 20Ni-4Cr aged 1000 h). These precipitates are identified as γ' , because (i) they have the same brightness in BSE-SEM as γ' precipitates in the bulk of the grain, and (ii) they frequently coalesce with the bulk γ' precipitates, as in 20Ni-8Cr aged 1000 h (circled in Fig. 3-3).

3.4.3 Lattice Misfit

Lattice misfit between the γ' and γ phases is given by $\delta = 2(a_{\gamma'} - a_{\gamma}) / (a_{\gamma'} + a_{\gamma})$ where $a_{\gamma'}$ and a_{γ} are the lattice constants of the two phases [39]. In contrast to Ni-based superalloys, Co-based superalloys typically have a positive misfit, i.e., the γ' -precipitates have a larger lattice constant than the γ -matrix [43,76].

Lattice misfit is important because dislocation motion and coarsening kinetics—however, there is not a clear “optimal” value of lattice misfit [40]. Low misfits ensure that γ' is shearable and coherent, and it lowers the driving force for coarsening. On the other hand, high misfit increases interfacial stress, which can inhibit dislocations as they shear through γ' . Misfit also plays an important role “rafting,” which is the morphological change γ' undergoes when coarsening under stress[41]. Thus, larger misfit tends to be better in low-temperature creep and higher misfit tends to be better at high temperature creep. For this reason, taking into account that γ tends to have a higher coefficient of thermal expansion than γ' , alloys with positive lattice misfit

should have improved creep properties because the misfit decreases as a function of temperature. Unfortunately, it is difficult-to-impossible to experimentally isolate the effects of lattice misfit because misfit strongly depends on elemental composition, but changing the elemental composition affects other factors which influence creep more-directly, such as solid solution strengthening[42,43].

Lattice plane spacings were first measured at APS on our samples aged for 168 h. However, the large, millimeter-sized as-cast grains and limited stage rotation made it difficult to collect diffraction peaks. One sample (10Ni-8Cr) provided three double-peaks ((111), (222), and (333) peaks, doubled for the γ' and γ phases); most, one or two double-peaks; and one (30Ni-4Cr), none. Recrystallized samples (aged for 72 h) were further measured with a laboratory XRD instrument and provided 2-7 visible double-peaks for each sample.

Experimental lattice misfits are plotted in Fig. 3-4. The values are the average of all visible peaks, evenly weighted for each peak. Since higher misfit values allow a higher number of distinguishable peaks in the laboratory XRD spectra, the impact of the APS misfit values has a smaller impact on the final calculated misfit value. A graph showing all identified peaks, as well as the experimental XRD spectra, is given in Supplemental Information, Figs. S3-12 to S3-14.

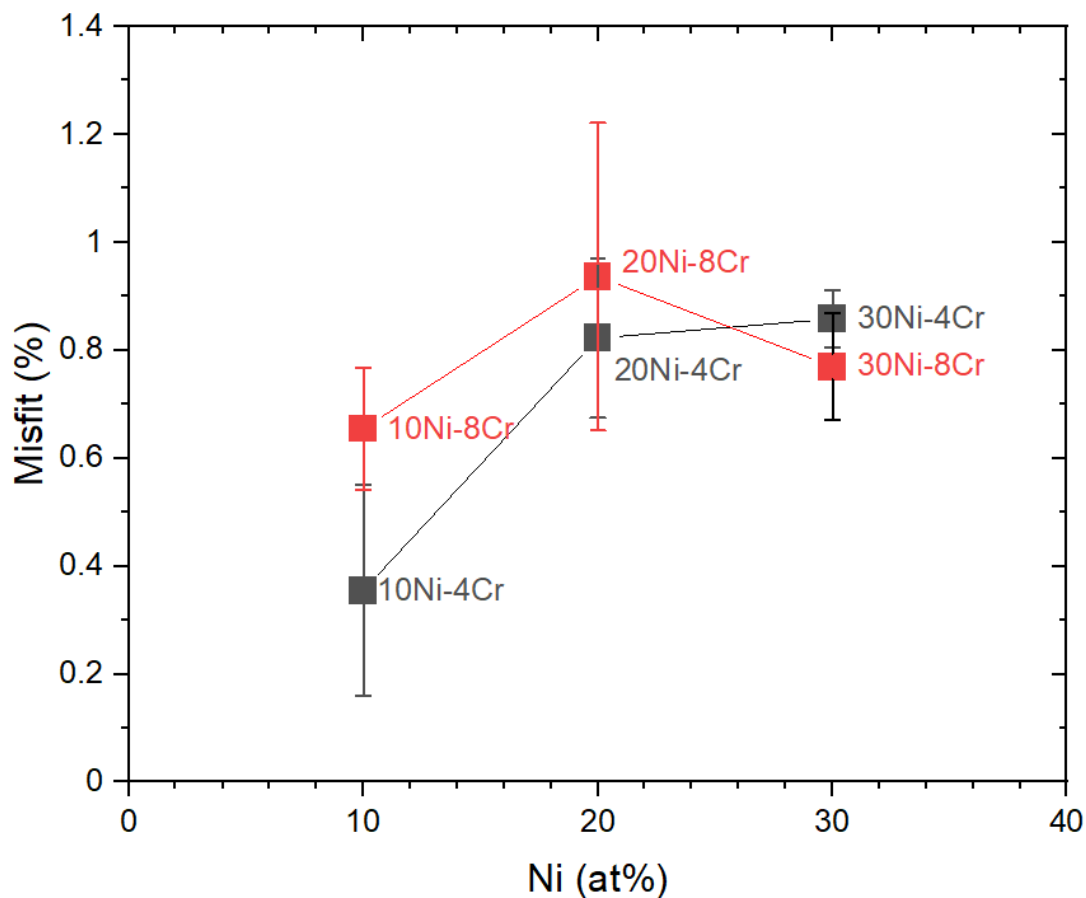


Figure 3-4. Plot of lattice misfit as a function of Ni content for the low- and high-Cr alloys. These data points are an average of all clear reflection pairs, regardless of whether they were collected from APS or lab XRD.

All our alloys, except for 10Ni4Cr, have an average misfit within $0.8 \pm 0.2\%$, consistent with positive misfit of 0-1% reported in other Co-based superalloys, both W-containing [13,40,45–47] and W-free [26,38,48]. Figure 3-4 shows, as a general trend, that Cr and Ni addition slightly increase misfit in our alloys, which is consistent with microstructure morphology changes, i.e. γ' precipitates becoming more cubic as Ni and Cr increases, suggesting a higher lattice misfit [10,65]. Misfit increase from 10 to 30% Ni, which agrees with results of increasing misfit for a W-free Co-Al-Ni-Ti-Cr alloys with Ni:Co 1:3 to 1:1 ratio [57]. The same study found that increasing Cr from 10 to 15% increases misfit in the Co-rich alloy, but further Cr additions to 20% decreases misfit

to values below the 10% Cr alloy. Chen et al. found, in W- and Mo-free alloys with composition Co-30Ni-12Al-4Ta-xCr, that Cr increases the γ lattice parameter and thus decreases misfit, from 0.98 to 0.33% as Cr increased from 0 to 12 at.%, [65]. In contrast to our trend for Ni, up to 10 at.% Ni additions to the W-free Co-8Ti-11V monotonically reduced misfit from 0.74 to 0.61% [67].

3.4.4 Oxidation

Weight gain per surface area is plotted as a function of oxidation time in Fig. 3-5a. Fig. 3-5b shows the square of the weight gain per surface area, which is used to calculate the parabolic rate constant k according to:

$$\left(\frac{\Delta m}{A}\right)^2 = kt, \quad (1)$$

where Δm is the mass gain, A is the surface area, t is time, and k is the parabolic rate constant [80,81].

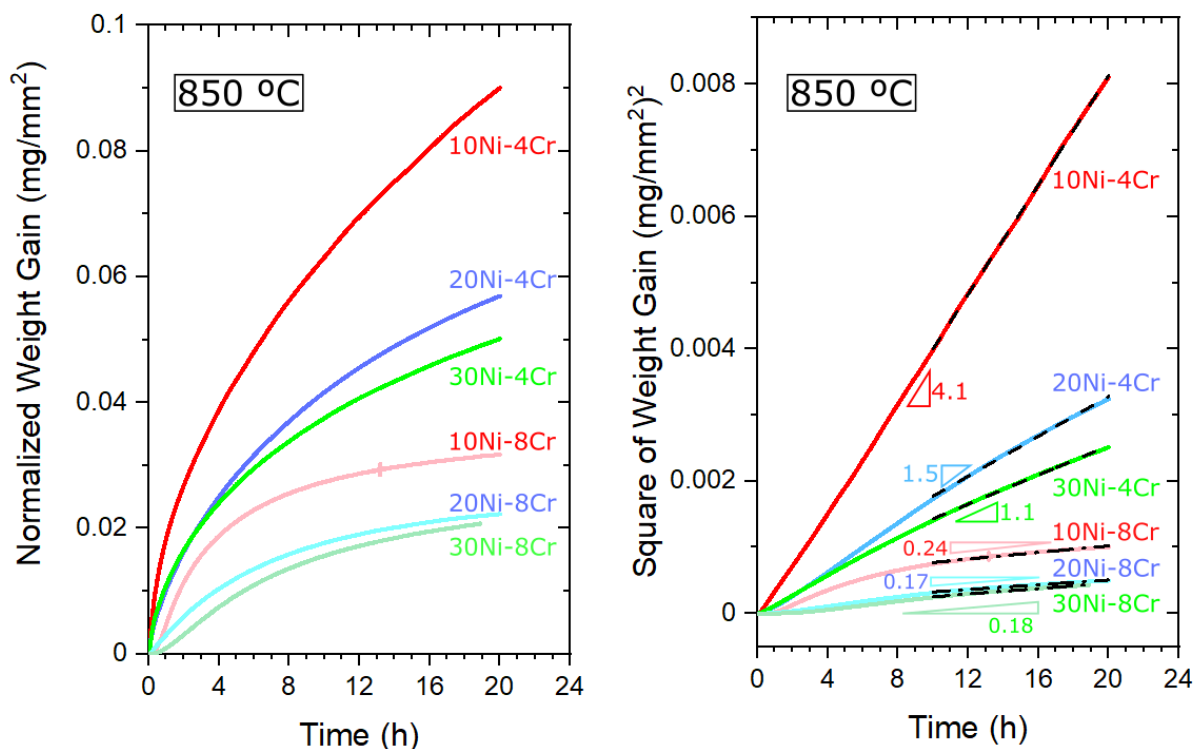


Figure 3-5. Oxidation behavior at 850 °C for all alloys, shown as plots of time dependence of: (left) mass gain normalized by initial surface area and (right) square of normalized mass gain, with line of best-fit according to Eq. (1) whose slopes (parabolic rate constant k) are given in units of $\text{mg}^2/(\text{cm}^4\text{h})$

It is apparent that the three low-Cr samples oxidize significantly faster than the three high-Cr samples. At constant Cr content, Ni additions also markedly improve oxidation resistance. The 30Ni-8Cr alloy was tested twice; the curve shown in Fig. 3-5 eliminates the first 1.3 h, which showed mass decrease, likely due to contaminant vaporization. The other 30Ni-8Cr sample (plotted in Fig. S3-15) showed a change in slope after 10 h, likely due to a crack forming which again subjected the sample to transient oxidation.

After TGA oxidation, the three low-Cr samples exhibited an oxide layer that was visibly spalling, unlike the three high-Cr samples. This spallation was especially obvious in 10Ni-4Cr, with the lowest Cr and Ni content. When viewing mounted and polished cross-sections in SEM,

10Ni-4Cr did not exhibit any oxide scale, presumably because it fully spalled off. The 20Ni-4Cr alloy exhibited regions of thick scale, and regions where the scale has spalled off.

In the early stages of oxidation, oxide growth is expected to be transient and does not follow the parabolic steady-state model. Transient oxidation rates are usually higher than steady-state oxidation rates, because of simultaneous oxidation of more- and less-protective elements, as well as thermal instabilities, fast nucleation growth of oxide grains, and an initially high chemical potential gradient [82]. For consistency, it is assumed that only the second half of the oxidation test is non-transient. Assuming steady-state parabolic growth starting at 10 h, the parabolic rate constants are given in Fig. 3-5 and span values between $k=0.17$ and $k=4.1$ $\text{mg}^2/(\text{cm}^4 \text{ h})$. Tirado Reyes et al. [26] reported markedly lower oxidation kinetics in their Ta-free 10Ni-8Cr(Nb) alloy, with $k = 0.08$ $\text{mg}^2/(\text{cm}^4 \text{ h})$ which is one-third of the k value for our 10Ni-8Cr alloy which contains both Nb and Ta. This indicates that Ta reduces the oxidation resistance, which could be confirmed by testing their 10Ni-8Cr(Ta) alloy, where all Nb was replaced with Ta.

Fig. 3-6 shows representative BSE image of cross-sections of the oxidized alloys and EDS composition maps for Co, Ni, Cr, and Al. Full EDS maps of all elements are given in the Supplemental Information, Figs. S16-S21.

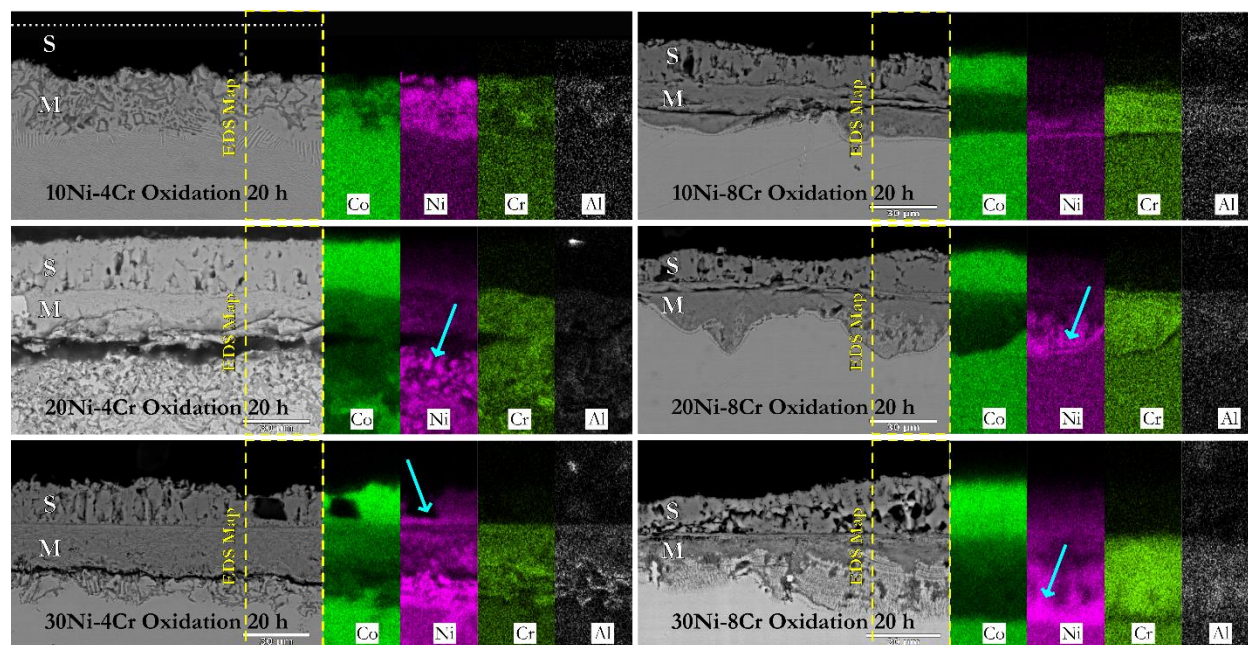


Figure 3-6. Backscattered SEM micrographs of cross-section of specimens oxidized in TGA instrument (850 °C / 20 h), showing top oxide surface scale (marked S), an intermediated mixed oxide scale (marked M) and the bulk alloy. The surface scale of 10Ni-4Cr is absent because of spalling prior to metallographic mounting.

In each alloy, the top surface scale (marked S in Fig. 3-6) is highly enriched in Co and O, with a slight Ni enrichment at the bottom of the scale (arrow in Fig. 3-6, 30Ni-4Cr). This scale consists of cracked, porous columnar grains. No such scale is visible for 10Ni-4Cr, most likely because it spalled off during the oxidation test, as discussed above.

Beneath the oxide scale is a “mixed-oxide” layer (marked M in Fig. 3-6), which is very rich in Ni (and to a lesser extent in Al, Cr, Ti, Nb, Ta, and V), but poor in Co, consistent with the outward diffusion of Co to the surface scale. Within this mixed-oxide layer, Ni shows a concentration gradient, being depleted near the top (close to the Co-rich top scale) and concentrated near the bottom (marked with an arrow in 20Ni-8Cr and 30Ni-8Cr in Fig. 3-6). Finally, under the Ni-rich portion of the mixed oxide layer, the alloy returns to its bulk composition.

30Ni-4Cr, as well as all Cr-rich alloys, display significant Al- and Cr-enrichment in the mixed oxide layer, suggesting that Ni additions improve the ability of Cr and Al to form a protective oxide. In Co-xNi-9Al-8W-8Cr-yB, where the Co:Ni ratio varied between ∞ and 0 and y was 0 and 0.4 at.%, Ni additions similarly improved oxidation resistance [83,84].

3.4.5 Creep Properties

The secondary creep strain rate $\dot{\epsilon}$ can be described by a power law equation:

$$\dot{\epsilon} = A\sigma^n \exp\left(\frac{-Q}{RT}\right)$$

where A is a constant, σ is stress, n is the stress exponent, Q is the activation energy, R is the ideal gas constant, and T is the absolute temperature [85]. Fig. 3-7 is a double-logarithmic plot of strain rate vs. stress for our six alloys, with values of n=10-12 measured for each alloy, in good agreement with n=6-12 reported for other γ - γ' Co-based superalloys [27,34,53–57], whose coherent, shearable γ' -precipitates inhibit dislocation climb and glide. Stress exponents are slightly higher than comparable alloys from Tirado Reyes et al. as shown in Fig. 3-8 [26,34].

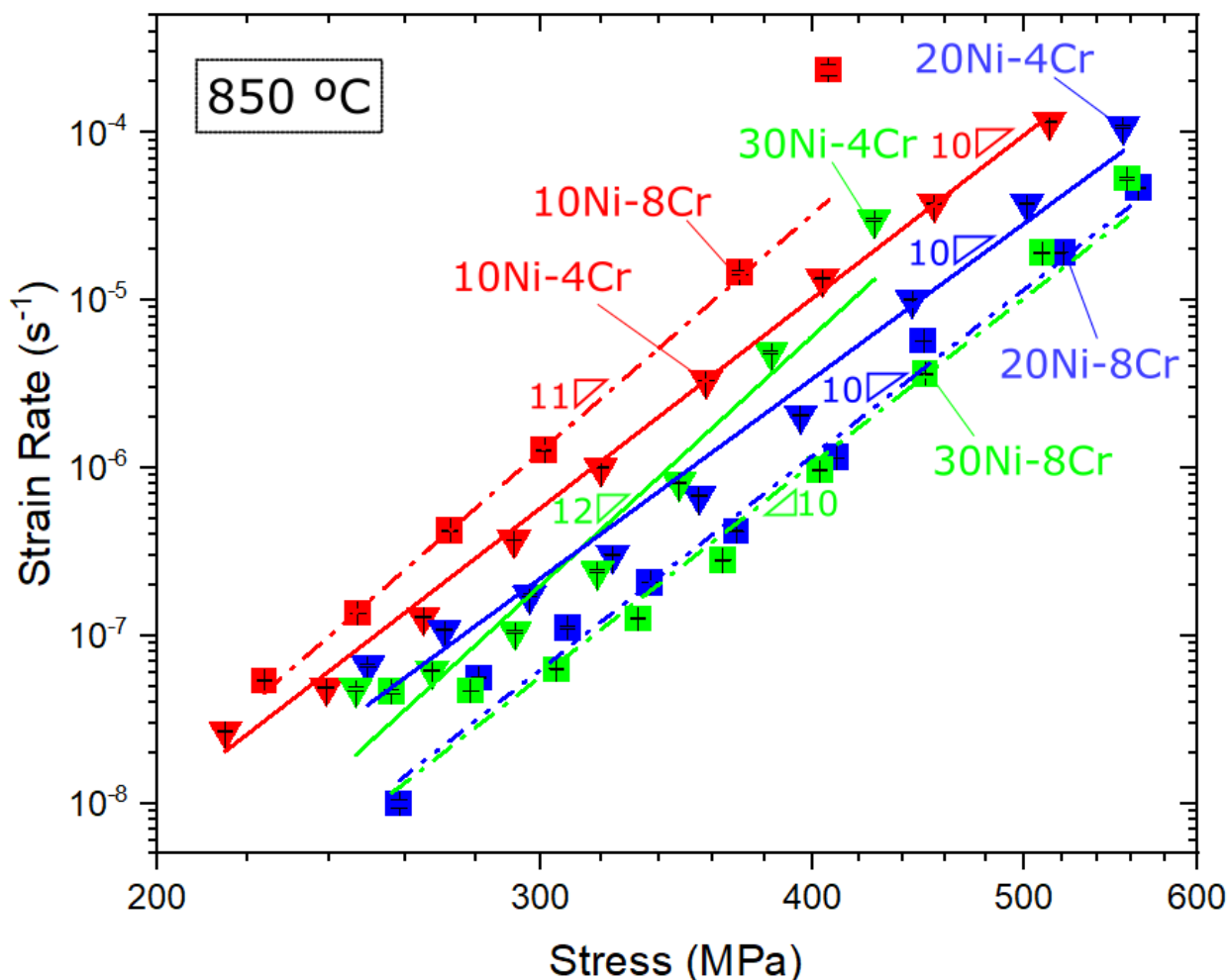


Figure 3-7. Double logarithmic plot of secondary strain rate vs compressive stress at 850 °C, with stress exponents given next to each curve. Color represents Ni content (red = 10%, blue = 20%, green = 30%) and symbol shape represents Cr content (triangle = 4%, square = 8%). Best-fit lines are shown, as solid lines for 4Cr alloys and dashed lines for 8Cr alloys.

It is apparent from Fig. 3-7 that increasing the Ni content from 10 to 20 % (replacing the equivalent amount of Co) offers a clear improvement in creep resistance, especially in the high-Cr alloys: strain rates, at a given stress, decrease by a factor ~ 30 . Creep resistance does not further increase as Ni concentration is increased from 20 to 30%. Also, doubling Cr concentration from 4 to 8% clearly reduces creep resistance in the 10Ni alloys (strain rate increases by a factor 1.5-3), but offers noticeable improvement in the 20Ni and 30Ni alloys. Comparing to related alloys from

Tirado Reyes et al., 10Ni-4Cr and 10Ni-8Cr, have creep resistance which is the same, or slightly better, than 10Ni-4Cr(Ta), 10Ni-4Cr(Nb), and 10Ni-8Cr(Nb), as shown in Fig. 3-8. This result is expected because the change from alloys with either 3%Nb or 3%Ta to our current alloys with 1.5%Nb-1.5%Ta should provide a slightly higher solid-solution strengthening within the shearable γ' -precipitates.

Reyes et al. found that an increase from 0 to 4% Cr slightly worsened creep resistance in their alloys with 3%Ta (and no Nb), but an increase from 4 to 8% Cr slightly improved creep resistance in their alloys with 3% Nb (and no Ta). In the Co-Al-W system, Povstugar et al. found a large decrease (an order of magnitude) with each addition of 4Cr [71]. While our alloys are less creep resistant than the high- γ' fraction Co-9Al-9W alloy, our 20/30Ni-8Cr alloys perform similarly to Co-9Al-9W-4Cr and significantly better than Co-9Al-9W-8Cr, as shown in Fig. 3-8.

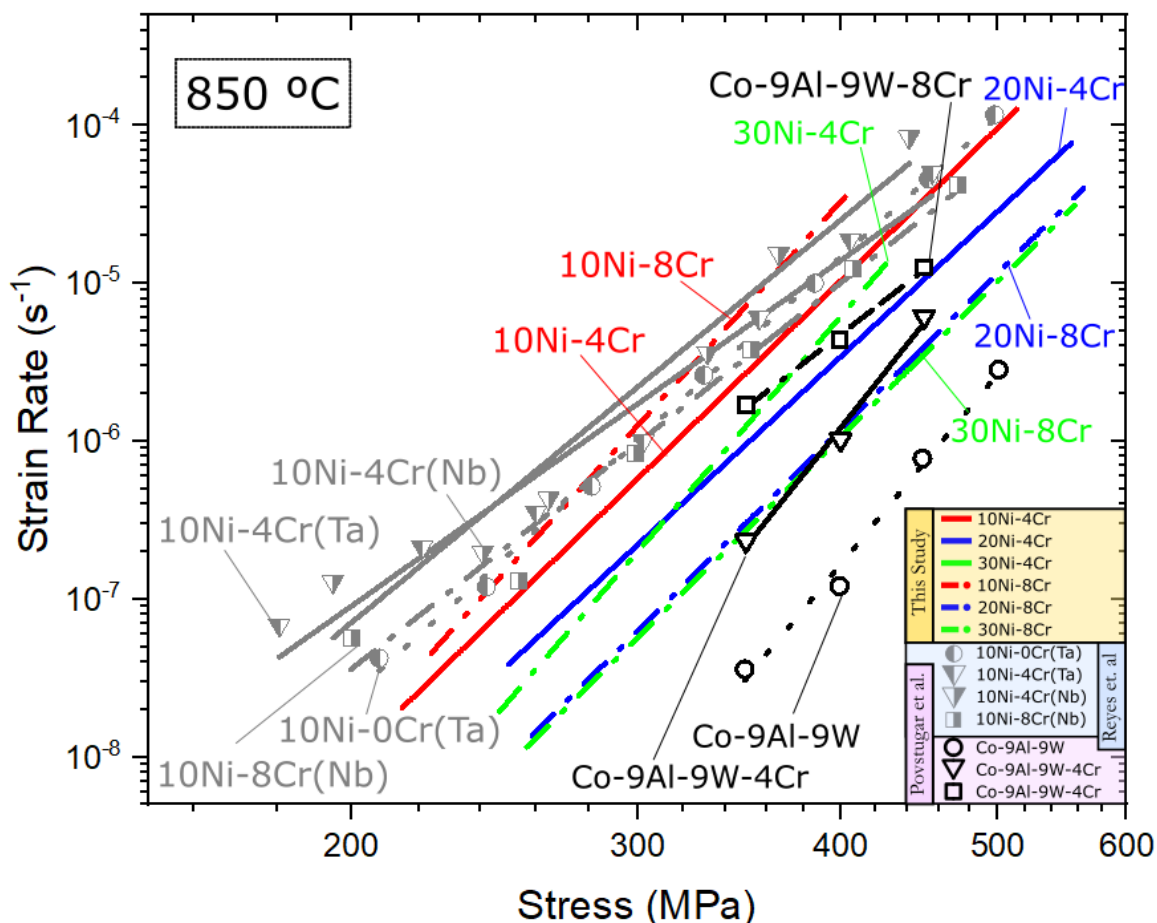


Figure 3-8. Double logarithmic plot of secondary strain rate vs compressive stress at 850 °C for the alloys in this study (red, green, blue, with data points shown in Fig. 3-7) compared to previous-generation alloys (gray), as well as W-containing alloys (black). Symbols which are fully filled are for alloys with 1.5Ta and 1.5Nb; symbols which are filled on the left half are for alloys with 3Ta-0Nb; symbols which are filled on the right half are for alloys with 0Ta-3Nb. Hollow symbols are for alloys with neither Ta nor Nb, and represent the Co-Al-W family [26,34,71].

Post-crept microstructures display n-type rafting in well-oriented grains, where precipitates are elongated in a direction perpendicular to the compressive stress, as expected from an alloy with positive lattice misfit [43]. A representative micrograph of 30Ni-4Cr is shown in Fig. 3-9, after creep under stresses ranging from 200 to 600 MPa and for 110 h. Rafting in 10Ni-4Cr appears more pronounced than in 10Ni-4Cr(Ta) [34], which suggests that partially substituting Nb for Ta

increases rafting, but these alloys showed similar creep strength. Representative post-creep micrographs for all alloys are shown in Fig. S3-22.

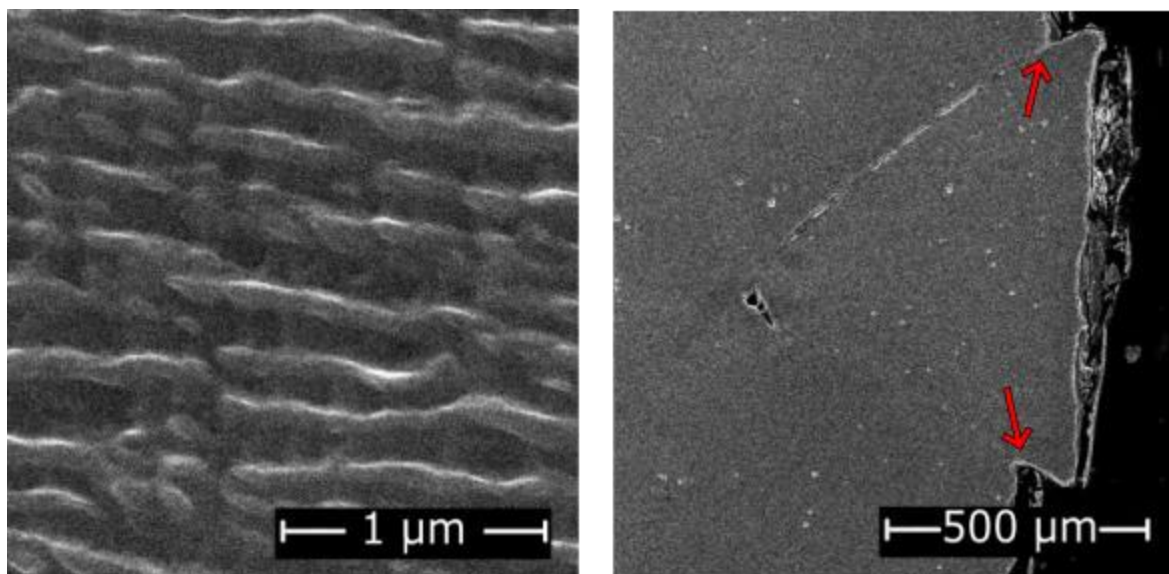


Figure 3-9. SEM micrograph of creep deformed alloys, with compressive stress applied in the vertical direction. (left) microstructure of γ' phase rafted horizontally for 30Ni-8Cr. (right) Grain boundary sliding in 30Ni-8Cr, highlighted in red

Figure 3-9b shows a clear example of grain-boundary sliding in 30Ni-8Cr (red arrows). Grain-boundary sliding or cracking was observed in 30Ni-4Cr and the three 8Cr alloys, indicating that more B might be added to future alloys to precipitate borides at the grain boundaries, thus decreasing grain-boundary sliding and improving creep resistance [91]. Grain-boundary cracking may be assisted by this extensive sliding, allowing fast oxygen ingress and thus oxide formation deep within the grain boundary, as shown in one example micrograph in Supplemental Fig. S3-22.

3.4.6 Hardness

Microhardness measured for each alloy in each aging condition are shown in Fig. 3-10.

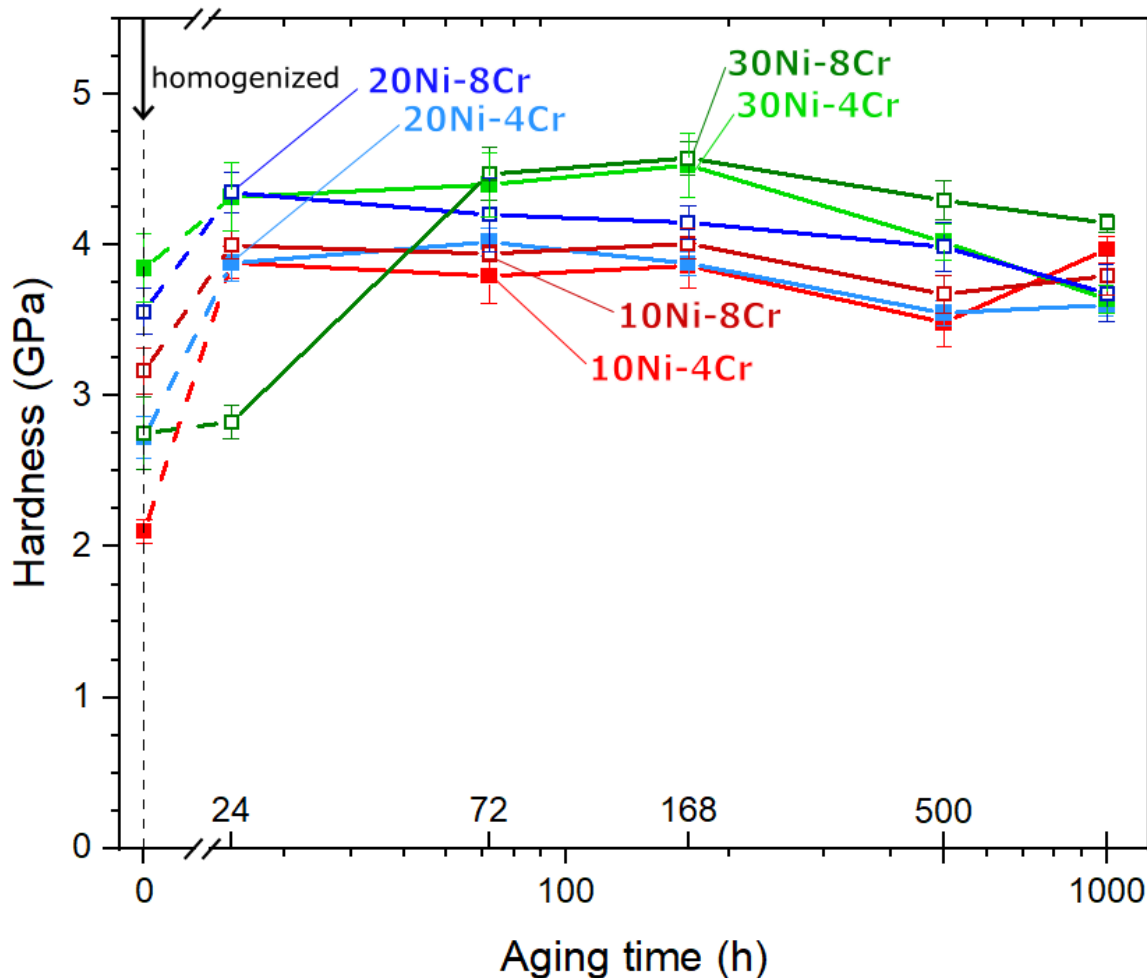


Figure 3-10. Plot of hardness as a function of aging time (on a logarithmic scale). Samples were tested in the as-homogenized state (0 h), and after aging at 850°C between 24 and 1000 h.

Except for 30Ni-8Cr and 10Ni-4Cr, all alloys were within error of their maximum hardness values after the shortest aging time of 24 h, which was maintained up to 72 h. Hardness then drops slowly up to the longest aging time of 1000 h, consistent with slow coarsening of the γ' precipitates, as shown in Fig. 3-10. The 30Ni-8Cr alloy is an outlier, with an as-quenched hardness which is unexpectedly low (as compared to its 30Ni-4Cr counterpart), and lack of significant hardening after 24 h aging (unlike all other alloys); also, 10Ni-4Cr showed an unexpectedly high

hardness value after 1000 h. These three outlier hardness values may be an artifact from imperfect quenching; as shown in the Supplemental discussion “Effect of Cooling Rate,” with various quenching rates, the hardness of the same composition under the same aging time may differ by as much as 0.6 GPa.

In general, additions of both Ni and Cr increase hardness of the alloys at peak (168 h) and beyond (after 500 h). This trend is expected because Ni and Cr generally improve γ' volume fraction and solid solution strengthening. Additionally, increased Ni and Cr increases lattice misfit, which means higher strain fields surrounding γ' precipitates which inhibit dislocation motion.

With peak hardness in the range of 4-4.5 GPa, these alloys are among the hardest W-free Co-based superalloys reported in literature, which mostly range from 2-4.5 GPa. Christofidou et al. reported 4.5 GPa in Co-27Ni-3Al-8Ti-11Cr as the highest hardness among their Co-based alloys [57]. They reported a decrease in hardness with Cr additions—consistent with Cr decreasing their lattice misfit, while Cr generally increases lattice misfit in our alloys. Gao et al. reported ~4.2 GPa as the peak hardness in their hardest alloy, Co-30Ni-7Al-3Ti [79]. Lass et al. also reported a 4.2 GPa peak hardness in their hardest alloy, Co-10Ni-7Al-4Ti-7W-1Ta [92]. Makineni et al. reported a 4.3 GPa peak value in their hardest alloy, Co-10Al-5Mo-2Ta [52].

Tirado Reyes et al. tested hardness after aging at 850 °C on two previous iterations of the 10Ni-4Cr alloy: Co-10Ni-5Al-xCr-3Ta-2Ti-0.04B (x=0 and 4 at.%). These had a peak hardness of 4.1 GPa after aging 1000 h and 4.2 GPa after aging 500 h, respectively [34]. Their 10Ni-4Cr(Nb or Ta) alloy displayed similar hardness-aging behavior as our 10Ni-4Cr(Nb+Ta), i.e., peak hardness after aging 1000 h. However, they found that increasing Cr from 0 to 4% slightly decreases

hardness, while we show here that increasing Cr from 4 to 8% slightly increases peak hardness. Overall, it appears that the substitution of 1.5Ta-1.5Nb for 3Ta results in a ~0.15 GPa hardness decrease in 10Ni-4Cr.

3.5 Conclusions

This study reports six W-free, Co-based superalloys with composition Co-xNi-5Al-yCr-3V-2Ti-1.5Nb-1.5Ta-0.08B, with Co partially replaced by Ni (x=10, 20, or 30 at.%) and/or Cr (y=4 or 8 at.%). The following conclusions are drawn:

- Solvus temperatures increase by 15-20 °C per 10 at.% Ni addition, and 15-20 °C as Cr doubles from 4 to 8 at.%; all alloys have a narrow freezing range of ~10-40 °C, and sample-to-sample variation in solidus/liquidus values are within error.
- Except for 10Ni-4Cr, average lattice misfits are between 0.6 and 1%, slightly increasing with Cr and Ni content, but generally within error of each other.
- The $\gamma + \gamma'$ microstructure is stable for all alloys up to 1000 h at 850 °C. As the microstructure coarsens in the 4Cr series, the γ' shapes becomes more ragged; in the 8Cr series, γ' maintains an approximately cubic morphology. Thick and thin γ channels are particularly noticeable in 10Ni-8Cr and 20Ni-8Cr after aging.
- The γ' area fraction increases from 32 to 49% with increasing Ni in the alloys with 4% Cr, and it remains constant at 45% in those with 8% Cr. The γ' area fraction of 10Ni-4Cr matches Co-10Ni-5Al-4Cr-2Ti-3Ta-3V-0.04B within error, so the substitution from 3Ta to 1.5Ta-1.5Nb does not affect γ' area fraction.

- The addition of Cr—and of Ni to a lesser extent—increases oxidation resistance which follows a parabolic law. The least oxidation-resistant alloy, 10Ni-4Cr, gains 5 times the weight (per unit surface area) as the most oxidation-resistant sample, 30Ni-8Cr, after 20 h at 850 °C.
- All alloys exhibit power-law creep behavior at 850 °C, with a stress exponent of 10-12. The addition of Ni slightly improves creep resistance for all alloys. Increasing Cr results in slightly improved creep resistance for alloys with 20 and 30% Ni, but slightly worse creep performance for alloys with 10% Ni. This drop was much less than reported by Povstugar et al. [71] for a Co-Al-W alloy.
- Crept samples display n-type rafting, consistent with the positive lattice misfit, and they show signs of grain-boundary sliding, indicative of insufficient grain-boundary precipitation.

3.6 Acknowledgements

This study was supported by the U.S. Department of Commerce, National Institute of Standards and Technology, as part of the Center for Hierarchical Materials Design (CHiMaD) at Northwestern University via award 70NANB14H012. This work made use of the MatCI Facility which receives support from the MRSEC Program (NSF DMR- 1720139) of the Materials Research Center at Northwestern University; and the IMSERC X-RAY and the EPIC facility of Northwestern University's NUANCE Center, which received support from the Soft and Hybrid Nanotechnology Experimental (SHyNE) Resource (NSF ECCS-1542205).

Synchrotron x-ray diffraction was performed at the DuPont-Northwestern-Dow Collaborative Access Team (DND-CAT) located at Sector 5 of the Advanced Photon Source (APS). DND-CAT is supported by Northwestern University, The Dow Chemical Company, and DuPont de Nemours, Inc. The Advanced Photon Source is a U.S. Department of Energy (DOE) Office of Science User Facility operated for the DOE Office of Science by Argonne National Laboratory under Contract No. DE-AC02-06CH11357.

The authors gratefully acknowledge Dr. Carla Shute (NU) for experimental assistance in the MatCI facility, Dr. Christos Malliakas for experimental assistance in the IMSERC facility, and Drs. Dennis Keane and Mike Guise for experimental assistance at APS. The following NU colleagues are acknowledged for helpful discussions: Dr. Fernando Reyes Tirado, Dr. Amir Farkoosh, Dr. Ding-Wen Chung, Dr. Fei Xue, Prof. David Seidman.

3.7 Competing Interests Statement

Declarations of interests: none

3.8 Supplementary Information

3.8.1 Composition

Alloy composition was verified using an average of 5 EDS spectra taken from different locations on the as-homogenized alloys.

Name	Co	Ni	Al	Cr	V	Ti	Nb	Ta	B
10Ni- 4Cr	73.12 ± 0.11	9.74 ± 0.07	4.98 ± 0.13	4.15 ± 0.03	3.02 ± 0.03	2.04 ± 0.03	1.37 ± 0.03	1.59 ± 0.05	-
20Ni- 4Cr	63.25 ± 0.24	19.43 ± 0.05	5.13 ± 0.15	4.11 ± 0.04	3.05 ± 0.04	2.06 ± 0.04	1.37 ± 0.04	1.59 ± 0.04	-
30Ni- 4Cr	52.65 ± 0.21	29.36 ± 0.25	5.44 ± 0.34	4.07 ± 0.17	3.14 ± 0.04	2.27 ± 0.38	1.37 ± 0.17	1.69 ± 0.13	-

10Ni-8Cr	68.93 ± 0.18	9.74 ± 0.08	5.04 ± 0.09	8.22 ± 0.04	3.02 ± 0.02	2.07 ± 0.03	1.41 ± 0.03	1.58 ± 0.04	-
20Ni-8Cr*	59.10 ± 0.08	19.54 ± 0.05	4.98 ± 0.02	8.29 ± 0.08	3.03 ± 0.00	2.07 ± 0.02	1.38 ± 0.06	1.61 ± 0.02	-
30Ni-8Cr	48.77 ± 0.17	29.66 ± 0.11	4.98 ± 0.15	8.19 ± 0.06	3.07 ± 0.06	2.08 ± 0.01	1.60 ± 0.08	1.65 ± 0.09	-

Table S 3-1. Average alloy composition (at.%), * average of 3 measurements only

3.8.2 DSC Curves

Raw DSC cooling curves are given in Figs. S3-1 and S3-2.

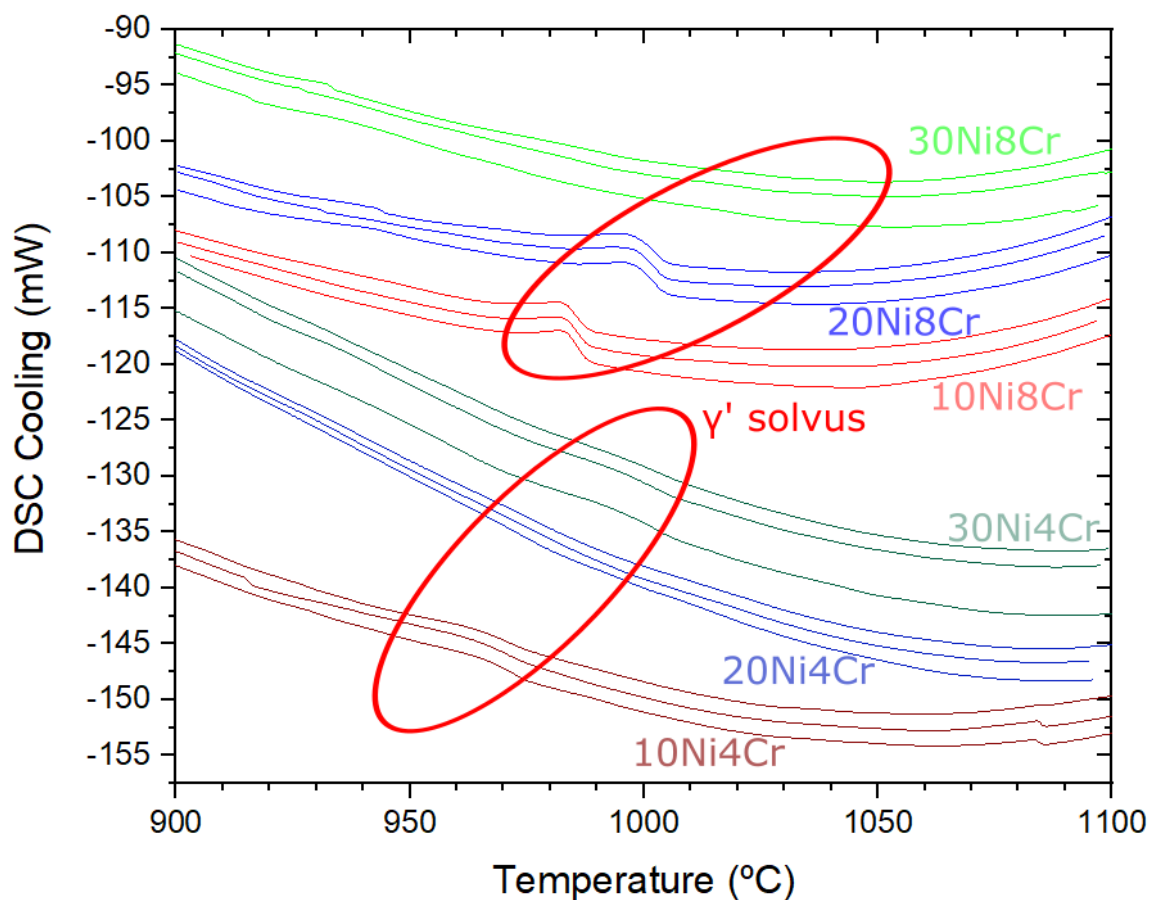


Figure S3-1. Raw DSC cooling curves (3 cycles) for each alloy showing the region determined as the γ' solvus temperature.

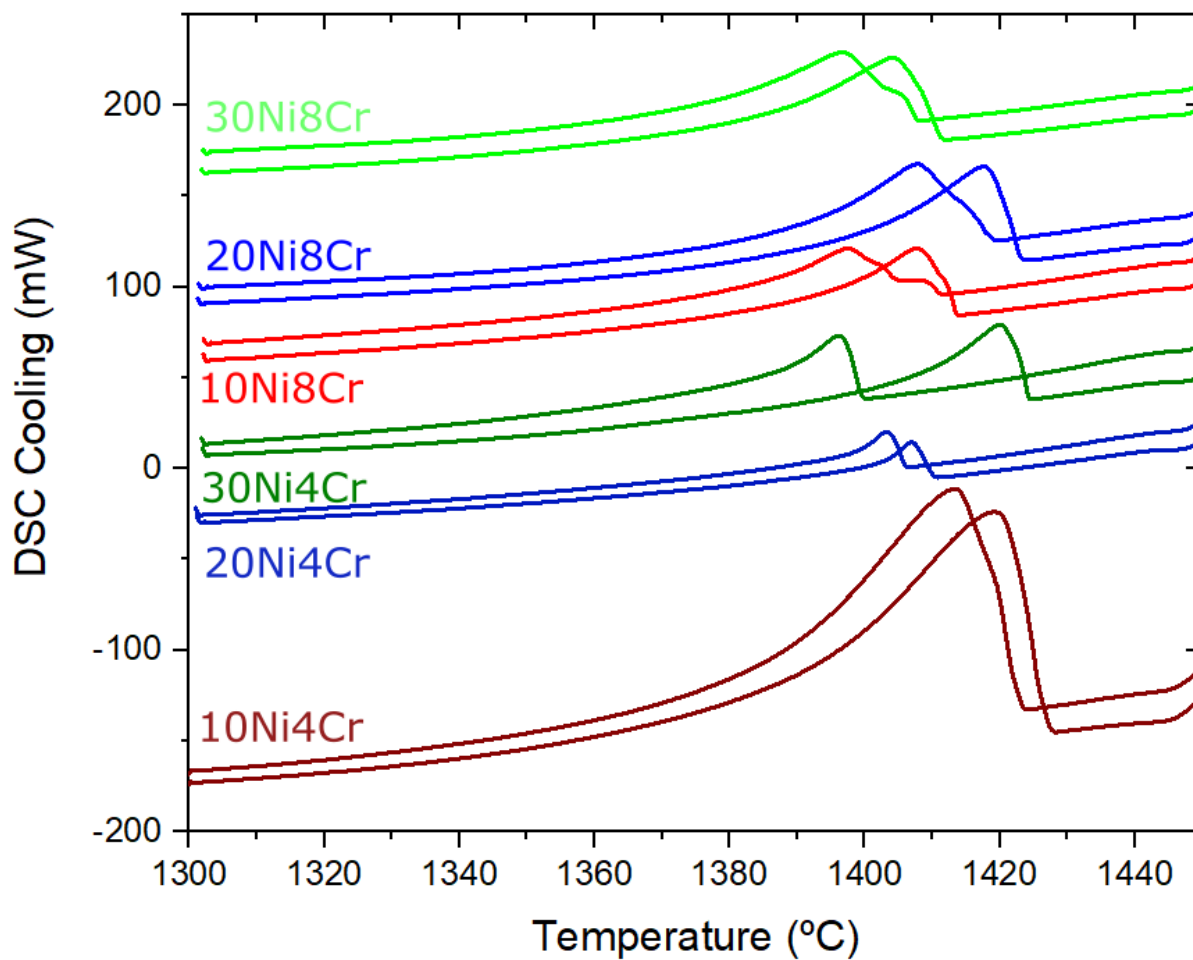


Figure S3-2. Raw DSC cooling curves (3 cycles) for each alloy showing the melting (solidus and liquidus) region for 2 cycles

3.8.3 Microstructure

Representative SEM (SE) micrographs are given for all alloys at all aging steps in Figures S3-S8.

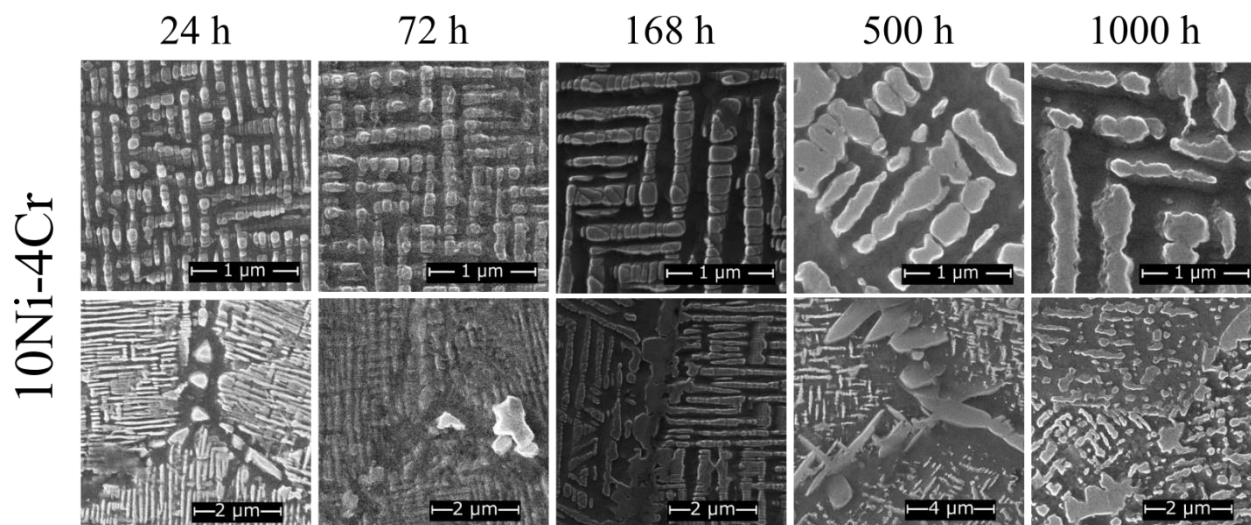


Figure S3-3. Representative SE micrographs for bulk (top row) and grain boundaries (bottom row) for 10Ni-4Cr aged 850 °C for 24, 72, 168, 500, and 1000 h.

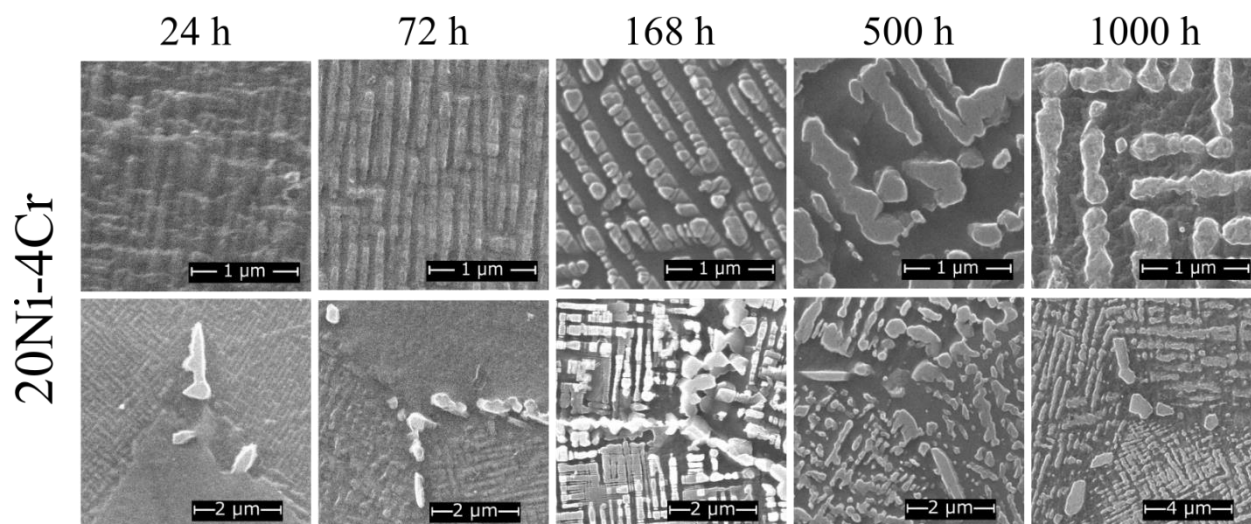


Figure S3-4. Representative bulk and grain boundary SE micrographs of 20Ni-4Cr aged 850 °C for 24, 72, 168, 500, and 1000 h.

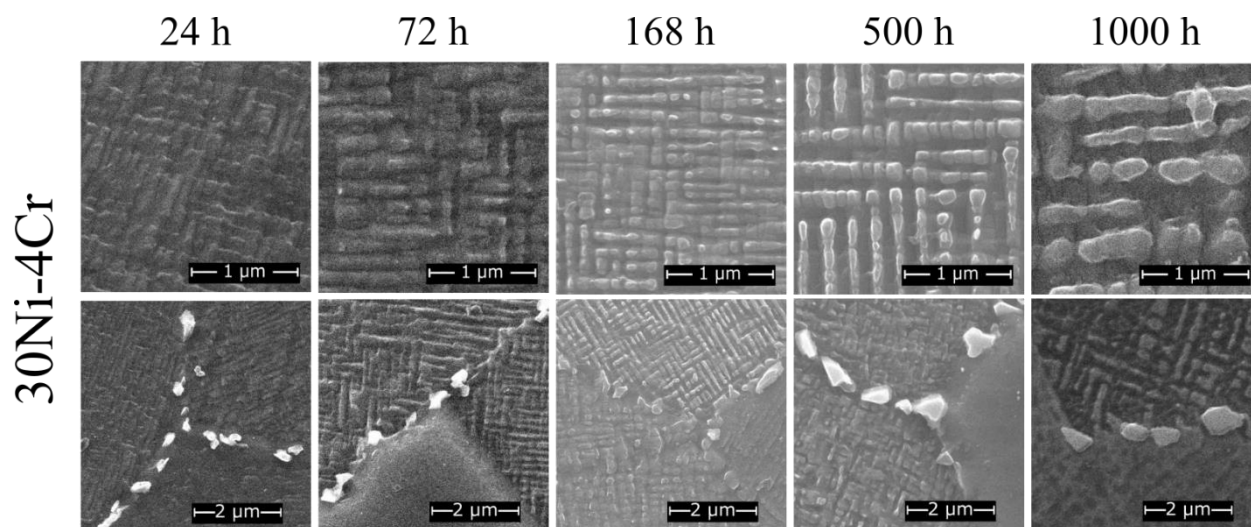


Figure S3-5. Representative bulk and grain boundary SE micrographs of 30Ni-4Cr aged 850 °C for 24, 72, 168, 500, and 1000 h.

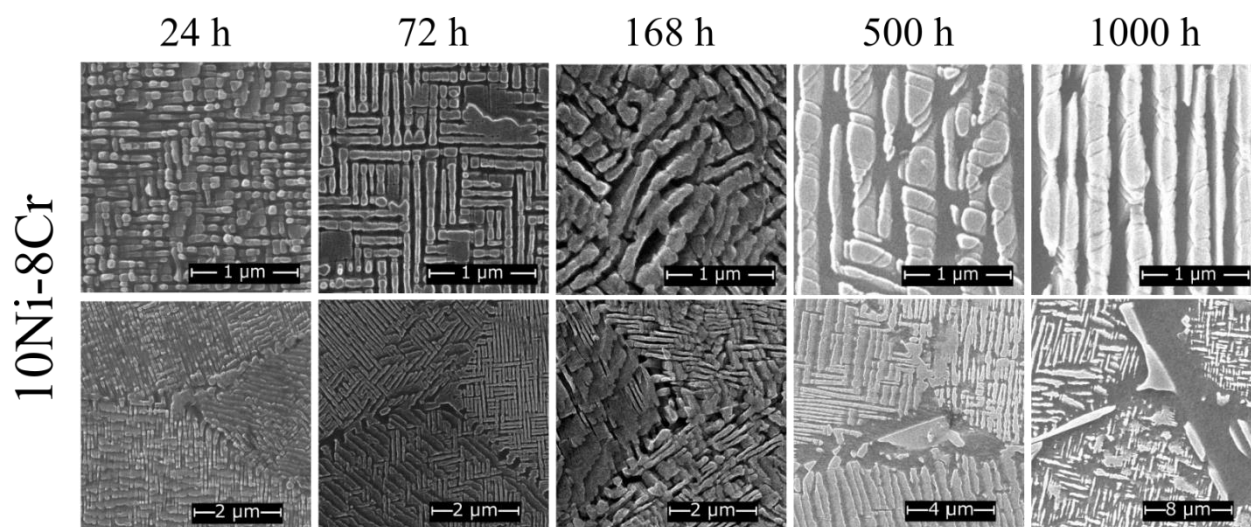


Figure S3-6. Representative bulk and grain boundary SE micrographs of 10Ni-8Cr aged 850 °C for 24, 72, 168, 500, and 1000 h.

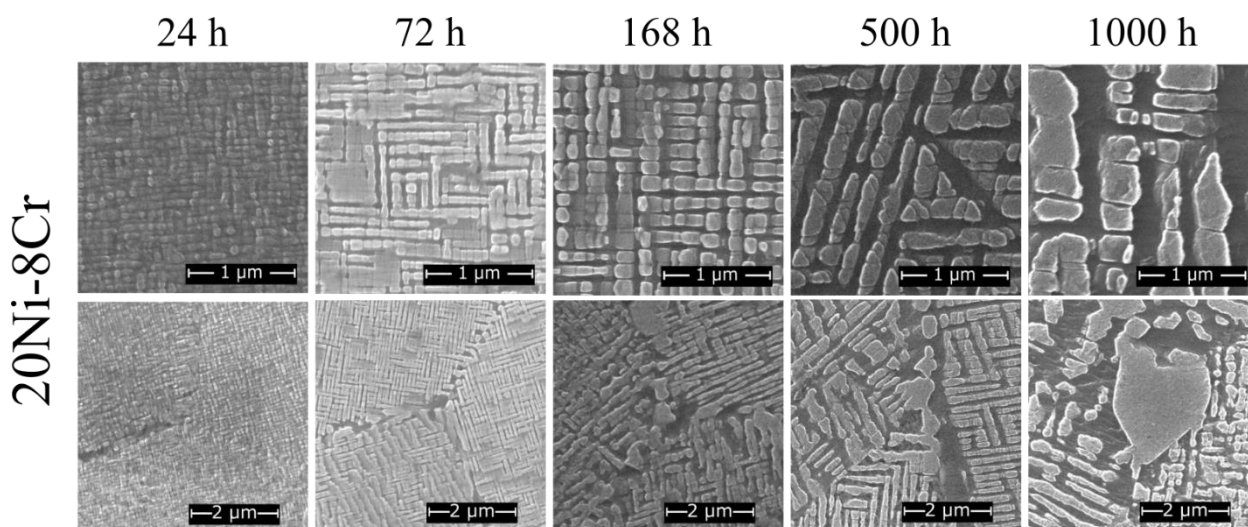


Figure S3-7. Representative bulk and grain boundary SE micrographs of 20Ni-8Cr aged 850 °C for 24, 72, 168, 500, and 1000 h.

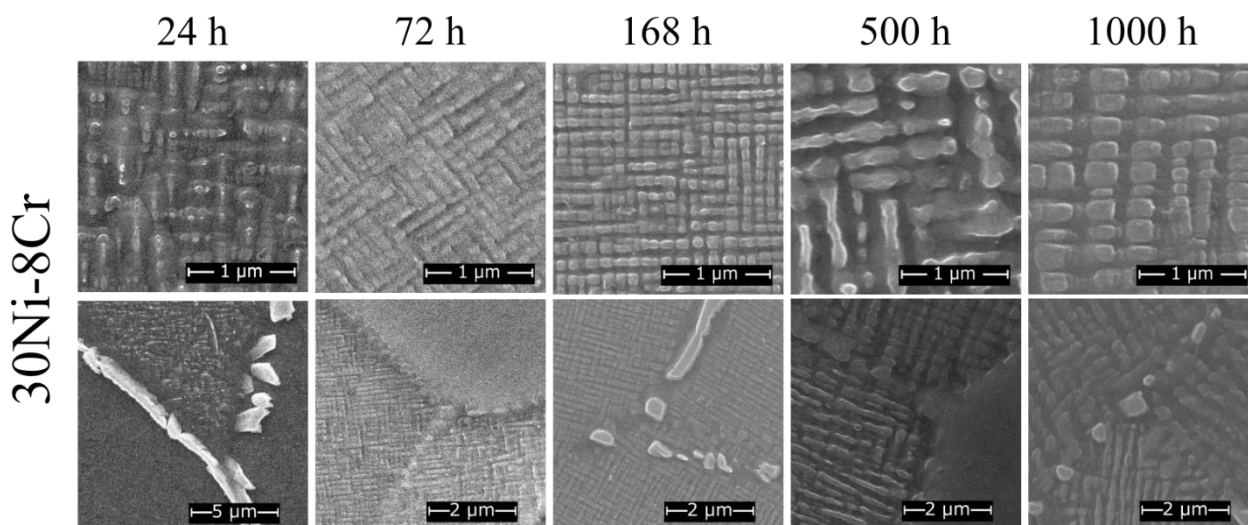


Figure S3-8. Representative bulk and grain boundary SE micrographs of 30Ni-8Cr aged 850 °C for 24, 72, 168, 500, and 1000 h.

3.8.4 Effect of Quenching Rate

Occasionally, when quenching samples in water at the end of the aging treatment, the quartz tube did not break immediately, resulting in a slower cooling curve. In these cases, precipitates with a different morphology than γ' were occasionally visible during SEM investigation.

Samples that showed one or more such precipitates included 10Ni-4Cr at 24h, 10Ni-4Cr at 500h (appeared in one of two samples), 20Ni-4Cr at 24h, 20Ni-4Cr at 72h (globular), 20Ni-4Cr at 500h (appeared in one of two samples), 30Ni-4Cr at 24h, 30Ni-4Cr at 168h (common), 30Ni-4Cr at 500h, 30Ni-4Cr at 1000h, 30Ni-8Cr at 24h, 30Ni-8Cr at 168h, 30Ni-8Cr at 500h (globular), and 30Ni-8Cr at 1000h (globular).

For example, Fig. S3-9 shows a backscatter SEM image of 20Ni-4Cr aged 500 h where the encapsulated tube failed to break (slower quench) and the same alloy and heat treatment with the standard fast quench.

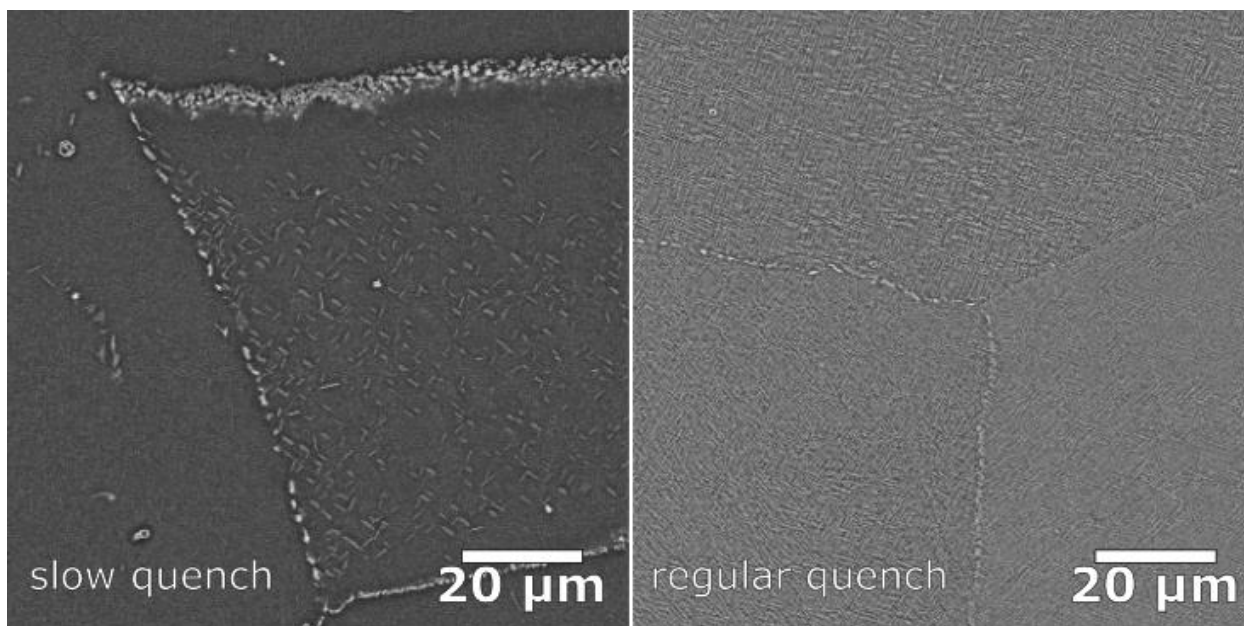


Figure S3-9(left) 20Ni-4Cr aged 500 hours where the encapsulation tube failed to break immediately, leading to a slow quench. (right) 20Ni-4Cr aged 500 hours with regular quench.

To confirm that these precipitates are the result of a slow cooling rate, rather than compositional inhomogeneities, three samples of 20Ni-4Cr were vacuum-encapsulated, aged at

850 °C for 1 week, and then cooled at vastly different rates. The first sample was quenched in water, the second placed on a ceramic brick without breaking the quartz capsule for “air cooling,” and the last was left in the furnace to slow-cool overnight, at a rate estimated to be < 5 °C/min.

Both the air- and furnace-cooled samples, unlike the water-quenched sample, show, beside the expected submicron γ' precipitates, other precipitates in all their grains. These precipitates appear as disc or as needles, so they may be disc-shaped. The largest of these has a diameter < 3 μm , with most being much smaller than 1 μm . An SEM image of a region in the furnace-cooled sample, especially dense with these precipitates, is given below in Fig. S3-10. The total area of these non- γ' precipitates is $< 1\%$, even in this precipitate-dense region.

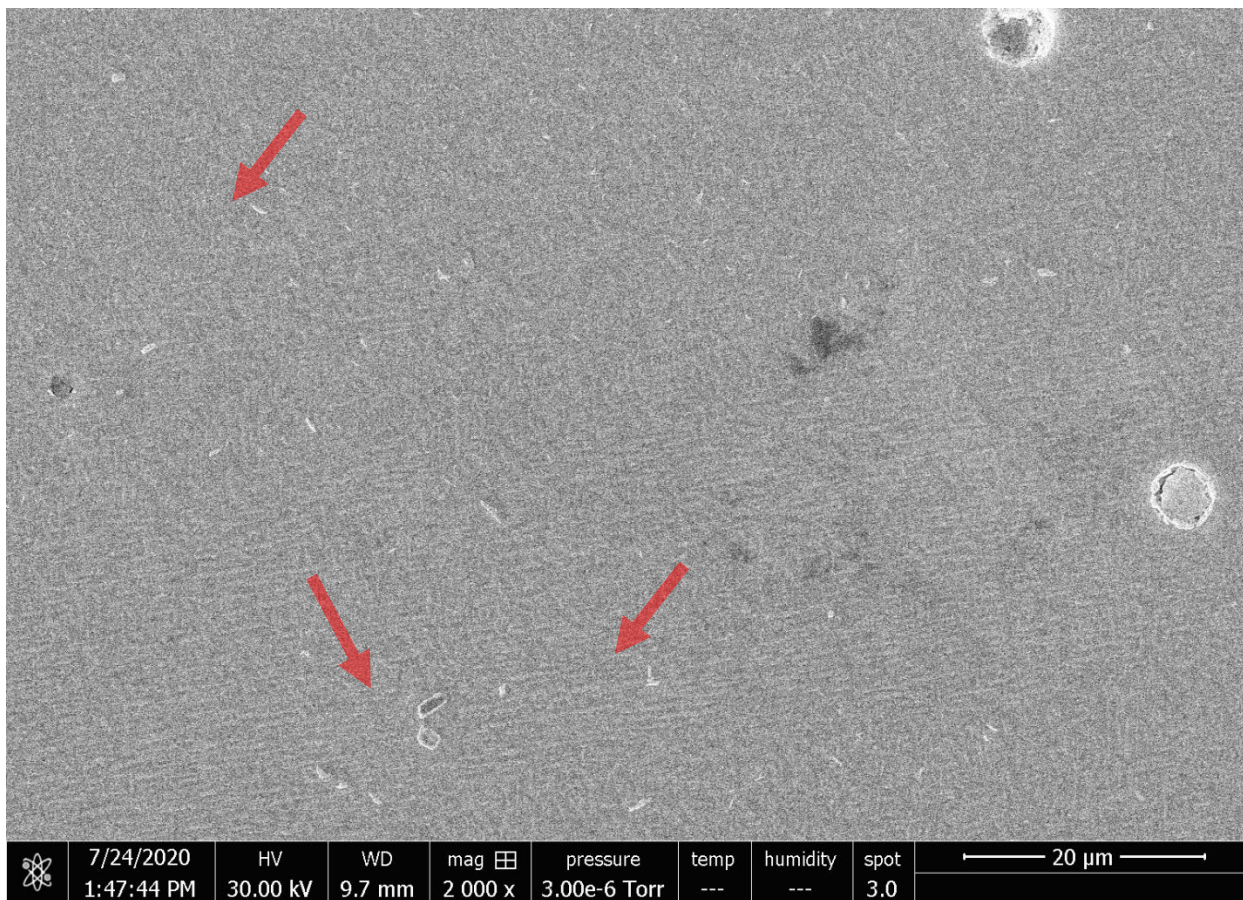


Figure S3-10. 20Ni-4Cr cooled slowly from 850 °C (furnace cooled), showing the region with highest density of non- γ' precipitates (a few are highlighted with arrows).

Hardness values of 3.4, 3.5, and 4.0 GPa were measured for the quenched, air-cooled and furnace-cooled samples, respectively. It is apparent that the furnace-cooled sample is significantly (15%) harder than the more-rapidly cooled samples. This may be due to a higher γ' fraction, e.g. due to precipitation of secondary or tertiary γ' ppt which form between the primary precipitates at lower temperatures, as seen in many Ni-based superalloys [5,64]. .

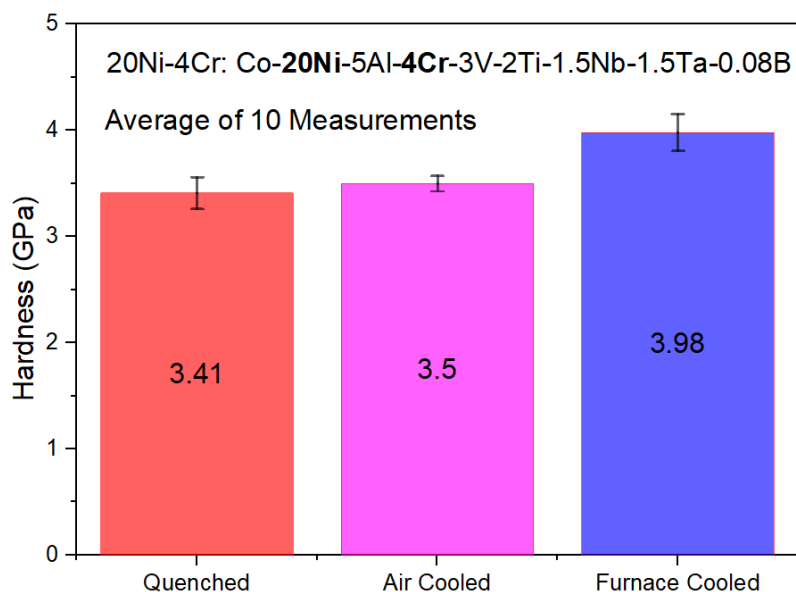


Figure S3-11. Vickers microhardness of 20Ni-4Cr with different cooling rates.

3.8.5 Lattice Misfit

The difference between synchrotron and laboratory sources are sometimes similar to the variance between different compositions because misfit values differ by index, aging condition, and X-ray method. In particular, 10Ni-4Cr, 10Ni-8Cr, and 20Ni-8Cr had many peaks that were difficult to resolve in the lab XRD. Zenk et al. [21] found generally good agreement between (111) and (002) indices in their Co-Al-W-Ti alloys, although, in at least one alloy, the misfit values differed by 50%. Yan et al. [77], when comparing lattice misfit from two different X-ray sources, found a difference of ~ 50% between the values given by synchrotron and neutron diffraction.

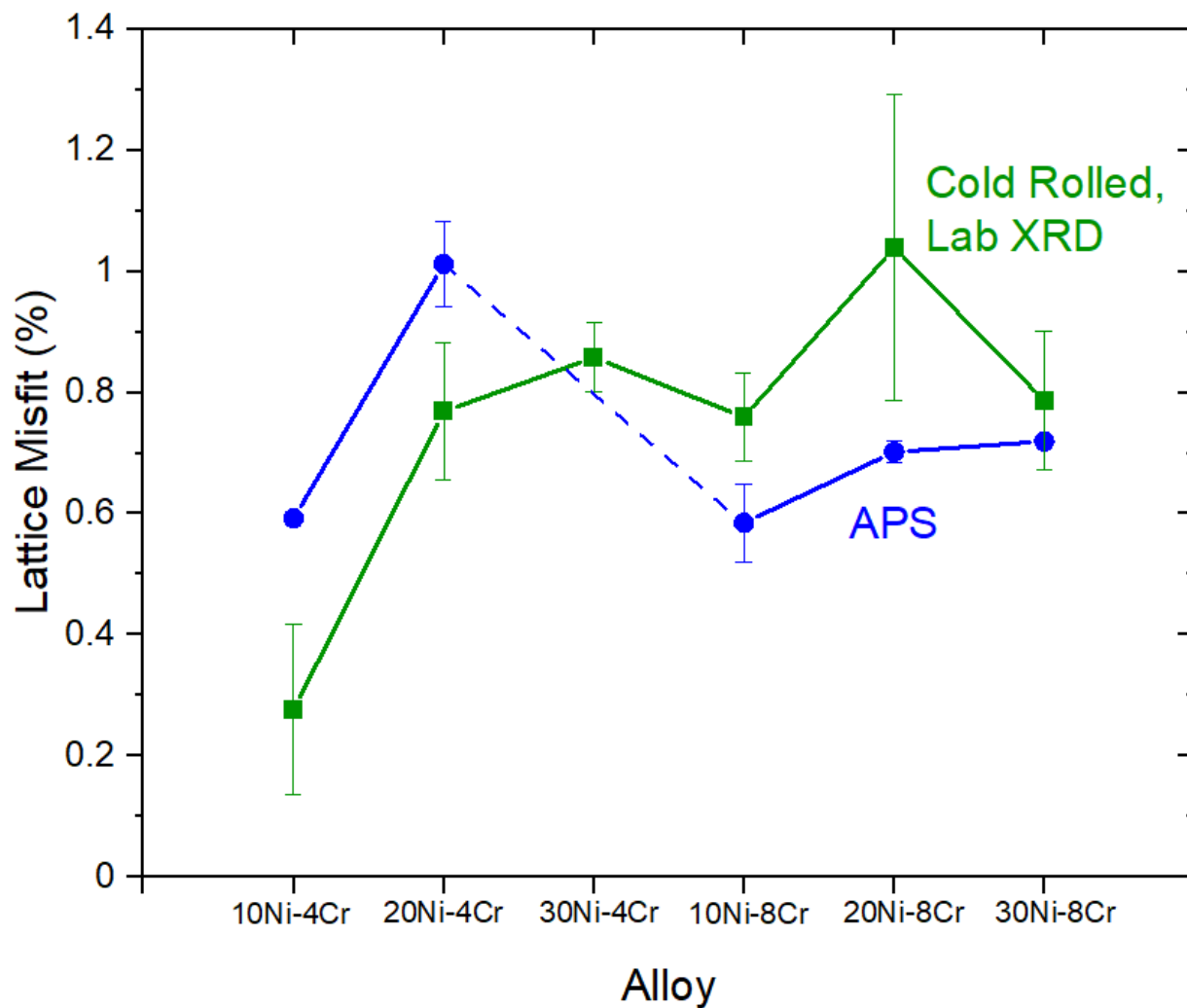


Figure S3-12. Lattice misfit for each alloy, according to x-ray source; blue data points correspond to the average misfit from peaks collected from the Advanced Photon Source (APS), and green data points correspond to the average misfit from peaks collected in the lab XRD.

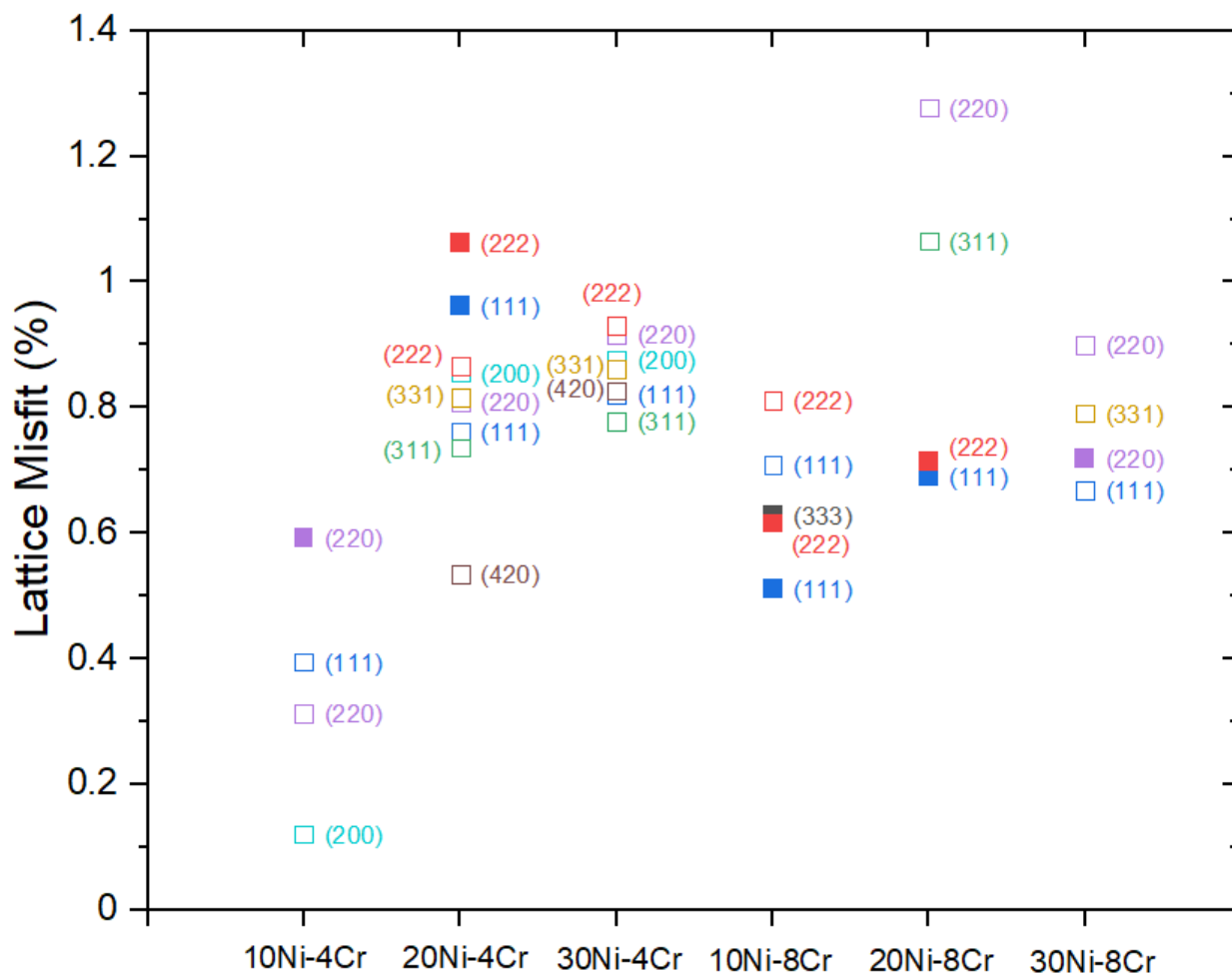


Figure S3-13. All misfit values collected for each alloy. Solid data points are from APS, hollow data points are from lab XRD, and the peak indices are given next to the data points.

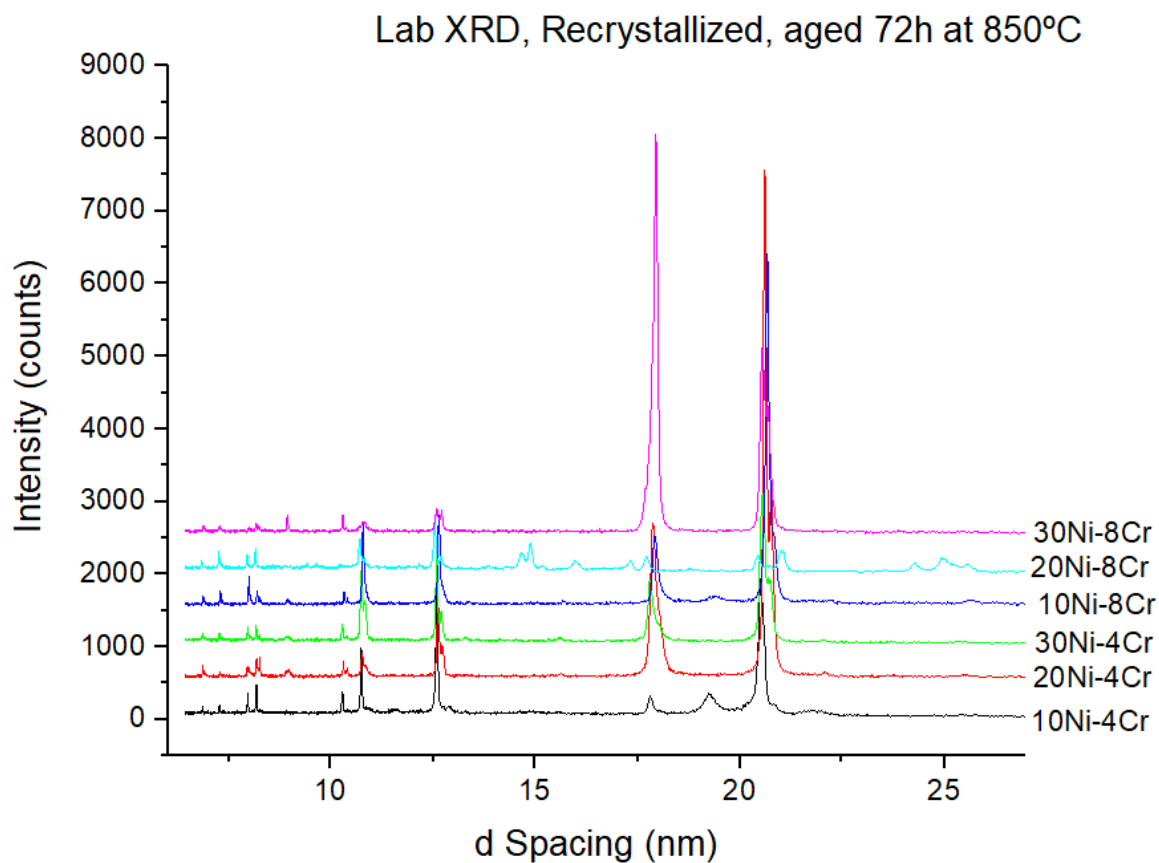


Figure S3-14. Full lab XRD spectra of recrystallized alloys.

3.8.6 Oxidation

The second 30Ni-8Cr sample, which was considered transient from 0-5 h and 10-15 h, showed rate constants $k_{30Ni-8Cr} = 0.14 \frac{mg^2}{cm^4h}$ in the range of 5-10 h, and $k_{30Ni-8Cr} = 0.27 \frac{mg^2}{cm^4h}$ in the range of 15-20 h.

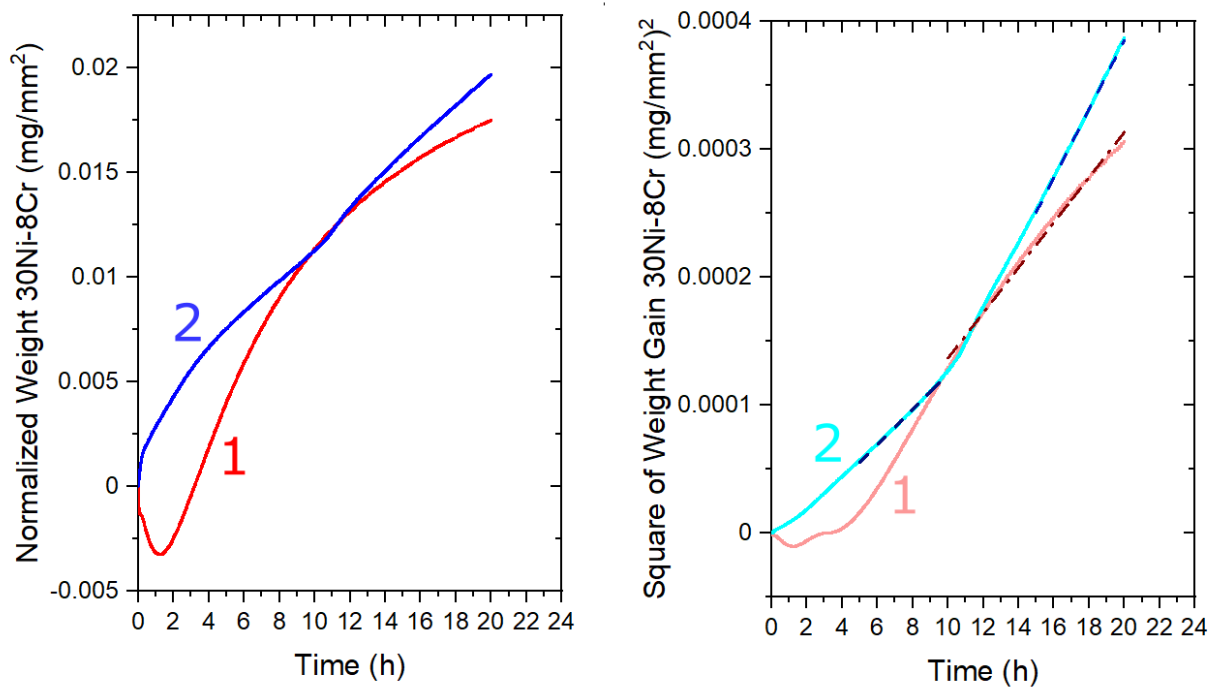


Figure S3-15. Oxidation plots of first and second 30Ni-8Cr samples. (left) normalized weight gain, (right) square of weight gain

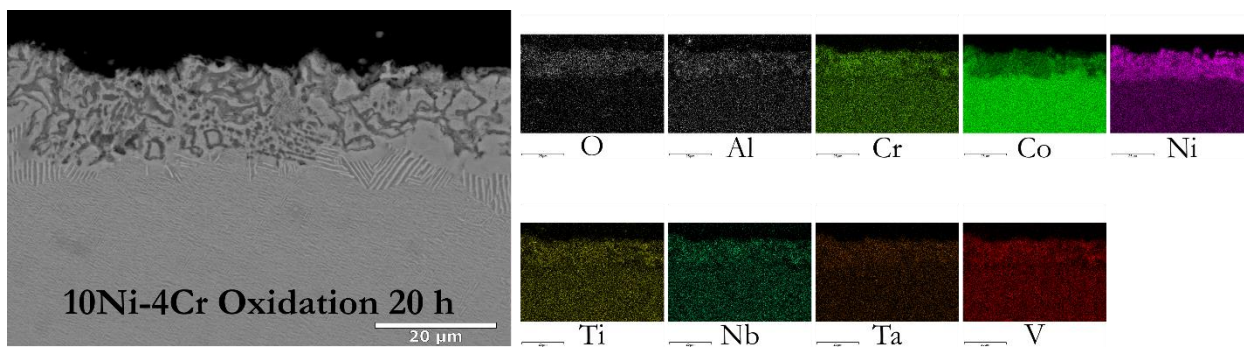


Figure S3-16. EDS compositional maps and backscatter image for 10Ni-4Cr after 20h oxidation at 850 °C.

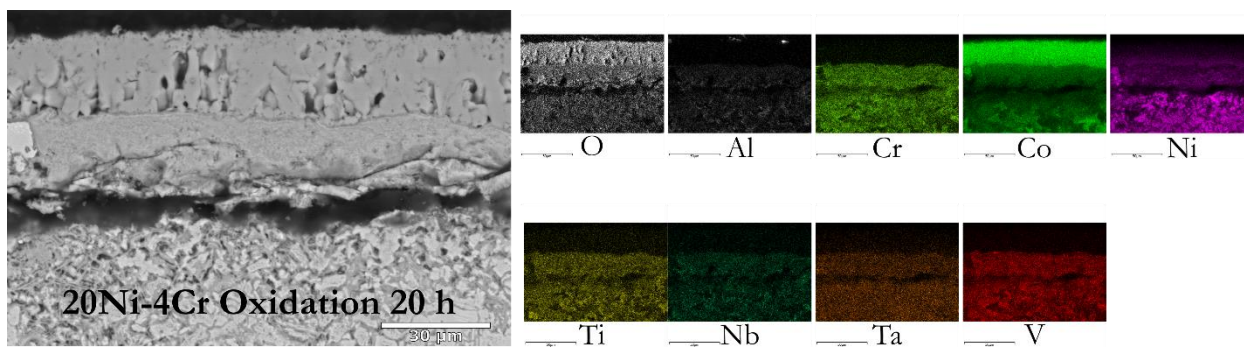


Figure S3-17. EDS compositional maps and backscatter image for 20Ni-4Cr after 20h oxidation at 850 °C.

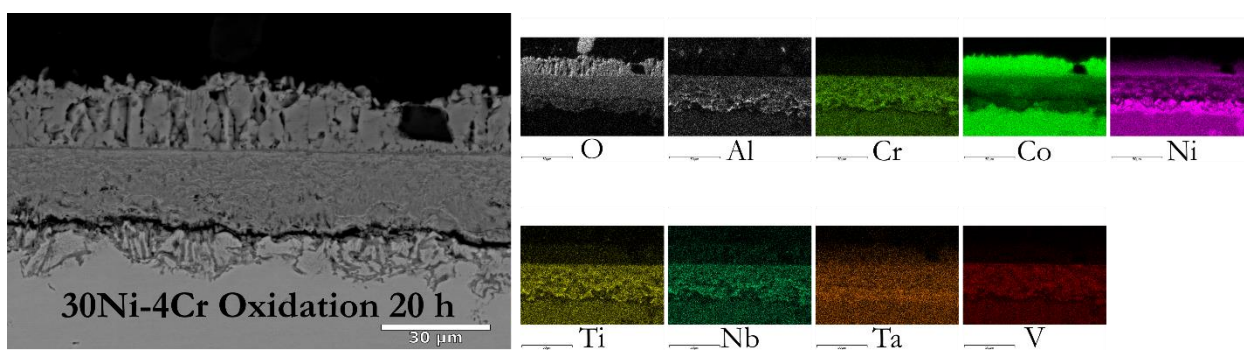


Figure S3-18. EDS compositional maps and backscatter image for 30Ni-4Cr after 20h oxidation at 850 °C.

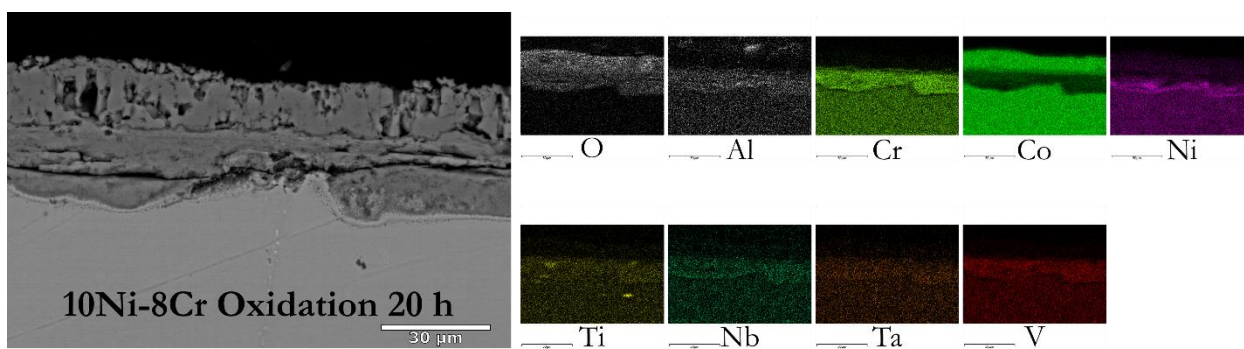


Figure S3-19. EDS compositional maps and backscatter image for 10Ni-8Cr after 20h oxidation at 850 °C.

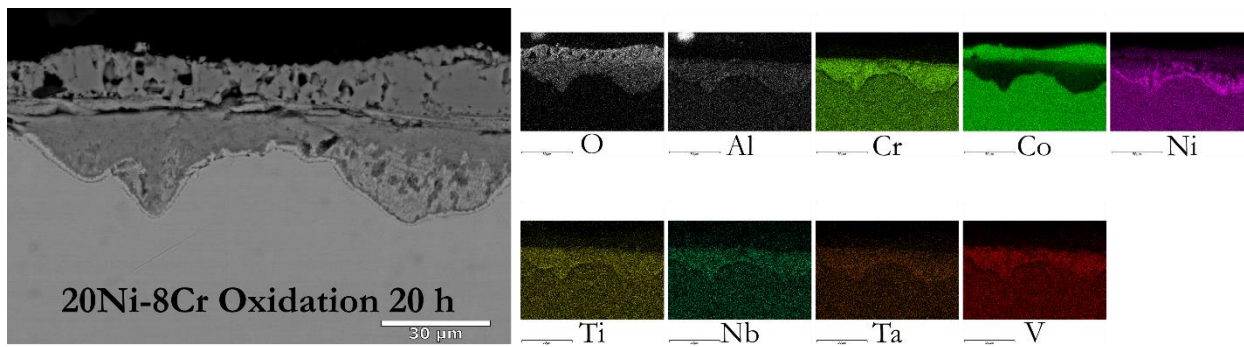


Figure S3-20. EDS compositional maps and backscatter image for 20Ni-8Cr after 20h oxidation at 850 °C.

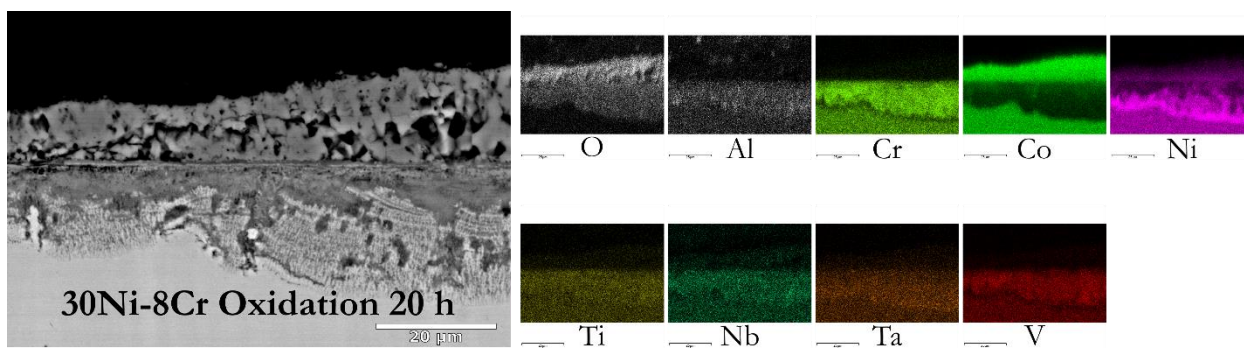


Figure S3-21. EDS compositional maps and backscatter image for 30Ni-8Cr after 20h oxidation at 850 °C.

3.8.7 Post-Creep Microstructure

Raw creep displacement-time curves are given in Fig. S3-22.

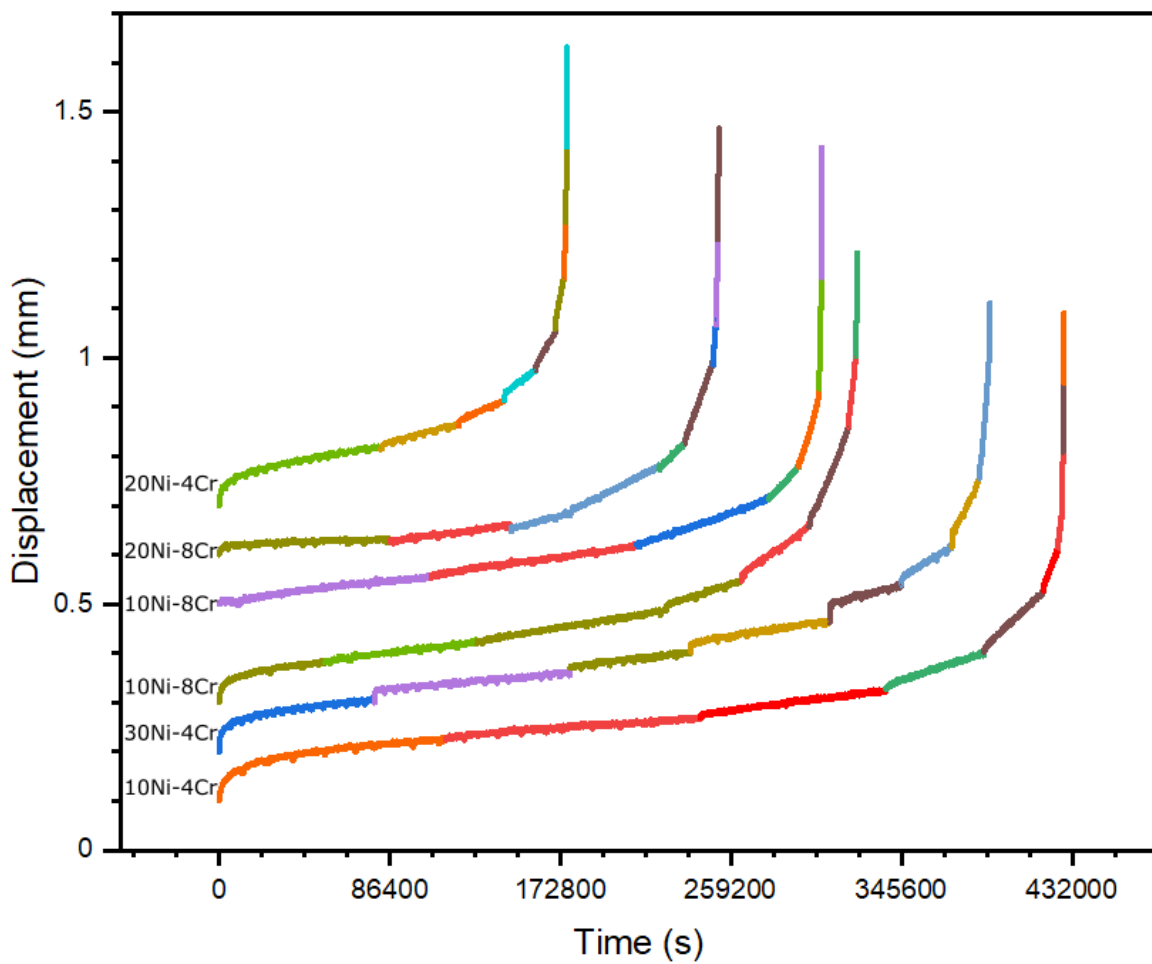


Figure S 3-22. Raw creep displacement vs time curves for all six alloys at 850 °C. Each color changes represents a weight change, the average stress of which is shown in Fig. 3-7.

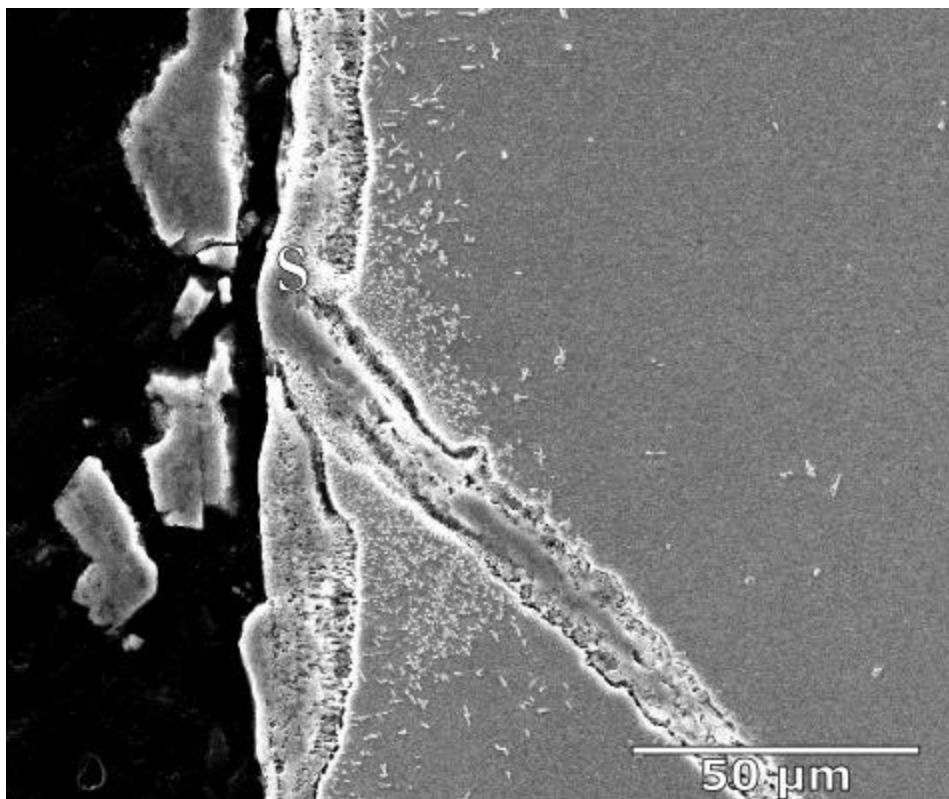


Figure S3-23. SEM micrograph of cross-section of 20Ni-4Cr after creep testing (850 °C for 49 h), showing surface oxide scale (S), and oxide penetrating into the bulk sample at a grain boundary. Creep stress was applied vertically.

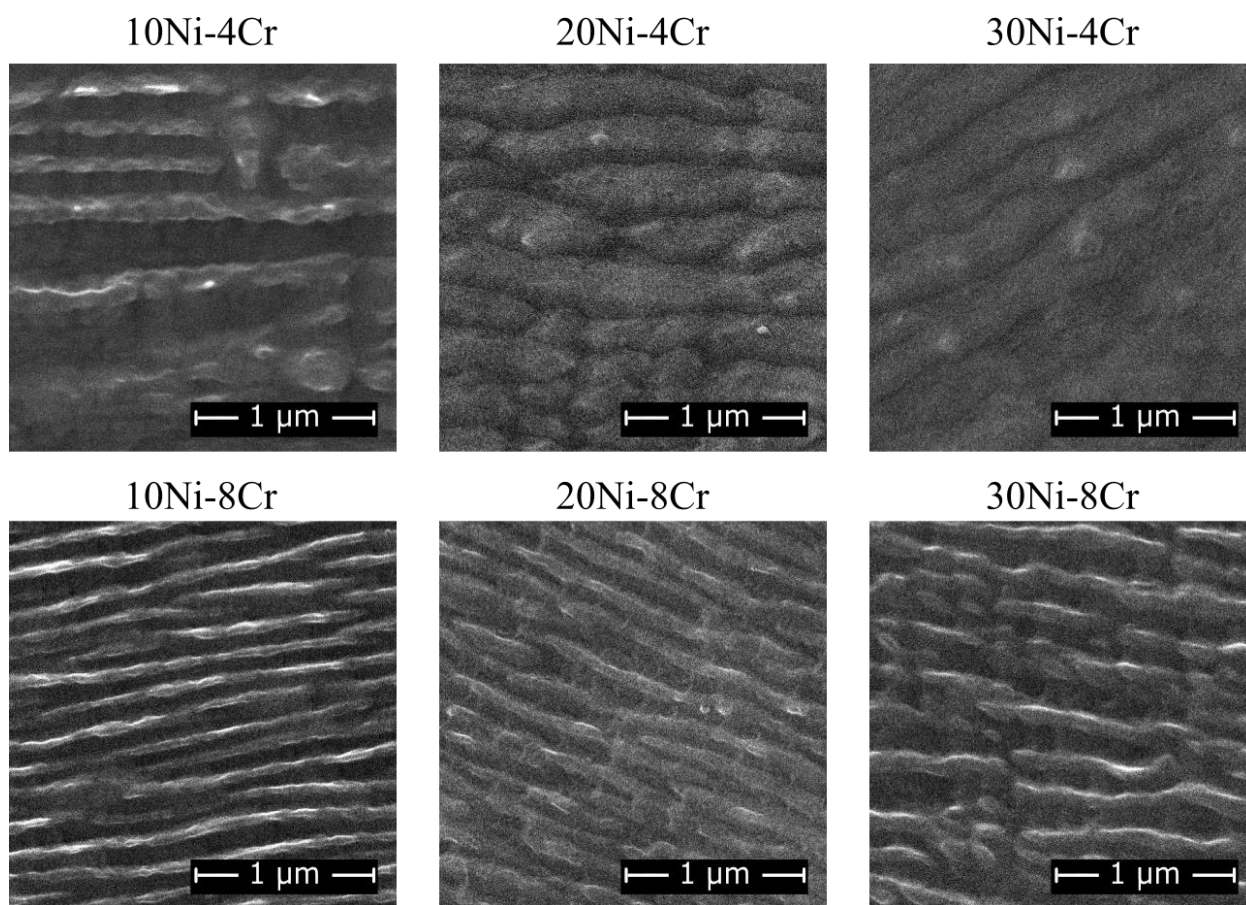


Figure S 3-24. SEM micrograph of creep deformed alloys, with compressive stress applied in the vertical direction.

4. Lattice misfit and aging of quaternary (Co,Ni)-12.5 at.%(Ta,Al) alloys with $\gamma + \gamma'$ microstructure

4.1 Abstract

Microstructure and lattice misfit were analyzed for seven Co-Ni-based alloys: the two binary Co-12.5Ta and Ni-12.5Al (at.%) alloys and five quaternary (Co-Ni)-(Al-Ta) alloys along the tie-line between the binary alloys. The γ' phase precipitated from the γ phase upon aging at 750 °C after 1 h for all alloys, and the γ' precipitates showed slow coarsening up to the longest aging time of 1000 h. Although the two alloys with highest Co and Ta content, Co-12.5Ta and Co-12.5Ni-10.7Ta-1.8Al, did not exhibit a single-phase γ microstructure after homogenization. Lattice misfit between the γ and γ' phases, as determined from neutron diffraction, increases from 0.44% to 1.58% with increasing Co/(Co+Ni) fraction from 0 to 69%. The Co- and Ta-rich alloys show increased propensity for discontinuous precipitation during aging at times between 1 h and 1000 h.

4.2 Introduction

Nickel-based superalloys offer exceptional properties for structural applications at temperatures up to ~ 1100 °C. These properties may be largely attributed to their $\gamma + \gamma'$ microstructure, which is derived from the $\gamma + \gamma'$ phase equilibria in the binary Ni-Al phase diagram (Fig. 4-1a) [93]. The γ phase is an FCC Ni-rich matrix, and γ' is an $L1_2$ -ordered precipitate with typical $\text{Ni}_3(\text{Al,Ti})$ composition, which forms on aging [2,4,45]. However, the trend towards applications with higher service temperatures has motivated research into the development of alloys with higher temperature capability. One class of alloys that have attracted particular interest are Co-based

superalloys with analogous microstructures to Ni-based superalloys. Such alloys have the potential to surpass the temperature capabilities of Ni-based superalloys because of their higher melting point. The most widely investigated Co-based $\gamma + \gamma'$ superalloys are based on the Co-Al-W ternary system and exhibit $L1_2$ - $\text{Co}_3(\text{W},\text{Al})$ precipitates[7]. However, other Co-based $L1_2$ - γ' phases exist in equilibrium with a FCC Co-rich γ matrix, such as Co_3Ti , $\text{Co}_3(\text{Nb},\text{V})$, and $\text{Co}_3(\text{Nb},\text{Ta})$ [11,32,94]. Co_3Ta is another $L1_2$ phase reported to form in a Co-rich γ matrix [95]. However, in binary Co-Ta alloys this phase can only precipitate metastably from the two-phase $\gamma + \lambda_3$ (previously identified as C36) region[96], as illustrated in Fig. 4-1b [97]. A metastable phase diagram of the Co-Ta system was calculated by Shinagawa et al.[96], which shows single-phase regions for γ -Co(Ta) and γ' - Co_3Ta , separated by a two-phase $\gamma + \gamma'$ region. For Co-12.5Ta at 750 °C, this calculated phase diagram predicts $\sim 50\%$ γ' volume fraction [96]. However, alloys strengthened by a high fraction of this phase may not be able to be homogenized in a single-phase region. It would be possible to homogenize a hypoeutectic composition, such as Co-5Ta, then quench and age at a lower temperature to prevent λ_3 formation. However, such an alloy would have a low fraction of $L1_2$ γ' phase and would likely still form some amount of needlelike Co_7Ta_2 .

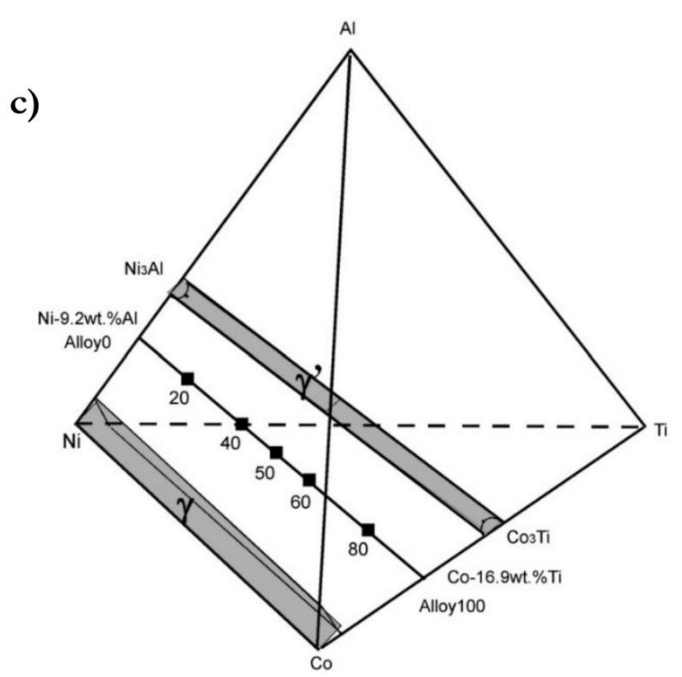
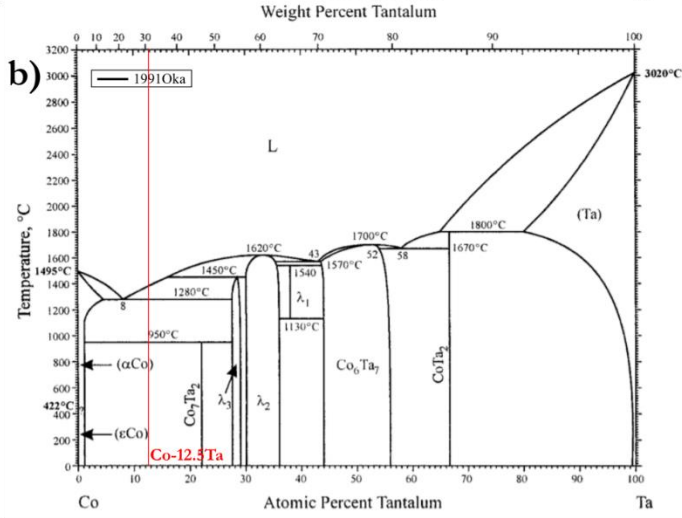
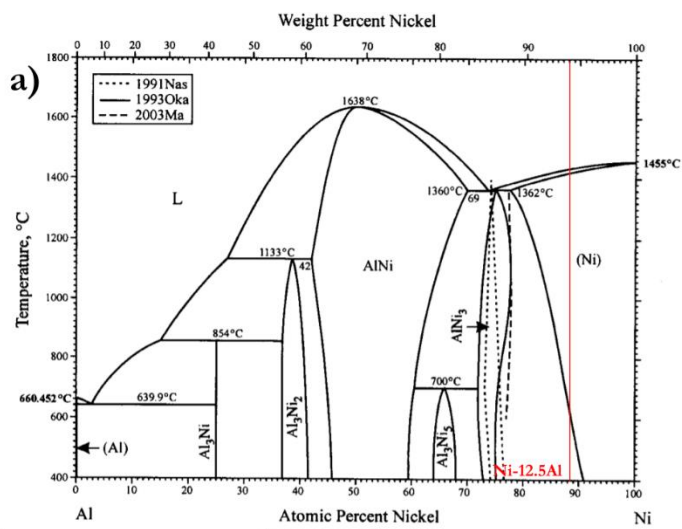


Figure 4-1 (Top) Ni-Al binary phase diagram with Ni-12.5Al composition highlighted, reproduced from [93]. (Middle) Co-Ta binary phase diagram with Co-12.5Al composition highlighted, reproduced from [97]. (Bottom) Partial quaternary isothermal section from the Co-Ni-Ti-Al system showing continuous $\gamma + \gamma'$ region, reproduced from [98].

In multinary Co-based superalloys, Ta plays an important role in forming more complex γ' compositions, which has facilitated these alloys achieving properties approaching those of early-generation Ni-based superalloys [26,34]. To better understand the effect Ta has, it is contended that studies of simpler Co-Ta based alloys, where Co is partially replaced by Ni and Ta by Al may be of value. This is reminiscent of studies of (Co,Ni)-(Ti,Al) alloys in which Ni was partially replaced by Co and Al by Ti. These studies lead to the identification of a continuous $\gamma + \gamma'$ two-phase field, as shown in Fig. 4-1c [55,98].

Thus, we investigate here whether a continuous $\gamma + \gamma'$ two-phase field also exists in the Co-Ni-Ta-Al quaternary system, with end-members being Co-rich binary Co-Ta alloys (consisting of γ -Co(Ta) + metastable $L1_2$ -Co₃Ta) and Ni-rich binary Ni-Al alloys (consisting of γ -Ni(Al) + stable $L1_2$ -Ni₃Al). We performed SEM and neutron diffraction and find that alloys Co(Co+Ni) fraction > 85% and Ta > 10 at.% exhibited a 2-phase $\gamma + \lambda_3$ microstructure after homogenization, with other alloys exhibiting a single phase γ . Upon aging for 1 hour at 750 °C all alloys initially precipitated γ' phase within the γ phase. Following longer aging times, high-Co alloys absorbed γ' to form a discontinuous precipitate, while all other alloys showed slow precipitate coarsening up to 1000 h. Lattice misfit and interfacial stress were calculated from the neutron diffraction data for the alloys that displayed a single phase after homogenization.

4.3 Experimental Methods

Seven alloys were cast with compositions that lie along the tie-line between Co-12.5Ta and Ni-12.5Al (all compositions here and later are given in at.%), according to Table 4-1. The alloys are named according to their Co/(Co+Ni) atomic fraction. Casting was performed in two steps. First, 500 g ingots of binary Co-12.5Ta and Ni-12.5Al were cast using vacuum induction melting (VIM) from 99% (or purer) raw elements. Then, 60 g finger-shaped ingots were prepared via vacuum arc remelting (VAR) by melting the correct ratio of the binary ingots.

Alloy designation	Co/(Co+Ni) or Ta/(Ta+Al) atomic fraction (%)	Co (at.%)	Ni (at.%)	Ta (at.%)	Al (at.%)	Homogenization Temperature (°C)
CoNi0	0	0	87.5	0	12.5	1380
CoNi14	14	12.5	75.0	1.8	10.7	1380
CoNi31	31	27.5	60.0	3.9	8.6	1330
CoNi50	50	43.5	44.0	6.2	6.3	1300
CoNi69	69	60.0	27.5	8.6	3.9	1300
CoNi86	86	75.0	12.5	10.7	1.8	1270
CoNi100	100	87.5	0	12.5	0	“

Table 4-1. Nominal compositions of the alloys and their respective homogenization temperatures.

After casting, ingots were encapsulated in fused silica tubes which were evacuated and backfilled with argon. Each encapsulated sample was homogenized for 20 h at temperatures between 1380 and 1270 °C, as shown in Table 4-1, and “true air cooled” by breaking the tube in

air upon removal. These temperatures were determined to be close to, but below, the solidus temperature of the alloy determined by Differential Scanning Calorimetry (DSC). The DSC data were acquired from cast samples using a Netzsch 404C instrument. For these measurements, heating and cooling rates were 10 °C/min, and the sample was contained within an alumina crucible alongside an identical empty alumina crucible for reference.

After homogenization but before aging, a large cylinder was cut from each ingot by electrical discharge machining (EDM). Neutron diffraction was performed on these samples using the POLARIS beam line at the ISIS facility (Chilton, UK), with a data acquisition time of about 30 minutes. The beam line has 4 detector banks: a very low angle detector with 2θ of 13°-15°, resolution 0.03 $\delta d/d$, and d range 0.5-21.0 Å; a low angle detector with 2θ of 28°-42°, resolution 0.01 $\delta d/d$, and d range 0.5-8.15 Å; a 90 degree detector with 2θ of 85°-95°, resolution 0.007 $\delta d/d$, and d range 0.3-4.1 Å; and a backscattering detector with 2θ of 130°-160°, resolution 0.005 $\delta d/d$, and d range 0.2-3.2 Å. For alloys CoNi0 to CoNi69, the cylindrical sample used for neutron diffraction consumed the entire ingot. As such, for these samples subsequent heat treatments and microstructural analyses were performed on the ring left after EDM cutting.

The neutron diffraction data were fitted in GSAS-II [99] using Pawley refinement on the 135° backscatter bank, as well as a combined Le Bail fit which considered data from all 4 banks. Initially, γ' peaks were fit based on the superlattice reflections, then tetragonal γ peaks were fitted, maintaining a 2:1 intensity ratio between peaks from the a and c tetragonal lattice parameters. The γ phase was assumed to have a tetragonal distortion due to interfacial stress [100,101], which is illustrated in Fig. 4-2 and is explained in detail in section 3.1.

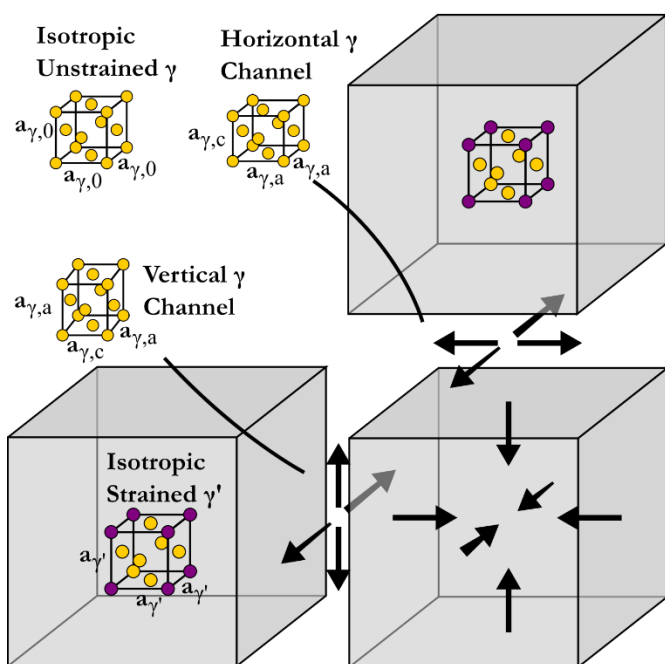


Figure 4-2. Schematic illustration showing how interfacial stress may result in a tetragonal distortion of the γ matrix. In an alloy with positive lattice misfit, the γ' lattice parameter is larger than that of the γ and hence experiences a hydrostatic compressive stress to maintain coherency. The γ , which exists as thin films between the γ' experiences biaxial tensile stress, stretching two parameters (a) and leading to a Poisson contraction of the third parameter (c). The short parameter is aligned perpendicular to the γ/γ' interface and is oriented differently in the horizontal and vertical γ channels.

Each alloy was encapsulated in Ar-backfilled glass ampoules and heat treated at 750 °C for 1, 10, 100, and 1000 h. The aged specimens were polished up to 4000 grit and lapped with colloidal silica. Chemical etching was performed with Kalling's or Carapella's reagent. In some cases, electrolytic etching was performed with nitric or phosphoric acid. To observe the changes in microstructure, Secondary Electron (SE) imaging and Backscatter Electron (BSE) imaging, as well as Energy Dispersive X-ray Spectroscopy (EDS) were performed on a Zeiss Gemini 300-70-97 Scanning Electron Microscope (SEM) operated with an accelerating voltage of 15 kV.

4.4 Results and Discussion

4.4.1 Lattice Misfit

The lattice parameters of the γ and γ' phases were obtained by fitting the neutron diffraction patterns with GSAS-II using a Pawley refinement on the highest resolution bank, and a simultaneous Le Bail refinement on all four banks. The results from the two methods differed by less than 0.01% and although each calculated peak location occurs at the correct position, the total fitting is not optimal because large grains in the sample lead to texturing effects. An example of one Pawley fit is given in Fig. 4-3.

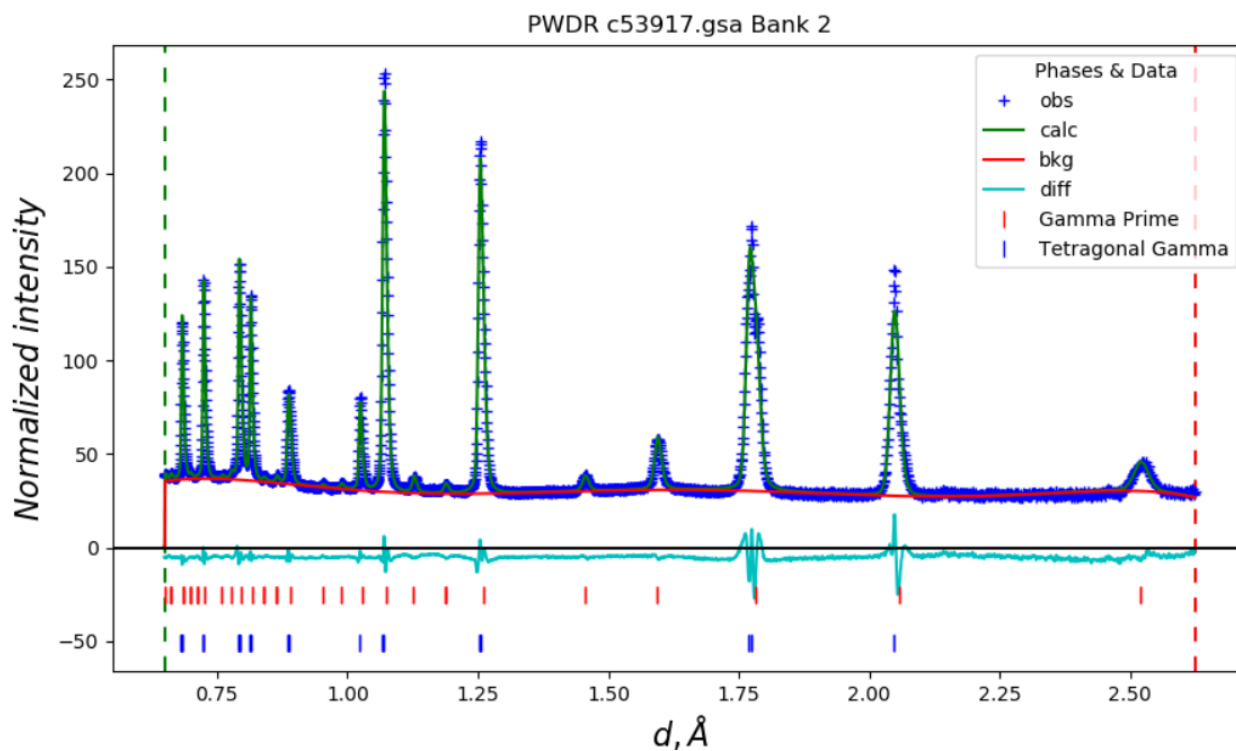


Figure 4-3. Neutron data from alloy CoNi0 in Bank 2, with the highest resolution, in blue. The red line is the background, and the green line is the calculated Pawley peak fitting. Red and blue dashes at the bottom indicate the locations of γ' and tetragonal γ peaks.

The resulting lattice parameters for γ' ($a_{\gamma'}$) and tetragonally distorted γ ($a_{\gamma,a}$ and $a_{\gamma,c}$) are given in Fig. 4-4. This graph also shows the unstrained lattice parameter for γ ($a_{\gamma,0}$), the calculation of which is explained below.

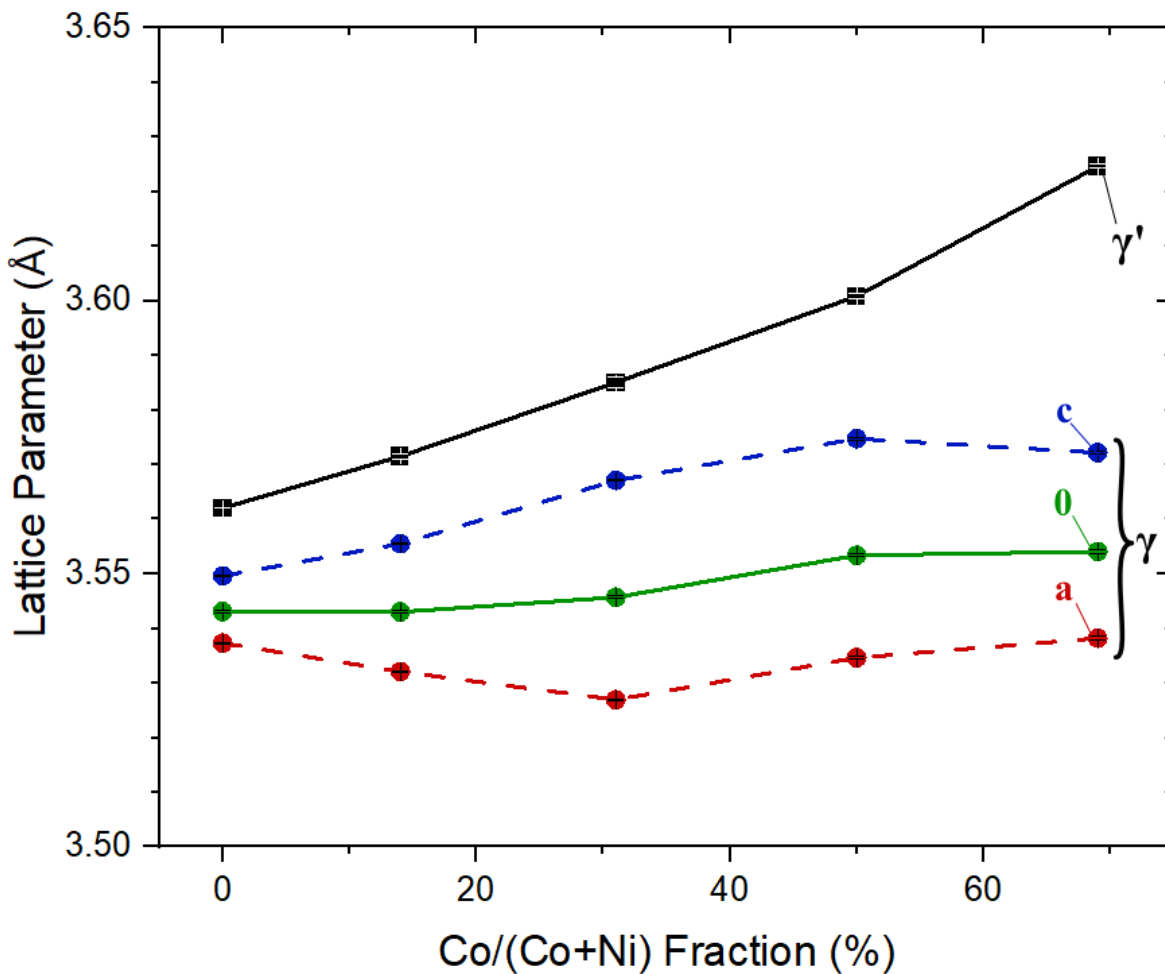


Figure 4-4. Lattice parameters for the γ' phase (black), the tetragonally-distorted γ phase (labelled "a" (red) and "c" (blue)), and calculated unstrained γ phase (green, labelled "0").

The γ' lattice parameter increases monotonically with increasing Co/(Co+Ni) fraction. Both tetragonal lattice parameters for the γ phase increase up to 50% Co/(Co+Ni), but decrease at the

final composition. A possible explanation for this decrease may be related to the precipitation of another phase, which is explained in section 3.3.

The lattice misfit δ between the γ' and γ phases is defined as $\delta = \frac{2(a_{\gamma'} - a_{\gamma})}{(a_{\gamma'} + a_{\gamma})}$, where $a_{\gamma'}$ and a_{γ} are the lattice constants of the two cubic phases[39]. In Ni-base superalloys, the lattice misfit is typically negative ($a_{\gamma'} < a_{\gamma}$), while in Co-based superalloys it is positive [43,76]. In alloys with high misfit, coherency stress at the interface can cause a tetragonal distortion of the cubic γ -phase [102]. In this case, it is useful to use $a_{\gamma,0}$ to represent the lattice parameter of the unconstrained cubic γ phase, $a_{\gamma,a}$ to represent the two identical lattice parameters of the tetragonal structure, and $a_{\gamma,c}$ to represent the third lattice parameter of the tetragonal structure. If the tetragonal distortion is negligible, $a_{\gamma,0} = a_{\gamma,a} = a_{\gamma,c}$.

With a tetragonal distortion due to interfacial stress, the unstressed cubic lattice parameter can be calculated as

$$a_{\gamma,0} = \frac{a_{\gamma,c} - \chi a_{\gamma,a}}{1 - \chi}$$

Where χ is related to Poisson's ratio $\chi = \frac{-2\nu}{1-\nu}$. For full details, see supplemental section 8.1.

The Poisson's ratios of pure Ni and Co are reported to be 0.305-0.315 and 0.31-0.33,[103–105] respectively, so this work will proceed with the assumption $\nu = 0.305$, or $\chi = -0.878$.

The final expression for lattice misfit is now written:

$$\delta = \frac{2(a_{\gamma'} - \frac{a_{\gamma,c} + 0.878a_{\gamma,a}}{1.878})}{(a_{\gamma'} + \frac{a_{\gamma,c} + 0.878a_{\gamma,a}}{1.878})}$$

Upper and lower error bars correspond to the standard error propagation formula,

$\Delta Q(a, b, c) = \sqrt{\left(\frac{\partial Q}{\partial a} \cdot \Delta a\right)^2 + \left(\frac{\partial Q}{\partial b} \cdot \Delta b\right)^2 + \left(\frac{\partial Q}{\partial c} \cdot \Delta c\right)^2}$, where Q is a function of a , b , and c , each of which have their own error, represented by Δ . The formula assumes an absolute error of 0.005 for the Poisson's ratio and uses esds error reported in GSAS-II.

The lattice misfit, as well as the calculated cubic γ and γ' lattice parameters, are shown in Fig. 4-5. As the Co/(Co+Ni) fraction increases, the misfit also increases monotonically. Interfacial stress generally increases as Co/(Co+Ni) fraction approaches 50%, and decreases ~200 MPa from CoNi50 to CoNi69.

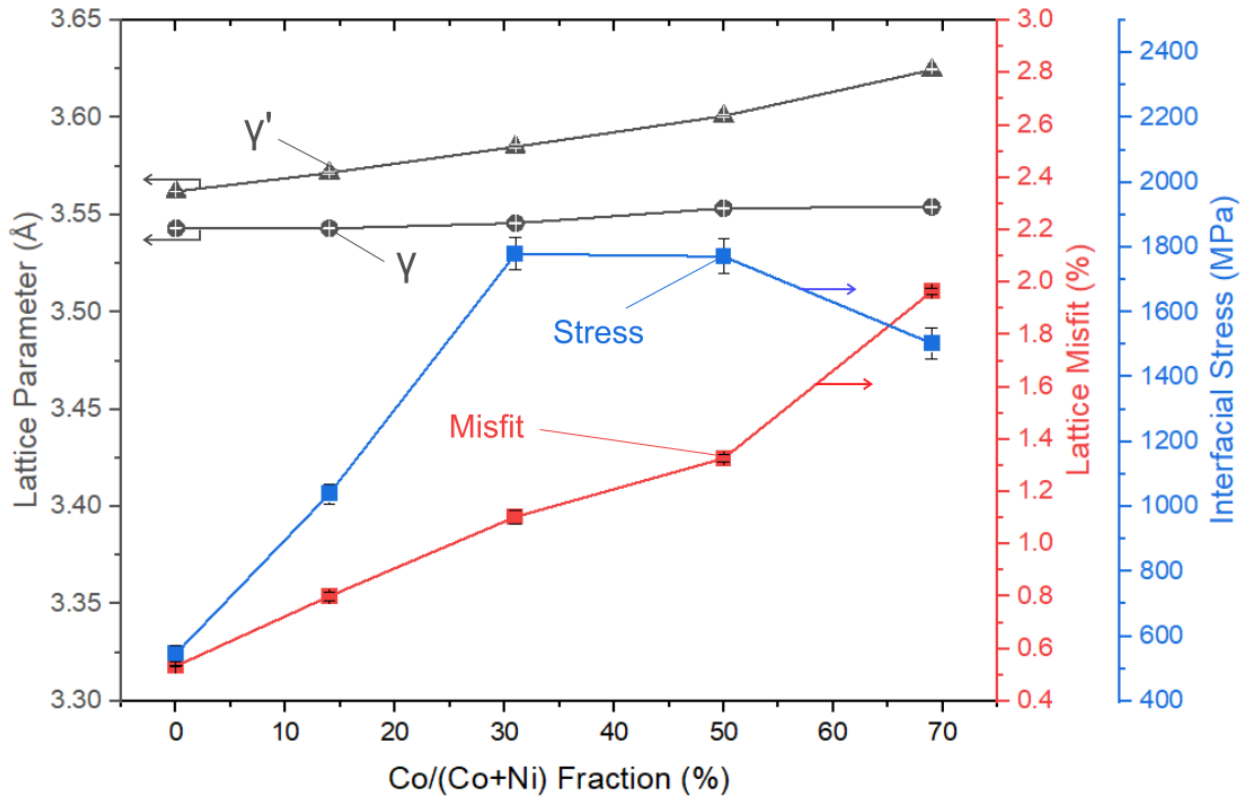


Figure 4-5. Lattice parameters for γ' (black triangles) and calculated cubic γ (black circles). Error bars for the lattice parameters are smaller than the markers used. Lattice misfit (%) is plotted in red (error bars smaller than markers), and interfacial stress (MPa) is in blue.

Given that $E\varepsilon_{\parallel} = \sigma_{\parallel}(1 - \nu)$ the planar interfacial stress is:

$$\sigma_{\parallel} = \frac{E}{1 - \nu} * \frac{a_{\gamma,a} - a_{\gamma,0}}{a_{\gamma,0}}$$

In a study of Ni-Co-Al-Ti alloys, Minshull [106] obtained values of the interfacial stress by assuming $E = 200$ GPa. The Young's modulus of pure Ni and pure Co are 199.5 and 211 GPa, respectively [103], so this work will proceed with the assumption that $E = 205$ GPa with an

absolute error of 5 GPa and the value of ν between 3 and 3.1 which corresponds to the highest and lowest stress, as shown in Fig. 4-5.

The magnitude of the interfacial stress follows a similar trend to the lattice misfit, generally increasing with increasing Co:Ni ratio, except for CoNi50 which shows ~500 MPa decrease from its neighbors.

4.4.2 Transformation Temperatures

DSC thermograms obtained from alloys CoNi14 to CoNi100 upon heating from the homogenized state are shown in Fig. 4-6. Around 700-800 °C, small peaks are measured, which are consistent with dissolution of secondary γ' precipitates. Slightly larger peaks in the range of 800-1200 °C indicate the true solvus temperature of primary γ' precipitates, although these peaks are small and sometimes difficult to detect, particularly in the case of CoNi14 and CoNi50. Since these alloys were not aged, the volume fraction and corresponding DSC signal of γ' precipitates is low and thus we are not confident enough to report this measurement.

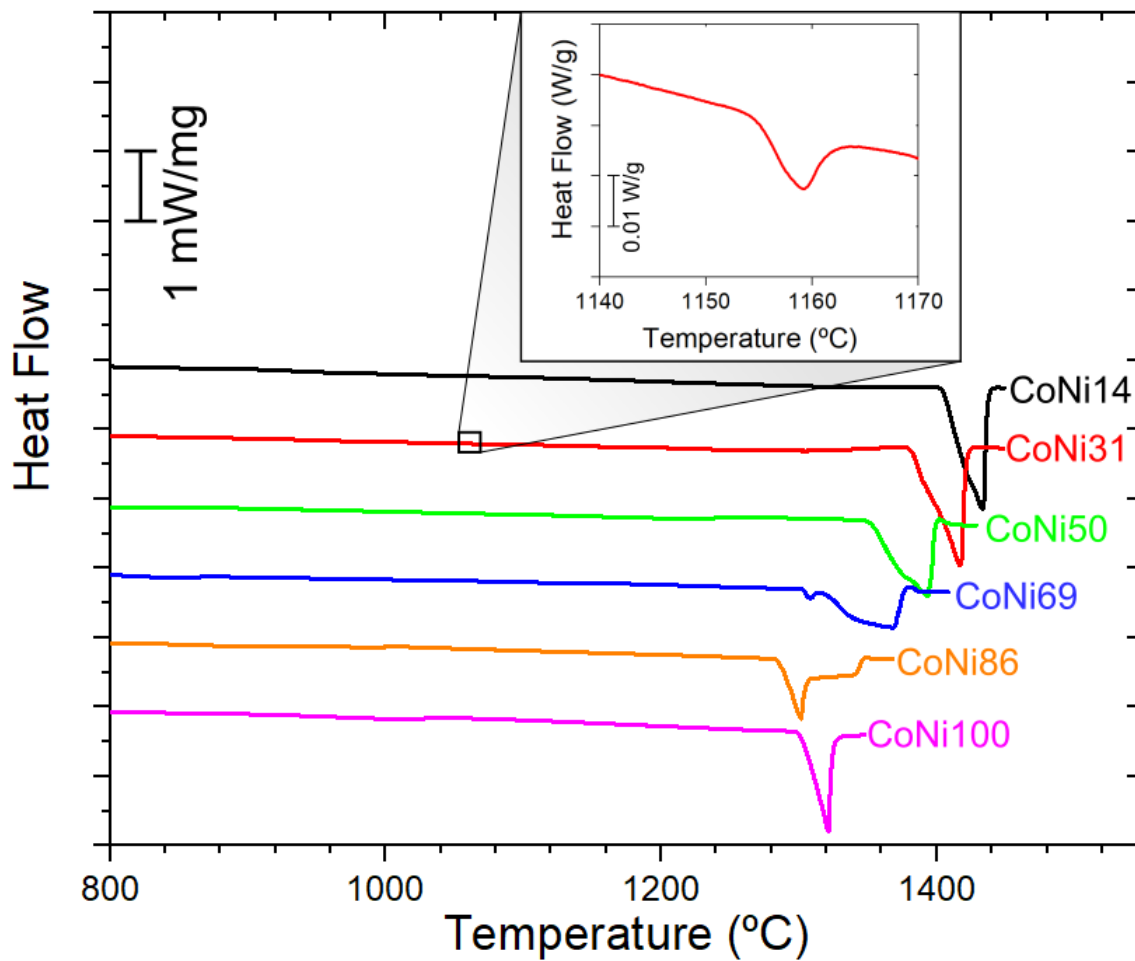


Figure 4-6. DSC thermograms on heating for alloys CoNi14-CoNi100. Because DSC data were collected on homogenized and air-cooled samples, the γ' fraction formed on cooling (rather than aging) was low, and therefore the solvus peaks are small. An expanded view of the most-visible solvus peak, in CoNi31, is presented in the inset figure.

The liquidus and solidus peaks are clear for all alloys, but CoNi69 to CoNi86 shows double endothermic peak due to a nearby eutectic reaction as predicted in the Co-Ta binary phase diagram (see Figure 4-1b) [107].

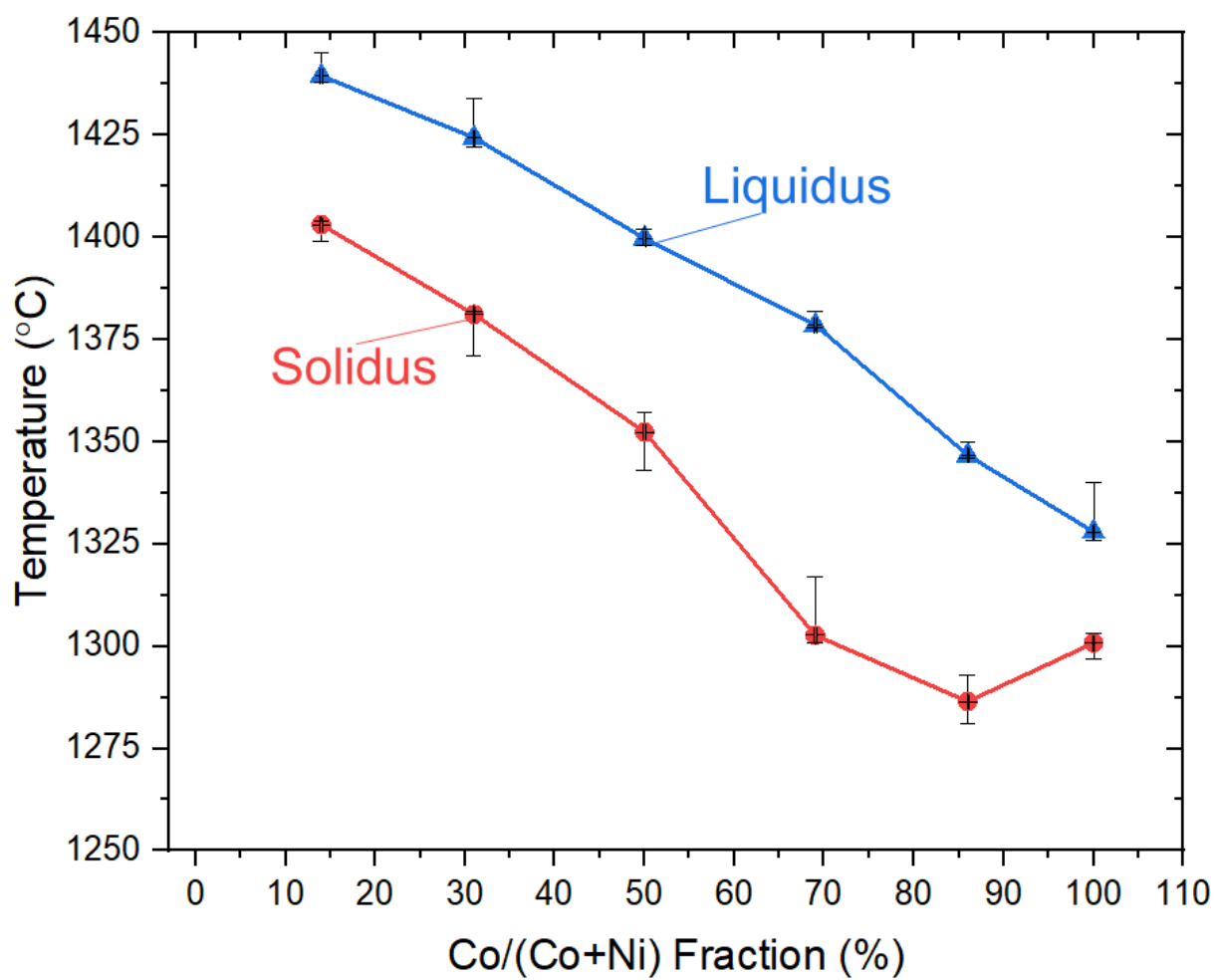


Figure 4-7. Solvus, solidus, and liquidus temperatures for alloys CoNi14-CoNi100. DSC data were not collected for CoNi0.

	Solidus (°C)	Liquidus (°C)
CoNi14	1403	1439.4
CoNi31	1381.1	1424.3
CoNi50	1352.4	1399.7
CoNi69	1302.7	1378.5

CoNi86	1286.5	1346.7
CoNi100	1300.8	1328

Table 4-2. Solvus, solidus, and liquidus temperatures for alloys CoNi14-CoNi100. DSC data were not collected for CoNi0. The solvus peak for CoNi0 and CoNi50 was especially difficult to ascertain.

Solidus and liquidus temperatures, reported in Table 4-2 and plotted in Fig. 4-7 decrease monotonically with increasing Co:Ni ratios,. Considering that traveling along the tie line between Ni-12.5Al and Co-12.5Ta leads near the $\gamma + \lambda_3$ eutectic at Co-8.5Ta and 1280 °C, it is not unexpected that solidus/liquidus values—and the freezing range between them— decrease as the alloys become richer in Co and Ta.

4.4.3 Aged Microstructure

SE images of alloys CoNi0 to CoNi50 aged at 750 °C for 1, 10, 100, and 1000 h are shown in Fig. 4-8. These alloys showed negligible amounts of other precipitates.

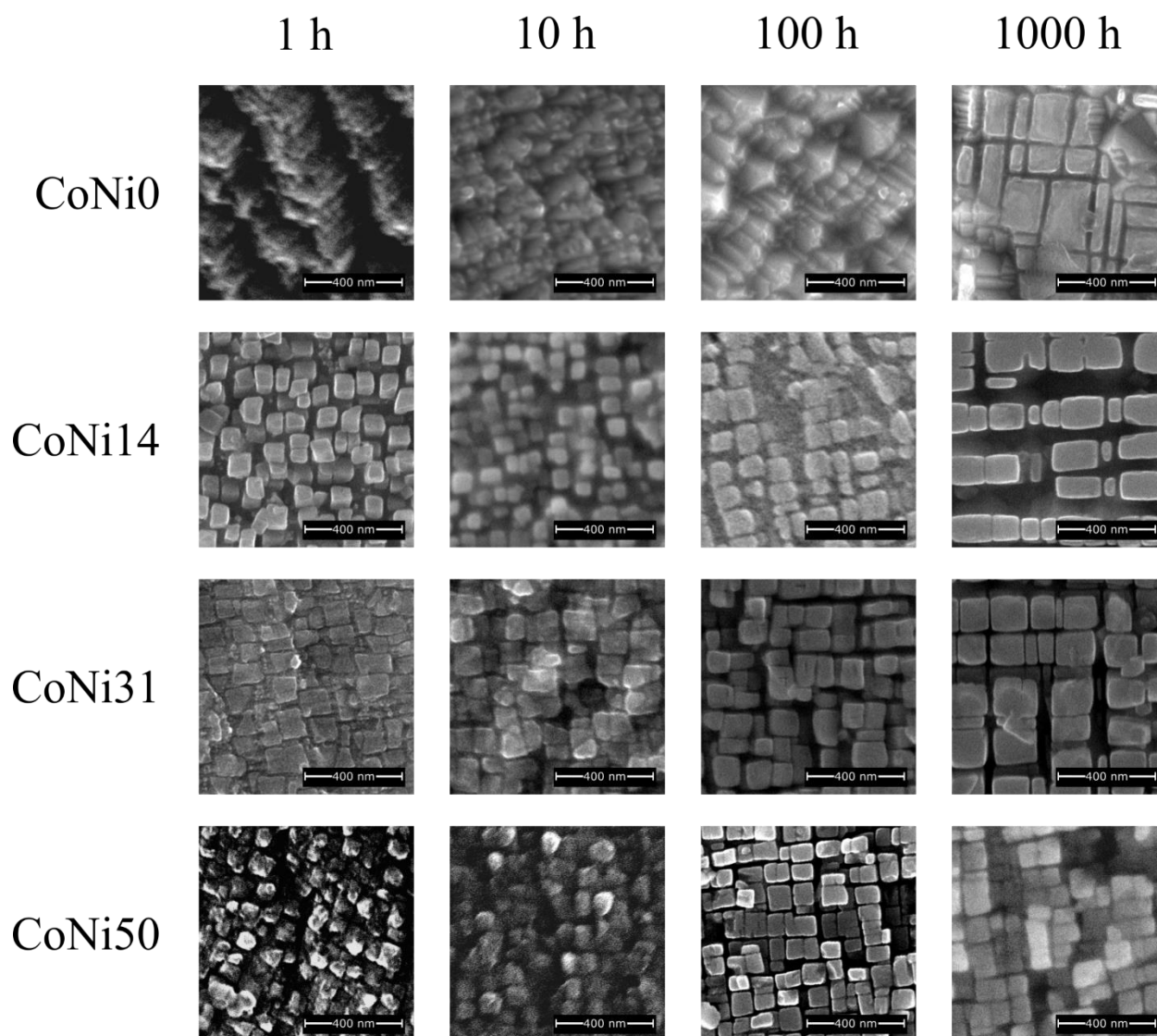


Figure 4-8. SEM images of $\gamma+\gamma'$ microstructure for alloys CoNi0-CoNi50, up to 1000 hrs. aging at 750 °C at 50,000x magnification

Alloys CoNi69, CoNi86, and CoNi100 did not achieve a single-phase microstructure during homogenization. CoNi69 precipitated large (200-400 nm) cuboidal precipitates that nucleated along with another type of needle shape precipitates, as shown in Fig. S4-2.

Alloys CoNi86 and CoNi100 show a two-phase microstructure, which is expected because they were homogenized in the two-phase $\gamma+\lambda_3$ region of the phase diagram. The dark phase is the γ matrix and the light phase is rounded λ_3 precipitates with a size of 1-50 μm and having various aspect ratios and partial interconnectivity. CoNi86 had a γ' volume fraction of $13\pm 2\%$, and 100Co-Ni had a γ' volume fraction of $36\pm 4\%$ based on ImageJ calculations of at least 100 precipitates at each aging time. There was no significant difference in the morphology of these precipitates at different aging times.

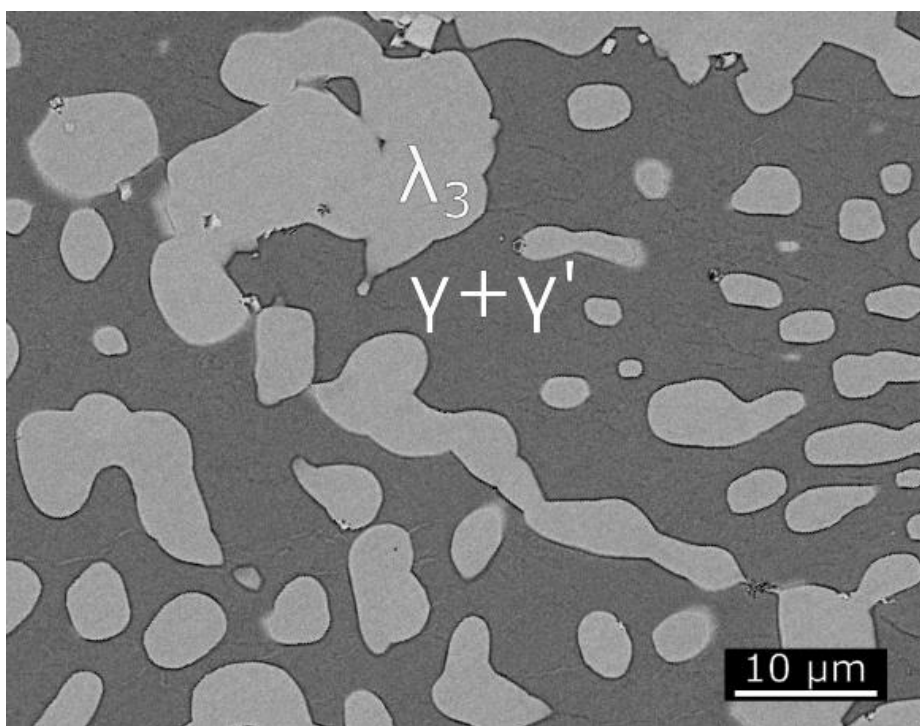


Figure 4-9. BS image showing microstructure of alloy CoNi100 after homogenization and aging for 1 hour

Nevertheless, alloys CoNi69-CoNi100 still precipitated upon aging cuboidal γ' within their γ phase, as shown in Fig. 4-10. However, for CoNi86 and CoNi100, the γ' was entirely consumed

by a discontinuous precipitate after aging for 1000 h, so these micrographs are missing in Fig. 4-10.

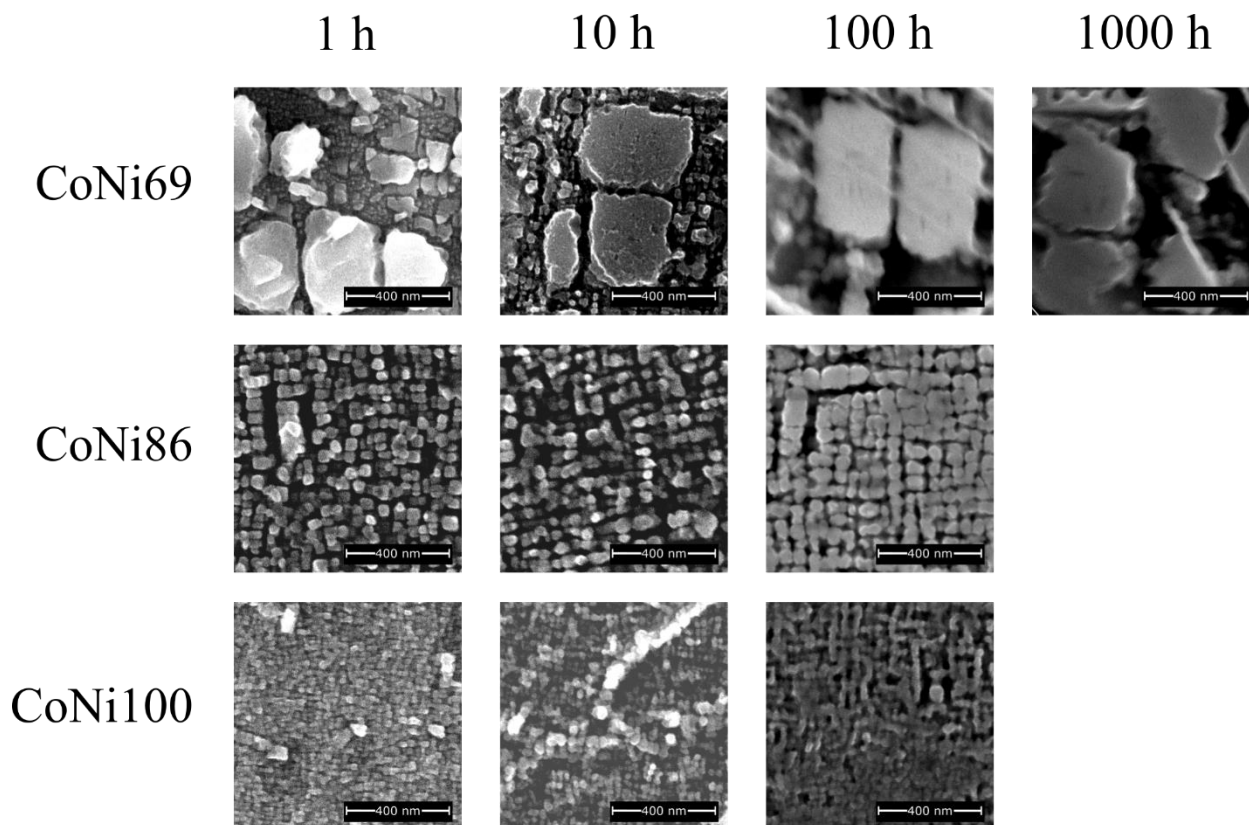


Figure 4-10. SE images of γ' and γ microstructure in alloys CoNi69 to CoNi100, aging up to 1000 hours. Cuboidal γ' was completely consumed by the lamellar discontinuous precipitate in alloys CoNi86 and CoNi100 at 1000 hours.

These alloys also showed discontinuous precipitation. Alloy CoNi69 showed a low fraction of needle-like precipitates and discontinuously precipitated lamellar phase (λ_3) after 1000 h aging, as shown in Fig. 14-11.

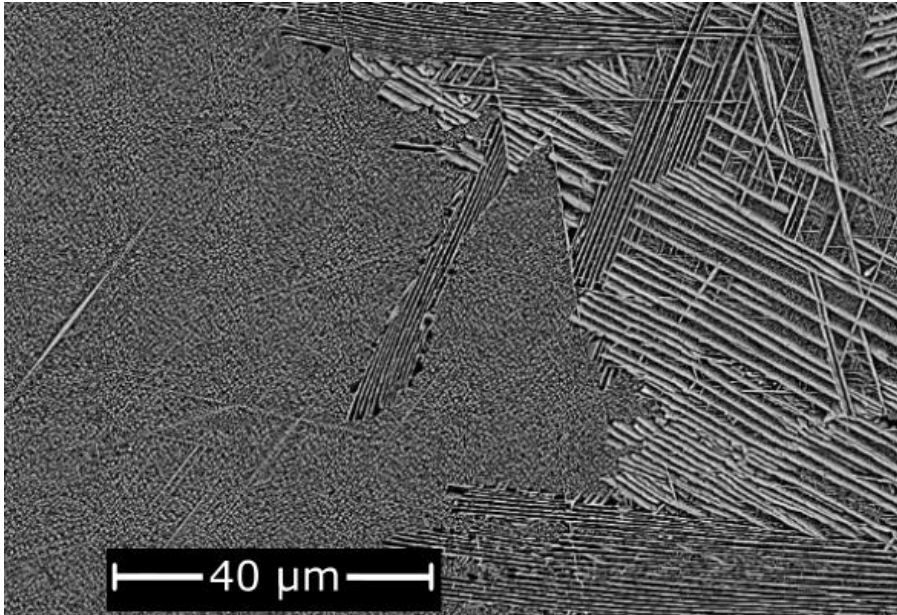


Figure 4-11. BSE image of a region with discontinuous precipitation in CoNi69 after 1000h aging at 750 °C.

Alloys CoNi86 and CoNi100 showed increasing amounts of discontinuous precipitation with aging time, and by 1000 h, all γ' was consumed by the lamellar phase. Fig. 4-12 shows an example of the growth of the lamellar λ_3 in alloy CoNi86 at 100 h.

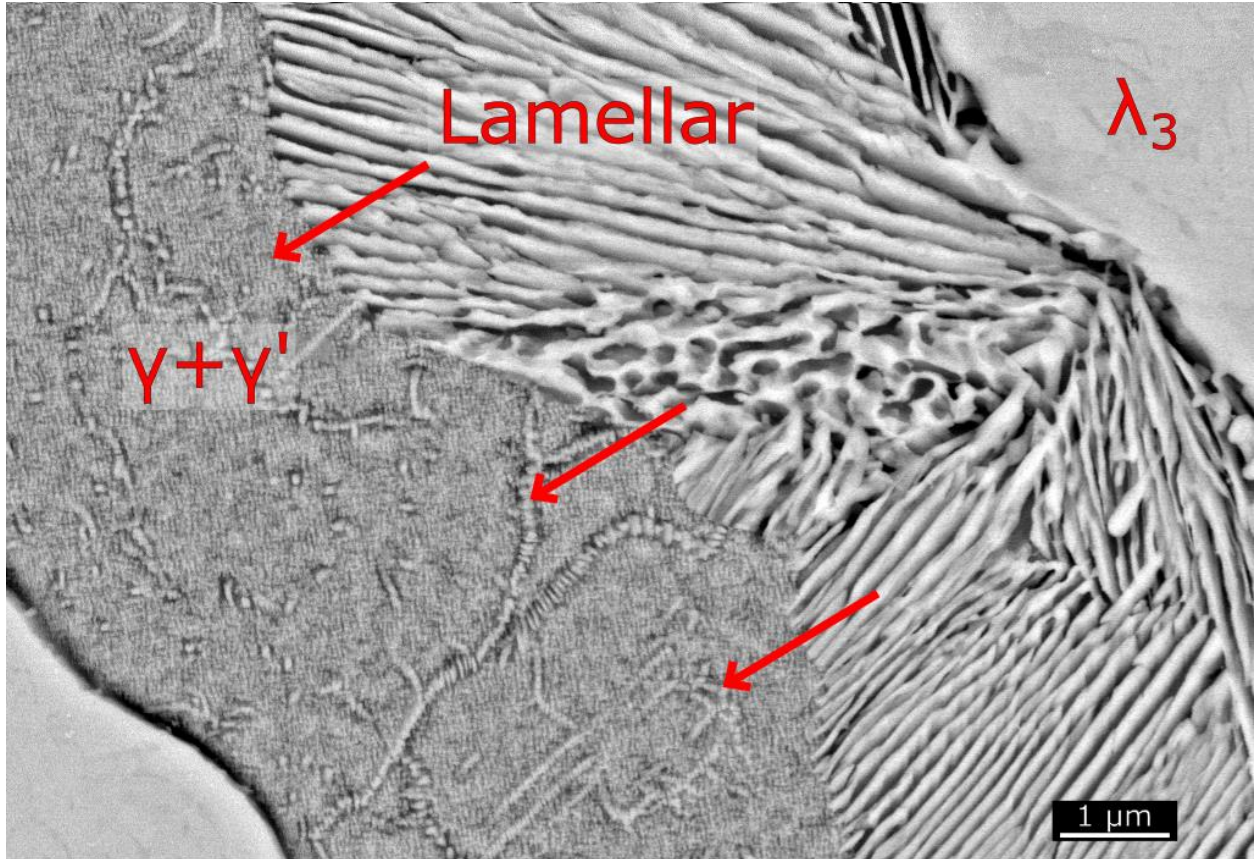


Figure 4-12. A region in alloy CoNi86 with lamellar λ_3 and cubic γ' phases, aged 10 h. As the alloy ages, the lamellar morphology consumes the cubic morphology, and completes consumption between 100 and 1000 h aging.

Low-magnification images for alloy CoNi69, CoNi86, and CoNi100 are shown in Fig. 4-13, which shows increasing fraction of discontinuous precipitation with aging time.

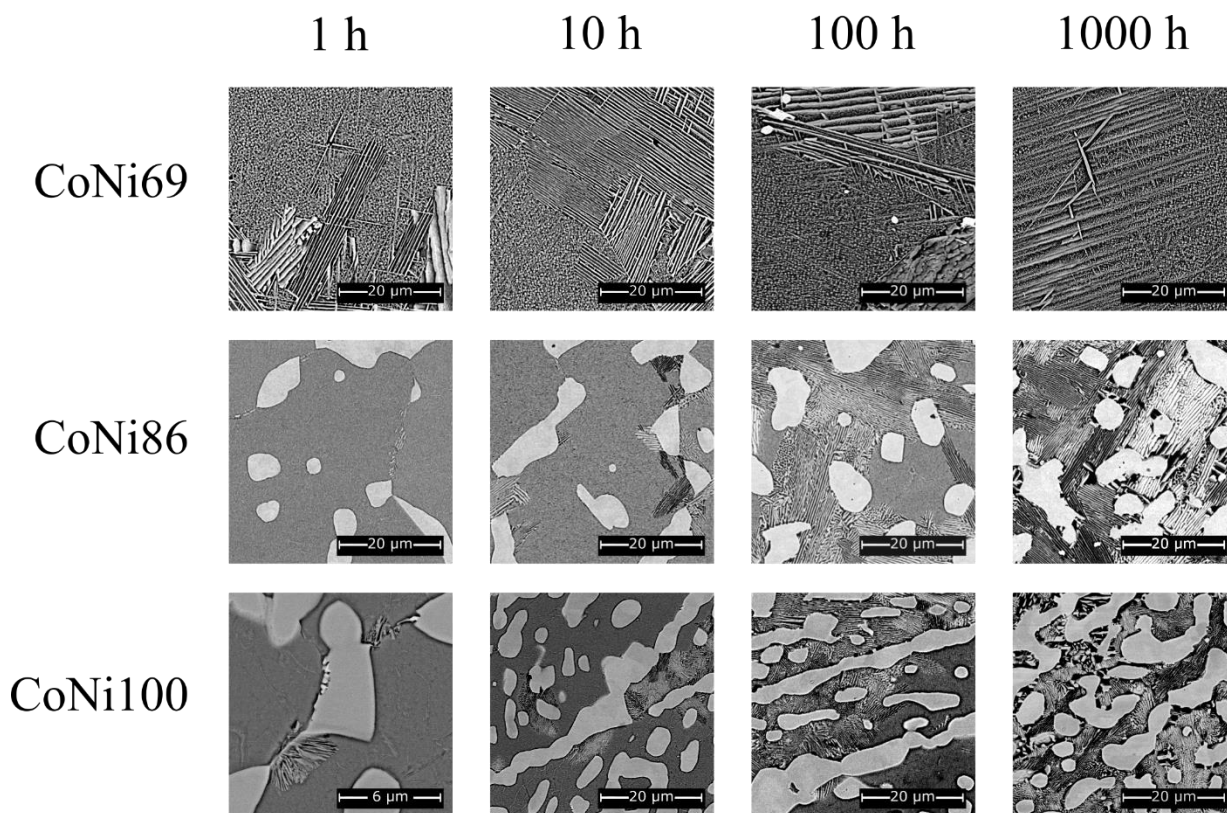


Figure 4-13. Backscatter electron imaging of discontinuous precipitation in alloys CoNi69 to CoNi100, aging up to 1000 h at 1,000x magnification. CoNi100 aged for 1 h is shown with higher magnification.

Discontinuous precipitation, also called cellular precipitation is when diffusion occurs along a boundary, so precipitates grow as the boundary migrates through the material. The microstructure appears similar to that of a eutectoid reaction, but the cellular reaction is typically expressed as $\alpha' \rightarrow \alpha + \beta$, where α' is the supersaturated version of the matrix phase α [108]. In this case, the reaction is $\gamma + \gamma' \rightarrow \gamma + \lambda_3$. Examples of discontinuous precipitation in Co-based alloys include Co_3Ti [55], Co_3Ta [106], and Co_3V phases [109]. Generally, such microstructures are deleterious for creep properties because they are very coarse compared to the cuboidal γ' precipitates [110]. In ternary Co-6Ta-6V and quaternary Co-10Ni-5.4Ta-6.6V alloys, discontinuous precipitation occurred with $\gamma + \text{C36}$ formation [11]. Reyes et al. fully prevented discontinuous precipitation with

partial Al substitution of Ta and V, in a quaternary Co-6Al-3Ta-3V alloy and other more complex compositions, achieving $\gamma+\gamma'$ microstructures stable for long times at elevated temperatures [34].

4.4.4 Electron Backscatter Diffraction

To investigate the structure of the precipitates that consume the $\gamma + \gamma'$ microstructure, EBSD was performed. The patterns were fitted with all possible Co-rich structures proposed by either Wang et al. [111] or Xu et al. [112]. The Aztec EBSD software identified both the lamellar discontinuous phase, as well as the globular phase (elsewhere called λ_3) present from the as-cast state as Co_3Ta with the crystal structure illustrated in Fig. 4-14. Note that this phase is expected to have C36 crystal structure according to Shinagawa et al. [96].

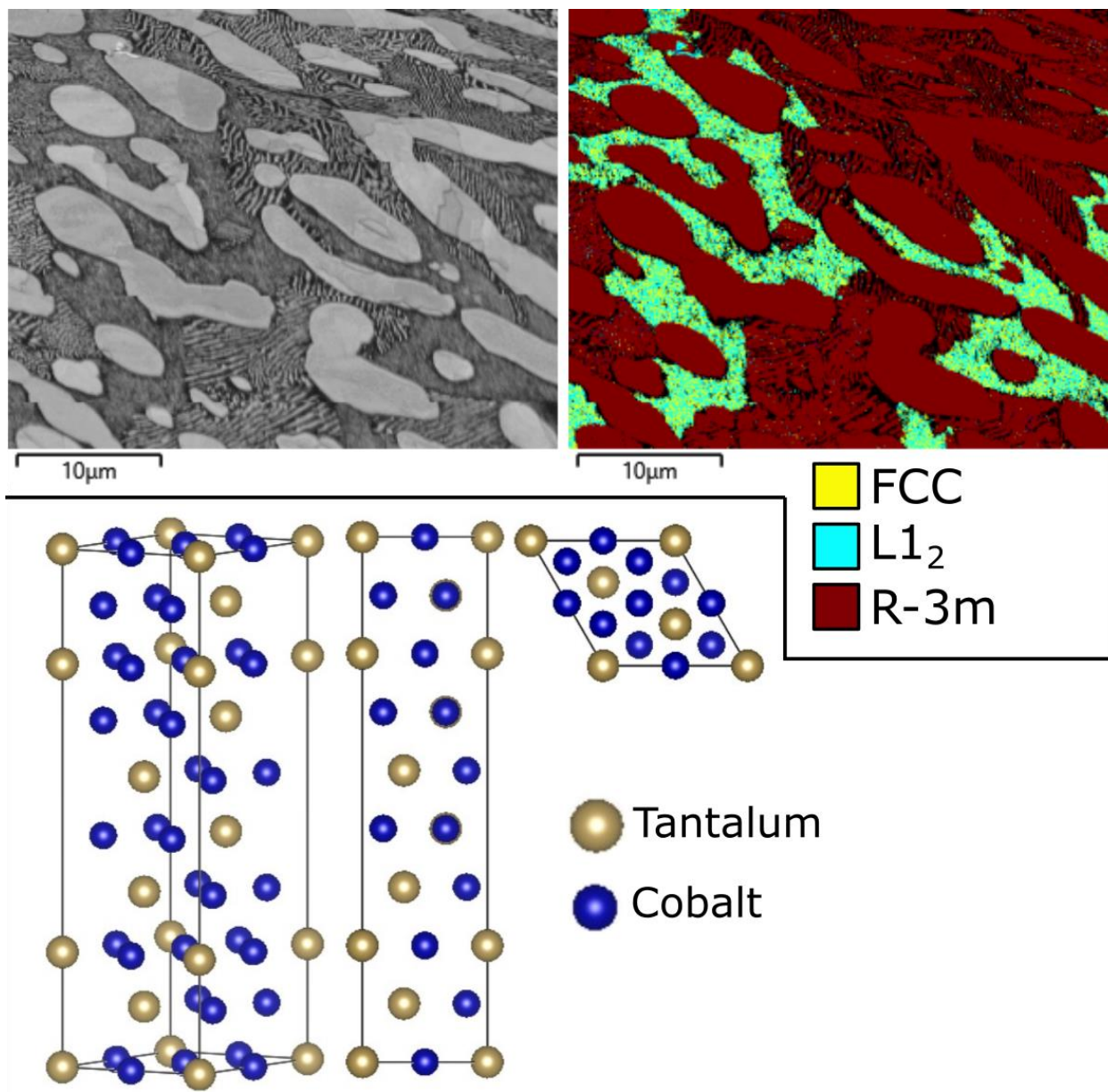


Figure 4-14. EBSD results for CoNi100 aged 100h (right) phase map showing the 3 identified crystal structures. Lamellar precipitates which discontinuously form appear to have the same crystal structure as the globular precipitates previously labelled λ_3 (left) electron image captures synchronously. (bottom) crystal structure for the phase with R-3m symmetry.

Due to the morphological similarity between precipitates in CoNi100 and CoNi86, we assume that the discontinuous precipitates in CoNi86 have the same crystal structure, with Ni substituting for Co and with Al substituting for Ta.

4.5 Conclusions

We studied here the quaternary space between binary Ni-12.5Al (with stable $L1_2$ - γ' -Ni₃Al precipitates forming in a γ -Ni(Al) matrix) and binary Co-12.5Ta (with metastable $L1_2$ -Co₃Ta or stable R-3m Co₃Ta). Results established the possibility of future Ni-Co-based superalloys and suggest that, while γ' remains metastable in Co-Ta alloys, the microstructure can be stabilized to some extent with additional elements such as Ni and Al. The following main conclusions are reached:

1. Upon solutionization, a continuous single-phase γ region does not exist for quaternary Co-Ni-Ta-Al alloys along the tie line between Ni-12.5Al and Co-12.5Ta, since the Co-rich alloys have two-phase $\gamma + \lambda_3$; nevertheless, the γ' phase precipitates from the γ region upon aging at 750 °C for all alloys studied.
2. After aging, a pure $\gamma + \gamma'$ region exists up to a Co/(Co+Ni) fraction of ~50%. At 69%, a needle-like phase precipitates, and above 85%, the λ_3 phase precipitates (with a volume fraction of 13% in CoNi₈₆, and 36% in 100Co-Ni). The γ phase still precipitates cuboidal γ' at low aging times, but this is consumed by a discontinuous precipitate at higher aging times. Both the λ_3 from casting, and lamellar discontinuous precipitates, have the same crystal structure with hexagonal R-3m symmetry.
3. Increasing Co/(Co+Ni) ratios results in a decrease in solidus and liquidus temperatures, consistent with the low eutectic point in the Co-Ta phase diagram. Since an important justification for superalloy transitioning from Ni to Co is the increase in solidus

temperature, using Co_3Ta -based precipitates for creep resistance would necessitate other elements to avoid the eutectic.

4. Increasing $\text{Co}/(\text{Co}+\text{Ni})$ ratios results in higher γ/γ' lattice misfit and increased tetragonal distortion of the γ phase.

4.6 Acknowledgements

This study was supported by Rolls-Royce plc. and the Engineering and Physical Sciences Research Council (EPSRC) for provision of material and funding. BCO and DCD were also funded by the U.S. Department of Commerce, National Institute of Standards and Technology, as part of the Center for Hierarchical Materials Design (CHiMaD) at Northwestern University via award 70NANB14H012. BCO gratefully acknowledges laboratory assistance—especially during pandemic working conditions—from Dr. Hon Tong Pang, George Wise, and Sue Gymer (University of Cambridge).

4.7 Competing Interests Statement

Declarations of interests: none

4.8 Supplemental

4.8.1 Calculation of Interfacial Strain

In one of their supplemental works[101], Neumeier et al. summarize several methods of calculating $a_{\gamma,0}$ from $a_{\gamma,a}$ and $a_{\gamma,c}$. Here, we use “approach IV A,” in accordance with Minshull[106] and Zenk et al.[21]. This approach assumes an isotropic material with plane stress σ_{\parallel} in the γ matrix, and no stress perpendicular to the interface, as illustrated in Fig. S4-1.

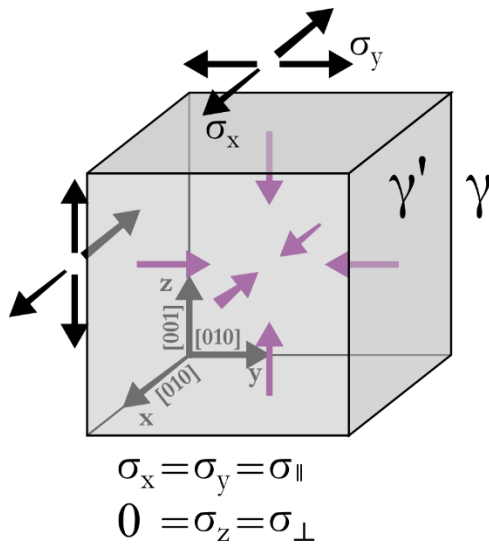


Figure S4-1. Schematic of γ and γ' for a positive misfit alloy, showing isotropic compression in the γ' and planar tension in the γ .

The elastic relationships can be written as:

$$E\varepsilon_x = \sigma_x - \nu(\sigma_y + \sigma_z)$$

$$E\varepsilon_y = \sigma_y - \nu(\sigma_x + \sigma_z)$$

$$E\varepsilon_z = \sigma_z - \nu(\sigma_x + \sigma_y)$$

where E is the elastic modulus, ε is strain, σ is stress, ν is Poisson's ratio, and the subscripts x, y, and z refer to orthogonal directions.

With the assumptions $\sigma_x = \sigma_y = \sigma_{\parallel}$ and $\sigma_z = \sigma_{\perp} = 0$, the matrix strains ε_{\parallel} and ε_{\perp} are:

$$E\varepsilon_{\parallel} = \sigma_{\parallel} - \nu\sigma_{\parallel}$$

$$E\varepsilon_{\perp} = -2\nu\sigma_{\parallel}$$

Rearranging gives the strain ratio χ :

$$\frac{\varepsilon_{\perp}}{\varepsilon_{\parallel}} = \frac{-2\nu}{1-\nu} = \chi$$

The matrix strains ε_{\parallel} and ε_{\perp} can be related to the strain which causes the tetragonal distortion from the ideal cube:

$$\varepsilon_{\parallel} = \frac{a_{\gamma,a} - a_{\gamma,0}}{a_{\gamma,0}}$$

$$\varepsilon_{\perp} = \frac{a_{\gamma,c} - a_{\gamma,0}}{a_{\gamma,0}}$$

Thus, the “corrected” cubic lattice parameter is

$$a_{\gamma,0} = \frac{a_{\gamma,c} - \chi a_{\gamma,a}}{1 - \chi}$$

The lattice misfit is then given as:

$$\delta = \frac{2(a_{\gamma'} - a_{\gamma,0})}{(a_{\gamma'} + a_{\gamma,0})}$$

Both Minshull [106] and Zenk et al.[21] assumed a Poisson’s ratio $\nu = 0.3$. However, the Poisson’s ratios of pure Ni and Co are reported to be 0.305-0.315 and 0.31-0.33,[103–105] respectively, so this work will proceed with the assumption $\nu = 0.305$, or $\chi = -0.878$.

The final expression for lattice misfit is now written:

$$\delta = \frac{2(a_{\gamma'} - \frac{a_{\gamma,c} + 0.878a_{\gamma,a}}{1.878})}{(a_{\gamma'} + \frac{a_{\gamma,c} + 0.878a_{\gamma,a}}{1.878})}$$

Upper and lower error bars correspond to $\nu = 0.3$ and $\nu = 0.31$; such a range in Poisson's ratio changes the final misfit value by less than 0.01%.

4.8.2 CoNi69 Needlelike precipitates

This micrograph shows a region on the homogenized sample of CoNi69 that contains both shapes of precipitate.

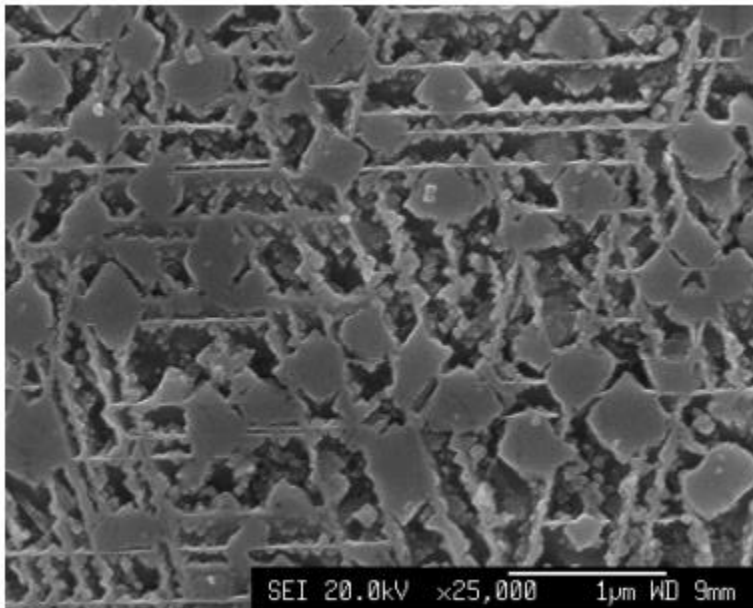


Figure S 4-2. Homogenized microstructure of alloy CoNi69, reproduced from Minshull.[106]. There are cuboidal precipitates and needle-like precipitates, and it appears that one nucleated from the other.

The effect of partial Fe substitution for Ni on microstructure, lattice misfit, oxidation, creep, and yield strength are investigated for six W-free cobalt-based superalloys with compositions Co-(30-x)Ni-xFe-yCr-5Al-3V-2Ti-1.5Nb-1.5Ta-0.08B (at.%), with three levels of Fe (x=12, 14, or 18) and two levels of Cr (y =4 or 8). Alloys with 12 and 14% Fe exhibit mostly γ/γ' microstructures after aging up to 1000 h at 850 °C, while those with 18% Fe display additional intermetallic phases. All alloys show positive lattice misfit from 0.56 to 0.34%, with Fe substitutions reducing lattice misfit by ~0.02% per 1 at.% Fe. Increasing Fe from 12 to 18 % reduces oxidation rates for both levels of Cr. Substitution of Ni by Fe also increases solvus temperature but reduces creep resistance at 850 °C as well as yield strength below 800 °C. By contrast, increasing Cr from 4 to 8 at.% (replacing Co) improves creep resistance at 850 °C.

5. Microstructure and Mechanical Properties of L1₂-strengthened Co-Fe-Ni-based Superalloys

5.1 Abstract

The effect of partial Fe substitution for Ni on microstructure, lattice misfit, oxidation, creep, and yield strength are investigated for six W-free cobalt-based superalloys with compositions Co-(30-x)Ni-xFe-yCr-5Al-3V-2Ti-1.5Nb-1.5Ta-0.08B (at.%), with three levels of Fe (x=12, 14, or 18) and two levels of Cr (y =4 or 8). Alloys with 12 and 14% Fe exhibit mostly γ/γ' microstructures after aging up to 1000 h at 850 °C, while those with 18% Fe display additional intermetallic phases. All alloys show positive lattice misfit from 0.56 to 0.34%, with Fe substitutions reducing lattice misfit by ~0.02% per 1 at.% Fe. Increasing Fe from 12 to 18 % reduces oxidation rates for both levels of Cr. Substitution of Ni by Fe also increases solvus temperature but reduces creep resistance at 850 °C as well as yield strength below 800 °C. By contrast, increasing Cr from 4 to 8 at.% (replacing Co) improves creep resistance at 850 °C.

5.2 Introduction

For the last seven decades, superalloys based on nickel, iron, and/or cobalt [1] have proven to be the optimal material for gas turbines blades and disks, which must maintain creep resistance at high temperatures for very long times under highly oxidative and corrosive environments. These three elements (Ni, Fe, Co) are highly soluble in each other, have very similar density and melting points, and excellent strength and toughness. Ni-based superalloys have seen much wider use than Co- or Fe-based superalloys because of their stable γ/γ' microstructures (fcc γ -matrix with coherent L1₂ γ' -precipitates), which impede dislocation motion, especially at high temperature, due to Kear-

Wilsdorf locking [2–5]. Ni-based superalloys can contain substantial Fe concentrations. Most notable among such alloys is IN718, which contains 18.5 wt% Fe, and is strengthened by γ' and γ'' precipitates [113–115]. This alloy shows a mild yield strength anomaly, reaching a peak of 510 MPa at 800 °C, which is attributed to γ'' and δ phases with composition Ni_3Nb [116]. Co- and Fe-based superalloys, traditionally strengthened with carbides rather than γ' precipitates, offer some advantages over Ni-based superalloys. For example, some Fe-based superalloys (e.g., V57 or A286) with significant Ni content can form low volume fractions of metastable γ' or γ'' precipitates at temperatures (730 °C for γ' , 650 °C for γ'') lower than for Ni-based alloys [114,117–120].

Recent developments have enabled γ' -strengthened Co-based superalloys [6,7]. In these alloys, the γ' phase is based on variations of the following L_{12} phases: $\text{Co}_3(\text{Al,W})$, Co_3Ti , $\text{Co}_3(\text{Nb,Mo})$, $\text{Co}_3(\text{Al,V})$, $\text{Co}_3(\text{Ti,V})$, $\text{Co}_3(\text{Nb,V})$, or $\text{Co}_3(\text{Ta,V})$ [8–12,14,121]. When fully alloyed, which typically includes Ni to widen the $\gamma + \gamma'$ phase field, Al and Cr for oxidation resistance, combinations of γ' -formers (e.g., Ti, W, Ta, Nb, V, Mo), and grain boundary strengtheners (e.g., C, B, Zr), these superalloys show comparable creep-, coarsening- and corrosion-resistance as their Ni-based counterparts, albeit with a positive, rather than negative, lattice misfit, which may improve their rafting behavior [15–19,23,122–124].

Co-based superalloys often include large amounts of Ni to stabilize the γ' phase, thus becoming “Co-Ni superalloys” [92,125–127]. As compared to both Co and Ni, Fe has a slightly lower density, a higher melting point, and a much lower cost (as shown in Table S5-1). Nevertheless, Fe is rarely added to γ' -strengthened Co-based superalloys because prior studies report a degradation in microstructure and properties upon Fe additions. For example, in Co-8.8Al-9.8W (all

compositions below are given in at.%) with 2% Fe additions (replacing Co), Omori et al. [128]. found that Fe is a strong γ -former (with a partitioning ratio $k_{\text{Fe}}^{\gamma/\gamma'} = 0.52$), that the γ' phase is metastable at 900 °C, and that the solvus temperature decreases from 1016 to 1003 °C. In a similar alloy, Co-9Al-7W-2Fe (at.%), Ooshima et al. [129] found that the small 2% Fe addition reduced the γ' volume fraction from 49 to 35% and the solvus temperature from 965 to 958 °C.

Bauer et al. [61] studied Co-9Al-9W-0.12B-xFe alloys with 8 and 16% Fe replacing Co. After aging at 900 °C for 200 h, the alloy with 8% Fe still exhibits γ' precipitates, but with large (>10 μm), needlelike, topologically close-packed (TCP) phases. In the alloy with 16% Fe, all γ' is replaced by globular TCP phases after aging. Additionally, the solvus temperature drops from 982 to 932 to 877 °C as Fe increases from 0 to 8 to 16% [61]. Cartón-Cordero found that Fe contamination from mechanical alloying in nominally Fe-free ternary Co-8Al-12.5W resulted in a softer matrix, fewer γ' precipitates, new $(\text{Fe,W})_2\text{C}$ precipitates, increased lattice parameter, and less coarsening resistance [130]. Yan et al. [122] substituted 20% Fe for Co in a Co-7Al-7W-xFe alloy, which produced the intermetallic χ phase in the γ matrix, with some discontinuously-precipitated γ' phase; the Fe addition reduced the γ' solvus from 845 to 778 °C, increased hardness from 468 to 568 HV, and dramatically improved oxidation resistance, albeit without producing a protective oxide layer. Lass [131] produced another set of alloys with composition Co-20Ni-10Cr-10Al-7W-0.1B-xFe ($x = 0, 5, 10, \text{ and } 15$, with Fe replacing Co), the γ' solvus of which decreased monotonically with Fe, by >100 °C as Fe increased from 0 to 15%. Increasing Fe also produced μ and B2 phases and for alloys with Fe contents of 10 and 15%, all γ' was lost after aging at 900 °C for 1000 h. The combination of Fe + Cr was found to be especially destabilizing for the $\gamma + \gamma'$

microstructure. Finally, in Co-30Ni-4Cr-10Al-6W-0.1B-xFe ($x = 0, 4, 8, 12$, with Fe replacing Co), the γ/γ' microstructure was stable up to 4096 h at 900 °C with only small amounts of β and μ phase, consistent with higher Ni and lower Cr concentrations stabilizing the $\gamma + \gamma'$ phase field [132]. However, with 12% substitution of Fe for Co, the solvus temperature decreases from 1036 to 985 °C, ambient-temperature hardness decreases from 2.9 to 2.5 GPa, the yield strength at 800 °C (at the anomalous yield peak) decreases from 510 to 440 MPa, and creep resistance at 850 °C also decreases strongly (the alloy with 12% Fe creeps ~60 times faster than the Fe-free alloy at 300 MPa) [132]. Replacement of Co with 4% Fe was reported to reduce the oxidation rate by more than half, with diminishing improvements as Fe concentration further increased to 8 and 12%. In addition, elevated Fe concentrations were observed to decrease lattice misfit, such that the γ' morphology changed from cuboidal to spheroidal. The Fe partitioning coefficient is $k_{\text{Fe}}^{\gamma'/\gamma} = 0.55$ in the alloy with 12% Fe, and Fe substitution does not significantly change partitioning of the other elements, as compared to the Fe-free alloy [132].

Despite the poor performance of Co replacement by Fe in the Co-Al-W-based systems described above, Fe addition may be less detrimental in Co-based superalloys that contain V as a γ' former, rather than W. Specifically, the existence of the $L1_2$ (Fe,Co) $_3$ V phase suggests that higher Fe additions may be possible in V-containing Co-based superalloys without destabilizing the $\gamma + \gamma'$ microstructure. The stable binary Co_3V phase has a 9-layer hexagonal structure, but it exhibits a metastable $L1_2$ structure [133–135]. A study of (Fe,Co) $_3$ V at 850 °C found that the $L1_2$ structure exists from 19 to 28 at.% Fe, with a FCC + $L1_2$ or hexagonal + $L1_2$ structure beyond these bounds [136]. With Ni added, (Fe,Co,Ni) $_3$ V can likewise be hexagonal or $L1_2$, depending on

the number of valence electrons per atom, which depends on the ratios of Fe, Co, and Ni. The single-phase Fe-21Co-20Ni-23V, Fe-31Ni-23V, and Co-16Fe-23V intermetallic alloys have the L1₂ structure and show high ductility (tensile elongation >35%) and a yield strength anomaly [137]. In some (Co,Fe,Ni)₃V alloys, a peritectoid reaction $\gamma + \sigma \rightarrow \gamma'$ occurs, where σ is a tetragonal phase [138,139]. The highest disordering temperature (analogous to a solvus temperature in a two-phase system) without σ occurs in (Fe₁₅Co₈₅)₃V, which is the minimum amount of Fe required to form the L1₂ phase. These alloys tend to fail by intergranular cracking, which is mitigated by replacing up to 2% V with Ti [137,140–146]. Finally, studies have also focused on complex concentrated alloys (“high entropy” superalloys) with $\gamma + \gamma'$ microstructures that typically show small positive lattice misfit [147,148]. One such superalloy, Co₂₈Fe₂₈Ni₂₈Ti₈V₈, exhibits a (Co,Fe,Ni)₃(Ti,V) L1₂ phase with 45% volume fraction in an FCC γ matrix after aging at 700 °C for 1 h, indicating short-term stability of the γ' phase [149]. Another Al_{0.2}CrFeCoNi₂Cu_{0.2} alloy exhibits a high volume fraction of γ' phase in a γ matrix, with Fe partitioning slightly to the γ matrix ($k_{\text{Fe}}^{\gamma/\gamma'} = 0.85$ [150]).

Here, we investigate the hypothesis that Fe may be beneficial (or at least not detrimental) in a Co-Ni-based γ/γ' superalloy system which uses V as a γ' -former rather than W or Mo, e.g., in the family of Co-Nb-V- or Co-Ta-V-base superalloys [11,26,32,34,151]. Furthermore, rather than replacing Co with Fe, we partially replace Ni with Fe in a W-free base alloy (Co-30Ni-5Al-4Cr-3V-2Ti-1.5Nb-1.5Ta-0.08B, at.%) while maintaining all other elements constant. A second variant of this alloy with twice the Cr content (8% Cr, replacing Co), is also studied, resulting in six alloys with various Fe, Ni and Cr content. The γ/γ' microstructure of these alloys is studied via

SEM and neutron diffraction, and their mechanical properties (yield strength and creep resistance) are measured at elevated temperature.

5.3 Experimental Methods

Six Co-(30-x)Ni-xFe-yCr-5Al-3V-2Ti-1.5Nb-1.5Ta-0.08B (at.%) alloys (with x=12, 14, 18 and y = 4, 8), with nominal compositions shown in Table 5-1, were cast and their compositions verified by Energy Dispersive Spectroscopy (EDS) using polished cross-sections of homogenized specimens in a FEI Quanta 65 Scanning Electron Microscope (SEM). Table 5-1 also shows related alloys from previous studies—the “base” alloy with 30Ni and 0 Fe, and a preliminary alloy with 20Ni and 10Fe, which is described in the Supplementary Information.

Alloy	Composition, at.%									
Label	Co	Fe	Ni	Al	Cr	V	Ti	Nb	Ta	B
Present study										
12Fe4Cr	52.9	12	18	5	4	3	2	1.5	1.5	0.08
14Fe4Cr	“	14	16	“	“	“	“	“	“	“
18Fe4Cr	“	18	12	“	“	“	“	“	“	“
12Fe8Cr	48.9	12	18	“	8	“	“	“	“	“
14Fe8Cr	“	14	16	“	“	“	“	“	“	“
18Fe8Cr	“	18	12	“	“	“	“	“	“	“
Related Alloys										
0Fe4Cr [152]	52.9	0	30	“	4	“	“	“	“	“
0Fe8Cr [152]	48.9	0	30	“	8	“	“	“	“	“
10Fe4Cr[153]	52.9	10	20	“	4	“	“	“	“	“
10Fe8Cr [153]	48.9	10	20	“	8	“	“	“	“	“

Table 5-1. Nominal compositions (at.%) of investigated alloys (with 12-18% Fe), and four literature alloys (with 0 and 10% Fe)

The six alloys were prepared twice: (i) as samples for microscopy, DSC, and neutron diffraction, and (ii) as samples for mechanical properties and oxidation. The latter alloys were arc melted in Ar as button-shaped ingots (~30 g) using pure elements - Co (99.9+%), Ni (99.95%), Al (99.5%), Cr (99.995%), V (99.7%), Ti (99.95%), Nb (99.8%), Ta (99.95%), and B (95-97%), purchased from Alfa Aesar (Tewksbury, MA) - with a flip between each of the 6 re-meltings. The former alloys were arc-melted into finger-shaped ingots (~50 g) from pure elements (Co, Ni, Fe, Al, Cr, Ti) and binary master alloys (38Ni-62V, 55Nb-45Ni, 85Ni-15Ta, and 33Al-67B). Samples were encapsulated in evacuated fused silica tubes, homogenized for 24 h at 1200 °C, and water quenched. Sections of the ingots were aged in evacuated fused silica tubes at 850°C for durations between 24 and 1000 h, followed by water quenching. After cylindrical samples were cut via EDM, the remaining material was remelted via the same process to allow more cylinders to be cut.

Vickers microhardness was measured with ten indents, spanning multiple grains, using a Wilson VH3100 Micro-hardness Tester operated with a 300 g load and 10 s indent times.

Differential Scanning Calorimetry (DSC) was performed using a Netzsch 404F1 instrument operating with an alumina pan under an Ar sample atmosphere and with heating and cooling rates of 10 °C/min. Homogenized samples were cycled twice in the solvus-liquidus range to collect solvus, solidus, and liquidus temperatures upon heating and cooling (no solvus associated with 1st heat).

To determine oxidation behavior, Thermal Gravimetric Analysis (TGA) was performed on homogenized samples in alumina pans using a Mettler Toledo TGA/DSC 3+ instrument over a 20 h time span at 850 °C under laboratory air flowing at 40 mL/min. Oxidized samples were mounted,

sectioned and polished before investigation with SEM and EDS, using the same conditions as described previously.

Lattice parameters from the γ and γ' phases in each alloy were obtained by neutron diffraction. A large (~7 mm diameter) cylinder was cut from each ingot by electrical discharge machining (EDM) before being aged at 850 °C for 72 h and water quenched. Neutron diffraction data from the samples was acquired using the Polaris beamline at the ISIS Neutron and Muon Source (UK) which has five detector banks. For these measurements, the samples were contained within 8 mm diameter deep drawn V cans, and each sample was tested for ~ 30 min. Lattice parameters were obtained from the diffraction data by simultaneous Le Bail fitting of the five banks with GSAS-II [154].

Yield strength was measured between 20 and 950°C on an MTS-5 servo-hydraulic compression tester in vacuum outfitted with a furnace. Cylindrical samples (10 mm height, 5 mm diameter) were prepared by electro-discharge machining from ingots that had been homogenized, aged in vacuum-encapsulated tubes at 850°C for 168 h, and water quenched. The cylindrical samples were placed between boron-nitride-lubricated SiC platens and deformed at a rate of 1 $\mu\text{m/s}$ ($\sim 10^{-4} \text{ s}^{-1}$ strain rate) until yielding. The yield strength was calculated as the 0.2% offset from the elastic region (with the elastic modulus corrected according to a sample-less compliance run on the MTS-5). After yield, load was removed, the temperature was increased to the next set point, with the sample thermocouple maintaining the new temperature with deviation <1 °C for at least 5 minutes. This procedure was repeated until tests had been done at the highest temperature of 950 °C, with a total plastic strain $<10\%$.

Compression creep tests were performed on a dead-load creep frame in air at 850°C. For these tests, cylindrical samples (with the same dimensions and heat-treatment as those samples for yield strength tests) were placed between boron-nitride-lubricated alumina platens and deformed at monotonically increasing compressive stresses ranging from 200-600 MPa, accumulating ~10% total strain. Minimum creep strain rate was determined at each stress level from the sample displacement rate after primary creep, measured by an extensometer and linear variable displacement transducer with a resolution of 10 μm (see Fig. 5-S6). Deformed specimens were sectioned longitudinally (with a cross-section parallel to the applied load) and imaged in SEM, using the protocols described previously.

5.4 Results and Discussion

5.4.1 Microstructure

After homogenization and aging at 850 °C, all six alloys displayed a $\gamma + \gamma'$ bulk microstructure, as illustrated in Fig. 5-1. Increased Cr and Fe concentrations lead to precipitation of Nb-rich phases at longer aging times. As shown in Fig. 5-3, non- γ' precipitates can generally be classified as (i) “globular”, rich in Nb and other heavy elements, and typically with circularity >0.5 , (ii) “needlelike”, rich in Nb and other heavy elements, with circularity <0.5 , and (iii) “TiAl shells”, with Al-rich core and Ti-rich shell, which appear in very few instances. The two 10Fe4Cr and 10Fe8Cr alloys shown in Fig. 5-S1 show $\gamma + \gamma'$ microstructures, with no other phases. The needlelike and globular precipitates closely resemble the TCP morphology in the Co-9Al-9W-0.12B-xFe alloys presented by Bauer et al., with 8 and 16% Fe, respectively [61].

Up to a maximum aging time of 1000 h, as shown in Fig. 5-1 and Fig. 5-2, the following microstructural observations are made: the 12Fe4Cr alloy shows grains that are almost entirely $\gamma + \gamma'$ (with total γ' fraction $\phi = 48 \pm 12\%$). Grain boundaries are mostly free of non- γ' precipitates and have no depletion zone, although globular precipitates occasionally appear on the grain boundaries, and occasional core-shell precipitates (Al-rich core with Ti-rich shell) are found within grains, as illustrated with an EDS map in Table S5-2. The 12Fe8Cr alloy displays almost entirely $\gamma + \gamma'$ within grains ($\phi = 42 \pm 7\%$). Occasionally globular and needlelike precipitates nucleate on and near the grain boundaries, with a volume fraction well below 1%. With an intermediate Fe concentration, the 14Fe4Cr alloy exhibits almost entirely $\gamma + \gamma'$ within grains ($\phi = 41 \pm 7\%$), with the occasional globular precipitate at the grain boundaries, and rare TiAl-rich core-shells in the grains. The 14Fe8Cr alloy exhibits almost entirely $\gamma + \gamma'$ within grains ($\phi = 44 \pm 4\%$) but shows clusters of globular precipitates in the bulk near the arc-melted surface, and always at triple junctions, with a total volume fraction of non- γ' precipitates of $\sim 0.1\%$. With a high Fe concentration, the 18Fe4Cr alloy displays mostly $\gamma + \gamma'$ within the grains ($\phi = 34 \pm 5\%$). Globular precipitates are present along portions of the grain boundaries, and always on triple junctions, with a small 1-3 μm width depletion zone (3% total volume fraction) after aging 1000 h. Both needlelike (0.1%) and globular (1%) precipitates appear within the grains after aging for 1000 h. Finally, the 18Fe8Cr alloy, with the highest Fe and Cr content, exhibits globular precipitates along all grain boundaries, accompanied by depletion zones (1-3 μm width, 33% total volume fraction). Needlelike and globular precipitates appear ubiquitously in the bulk grain, with a total non- γ' precipitate fraction of 6.1%. In the $\gamma + \gamma'$ region, the γ' fraction is $34 \pm 5\%$.

It is apparent from Fig. 5-1 that γ' precipitates steadily coarsen in all alloys up to 1000 h aging time. The γ' volume fraction does not significantly change as aging proceeds, with the exception of the two Fe-rich alloys (18Fe4Cr and 18Fe8Cr) which lose γ' at the expense of globular and needlelike intermetallic phases (as shown in Fig. 5-2).

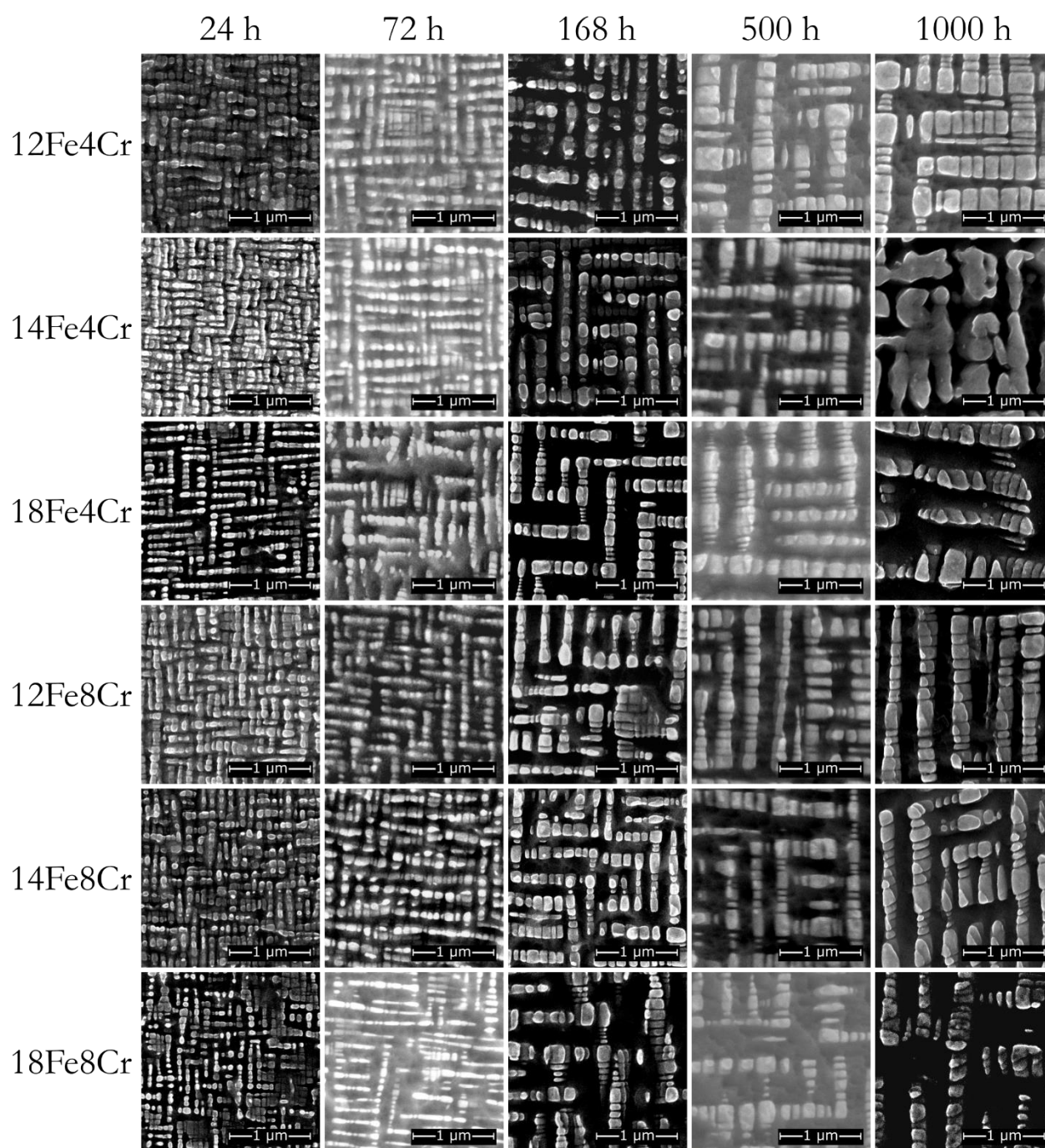


Figure 5-1. Secondary electron SEM micrographs of representative grain interiors showing $\gamma + \gamma'$ microstructure in alloys aged at 850 °C between 24 and 1000 h.

As illustrated in Fig. 5-1, there is little γ' circularity change, regardless of Fe or Cr content as the alloys are aged. Chromium additions appear to reduce coarsening rate, as γ' precipitates in the 8Cr alloys appear smaller, with less coalescing, than their 4Cr counterparts after 1000 h aging. The γ' volume fraction decreases with increasing Fe, as shown in Table S5-3, where a true γ' volume fraction is calculated by multiplying the fraction of γ' measured metallographically within the $\gamma + \gamma'$ region, by the volume fraction of these region. More detailed statistics are given in Table S5-4.

Fig. 5-2 shows, for all six alloys, SEM micrographs of a representative grain-boundary triple junction for aging times spanning 24 to 1000 h. Precipitates at grain-boundaries are mostly γ' but clearly serve as a nucleation site for needlelike and globular precipitates, if present.

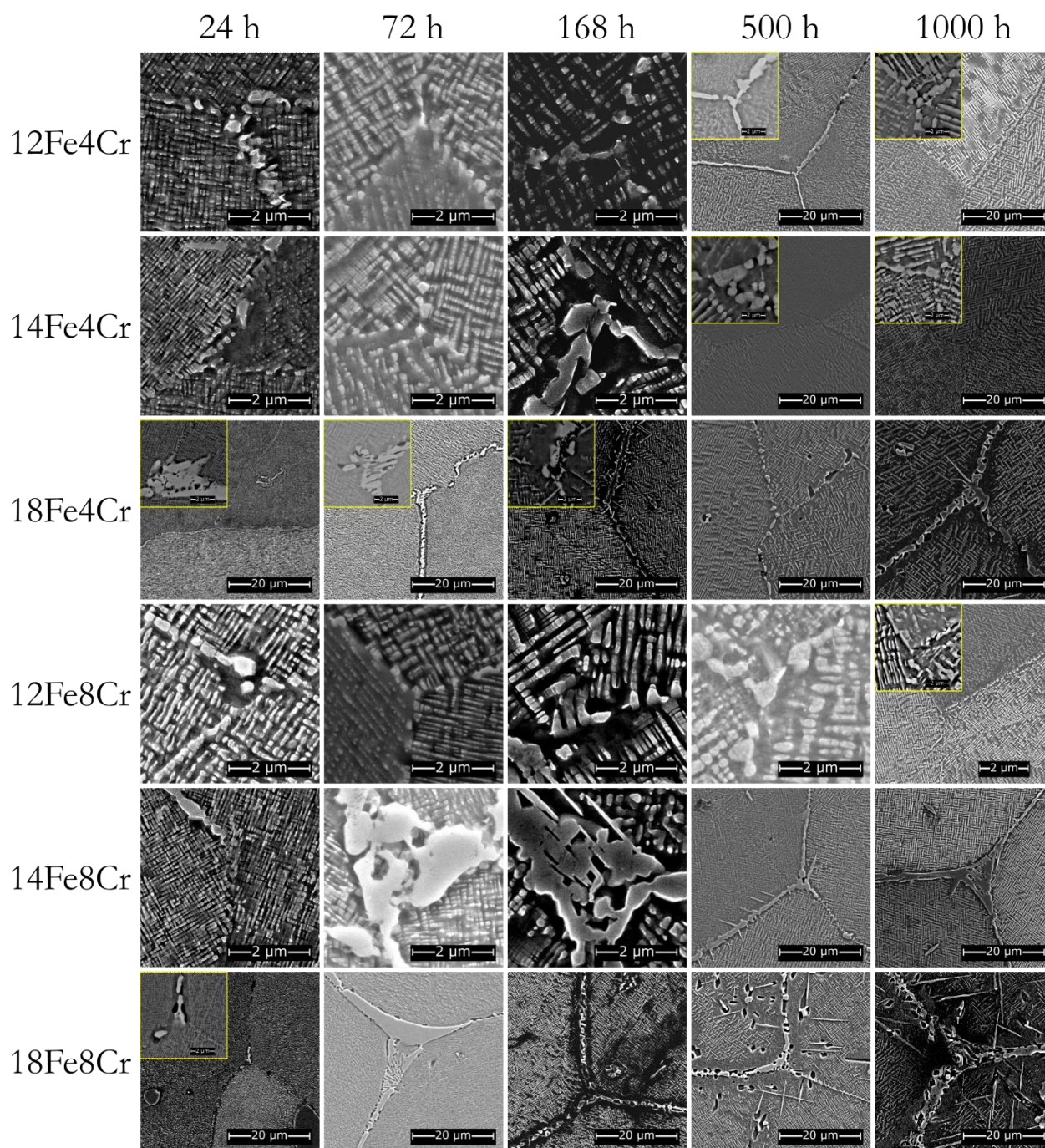


Figure 5-2. Secondary electron SEM micrographs showing representative grain triple junctions in alloys aged at 850 °C between 24 and 1000 h. Some higher-magnification backscatter inserts are included, all with 2 μm scalebars, to illustrate triple junction precipitates.

Fig. 5-3 shows a lower-magnification SEM micrograph of the alloy with highest Fe and Cr additions (18Fe8Cr) after the longest aging time (1000 h), which highlights the different types of precipitates. Other alloys show precipitates with the same morphologies, but in much lower amounts.

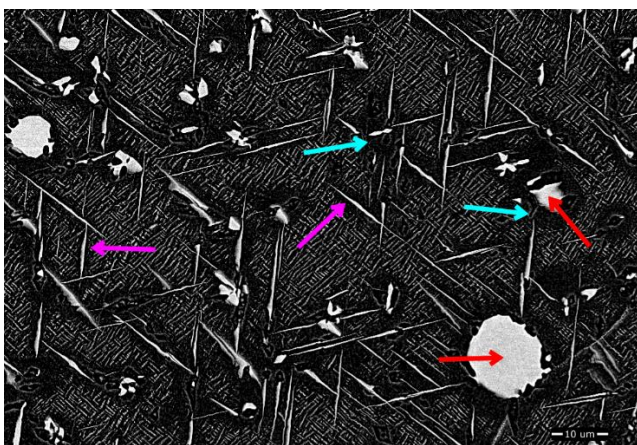


Figure 5-3. Secondary electron SEM micrographs showing 18Fe8Cr alloy aged 1000 h at 850 °C, with $\gamma + \gamma'$ matrix containing globular precipitates labelled with red arrows, needle-like precipitates with purple arrows, and depletion zones with blue arrows.

In our previous series of Fe-free Co-based superalloys, Co-xNi-5Al-4Cr-3V-2Ti-1.5Nb-1.5Ta-0.08B, Ni substitution of Co was shown to increase the γ' volume fraction from 32% ($x = 10\%$) to 37% ($x = 20\%$) and to 49% ($x = 30\%$)[152]. Our current 12Fe4Cr alloy, with 18% Ni and 12% Fe, has identical γ' volume fraction as the previous alloy with 30% Ni and 0% Fe, suggesting that substituting almost half of Ni with Fe does not affect the $\gamma + \gamma'$ microstructure of these V-containing alloys. Other alloys with W-containing γ' precipitates, as discussed in the introduction, show a reduction in γ' volume fraction and solvus temperature with as little as 2% Fe replacing Co, and a destabilized γ/γ' microstructure with 5% Fe.

Compared to other Co-based superalloys with high Fe content, our V-containing alloys have significantly higher γ' fraction and lower fractions of undesirable non- γ' phases, as shown in Fig. 5-4. For example, in Co-9Al-7W and Co-9Al-7W-2Fe aged for 96 h at 850 °C, a 2 at.% Fe addition (replacing Co) reduces γ' volume fraction from 49 to 35% [129]. In 20Ni-10Cr-10Al-7W-0.1B-xFe alloys (x= 0–15) aged for 168 h at 800 °C (no γ' volume fraction reported), B2 and μ phases are present at the lowest Fe concentration (5%) and increase with increasing Fe content [131]. In Co-7Al-7W (62% γ' fraction) and Co-7Al-7W-20Fe (no γ' fraction reported) aged for 200 h at 765 °C, high amounts of χ and B2 phases appear in the latter alloy [122]. In Co-9Al-9W-0.12B-xFe (x = 0–16) aged 200 h at 900 °C, the Fe-free alloy shows 58% γ' and the alloys with 8 and 16% Fe (no γ' fraction reported) shows similar “needlelike” and “globular” phases as our 18Fe alloys [61]. Finally, Co-30Ni-4Cr-10Al-6W-0.1B-xFe (x = 0–12%) alloys, aged for 4096 h at 900 °C, show a γ' fraction decreasing from 40 to 25% and forming up to 2.5% area fraction of B2 and μ within grains [132]. The γ' precipitate shape changes from cuboidal to spheroidal with increasing Fe, unlike in our alloys whose γ' precipitates remain cubic in shape, regardless of Fe content.

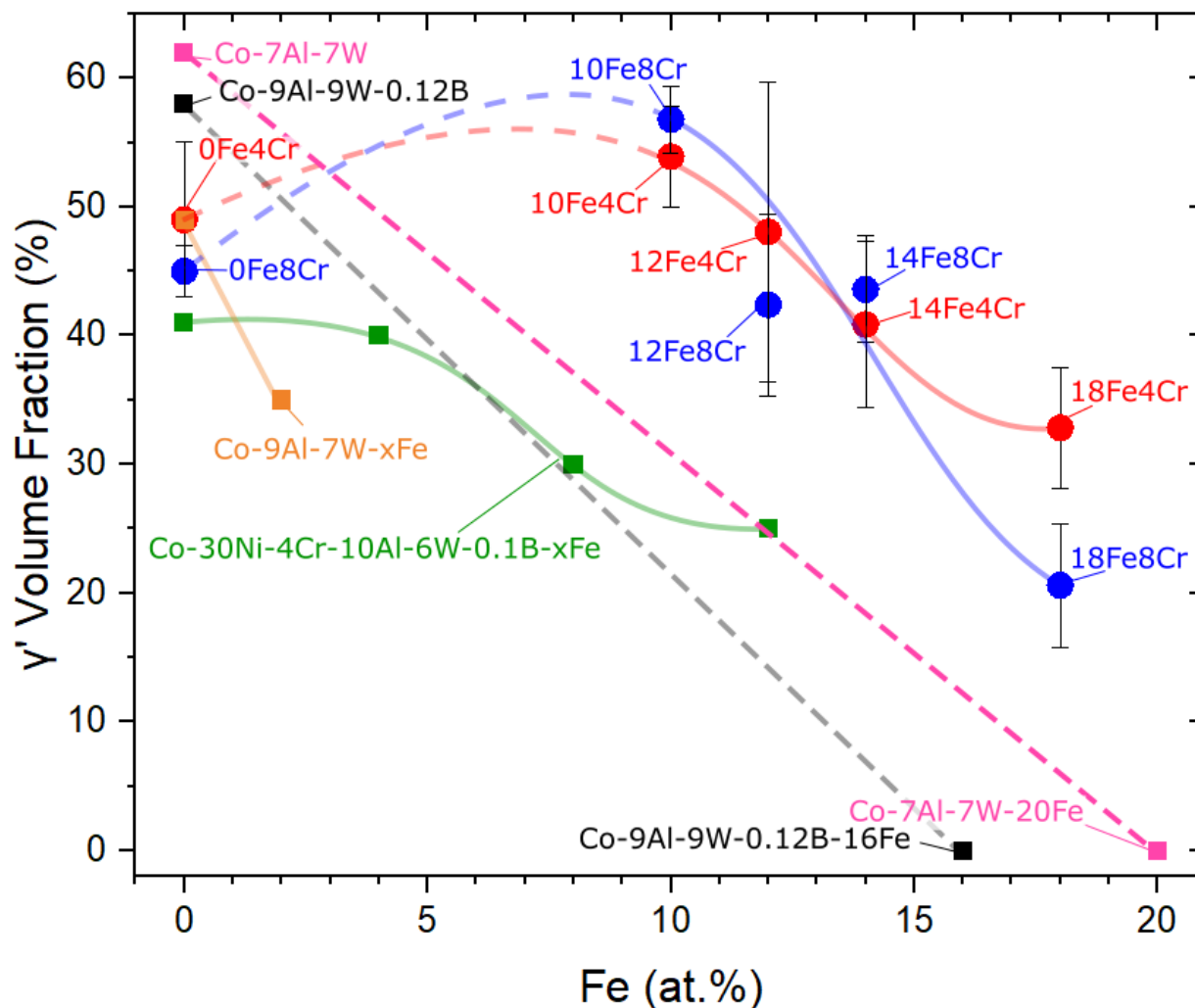


Figure 5-4. Plot of γ' volume fraction as a function of Fe concentration for our six Fe- and Cr-containing alloys aged for 1000 h at 850 °C. Reference 0Fe and 10Fe alloys from previous studies [152,153] are also connected to the red and blue lines. Literature data are shown for Co-9Al-7W-0/2Fe aged for 96 h at 850 °C [129], Co-7Al-7W-0/20Fe aged for 200 h at 765 °C [122], Co-9Al-9W-0.12B-0/16Fe aged for 200 h at 900 °C [61], and Co-30Ni-4Cr-10Al-6W-0.1B-xFe aged for 4096 h at 900 °C [132].

In summary, our W-free 18Fe4Cr alloy exhibits much lower undesirable intermetallic formation than W-containing Co-7Al-7W-20Fe, Co-20Ni-10Cr-10Al-7W-0.1B-15Fe, Co-9Al-9W-0.12B-16Fe, despite the similar Fe content and longer aging times. When investigated with EDS, the TCP precipitates are Nb-rich, so it is possible that replacing Nb with another γ' -former

(such as additional V, Ti, or Al) may further reduce or even eliminate these TCPs. Atom probe tomography is of interest as a follow-up study to determine if partitioning of Fe in the γ' phase is higher in our V-containing alloys than in W-containing alloys, which may explain the lower propensity for undesirable intermetallic formation in the γ matrix (as Fe concentration in γ is reduced).

5.4.2 Transformation Temperatures

Solvus, solidus, and liquidus temperatures are reported in Fig. 5-5 for our alloys, and compared to those of Fe-free 0Fe-4Cr and 0Fe-8Cr alloys (measured with a different DSC instrument) [152]. Original DSC curves are given in Fig. 5-S3.

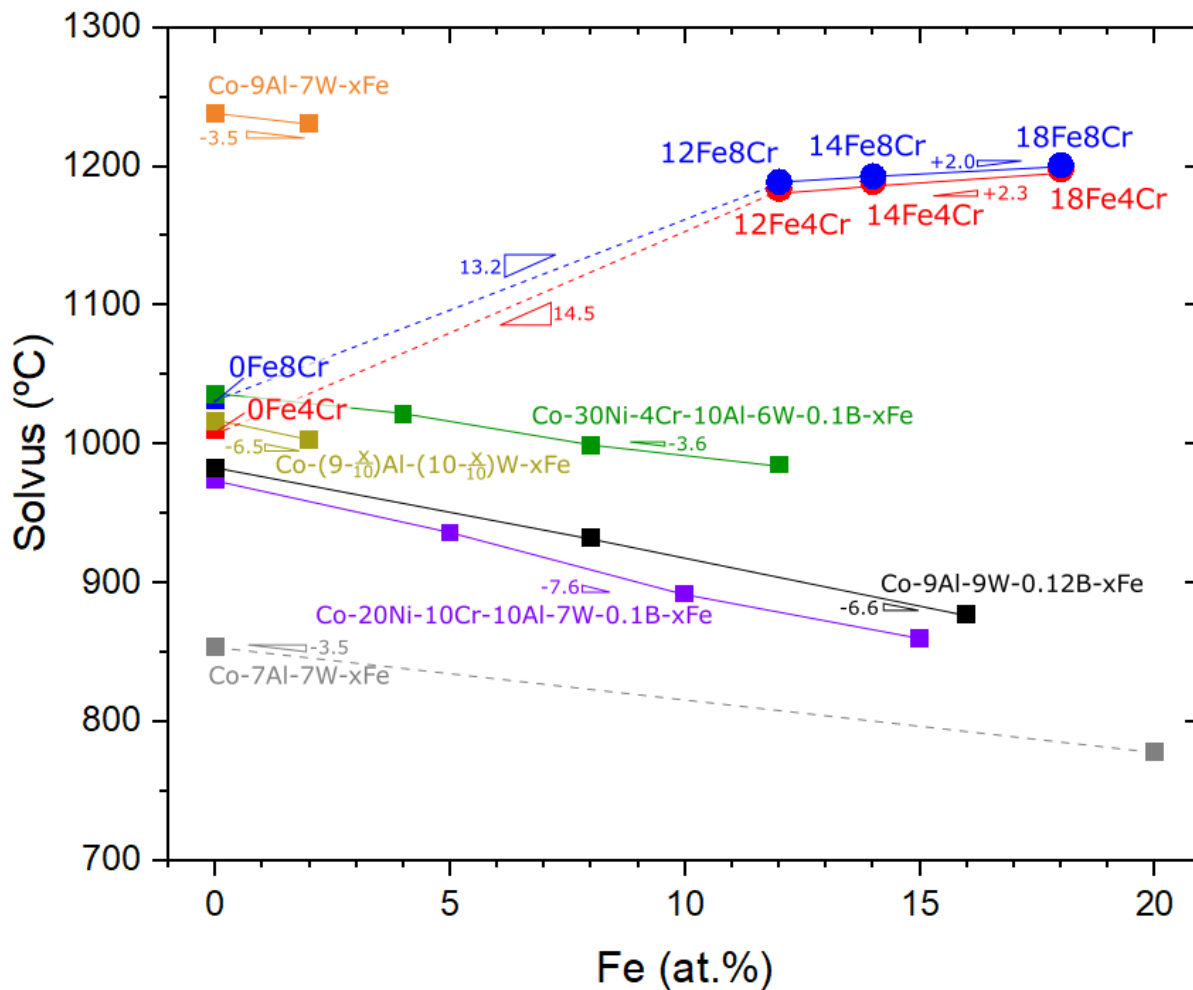


Figure 5-5. Plot of solvus, solidus, and liquidus temperatures as a function of Fe concentration for all 6 alloys, as well as literature data [61,122,128,129,131,132,152].

Replacement of Ni by Fe, from 0 to 12 at.%, increases solvus by ~160 °C, and an additional 10-15 °C increases accrues as the Fe content increases from 12 to 18%, in both 4Cr and 8Cr series. Doubling Cr from 4 to 8 at.% (replacing Co) results in a consistent ~5 °C increase in solvus and 5-10 °C decrease in solidus and liquidus temperature for all our Fe-containing alloys. At constant Cr concentration, in the range of 12Fe to 18Fe, solidus and liquidus temperatures are largely

independent of Fe content. However, the increase from 0 to 12 at.% Fe reduces solidus by 75-132 °C and liquidus by 23-78 °C.

The solvus behavior of these alloys, as Fe substitutes for Ni (in the presence of Co), is opposite of that reported in the Co-Al-W system, as Fe substitutes for Co. As shown in Fig. 5-5 and Table S5-5, every literature alloy reports a 3-8 °C linear decrease in solvus per additional at.% Fe. Thus, our high-Fe alloys have a solvus temperature 300-400 °C higher than W-bearing alloys with similar 14-20 at.% Fe [61,122,128,129,131,132]. Comparing our 0Fe to 18Fe series suggests that solvus increases by an average of 10 °C/at.% Fe. However, this value compares alloys that were measured with different experimental methods. Comparing only the results in the present study yields a moderate increase of ~3 °C/at.% Fe. Further study would need to determine whether small (<12 at.%) substitutions of Fe truly increase solvus so markedly.

For a $(\text{CoNiFe})_3\text{V}$ -based γ' phase, the valence rule outlined by Liu [137] to achieve a cubic (i.e., $L1_2$) rather than an hexagonal crystal structure occurs when the ratio $(8Co + 8.75Ni + 7.25Fe)/(Co + Ni + Fe)$ is below a critical value of 7.9, where Co , Ni , and Fe are atomic concentrations of each element. Thus, the substitution of Fe for Ni is more $L1_2$ -stabilizing than the substitution of Fe for Co. This criterion assumes that the corner atoms of the $L1_2$ cell are always V; we propose that an extended application of the valence rule suggests that substituting some V with lower-valency $L1_2$ -formers, such as Ti or Al, may further stabilize the cubic $L1_2$ phase. Suppressing undesirable intermetallic formation at high Fe levels is critical. As shown in the previous section 3.1, non- γ' precipitate formation sequesters γ' -forming elements, reducing γ' volume fraction[137]. The ability of Ni to widen the $\gamma + \gamma'$ phase field is well-known for most Co-

based superalloys [61,155,156], but is unproven for alloys with Fe-containing γ' . Based on γ' volume fractions, intermediate (<14 at.% Fe) substitutions of Fe + Ni for Co seem as beneficial as similar substitutions of only Ni [152]. Likewise, the ~ 5 °C increase in solvus due to a Cr increase from 4 to 8% is opposite to the trend shown in Co-Al-W alloys [18] but similar to the trend shown in W-free alloys. In fact, this is a smaller increase than exhibited in Fe-free alloys of similar composition [152]. In another W-free series of Co-30Ni-12Al-4Ta-xCr alloys [65], the solvus temperature increases by 5 and 3 °C as Cr increases from 0 to 4 to 8 at.%, finally decreasing by 17 °C between 8 and 12 at.% Cr.

5.4.3 Lattice Misfit

Lattice misfit between the γ' and γ phases is given by $\delta = 2(a_{\gamma'} - a_{\gamma}) / (a_{\gamma'} + a_{\gamma})$ where $a_{\gamma'}$ and a_{γ} are the lattice constants of the two phases [39]. In contrast to Ni-based superalloys, Co-based superalloys have a positive misfit, i.e., the γ' -precipitates have a larger lattice constant than the γ -matrix [43,76].

Lattice parameters $a_{\gamma'}$ and a_{γ} are plotted against each other in Fig. 5-6, along with reference lines of constant lattice misfit. An example neutron diffraction peak fit used to determine lattice parameter is given in Fig. S5-4. Replacement of Ni by Fe increases a_{γ} , which reduces misfit by about 0.02% per 1 at.% Fe in the 4Cr series, as $a_{\gamma'}$ slightly increases with increasing Fe. Except for 18Fe8Cr, which precipitates additional phases, doubling Cr content from 4 to 8 at.% (replacing Co) has a negligible effect on misfit, because both $a_{\gamma'}$ and a_{γ} decrease by a similar amount.

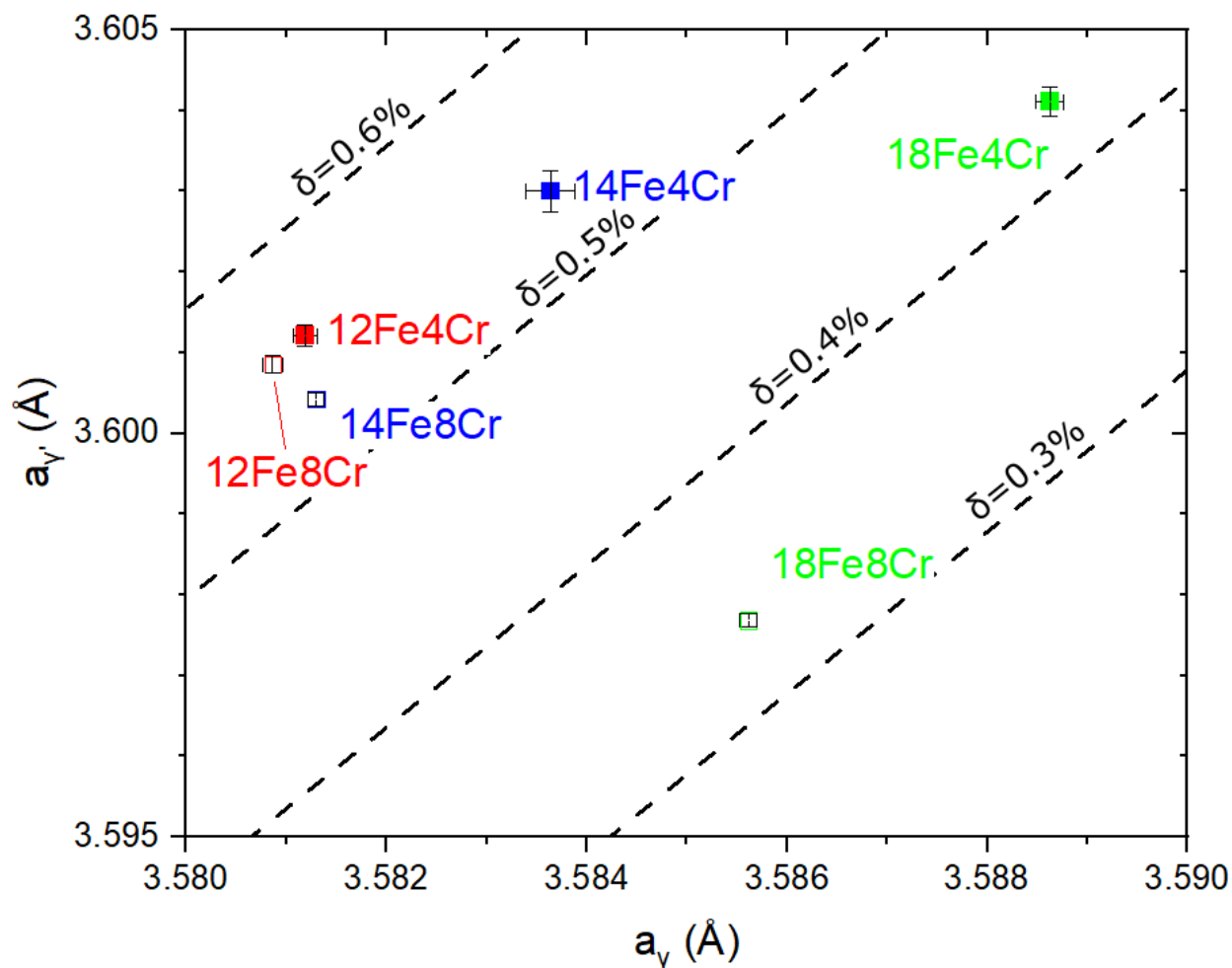


Figure 5-6. Plot of lattice parameter $a_{\gamma'}$ for γ' phase (y-axis) vs. γ phase (x-axis) for 4Cr alloy series (solid symbols) and 8Cr alloys (hollow symbols). Dotted lines represent constant lattice misfit δ . Error bars correspond to esds values from GSAS-II.

Similarly to our 4Cr series, a study of Co-30Ni-4Cr-10Al-6W-0.1B-xFe ($x = 0-12$ at.%) found that Fe replacement of Co linearly increases both $a_{\gamma'}$ and to a greater extent a_{γ} , such that that lattice misfit decreases from 0.21% to 0.02% [132]. This trend is consistent with their observation that the γ' precipitates become more spherical at high Fe concentrations unlike in our alloys, which

supports our lack of major misfit change with increasing Fe. For their above alloy with 12% Fe, Fe partitions to the γ phase ($k_{\text{Fe}}^{\gamma'/\gamma} = 0.55$), indicating that Fe is a γ former.

One study [128] predicted that, if Cr partitions to γ' , it decreases $a_{\gamma'}$ as shown in our alloys. Chung et al. [90] showed that Cr may sometimes partition heavily to γ in Co-Al-W. In that study, increasing Cr from 0 to 12 at.% consistently reduced $a_{\gamma'}$ by a higher magnitude than the change to a_{γ} , such that lattice misfit monotonically decreased. In a similar alloy with V-rich γ' , but without Fe or large amounts of Ni, Cr partitions to γ , with a partitioning ratio $k_{\text{Cr}}^{\gamma'/\gamma} = 0.5-0.68$ [26]. It is possible that the partial substitution of Ni by Fe in our alloys causes Cr to partition more equally (where equal partitioning means $k_{\text{Cr}}^{\gamma'/\gamma} = 1$) across γ and γ' . However, Xue et al. [132] found that 12 at.% Fe addition to Co-30Ni-4Cr-10Al-6W-0.1B (where Co is replaced by Fe while Ni remains constant) does not affect $k_{\text{Cr}}^{\gamma'/\gamma}$, which is ~ 0.45 in both cases.

5.4.4 Oxidation behavior

Weight gain per surface area is plotted as a function of oxidation time at 850 °C in Fig. 5-7(a). After discarding the first 10h to avoid capturing transient oxidation behavior, the remaining curve was fitted to the parabolic rate constant k according to:

$$\left(\frac{\Delta m}{A}\right)^2 = kt, \quad (2)$$

where Δm is the mass gain, A is the surface area, t is time, and k is the parabolic rate constant [80,81]. The values for the parabolic rate constant k are plotted in Fig. 5-7(b) as a function of Fe concentration in our six alloys.

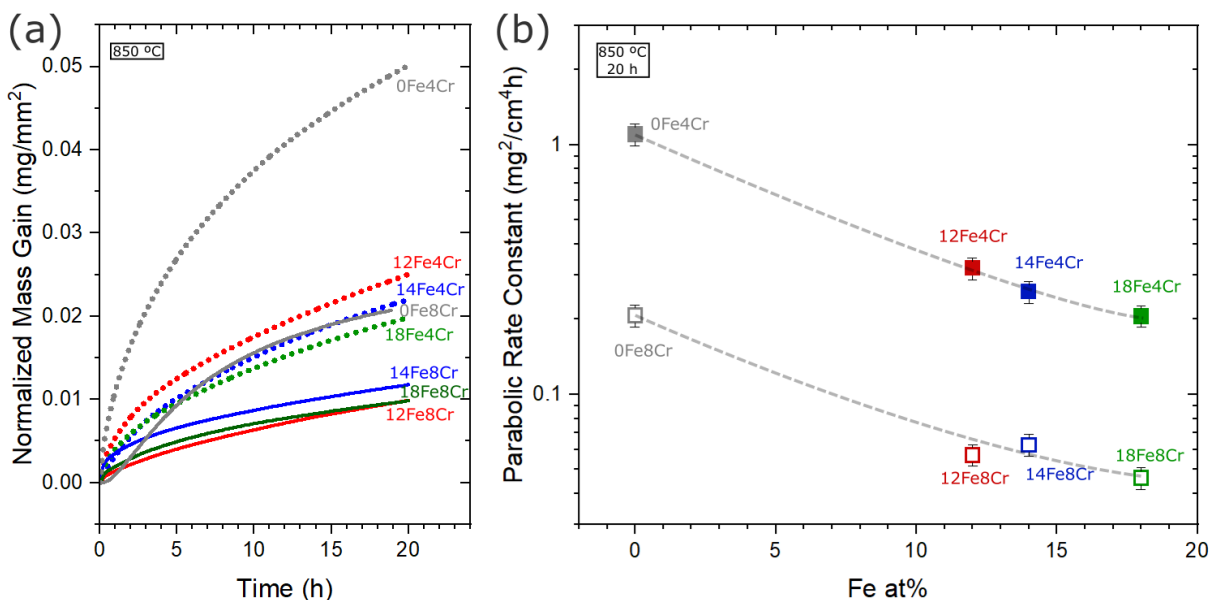


Figure 5-7. Oxidation behavior in dry air at 850 °C for up to 20 h. (a) plot of mass gain per surface area as a function of time. (b) plot of parabolic oxidation rate constant vs Fe content. Also shown in both figures are results for 0Fe4Cr and 0Fe8Cr alloys, collected using the same instrument [152].

As expected, doubling Cr from 4-8 at.% dramatically reduces the parabolic rate constant, by a factor ~5. Increasing Fe also significantly reduces parabolic rate constant, with a substitution of Fe from 0-12 at.% reducing the rate constant by a factor ~3, for both Cr concentrations. Increasing Fe from 12-18 % reduces rate constant by about 0.018 mg²/cm⁴h per at. % Fe in the 4Cr series, and 0.002 mg²/cm⁴h per at.% Fe in the 8Cr series.

Fig. 5-8 shows representative micrographs of cross-sections of the oxidized alloys and corresponding EDS elemental maps for Co, Fe, Ni, and O. Full EDS maps of all elements are given in the Supplemental Information Fig. S5-5.

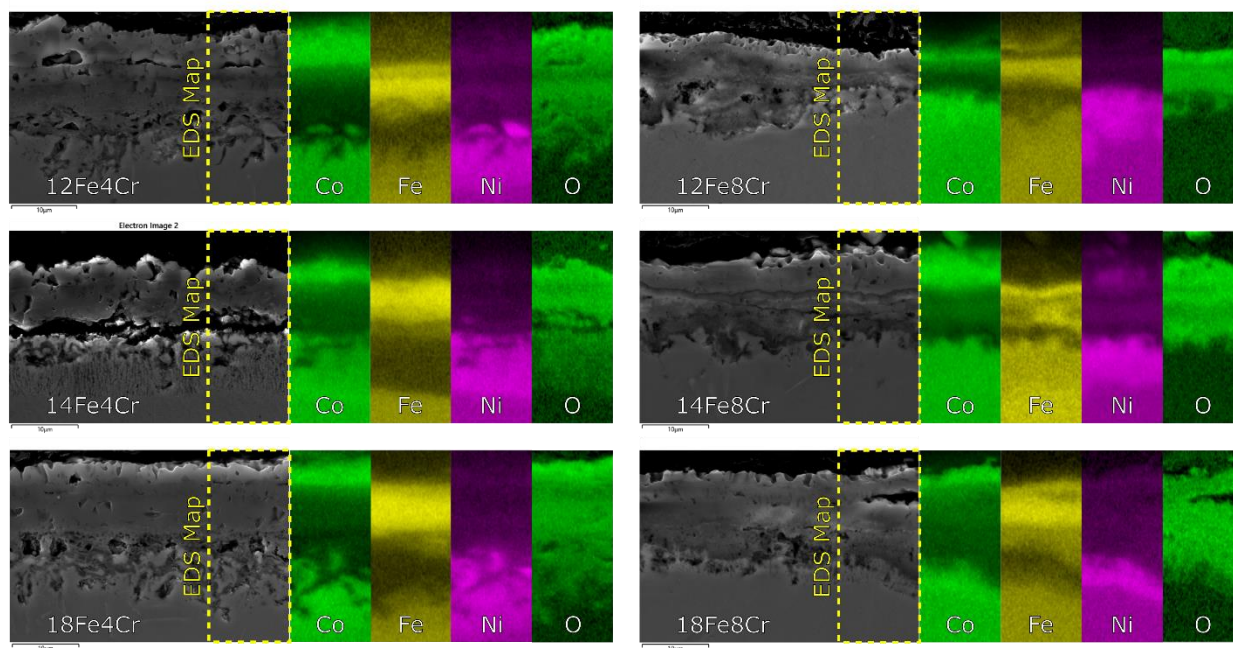


Figure 5-8. Secondary electron micrographs of cross-sections of specimens oxidized in TGA instrument (850 °C / 20 h), showing three distinct oxide layers: a top scale enriched in Co, a middle layer enriched in Fe, and a bottom layer enriched in Ni and other elements, as illustrated in EDS elemental maps.

For all six alloys, three distinct oxide layers are observed: the top layer (in contact with the atmosphere) is enriched in Co, the middle layer is enriched in Fe, and the bottom layer (in contact with the alloy) is enriched in Ni and other elements (Cr, Al, Nb, Ta, V). This behavior is similar to the 0Fe4Cr and 0Fe8Cr alloys reported previously [152], with an additional Fe-rich oxide layer which explains the reduced oxidation rate.

The bottom layer also appears to be an interdiffusion layer, with voids and additional precipitates forming. In addition to its appearance in the bottom layer, V appears to be enriched at the boundary between the Co-rich and Fe-rich oxide layers, as visible in Fig. S5-5. This thin V-enriched layer does not appear in the 0Fe4Cr or 0Fe8Cr alloys.

Compared to Co-30Ni-4Cr-10Al-6W-0.1B-xFe ($x = 0, 4, 8, \text{ and } 12$) [132], our alloys show identical oxidation products (top layer enriched in Co, middle layer enriched in Fe, bottom layer

enriched in Ni and other elements). In their -4Cr alloys, Fe did not provide additional oxidation resistance beyond their first Fe increment (4 at.%), while our -4Cr and -8Cr alloys continued benefiting from Fe even up to 12 at.%.

5.4.5 Hardness

Microhardness measured for each alloy in each aging condition are shown in Fig. 5-9.

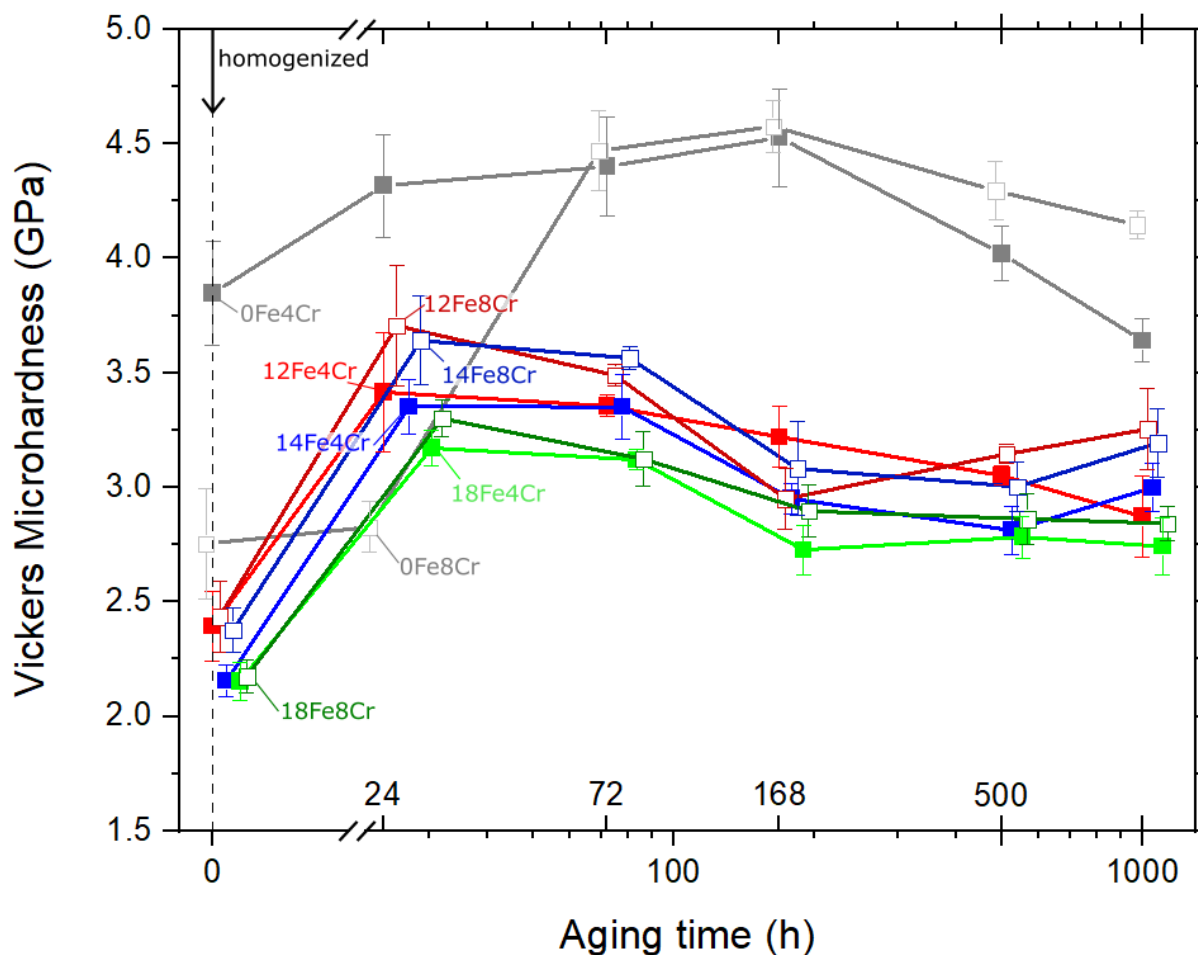


Figure 5-9. Time evolution of microhardness for all 6 alloys aged at 850 °C. Error bars represent the standard deviation of 10 indents. Small offsets are added in the x-axis to improve readability.

All Fe-containing alloys achieve peak-hardness after 24 h, within experimental error, and hardness then slowly decreases between 24 and 1,000 h. The alloys with higher Cr contents (-8Cr) are equal, or stronger than their lower Cr (-4Cr) counterparts at all aging times (except for an anomalously low hardness for 12Fe8Cr at 168 h). The substitution of Fe for Ni also has a minor weakening effect at all aging conditions. This aligns with the γ' volume fraction reduction occurring with increased Fe content. Interestingly, the non- γ' precipitates, which appear at longer aging times in the 18Fe alloys, do not have a significant hardening or softening effect.

Our alloys, with peak hardness in the range of 3-3.75 GPa, are comparable, or slightly softer than, other Co-based superalloys, which mostly range from 2 to 4.5 GPa. These alloys are weaker than their Fe-free variants (0Fe4Cr), which have peak hardness \sim 4.5 GPa [152]. However, these W-free alloys are significantly harder than the strongest W- and Fe-containing alloys; for example, our 12Fe8Cr alloy shows 3.7 GPa hardness while a Co-30Ni-12Fe-4Cr-10Al-6W-0.1B alloy has hardness values below 3 GPa [132].

5.4.6 Temperature Dependence of Yield Strength

Yield strength is plotted against temperature in Fig. 5-10 for our six alloys, as well as various literature alloys. Data is tabulated in Table S5-6.

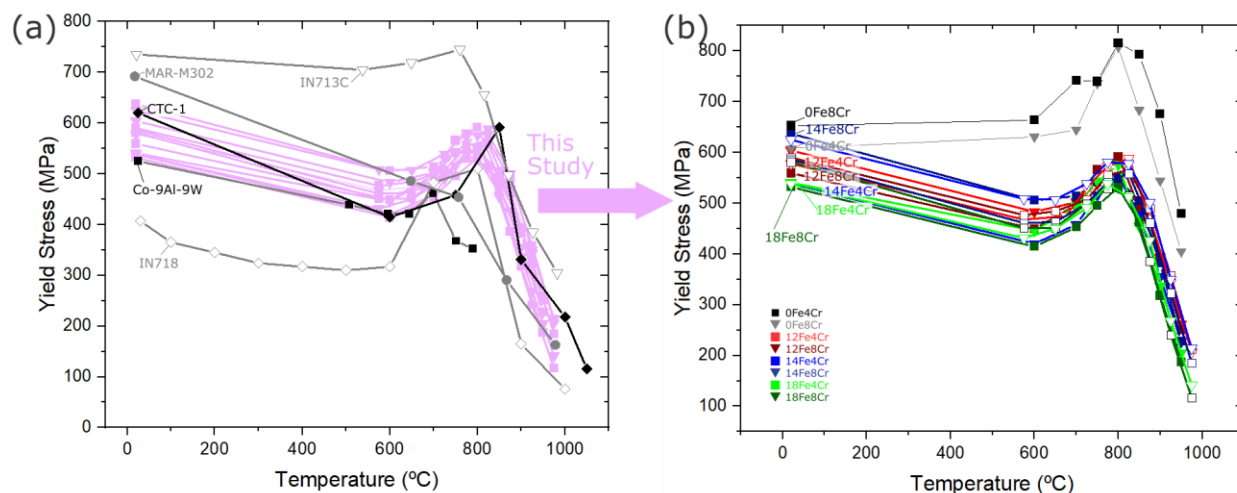


Figure 5-10. (a) Plot of yield strength vs temperature for experimental alloys, as well as literature alloys: Co-9Al-9W [157], CTC-1 with composition Co-11Ti-15Cr [10], MAR-M302 (non- γ' -strengthened commercial Co-based superalloy) [158], IN713C (γ' -strengthened commercial Ni-based superalloy with up to 2.5% Fe) [159], and IN718 (γ' - and γ'' -strengthened commercial Ni-based superalloy with 18 wt.% Fe) [116]. Gray and black symbols are from the literature; hollow symbols are Ni-based alloys. (b) Plot of yield strength vs temperature for our alloys, showing the first test of each alloy as solid symbols, and the second test as hollow symbols.

All our alloys show similar anomalous yield strength behavior, with a sharp peak in strength at 800 °C. At ambient temperature, the yield stress of four of the six alloys are similar (~540 MPa), whereas 12Fe4Cr and 14Fe8Cr are significantly stronger. At higher temperatures, there is a general trend that Fe-leaner alloys are stronger than Fe-richer alloys. This trend is more obvious in the W-containing alloys Co-30Ni-4Cr-10Al-6W-0.1B-xFe ($x = 0, 4, 8,$ and 12) studied by Xue et al. [132]. Just like our alloys, the strength does not monotonically decrease with Fe, but Fe additions (replacing Co) lead to a generally weakening trend, and alloys with 12 at.% Fe have their yield strength reduced by ~15% across the entire temperature range. Their alloy with 12 at.% Fe also shows a reduction in the temperature of the peak anomalous strength, from 850 to 750 °C, unlike

in our alloys. This is likely because Fe replacement of Co decreases solvus temperature in their alloys, but Fe replacement of Ni increases solvus in our alloys.

Below the anomalous peak of 800 °C our alloys are weaker than the commercial, cast Ni-based superalloy IN713C [159]. However, above 800 °C the strong boost of strength provided by the anomalous yield strength mechanism makes our alloys comparable to IN713C. Compared with a commercial, γ' -free Co-based superalloy (cast MAR-M302), our alloys have weaker room temperature strength, but significantly surpasses its performance by 800 °C. Our alloys are also stronger, over the entire temperature range, than Co-9Al-9W [157] and IN718 (a Fe-containing Ni-based superalloy) [116]. The latter alloy was specifically unaged to produce an anomalous yield strength, but typical IN718 shows much higher room-temperature strength, with little-to-no anomalous yield behaviour [160]. Recently, Co-11Ti-15Cr was identified as the Co-based superalloy with the best-performing yield strength vs. temperature behavior [10,113]. As shown in Fig. 5-10, this Co-11Ti-15Cr alloy, with 66% γ' volume fraction, shows very similar temperature dependence of the yield strength compared to our alloys, although its peak strength temperature is somewhat higher (850 vs. 800 °C).

The slight weakening effect caused by substituting Fe for Ni is most probably due to the decrease in γ' volume fraction in our alloys as the Fe/Ni ratio increases. This is illustrated in Fig. 5-11., where peak yield strength (800 °C) for each of our alloys is plotted vs their γ' volume fraction.

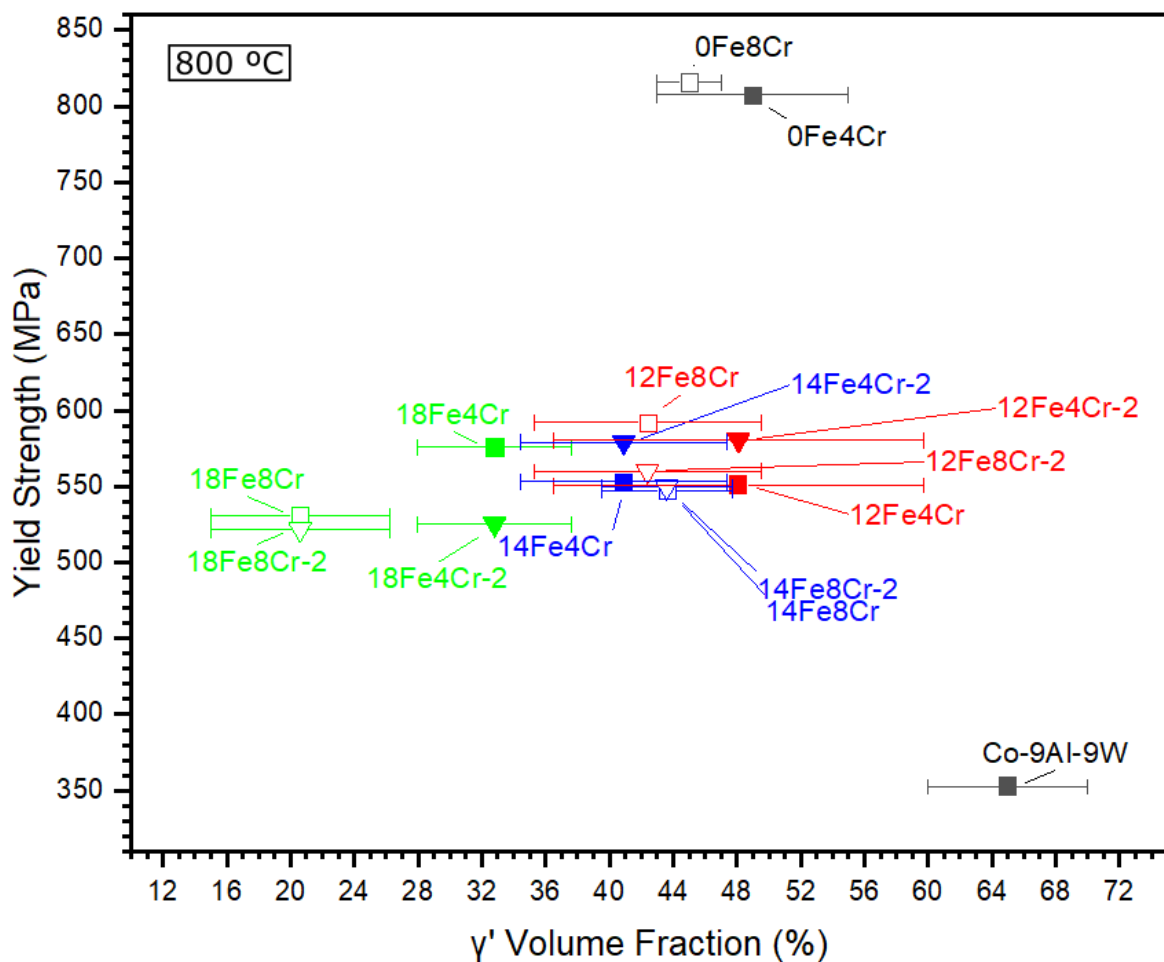


Figure 5-11. Plot of yield strength (peak value at 800 °C) vs γ' volume fraction, for our six Fe-containing alloys and reference Co-9Al-9W at 789 °C [157]. Our data contains two tests: one at 800 °C, and the other (labeled with “-2”) interpolated from results at 775 and 825 °C.

Compared to Co-30Ni-4Cr-10Al-6W-0.1B-xFe ($x = 0, 4, 8, \text{ and } 12 \text{ at.}\%$)[132], our alloys showed peak yield strength near the same temperature (800 °C), although this temperature decreased with Fe in Xue et al.’s study but stayed constant in ours. Nevertheless, Fe additions weakened both sets of alloys. Comparing our 12Fe4Cr to Co-30Ni-4Cr-10Al-6W-0.1B-12Fe, our alloy shows significantly improved peak yield strength (551 MPa at 800 °C compared to 462 MPa at 750 °C).

5.4.7 Creep Properties

The creep behavior at 850 °C is shown for our six experimental Fe-containing alloys in Fig. 5-12, where the secondary creep strain rate $\dot{\epsilon}$ is plotted vs. stress σ in a double-logarithmic plot, according to the Norton power-law equation:

$$\dot{\epsilon} = A\sigma^n \exp\left(\frac{-Q}{RT}\right)$$

where A is a constant, n is the stress exponent, Q is the activation energy, R is the ideal gas constant, and T is the absolute temperature. Values for stress exponent n range from 11 to 12, except for 12Fe4Cr which shows a slightly higher value (n=14). These high n-values are typical in superalloys, including the Co-Al-W system, various W-free systems, or the previous Fe-free iteration of our alloys, which reflect shearing by dislocations of the coherent γ' precipitates [34,71,86,89,132,152].

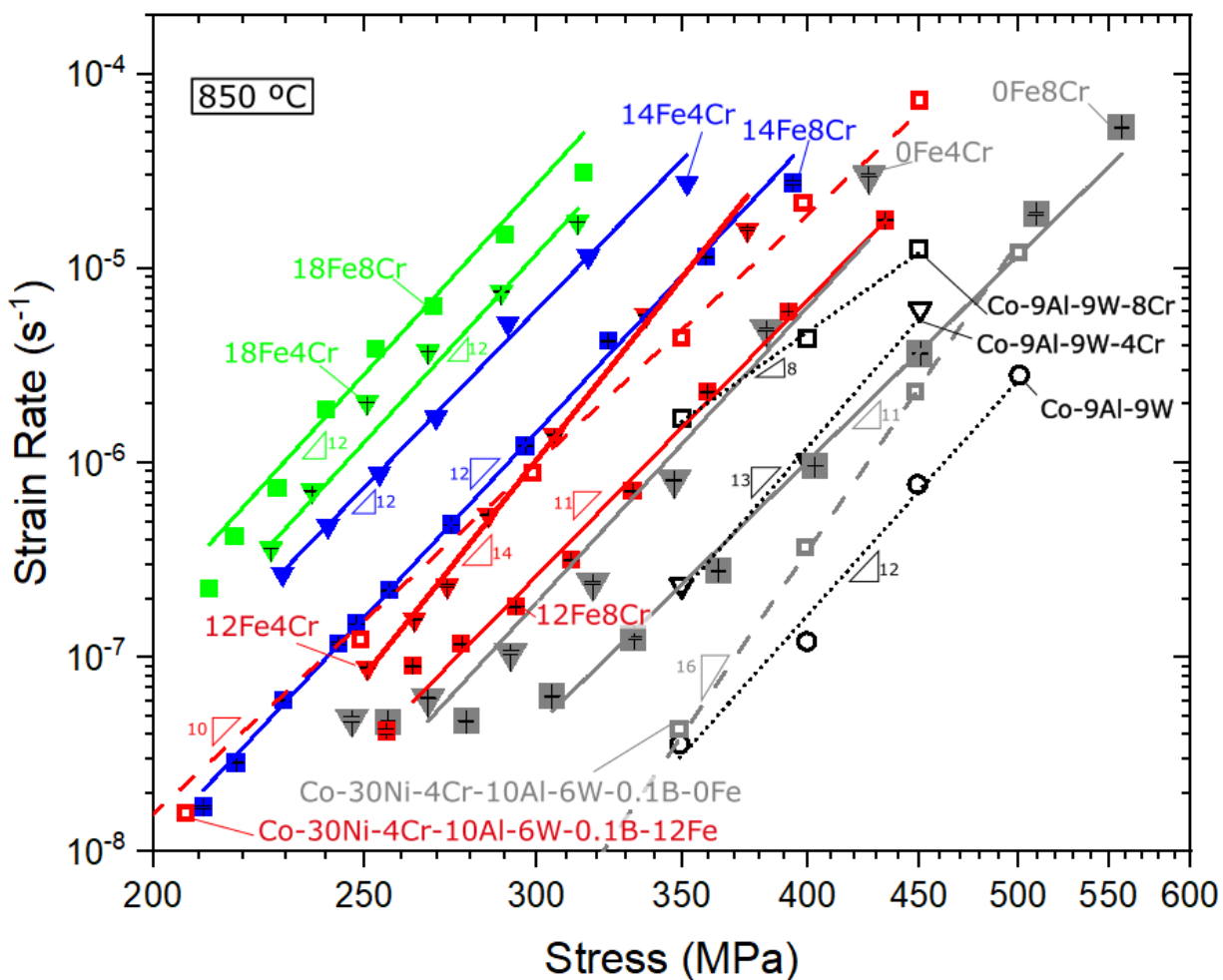


Figure 5-12 Double logarithmic plot of compressive strain rate vs. stress at 850 °C for our experimental Fe-containing alloys with two Cr concentrations (4 and 8 at.%), as well as the reference alloy (0Fe)[152], with 4 or 8 at.% Cr. Also shown is Co-9Al-9W with 0, 4, 8 at.% Cr[71].

As Fe replaces Ni in our alloys, their creep resistance is reduced by 5-20 MPa per at.% Fe substitution (at every stress level, because the alloys have near-identical stress exponent). By contrast, increasing Cr from 4 to 8 at.% (replacing Co) provides an increase in creep resistance of similar magnitude. As the increase in creep resistance is not due to an increase in γ' volume fraction or lattice misfit (see Fig. 5-4 and 5-6), it is thus likely due to solid-solution strengthening. Indirect

effects may also be linked to the ability of Cr to improve γ' coarsening resistance, which results in smaller precipitates that impede dislocations more effectively. The strengthening effect of Cr does not apply to the 18Fe alloys, as 18Fe8Cr is weaker than 18Fe4Cr. For the former alloy, the reduction in creep resistance is almost certainly due to Cr additions destabilizing the γ/γ' 18Fe microstructure and producing TCPs.

To our knowledge, creep resistance has only been studied in one other Fe-containing Co-based superalloy series, Co-30Ni-4Cr-10Al-6W-0.1B-xFe ($x = 0-12$, replacing Co) which likewise shows a reduction in creep resistance with increasing Fe content[132]. Their alloys show especially reduced creep resistance at lower stresses, such that the strain rate exponent n is reduced from 12 to 8. In contrast, our Fe-containing alloys showed a constant $n = 11-12$ (with the exception of 12Fe4Cr which has $n = 14$).

Post-creep microstructure shows typical n-type rafting, as expected from positive-misfit alloys in compression[39,124,152]. Rafting appears similar between alloys but varies depending on grain orientation. Fig. 5-13 shows particular grains that exhibit higher levels of rafting for each alloy.

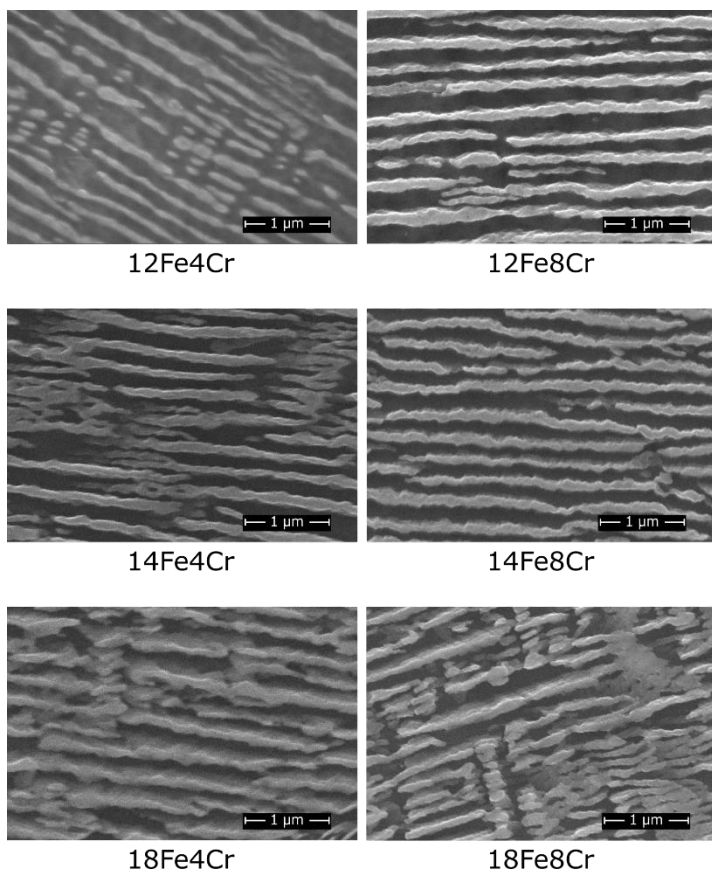


Figure 5-13. Secondary SEM images of specimens after compressive creep (stress was applied in the vertical direction) at 850 °C. Images were chosen to display the most pronounced examples of n-type rafting, the severity of which depends on grain orientation.

The high tolerance for Fe in our alloy series allows relatively high levels of Cr which further improve strength, coarsening resistance and oxidation resistance without forming additional deleterious phases. Overall, the partial replacement of Ni with Fe degrades mechanical properties by decreasing γ' volume fraction. However, the detrimental effects of Fe in our alloys are greatly reduced compared to other Co-based alloys, and future investigations in this system (such as replacing TCP-prone Nb for more V, Al, or Ti) may yield a Co-Ni-Fe alloy, with similar mechanical properties to current Co- and Co-Ni-based superalloys and with a significantly lower alloying element cost.

5.5 Conclusions

A series of six γ' -forming Co-Ni superalloys was studied with various concentrations of Fe (which partially replaces Ni) and Cr (which partially replaces Co): Co-(30-x)Ni-xFe-yCr-5Al-3V-2Ti-1.5Nb-1.5Ta-0.08B, at.% (x = 12, 14, 18 and y = 4, 8). The following main conclusions are reached:

1. *Microstructure:* While Ni \rightarrow Fe substitutions do not have a significant effect on γ' morphology, increasing Fe decreases γ' volume fraction, especially at 18% Fe due to non- γ' precipitates and associated depletion zones. Increasing Cr from 4 to 8% (Co \rightarrow Cr) achieves improved coarsening resistance. However, at 18% Fe, doubling Cr content leads to more non- γ' phases, suggesting that the combination of high Fe and high Cr destabilizes the γ' precipitates. However, Fe is much less γ' -destabilizing in this system compared to other Co-based superalloys, in particular those containing W.
2. *Transformation Temperatures:* Ni \rightarrow Fe substitutions increase solvus temperature by an average of 3 °C per 1 at.% Fe, with negligible changes to solidus and liquidus temperatures. Co \rightarrow Cr substitution (from 4 to 8% Cr) results in a consistent ~5 °C increase in solvus, and 5-10 °C decrease in solidus and liquidus temperatures.
3. *Lattice Misfit:* Misfit values range from 0.56% to 0.34%, with Ni \rightarrow Fe substitution decreasing lattice misfit of ~0.02% per 1 at.% Fe in the 4Cr series. Co \rightarrow Cr substitution reduces both $a_{\gamma'}$ and a_{γ} equally at 12 and 14% Fe, such that the lattice misfit is mostly constant.

4. *Oxidation:* Doubling Cr from 4 to 8 at.% (Co→Cr substitution) reduces oxidation rates by a factor ~5. Ni→Fe substitutions also significantly reduce oxidation rate: as Fe increases from 0 to 12 at.% oxidation rate constants are reduced by a factor ~3, regardless of Cr.
5. *Mechanical Properties:* Ni→Fe substitution generally weakens the alloys in creep, yield strength at all temperatures, and hardness (likely due to a reduced γ' volume fraction), but Co→Cr substitution strengthen the alloys (likely due to solid-solution strengthening). A marked yield strength anomaly is observed at 800 °C (with yield strength of 530-590 MPa) with only weak dependence on Fe and Cr content. For creep at 850 °C, Ni→Fe substitution clearly reduces creep resistance: at constant strain rates, the stress decreases by 5-20 MPa per at.% Fe substitution. Except for the highest Fe concentration, Co→Cr substitution (from 4 to 8 at.%) improves creep stress by ~20 MPa, consistent with solid-solution strengthening.

5.6 Acknowledgements

This study was supported by the U.S. Department of Commerce, National Institute of Standards and Technology, as part of the Center for Hierarchical Materials Design (CHiMaD) at Northwestern University (NU) via award 70NANB14H012. This study was further supported by Rolls-Royce plc. and the Engineering and U.K. Physical Sciences Research Council (EPSRC) for provision of material and funding at the University of Cambridge. This work made use of the MatCI Facility which receives support from the MRSEC Program (NSF DMR- 1720139) of the Materials Research Center at Northwestern University; and the IMSERC X-RAY and the EPIC

facility of Northwestern University’s NUANCE Center, which received support from the Soft and Hybrid Nanotechnology Experimental (SHyNE) Resource (NSF ECCS-1542205).

The authors gratefully acknowledge Dr. Carla Shute (NU) for experimental assistance in the MatCI facility, Dr. Christos Malliakas for experimental assistance in the IMSERC facility, Dr. Hon Tong Pang for experimental assistance with DSC at the University of Cambridge, Dr. Nick Jones for experimental assistance with arc melting at the University of Cambridge, and Dr. Ron Smith (ISIS Neutron and Muon source) for collecting Neutron Scattering data (RB2190134-1) . BCO gratefully acknowledges laboratory assistance and training—especially during pandemic working conditions—from Dr. Hon Tong Pang, George Wise, and Sue Gymer (University of Cambridge). The following NU colleagues are acknowledged for helpful discussions: Dr. Amir Farkoosh, Dr. Ding-Wen Chung, Dr. Fei Xue. Dr. Yoshiki Kumagai, Dr. Hyeji Im.

5.7 Competing Interests Statement

Declarations of interests: none

5.8 Supplementary Information

5.8.1 Element Cost

Element	Density [g/cm ³]	Melting Point [°C]	Price [USD/kg]
Fe	7.87	1537	0.42
Co	8.85	1495	33
Ni	8.90	1453	14

Table S 5-1. Density [161], melting point [161], and 2021 cost [162] for elemental Fe, Co, and Ni. Historic Co prices have been very volatile, and Co has a high supply risk score [163].

Additionally, Fe additions can further reduce the manufacturing cost because it allows the use of ferroalloys, rather than pure elements, as raw materials: for example, the cost of a Fe-V ferroalloy is typically much lower than that of pure Fe and pure V.

5.8.2 Composition

Alloy	EDS Composition, at.%								
Label	Co	Fe	Ni	Al	Cr	V	Ti	Nb	Ta
12Fe4Cr	52.48	12.36	17.49	5.42	4.17	3.08	2.03	1.44	1.52
14Fe4Cr	52.22	14.31	15.53	5.63	4.18	3.07	2.07	1.50	1.49
18Fe4Cr	52.20	18.27	11.78	5.45	4.14	3.06	2.06	1.51	1.52
12Fe8Cr	48.33	12.24	17.44	5.44	8.32	3.11	2.08	1.48	1.55
14Fe8Cr	48.32	14.22	15.59	5.44	8.29	3.10	2.07	1.45	1.51
18Fe8Cr	48.13	18.28	11.81	5.49	8.30	3.10	2.04	1.41	1.44

Table S 5-2. Measured composition from homogenized samples via at least 5 randomly selected EDS spots. B was left out, as it is below the reliable detection limit.

5.8.3 Microstructure

Representative SEM SE images are given for all alloys at all aging steps in Fig. 5-1 and Fig. 5-2.

Alloy	γ' Volume Fraction (%)	Standard Deviation (%)	Minimum (%)	Maximum (%)	Number of Images	$\gamma + \gamma'$ Region (%)	True γ' Volume Fraction (%)
10Fe4Cr	54	4	48.3	62.9	12	100	53.9
10Fe8Cr	57	3	52.5	61.2	9	100	56.8
12Fe4Cr	48	12	36.2	72.1	6	100	48.1
12Fe8Cr	42	7	29.8	60.7	11	100	42.4
14Fe4Cr	41	7	33.4	54.3	9	100	40.9
14Fe8Cr	44	4	37.9	50.5	9	100	43.6
18Fe4Cr	34	5	29.3	41.9	9	96 \pm 2	32.8
18Fe8Cr	34	5	27.1	42.6	7	61 \pm 16	20.6

Table S 5-3. γ' volume fraction according to ImageJ thresholding for all 6 alloys, as well as 10Fe4Cr and 10Fe8Cr from Ref [153], aged 1000 h at 850 °C

Table S5-4 shows ImageJ analysis for the area fraction of needlelike precipitates, globular precipitates, depletion zone, and $\gamma + \gamma'$ region. Note that the total area of needlelike + globular precipitates is accurate, but the distinction between the two is not always clear. The $\gamma + \gamma'$ regions were calculated from the remaining area.

Alloy	Needle-like Fraction (%)	Globular Fraction (%)	Depletion Zone Fraction (%)	$\gamma + \gamma'$ Region (%)	Number of Images
18Fe4Cr	0.1 ± 0.1	1 ± 0.5	3.3 ± 1.4	96 ± 2	8
18Fe8Cr	2.6 ± 1.1	4 ± 2	33 ± 10	61 ± 16	6

Table S 5-4. Volume fraction of needlelike precipitates, globular precipitates, and depletion zones for 18Fe4Cr and 18Fe8Cr after 1000 h aging at 850 °C

Fig. S5-1 shows typical microstructure of previous alloys 10Fe4Cr and 10Fe8Cr [153].

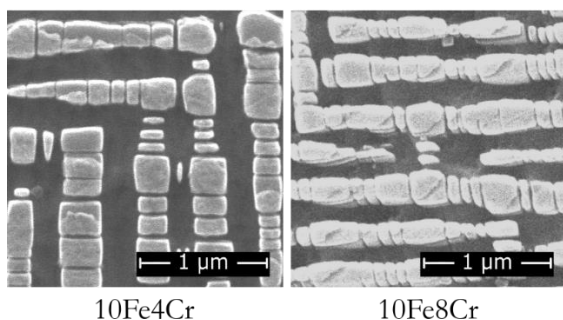


Figure S 5-1. Typical microstructure of 10Fe4Cr and 10Fe8Cr, aged 1000h at 850 °C.

Fig. S5-2 Shows EDS linescan data for a particularly pronounced example of an Al-core Ti-shell precipitate, in alloy 14Fe8Cr aged 500h. The linescan plot is normalized and offset for clarity.

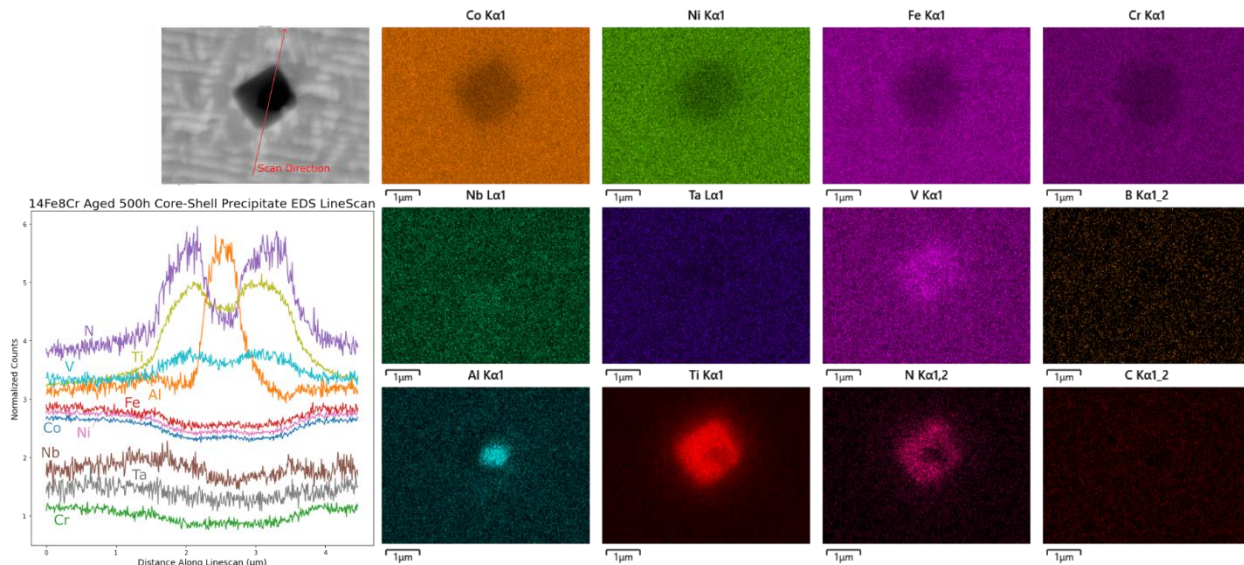


Figure S 5-2. Normalized EDS line-scan and EDS elemental maps for a core-shell precipitate in 14Fe8Cr aged for 500h at 850 °C.

5.8.4 Transformation Temperatures

Alloys (at.%)	Fe Concentration (at.%)	ΔT (°C/at.%)	Reference
	Replacing Co		
Co-xFe-7Al-7W	x = 0, 20	-3.4	[122]
Co-xFe-9Al-7W	x = 0, 2	-3.5	[129]
Co-xFe-9Al-9W-0.12B	x = 0, 8, 16	-6.6	[61]
Co-xFe-(9 - $\frac{x}{10}$)Al-(10 - $\frac{x}{10}$)W	x = 0, 2	-6.5	[128]
Co-20Ni-xFe-10Cr-10Al-7W-0.1B	x = 0, 5, 10, 15	-7.6	[131]
Co-30Ni-xFe-4Cr-10Al-6W-0.1B	x = 0, 4, 8, 12	-3.6	[132]
	Replacing Ni		
Co-(30-x)Ni-xFe-4/8Cr-5Al-3V-2Ti-1.5Nb-1.5Ta-0.08B	X = 0, 12	+13.8	[152], present work
Co-(30-x)Ni-xFe-4/8Cr-5Al-3V-2Ti-1.5Nb-1.5Ta-0.08B	x = 12, 14, 18	+2.7	present work

Table S 5-5. List of Co-based superalloys containing Fe (literature and present study), with change in solvus temperature (ΔT) per 1 at.% addition of Fe replacing Co or Ni

Fig. S3 shows the first DSC cooling curve, with peak corresponding to the solvus temperature.

Multiple peaks were averaged to determine the solvus temperature reported in Fig. 5-5.

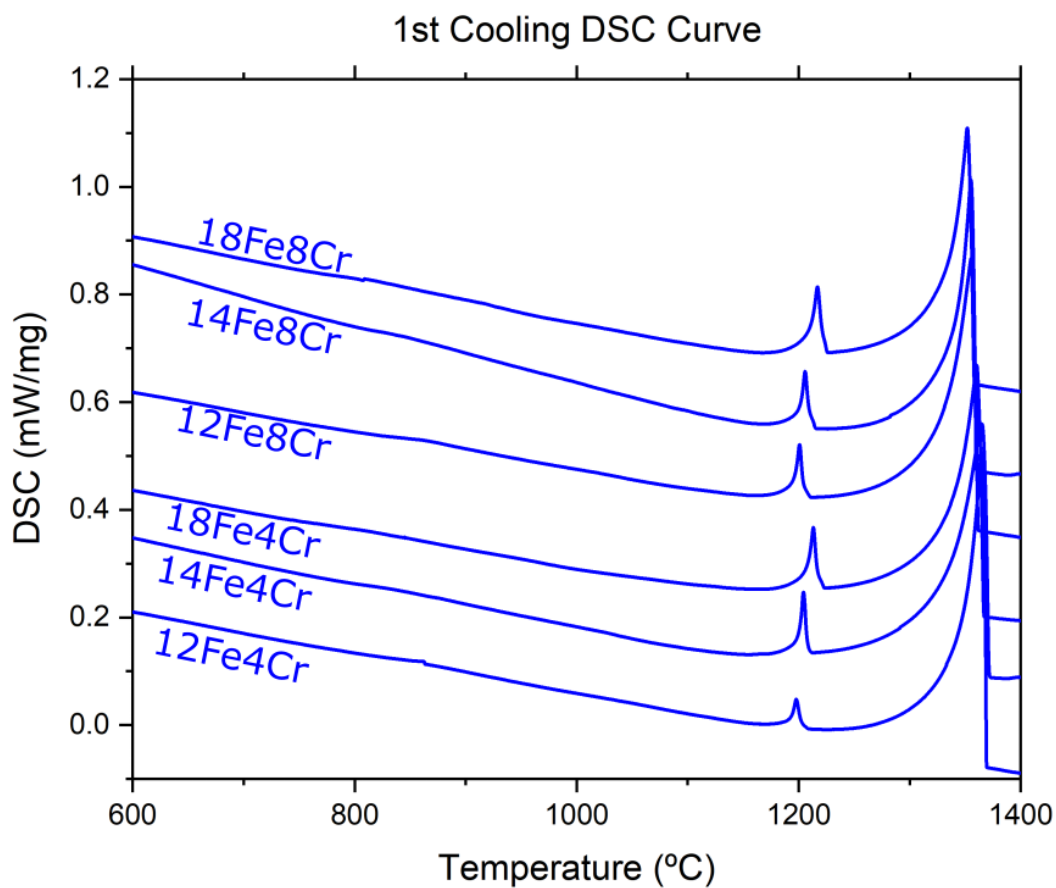


Figure S 5-3. 1st DSC cooling curve (heat flux vs. temperature) for all 6 alloys. Peak near 1200°C is the solvus temperature.

5.8.5 Lattice Misfit

Fig. S5-4 shows an example LeBail fit in GSAS-II, corresponding to bank 4 in 12Fe4Cr.

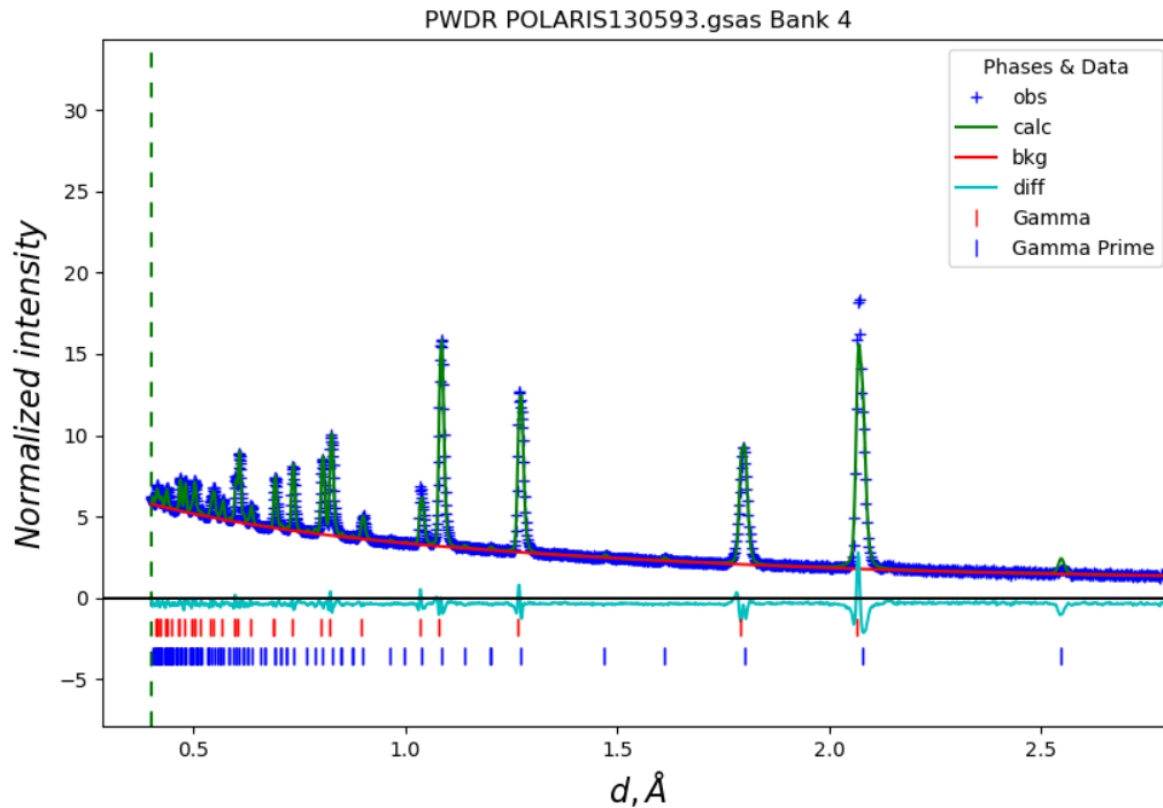


Figure S 5-4. Example of neutron diffraction peak fitting using GSAS-II. This figure shows fitting for bank 4 in $12\text{Fe}4\text{Cr}$, which was fit simultaneously with other banks using Le Bail fitting.

5.8.6 Oxidation

Fig. S5-5 shows full EDS maps for all samples oxidized for 20h at 850 °C.

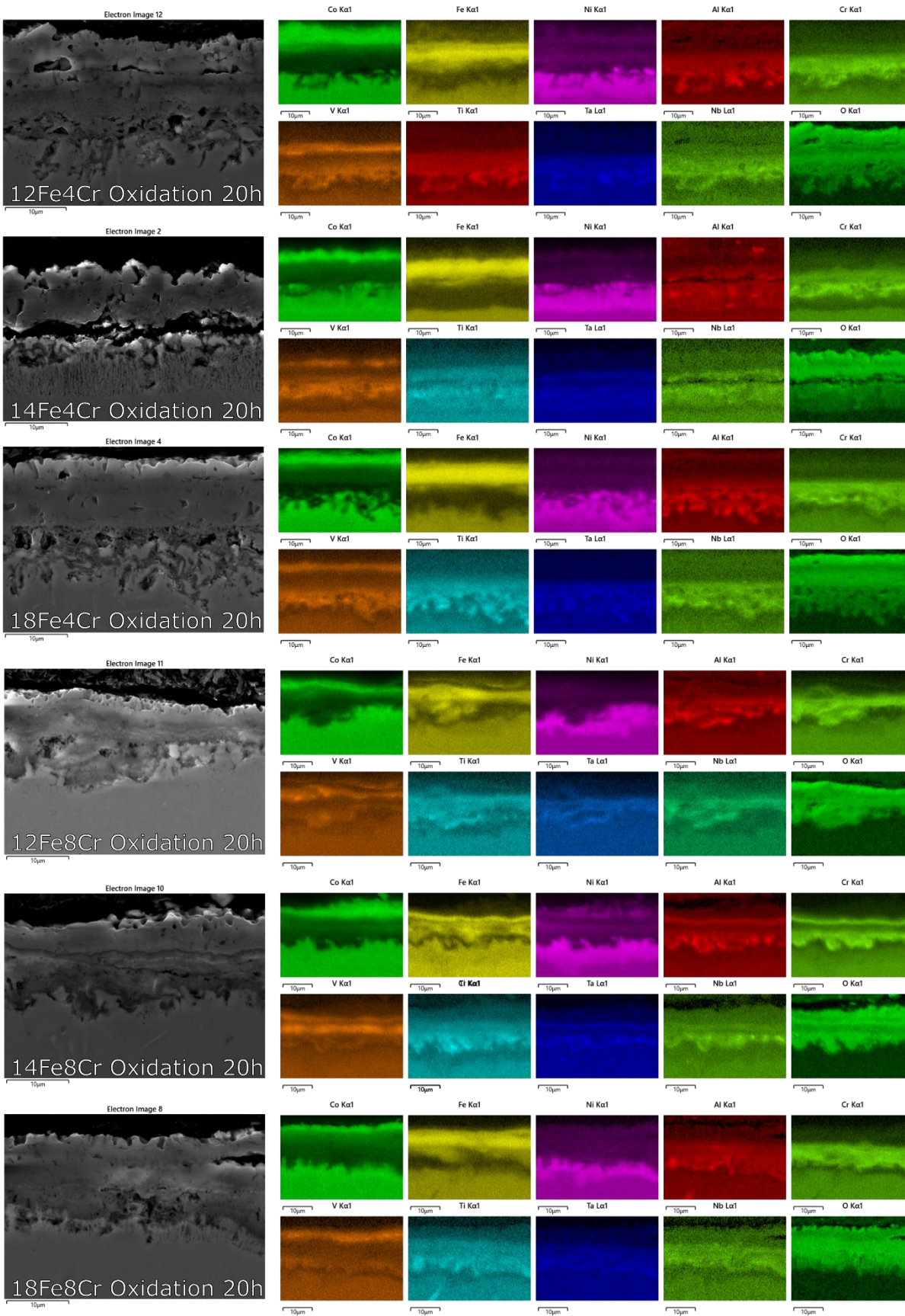


Figure S 5-5. Full EDS maps for samples oxidized at 850 °C for 20h.

5.8.7 Mechanical Tests

Fig. S5-6 shows an example compressive displacement vs time plot, which is used to determine steady-state creep rates in Fig. 5-12.

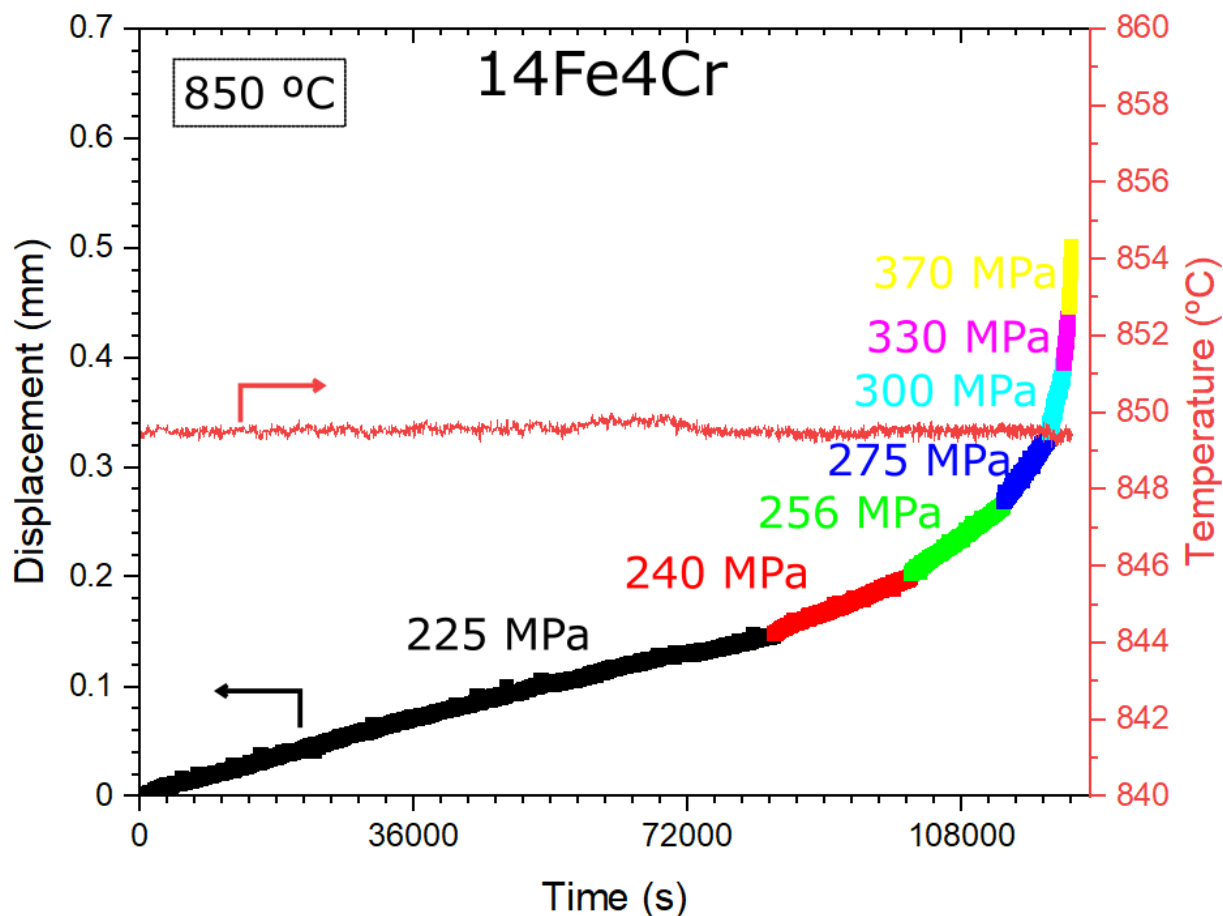


Figure S 5-6. Displacement vs time curve for 14Fe4Cr crept at 850 °C at increasing stresses. Temperature vs. time curve (right y-axis) shows excellent temperature stability over the 34 h duration of the test.

Yield strength vs temperature is given in Table S5-6, which corresponds to Fig. 5-10.

Temperature (°C)	Yield Stress (MPa)							
	0Fe4Cr	0Fe8Cr	12Fe4Cr	12Fe8Cr	14Fe4Cr	14Fe8Cr	18Fe4Cr	18Fe8Cr
20	608	653	604	559	538	637	541	532

600	631	664	483	449	420	506	446	414
700	644	741	502	497	458	514	494	453
750	736	740	538	566	516	542	544	496
800	807	816	551	592	553	547	576	531
850	683	793	495	491	477	504	455	463
900	544	676	393	394	355	382	337	318
950	405	479	261	250	227	228	205	187
2nd Run								
			12Fe4Cr	12Fe8Cr	14Fe4Cr	14Fe8Cr	18Fe4Cr	18Fe8Cr
20			578	590	625	586	538	581
575			468	476	508	461	431	451
675			475	484	507	463	450	452
725			531	507	539	499	490	499
775			573	556	581	541	538	529
825			588	565	577	558	512	514
875			469	490	501	461	427	386
925			343	358	350	323	268	241
975			206	213	214	185	142	117

Table S 5-6. Yield stress for each alloy (sample 1 and sample 2) as a function of temperature. Data corresponds with plotted values in Fig. 5-10.

6. Machine-Learning Prediction of Steady-State Creep Strain Rate in γ/γ' Cobalt-based Superalloys

6.1 Abstract

A machine-learning model was built to predict the strain rate in the steady-state regime of any Co-based superalloy at a particular temperature and stress, given inputs of alloy composition, heat treatment history, and microstructure (γ' precipitate volume fraction). The model is trained on nearly 1,000 distinct Co-based superalloys with γ/γ' microstructure reported in the recent literature. Instead of using CALPHAD-predicted inputs which have proven unreliable (especially in newer alloys systems such as these), we have developed additional intermediary machine-learning models for six materials properties. These models require only a compositional input to predict solvus-, solidus-, and liquidus temperatures, peak hardness, and lattice misfit and yield strength (at ambient and elevated temperature). These intermediate materials properties results are fed back into the creep prediction ML model to improve its accuracy. Additionally, we validated results by predicting intermediate- and creep-properties for 16 new alloys, and experimentally determining those values.

6.2 Introduction

Superalloys' remarkable strength at high temperature, due to the ability of $L1_2$ - γ' precipitates to impeded dislocation motion, have made them the material of choice for various applications such as natural-gas- and jet-engine turbine blades and disks[2]. These highly-stressed parts, which

operate for long times at temperatures in the range 700-1000°C, are currently limited by creep life. When developing new superalloys, creep resistance is thus one of the predominant properties (together with oxidation resistance) that metallurgists seek to optimize.

Creep deformation in alloys typically occurs in three regimes, given a constant stress and temperature. In the secondary regime, dislocation density has equilibrated, and creep rate stays mostly constant. This “steady-state,” minimum creep regime is where a part spends the majority of its lifetime, and where deformation can most easily be calculated and predicted. Thus, most alloys are optimized for a low steady-state creep rate.

Despite its importance, creep is infrequently measured by research groups because it requires long times and large amounts of alloys. In ~1,000 individual alloys added to the database for this project, there were 132 unique alloy compositions with reported creep measurements. Thus, methods to predict creep life before performing experiments, or even before casting the alloy, can greatly accelerate superalloy design.

In an early attempt to predict creep life using constitutive models, MacLachlan and Knowles used modified damage mechanics equations for four commercial superalloys with well-known properties [164]. Vladimirov et al. used an extension of Cailletaud single-crystal plasticity to model all three stages of creep life, starting with uniaxial creep data of the same alloy [165]. Fedelich used constitutive models to predict the interaction between creep and rafting in the well-studied commercial CMSX-4 Ni-based superalloy [166]. One of the most versatile constitutive models is from Kim et al., which combines microstructural features with CALPHAD predictions to predict creep life in various Ni-based superalloys [167]. Sulzer and Reed have also developed a

complex constitutive model for predicting creep at intermediate stress and temperature, which uses various physical parameters [168].

However, these methods all require additional knowledge of the potential alloys, typically from experimental results of the same alloy or from CALPHAD (CALculation of PHase Diagrams). While much work is ongoing to improve databases for Co-based superalloys, these databases cannot accommodate combinations of >10 elements, which are typical for cutting-edge superalloys. As we have also seen in Fig. 6-1, databases designed for Ni-based superalloys (TCNI-11) cannot yet reliably predict properties of Co-based superalloys.

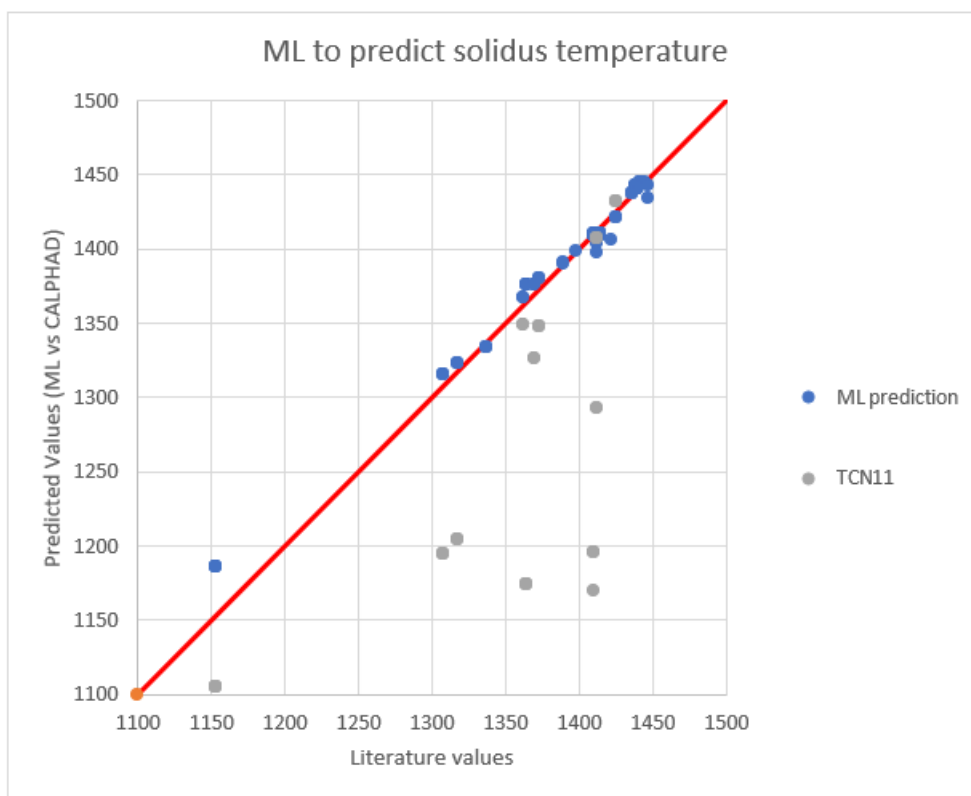


Figure 6-1. Early stage of the ML model, predicting solidus temperature. Blue dots are from our machine-learning model, and gray dots are from CALPHAD, using the most up-to-date TCNI-11 database (as of 2022). Predicted values which lie on the red line exactly match experimental results.

Machine learning (ML) is a powerful new tool for the prediction of alloy properties, which is especially adept at finding complex relationships between material descriptors (e.g., composition and phase fractions) and material properties (e.g., hardness and strength). One of the first applications of machine-learning to Ni-based superalloys was from Venkatesh and Rack, who used a neural network to predict creep in Inconel 690, given a set of prior creep experiments performed on the same alloy [169]. Yoo et al. used a Bayesian neural network with Markov chain Monte-Carlo method to relate single crystal creep behavior to the Ni-based superalloy composition [170]. He et al. used constrained neural networks with error estimates to predict creep rupture for the same alloy with greater accuracy than interpolating between the experimental creep rupture values [171].

One of the most innovative approaches to creep life prediction is the “divide-and-conquer” approach described by Liu et al. Their method, which we partially mimic here, involves k-means clustering alloys into different groups, then training each group on its own ML model. This is especially powerful because creep is controlled by various mechanisms, depending on the alloy microstructure, temperature, stress, etc. Compared to their best “undivided” model (Random Forest (RF) with a coefficient of determination $R^2=0.71$), their divide-and-conquer approach had $R^2 = 0.92$.

We anticipate this approach to be even more powerful in our dataset, as we include alloys from many different Co-based superalloy subgroups, with a *much* wider composition range than typical Ni-based superalloys. Compared to Liu et al.’s dataset, where composition of each element typically varies by a few percents and where most alloys share the same elements, the range of

composition varies here by more than 10% for many of our elements. We also include data from alloys processed via different methods (e.g., single crystal and arc melted) as well as both load directions (compressive and tensile) to train with as much data as possible. As with most ML models, this tool is designed to help explore the design space, rather than calculate an exact creep measurement for known alloys under different conditions.

6.3 Data Collection Methods

We have attempted to compile an exhaustive property list of every Co-based superalloy published by the end of 2022. Here, we define Co-based superalloy as an alloy with at least 40 at% Co and an FCC- γ + L1₂- γ' (γ/γ') microstructure. Data were collected and transcribed into the database entirely by human labor. In addition to directly searching for papers, backtracking through citations to find earlier work, and reading the table of contents every month from major publishers, we have also used Google Scholar to find all papers which cited influential works in the Co-based superalloy space—most notably, Sato et al.'s 2006 [7] rediscovery of Co-based superalloys. In total, 1,380 papers were perused to determine if they contained data pertinent to our dataset. A few papers were not included, typically because they were not written in English, or because we could not get online access or a copy through an interlibrary loan. It is also possible that some papers slipped through the cracks, or that we missed a piece of useful data when skimming the article. However, we believe this dataset is as exhaustive as reasonably possible, and it is also being used to write a literature review for Co-based superalloys.

When possible, we used data in written form where numbers could be copied and pasted without introducing interpretation error. If data numbers were not easily accessible in the main text, but plotted in a figure, we used the WebPlotDigitizer [172] to approximate the value based on pixel measurements. Thus, the precision reported in such cases does not correspond with the actual experimental precision.

When room temperature was reported, we normalized this value to be 25 °C, so as to prevent the model from using the exact value as an artifact (e.g., if humans can tell which research group produced which “room temperature” measurement, the ML algorithm might be able to do it as well).

Alloy composition, if measured by multiple methods, was reported with the following priority: first, Inductively Couple Plasma techniques (ICP); second, Energy Dispersive Spectroscopy (EDS); third, nominal composition.

Lattice misfit – defined as $2(a_{\gamma'} - a_{\gamma}) / (a_{\gamma'} + a_{\gamma})$, where $a_{\gamma'}$ and a_{γ} are the lattice constants of the two phases [39] can be experimentally determined in various ways, notably via (synchrotron) X-rays or neutron diffraction. It can be measured by fitting multiple peaks simultaneously in a program such as GSAS-II [173] or by applying Bragg’s law to single peaks fitted with an equation such as pseudo-Voigt.

Solvus, solidus, and solidus temperatures were measured by techniques such as Differential Scanning Calorimetry (DSC) or Thermal Gravimetric Analysis (TGA). On heating, the solvus temperature is reached when the γ' phase dissolves, the solidus temperature when the alloy first begins to melt, and the liquidus temperature when the alloy is fully liquid.

Volume Fraction is the volume % of γ' precipitates. This is typically measured on SEM cross sections using image processing software such as ImageJ, along with a stereographical area-to-volume correction if necessary. Volume fraction may also be calculated via the lever rule, if the composition of γ and γ' are precisely known and the alloy has no other phases present. If both methods are reported, image analysis was given priority.

Hardness was typically measured at room temperature via Vickers micro-indenters, as a function of aging temperature and time. To simplify the dataset, we typically only reported the *peak* hardness for a particular aging temperature.

Yield strength (0.2% offset) was measured at room temperature or elevated temperature, in compression or tension. Reported data only include the yield strength and temperature, despite the importance of other features such as grain size, precipitate size, γ' volume fraction, etc.

Creep was measured at elevated temperature, in compression or tension. Reported data include the steady-state (or minimum) creep rate, temperature, stress, load direction (categorically, as compressive or tensile), γ' volume fraction, grain size (categorically, as single crystal or polycrystal), and processing parameters (solutionization and aging temperatures and times). The creep rate was converted to a time (i.e., time to 1% strain under steady-state conditions) assuming no primary creep, as it is a more intuitive description of the creep resistance.

The most-useful information missing in our dataset was the individual **compositions of the γ and γ' phase**. This was not feasible to collect, due to the time cost of entering dozens of values into a spreadsheet for each alloy. In the future, this aspect may be improved via a data scraper, but was beyond the scope of the current project.

6.3.1 Experimental Errors

As the saying goes, “garbage in, garbage out.” It is important to note sources of error in the database, including errors transcribing data, errors in the published literature, and experimental error.

For alloy composition, experimental error of <1 at.% from nominal is typical. Unfortunately, many papers did not verify their composition experimentally, so we had to accept the nominal composition as the actual composition in many cases (when ICP and EDS data were absent, see above).

For lattice misfit, relative error can be as high as 50% depending on material processing [174] or collection method (X-ray vs. neutron diffraction) [77]. In our previous work, we have found that error bars of 20% (e.g., misfit = $1 \pm 0.2\%$) are typical when measuring misfit on the same sample from different experimental methods or on different diffraction peaks [152]. Misfit may additionally be sensitive to temperature and stress (e.g., from thermal expansion of the two phases), muddling the relationship between an alloy aged at elevated temperature and measured at room temperature, compared to an alloy measured directly at the aging temperature.

DSC measurements may vary significantly depending on experimental conditions such as sample heat treatment, cover gas, heating/cooling rate, and even the sample dimensions and degree of polishing. Even controlling for these variables, in our unpublished experimental work, we found that these values typically vary by 5-20 °C when performing repeat measurements. Repeat DSC

measurements are currently not standard, so error bars are typically unreported or correspond to the <5 °C uncertainty with identifying the transformation temperature in a single DSC curve.

Hardness experimental methods may differ slightly (e.g., different indentation time or force), but alloy processing introduces the most variability across samples. Peak hardness typically varies depending on grain orientation, as well as grain size and precipitate size. Although processing parameters (e.g., aging time and temperature) were collected for creep results, they were not collected for the hardness results. Thus, trying to assign a single peak hardness value to an alloy should be treated with at least 50 HV error.

Yield strength values include single crystal and polycrystal, tension and compression, with a variety of strain rates. Strain rate is typically $\sim 10^{-4}$ s⁻¹, but this varies by research group. Additionally, some groups do not report strain rate, so the values which entered the machine-learning dataset include only composition, temperature, and yield stress. While yield strength prediction could be improved by including microstructural features, since creep prediction was the primary focus, those parameters were beyond the scope of this dataset. Additionally, we have seen in our own work [175] that yield strength may vary almost 100 MPa for the same alloy, simply from the random orientation of grains for oligocrystalline samples (with only a few grains over their cross-section). This is probably an upper limit of error, and polycrystalline samples without texture can be expected to show repeatability within 10 MPa.

Like yield strength, **creep resistance** may also be highly dependent on grain orientation. In this case, we controlled for microstructural feature (γ' volume fraction, single- or polycrystal, aging time, etc.); however, there may still be differences in grain orientation between nominally

identical samples. This effect is further exacerbated by rafting (γ' microstructure evolution, which depends on crystal orientation, lattice misfit, and load direction). Bocchini et al. reported 1-2 orders of magnitude variation of steady-state creep rate within the same Co-9.5Al-7.5W alloy depending on their rafting state [8]. In our unpublished work, the largest difference between two identical creep samples was a tenfold difference in creep rate (at a given stress), with typical values being ~1.5-2x different. Considering the various sources of creep data, error bars for minimum creep rate are conservatively taken as $\pm 1/3$ order of magnitude ($\pm 33\%$), so for example $6 \pm 2 \cdot 10^{-8} \text{ s}^{-1}$.

In cases where supporting data were not reported (e.g., reporting an alloy as “homogenized” but without specifying temperature), we have used a likely value based on factors such as solvus temperature or experimental procedures used in other literature from the same research group. Since γ' **volume fraction** is an especially powerful predictor of creep life, in cases where the authors did not report volume fraction, but did include SEM images, we have visually estimated the volume fraction to the nearest 25% (i.e., choosing one of the four values of 25, 50, 75 and 100%). If SEM images were also absent, we have omitted the creep measurement from the dataset. In instances where samples were slow-cooled from the solutionized state, the aging temperature was reported as 50 °C. Additionally, we have not considered the volume fraction of deleterious phases (e.g., B2, TCPs) because of inconsistent reporting methods in the literature. High volume fractions of TCPs reduce γ' volume fraction and may increase creep rates via cavitation. Alloys with TCPs present in polycrystalline samples may also be TCP-free in single crystal samples. Thus, our model is particularly useful for alloys which have no additional phases beyond γ and γ' .

Using the model to predict the volume fraction of an alloy which does not have γ' will most likely result in a false positive value, since the dataset includes almost no examples of such alloys.

When collecting plot data using the WebPlotDigitizer, the program introduces a base error of ~ 2 pixels. Despite this, it displays a high level of precision by default. Since the precision does not affect the machine-learning results, we have not rounded values to reflect realistic measurement precision. Additionally, the program adds another avenue for human errors such as mistyping an axis label (e.g. reporting temperature in K instead of $^{\circ}\text{C}$), or from situations where the Figure axes were potentially misleading (e.g. having major ticks which slightly misalign with the top and bottom of the graph). While we were careful when collecting these data and used statistical tools to look for gross errors, it is inevitable that some mistakes were introduced when digitizing thousands of datapoints by hand.

We also note that the published papers themselves, even in reputable journals, exhibit an astonishing frequency of numerical errors. For alloys which reported the concentration of all elements, rather than leaving Co as “balance,” the total frequently did not sum to 100%. There are several instances where the reported lattice parameters for γ and γ' do not equate to the reported misfit. We also found instances where a figure, or section title, incorrectly labelled an alloy, and we had to use context to assign the alloy under consideration.

6.4 Computational Methods

The initial machine-learning design involved:

1. Literature data collection of alloy composition and creep stress, temperature, and steady-state strain rate (as described above).
2. Application of elemental descriptors based on alloy composition.
3. TCNI-11 CALPHAD predictions of diffusivity, volume fraction, solidus, liquidus, and lattice misfit.
4. Splitting data into 90% training set and 10% test set
5. Applying a machine-learning algorithm to the training set, predicting the result (time to 1% strain under steady-state creep at a particular temperature and stress) on the test set, and comparing the predicted and experimental results.

In this initial model, we used four different sets of chemical descriptors (JARVIS [176], Magpie [177], CFID [178], and basic elemental fraction) and three different regression models (Gradient boosting, random forest, and linear regression). Optimizing for low mean-squared error (MSE), we found best results using Magpie descriptors in conjunction with a random forest regressor and we thus have continued the rest of the modeling with this combination.

As described in the section “Data Collection Methods,” in addition to data strictly pertaining to creep, we collected data on properties which may influence creep, or are correlated with creep. Originally, we planned to use properties which could be predicted by CALPHAD. For example, we would use solidus temperature as in input to the creep regressor. If the solidus was reported in the literature, we use the experimental value. If the solidus was not reported, we use the CALPHAD-predicted value.

Unfortunately, the CALPHAD database designed for Co-based superalloys [179] did not have enough elements; using this would require discarding 2/3 of an already small dataset due to missing elements. The database designed for Ni-based superalloys, TCNI-11, showed poor prediction accuracy, as shown in Fig. 6-1.

Thus, we created “intermediary” ML models. Using the same method as previously described, we collected literature data to train models on additional properties, and used random forest regressors to predict those properties, comparing them against a 10% test data. Since we were not reliant on CALPHAD, we chose properties that correlate closely with creep (e.g., high temperature yield strength) or had abundant data (e.g., hardness). In total, we developed seven models to predict (i) lattice misfit, (ii) solvus temperature, (iii) solidus temperature, (iv) liquidus temperature, (v) γ' volume fraction, (vi) peak hardness, and (vii) yield strength as a function of temperature. Beside improving creep predictions, each of these predictions is valuable in their own right: for example solvus temperature puts an upper bound for the creep temperature, and lattice misfit correlates strongly with coarsening behavior. However, since any experimental value is still more trustworthy than its ML-predicted counterpart, if an experimental value exists, it supersedes the ML-predicted one. Note again that the intermediary model which predicts volume fraction should not be used to predict the volume fraction of an unknown alloy, although it may predict how the volume fraction of known γ/γ' alloy changes with aging temperature.

The last influence from CALPHAD was the effective diffusivity of each alloy. However, since we found that the impact of the effective diffusivity on creep prediction was essentially nil, we completely eliminated it from the current iteration of the model so as to increase the

accessibility of the program, and to allow its use without requiring any proprietary software. The model can easily accommodate additional data from CALPHAD, if the data are trustworthy, but the model presented here does not include any CALPHAD inputs.

Finally, we implement our version of Liu et al.'s "Divide-and-Conquer" approach. Using alloy composition, magpie descriptors, processing parameters (i.e., solutionizing temperature and time, 1st step aging temperature and time, 2nd step aging temperature and time), test conditions (i.e. temperature, compression/tension), microstructure (i.e., polycrystal/single crystal, and γ' volume fraction), and results from the intermediary ML models, we k-cluster each alloy into k groups. Each group is separately trained on their own random forest regressor. Test data are then assigned to one of the k groups, and predicted with the corresponding regressor. This step was implemented to capture broad differences in alloys. For example, conventional wisdom suggests that a single crystal Co-Al-W alloy would have different creep mechanisms activated compared to a polycrystalline Co-Ti alloy; k-clustering and fitting these with different regressors would thus lead to better fitting compared to a single regressor that applies to both.

In summary, our machine-learning creep prediction model follows the following steps:

0. Build intermediary ML models to predict values of solvus-, solidus-, liquidus temperatures, lattice misfit, peak hardness, and yield strength.
1. Add these ML-predicted values to the creep input dataset and unless experimental values exist.
2. Divide the data into k groups using K-means clustering.
3. Train a random forest regressor for each of the k groups.

4. Divide the test data into the same k groups, applies the relevant regressor, and predicts the time to 1% strain under steady-state creep for a given temperature and stress.
5. Repeat all steps (100 times in total) with a different test/training split, to further assess the robustness of the predictions and to ensure that our assessment of the model's accuracy is not influenced by an outlier test/training split.

A visual schematic of the computational flow, and the state of the database, is shown in Fig. 6-2. When we have tuned the model to provide the best prediction on the test data, we can use data validation to predict the creep properties of alloys that were never entered into the database. Additionally, we can generate a matrix of compositions in a design space which we want to explore, and we can use the model as a guide to assess if various compositions have a promising predicted creep response that would be worth validating experimentally.

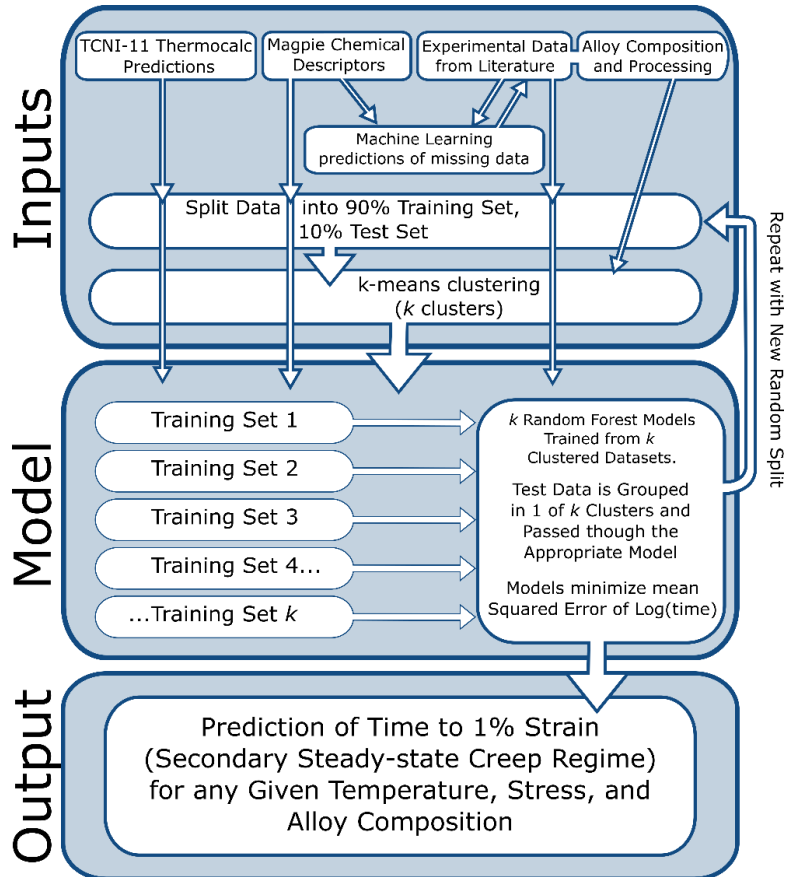
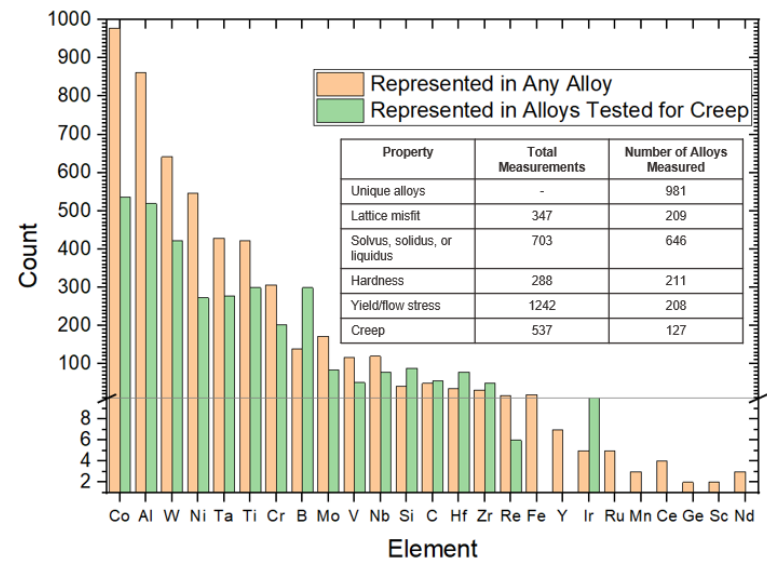


Figure 6-2. (top) Elements and properties represented in the database, (bottom) Schematic showing the model design.

6.5 Results and Discussion

The database was split into three sections: 90% of the literature data was used to train models (“training data”), and 10% of the literature data was not used to train the model but held back to test how well the model performs (“test data”). Finally, we collected 16 new experimentally tested alloys, which were not added to the database at all (“validation data”).

The validation data consists of 16 alloys studied in this thesis project:

- 4 W-containing alloys which contain Fe (no creep has yet been reported for Fe-containing alloys),
- 6 alloys which are both W-free (uncommon in the literature) and Fe-free,
- 6 alloys which are W-free but Fe-containing.

The compositions for validation data were chosen to be very different from any other alloys reported in the literature, and expected to be largely unintuitive to human researchers, assessing to what extent the program can use chemical descriptors and intermediary properties to predict compositions which are very much outside the range of the database.

We also present figures for each of the six intermediary models in a consistent format, as described below. The “**test fit**” figures show the result of the ML-predicted values of each data point, compared with the experimental values of the test data. These have a guide line ($y=x$); points which fall on the line are points where the predicted value exactly matches the experimental value. The fitness function for the models is mean squared error (MSE) which is the square of the distance of each predicted value to its experimental value. Each test fit plot has an associated MSE, printed at the top of the figure. We have generated 100 of each fitting

plot to account for different test/training splits—here, we only show the plot corresponding to the first seed, “seed 0.”

We also present “**feature importance**” figures. These show all the inputs for a particular model, as well as the relative importance of each input feature, on a scale from 0 to 1.

When predicting intermediary properties for the creep dataset (where we typically do not have an experimental measurement to compare), we still try to account for the variability between different splits of the test and training data, so we use all 100 models previously trained with a different 90% subset of the training data. In our “**standard deviation**” figures, we plot the standard deviation of those 100 predictions, for all creep points. We then train a model with 100% of the property data. This additional, 101st prediction is our “final value” which we use going forward. In our “**accuracy**” figures, we subtract the average of the previous 100 values from the 101st “final” value. Both “**standard deviation**” and “**accuracy**” plots address the reproducibility of the ML prediction when the training data is varied.

6.5.1 ML Prediction of Lattice Misfit

The model for lattice misfit was trained on alloy composition, magpie descriptors, and test temperature. Fig 6-3 shows the predicted lattice misfit after training the model.

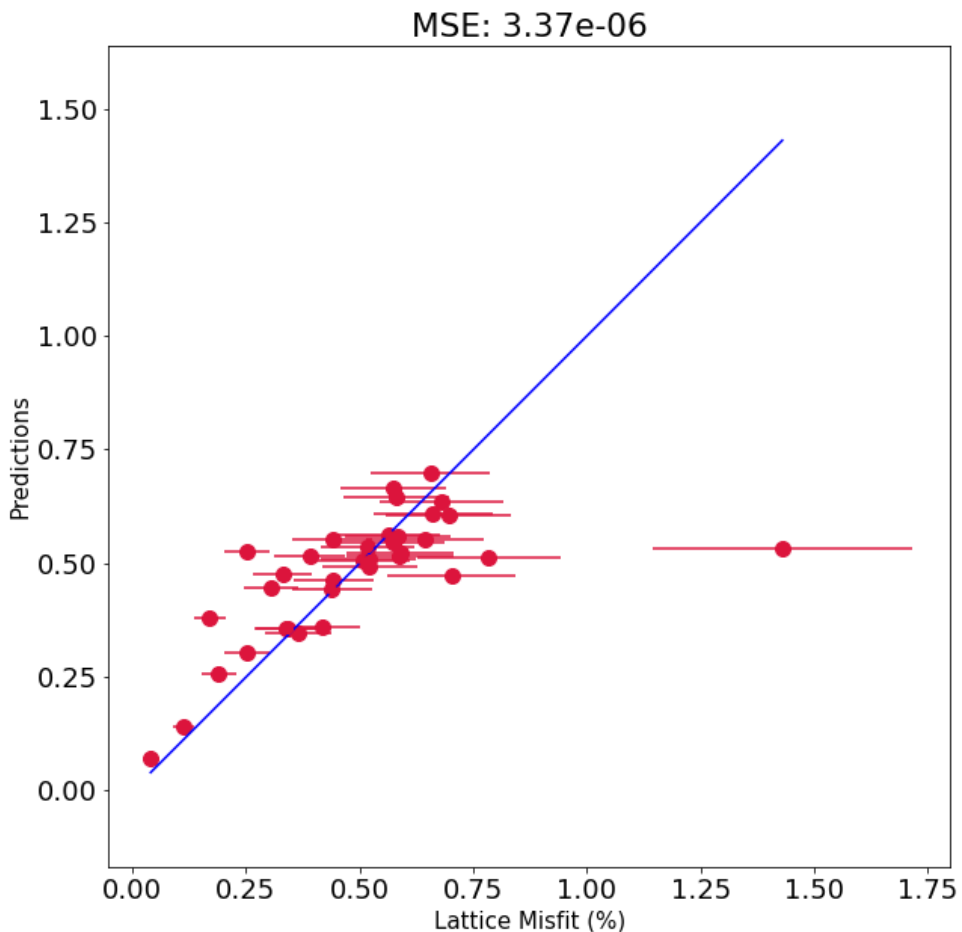


Figure 6-3. Test fitting of the predicted lattice misfit value (%) vs the experimental misfit value. Error bars correspond to our estimated reproducibility of this experimental measurement, taken as $\pm 20\%$ of the misfit value.

Note that the test fit (“seed 0”) shown in Fig 6-3 has one major outlier—this is not unexpected, considering the few major outliers overall, as shown in the Fig 6-4b histogram. Aside from this outlier, nearly all the test points fall within error of the experimental measurements, suggesting that this model performs very well.

The importance of the various features used to fit the misfit regressor are given in Fig 6-4a. As expected, the elemental compositions play a major role, especially Ta and Al. Temperature is also a strong predictor, as expected.

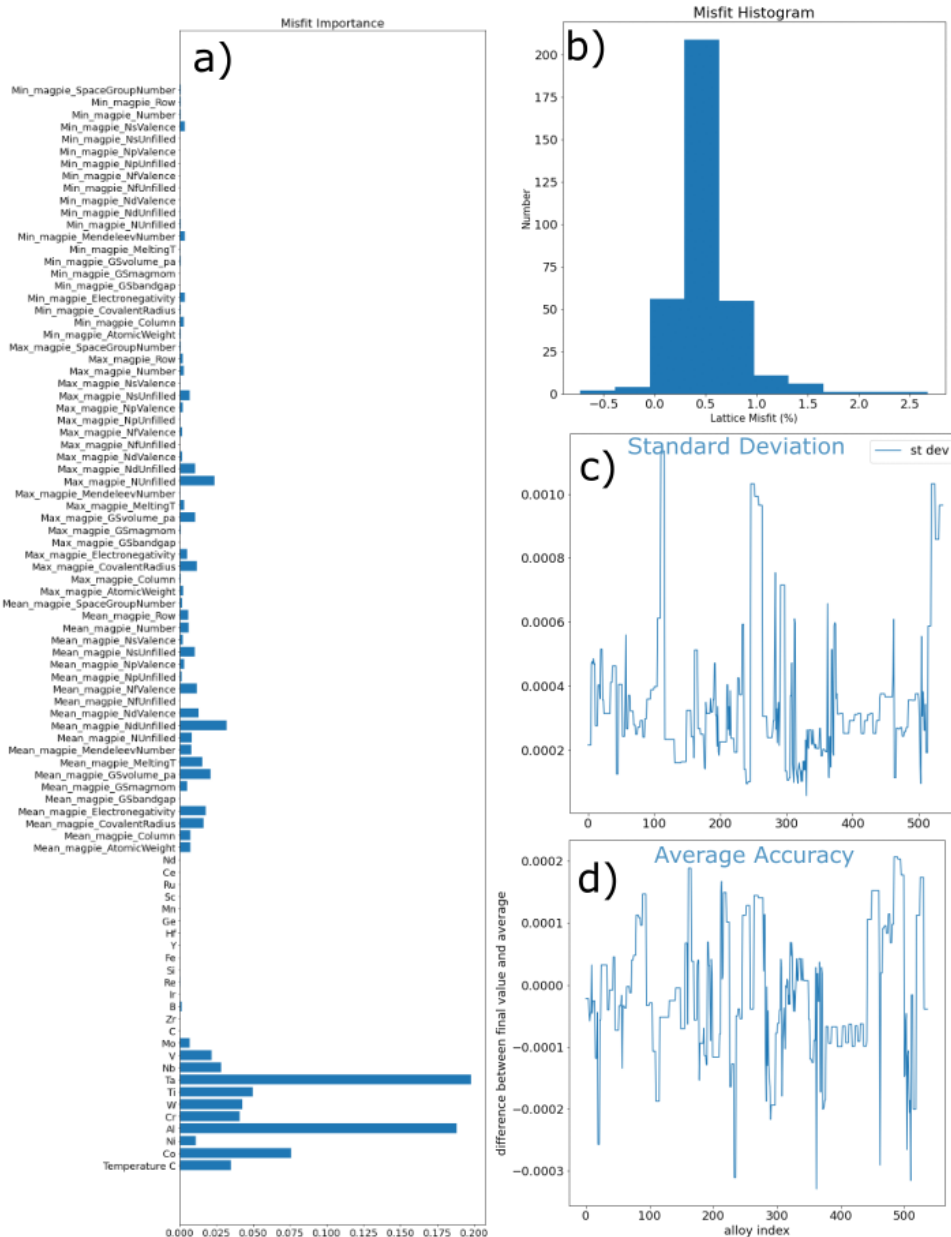


Figure 6-4. Plots for (a) misfit feature importance, (b) histogram of database measurements, (c) standard deviation, and (d) average accuracy plot.

The standard deviation and accuracy values shown in Fig 6-4c and 6=4d are well within the 0.2% variation we would expect in experimental measurements, further suggesting that this model has little room for improvement.

6.5.2 ML Prediction of Solvus Temperature

The model for solvus was trained on alloy composition and magpie descriptors. Fig. 6-5 shows the predicted solvus values after training this model.

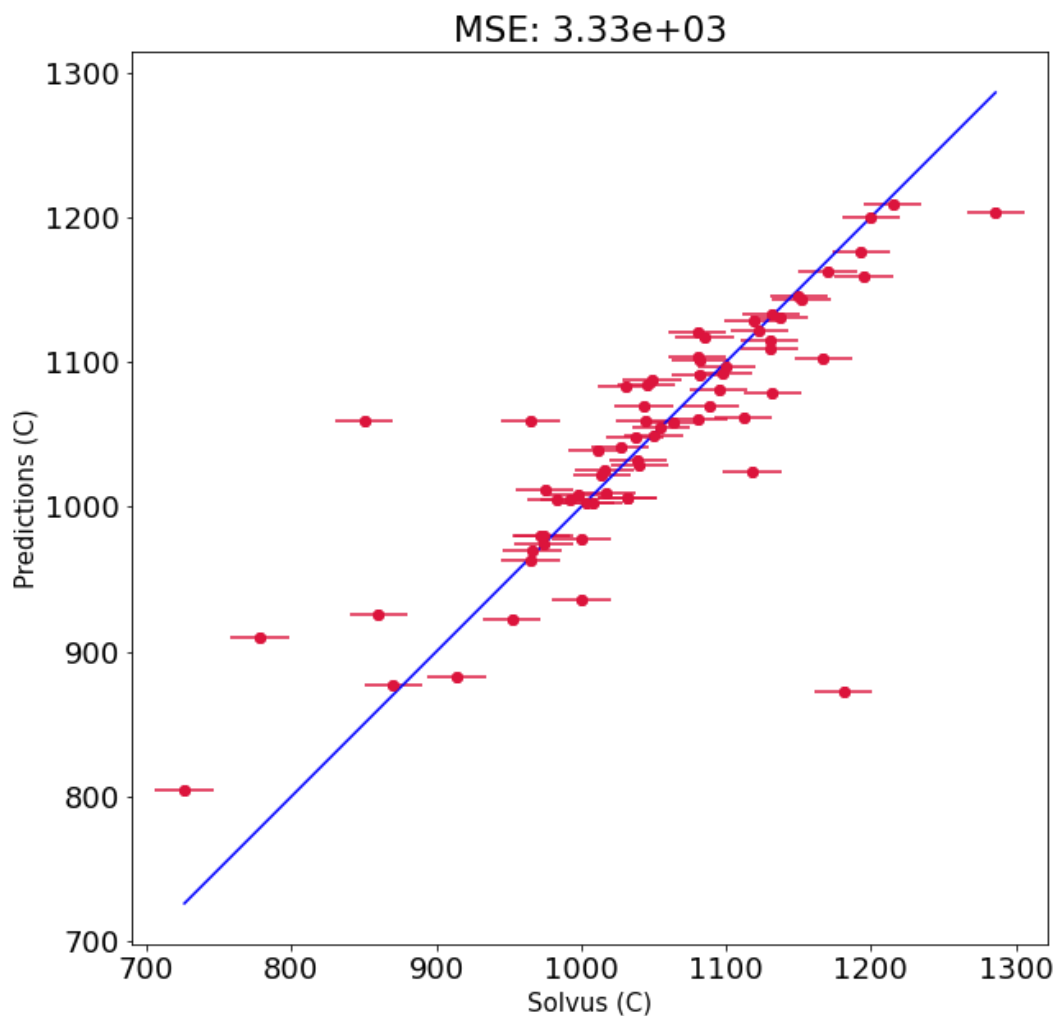


Figure 6-5. Test fitting of the predicted solvus temperature vs the experimental value. Error bars correspond to our estimated reproducibility of this experimental measurement, taken as ± 20 °C.

Although there are several major outliers (>100 °C different from the experimental value), most of the values fall within the estimated error of the experimental solvus (± 20 °C).

The importance of the various features used to fit the solvus regressor are given in Fig 6-6a. As expected, the elemental composition plays a major role, especially Ta, Ti, and W; this is consistent with these elements being the highest-melting elements with the widest composition range.

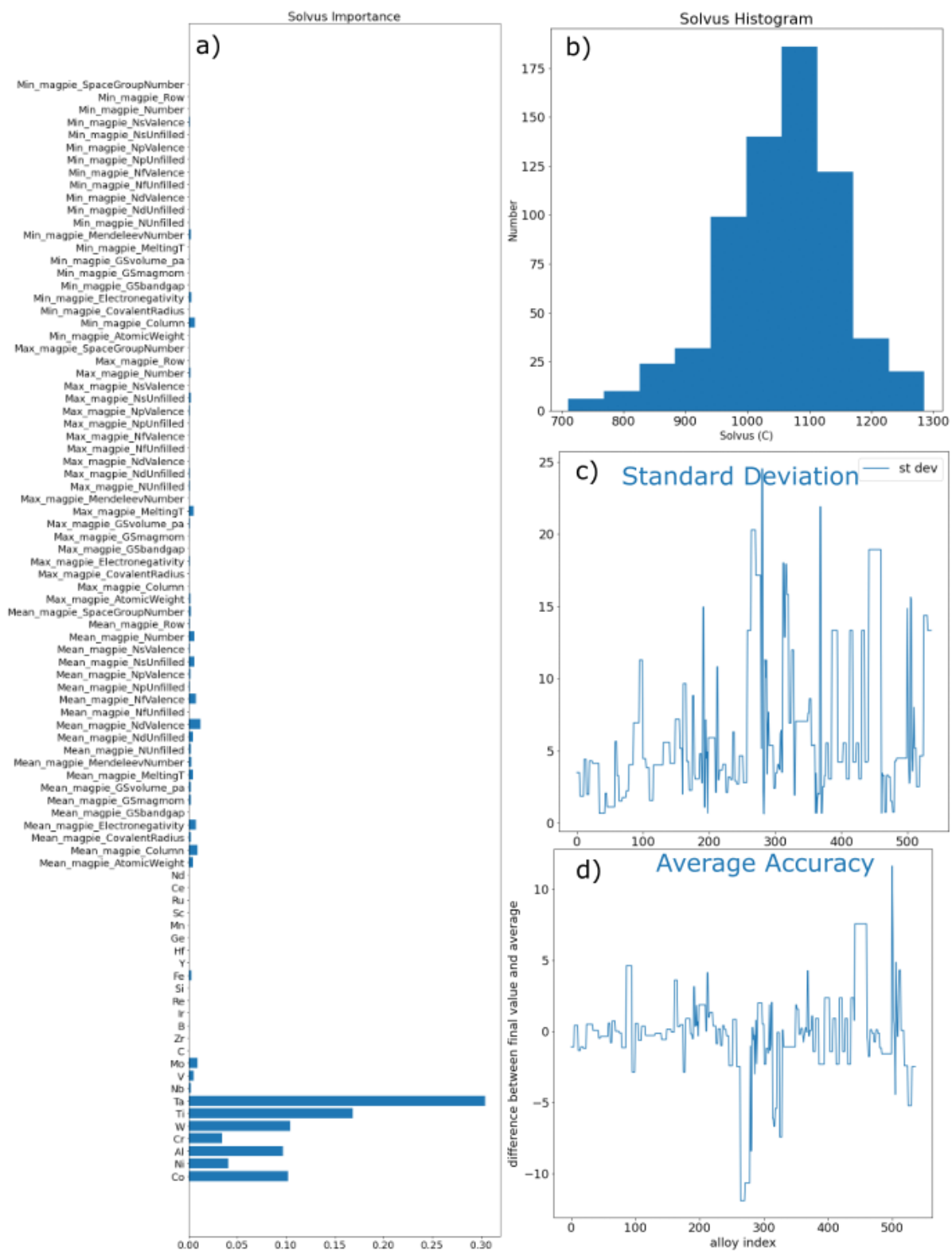


Figure 6-6. Plots for (a) solvus feature importance, (b) histogram of database measurements, (c) standard deviation plot, and (d) average accuracy plot.

While the average accuracy in Fig. 6-6 d) is typically below 10 °C, and therefore within the estimated experimental error, the standard deviation frequently exceeds 10 °C and can reach values as high as 25 °C. Overall, the model to predict solvus is reasonably accurate.

6.5.3 ML Prediction of Solidus Temperature

The model for solidus was trained on alloy composition, magpie descriptors, and solvus temperature. Fig. 6-7 shows the predicted solidus values after training this model.

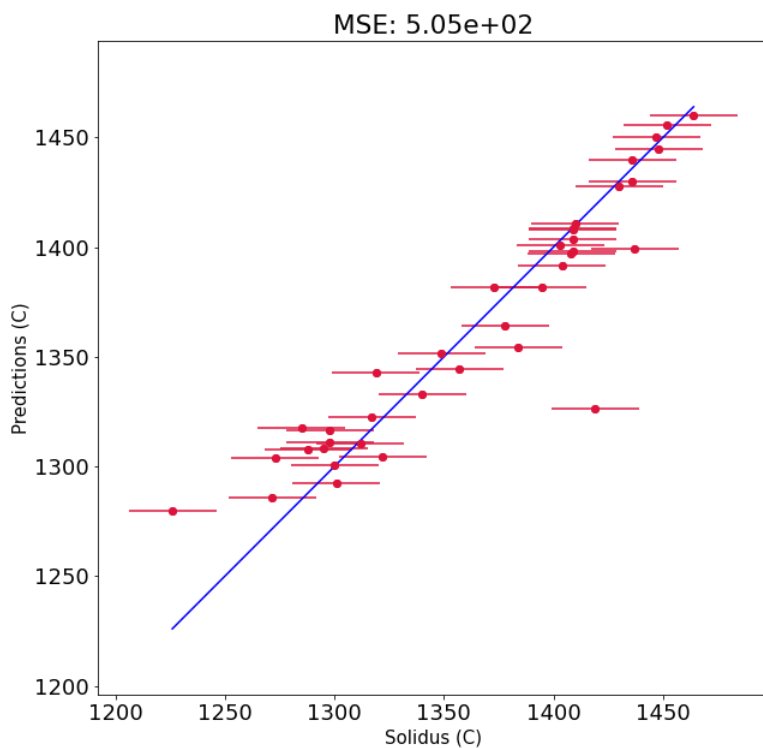


Figure 6-7. Test fitting of the predicted solidus temperature vs the experimental value. Error bars correspond to our estimated reproducibility of this experimental measurement, taken as ± 20 °C.

There are two large outliers, but nearly every prediction falls within 20 °C of the measured solidus temperature. Fig. 6-8 a) shows that Ti is very impactful in predicting the solidus temperature, followed by W and by the previously-predicted (or known) solvus temperature. These three feature stand far beyond any other elements or chemical descriptors.

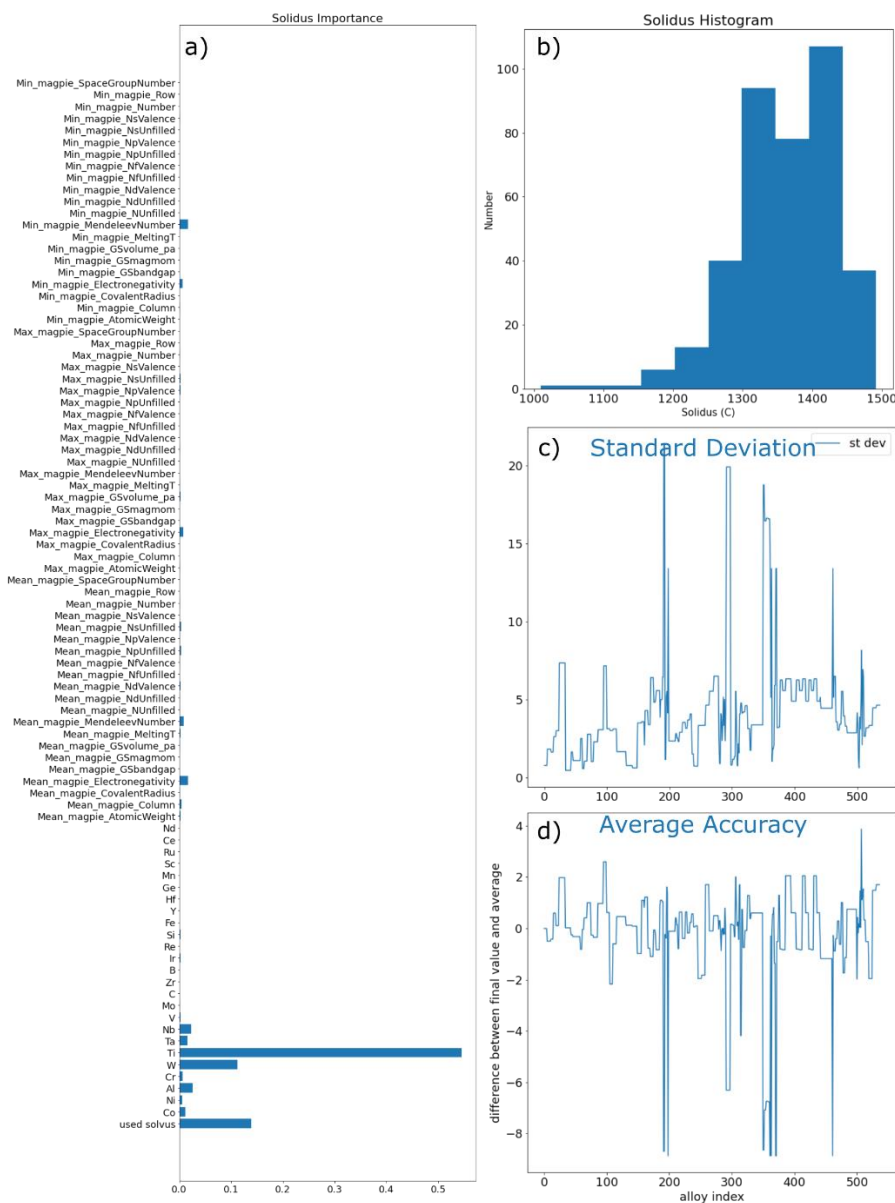


Figure 6-8. Plots for (a) solidus feature importance, (b) histogram of database measurements, (c) standard deviation plot, and (d) average accuracy plot

As shown in Fig. 6-8, the average accuracy is $< 10^{\circ}\text{C}$ —well within experimental error. The standard deviation can be as high as 20°C , which is higher than the expected standard deviation ($\sim 10^{\circ}\text{C}$) from repeatedly measuring solidus with the same experimental methods, but on-par with the deviation from measuring solidus with different experimental measurements (e.g., some

researchers measure on cooling, others measure on heating, and others may report the average of heating and cooling).

Overall, this intermediate prediction of solidus is as accurate as reasonably possible. Surprisingly, the solvus temperature was not the most important feature, perhaps due to the solvus prediction being less reliable.

6.5.4 ML Prediction of Liquidus Temperature

The model for liquidus was trained on alloy composition, magpie descriptors, solvus temperature, and solidus temperature. Fig. 6-9 shows the predicted liquidus values after training this model.

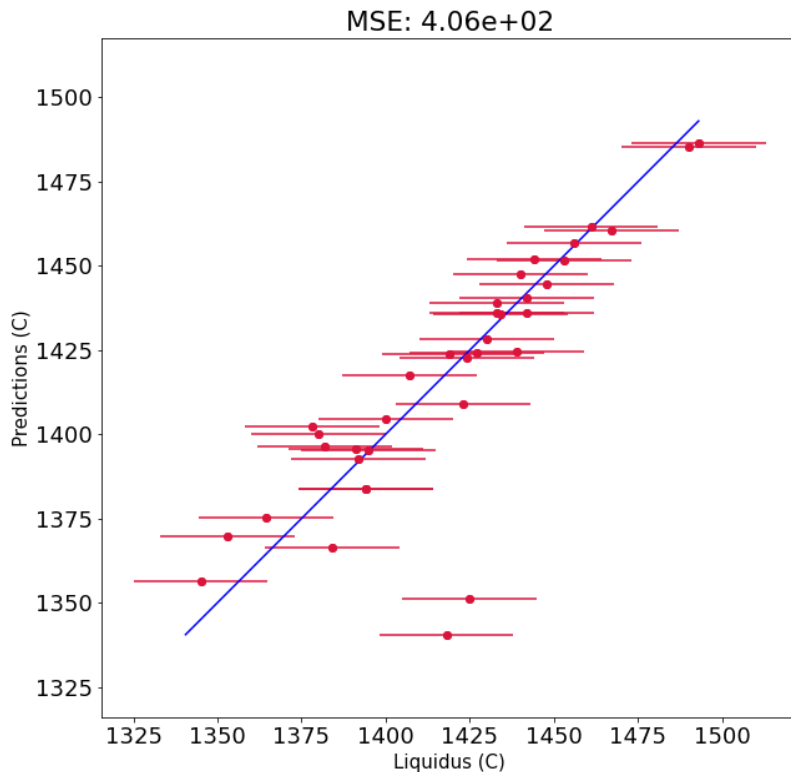


Figure 6-9. Test fitting of the predicted liquidus temperature vs the experimental value. Error bars correspond to our estimated reproducibility of this experimental measurement, taken as ± 20 °C.

Aside from two clear outliers, all other predicted test data falls within $\sim 20^\circ\text{C}$ of the experimental result. Once again, as shown in Fig. 6-10 a), Ti is the most influential element, followed this time by Al. However, by far the most important feature is the solidus temperature. This makes physical sense, as solidus and liquidus temperature are much more directly related to each other than to solvus temperature.

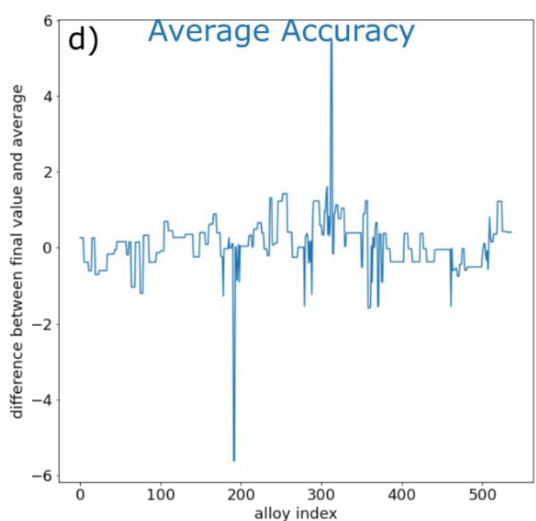
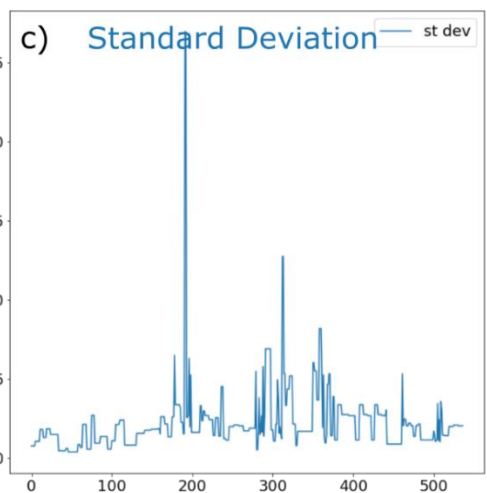
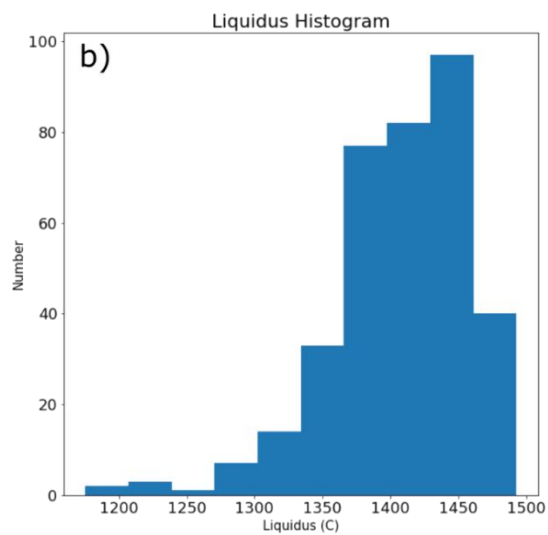


Figure 6-10. Plots for (a) liquidus feature importance, (b) histogram of database measurements, (c) standard deviation plot, and (d) average accuracy plot

The standard deviation and accuracy of the liquidus prediction are within 5 °C for most alloys, as shown in Fig. 6-10 b) and c). This is a very good experimental result, likely due to the close correlation between solidus and liquidus. In a previous iteration of this liquidus model, our MSE fitting function improved by over an order of magnitude by letting it use the solidus data.

6.5.5 ML Prediction of Volume Fraction

The model for γ' volume fraction (Vf) was trained on alloy composition, magpie descriptors, solvus temperature, solidus temperature, and liquidus temperature. Fig. 6-11 shows the predicted Vf values after training this model.

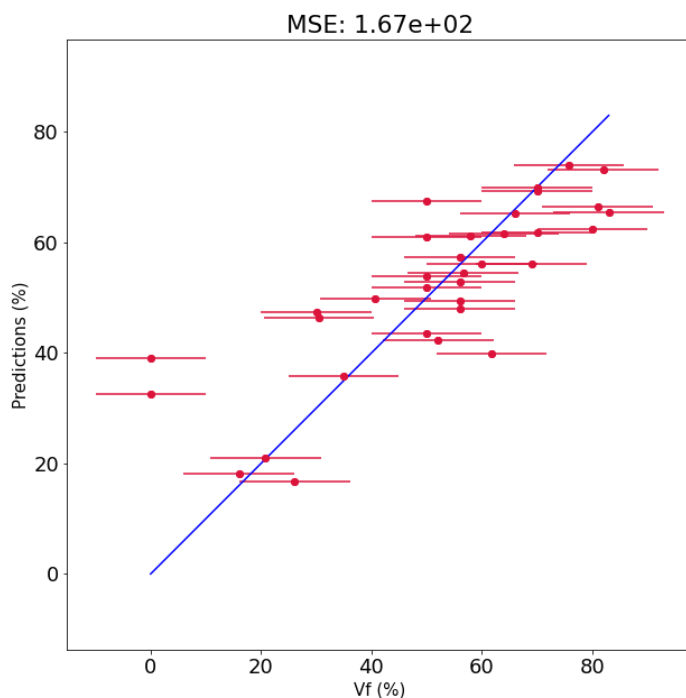


Figure 6-11. Test fitting of the predicted γ' volume fraction (Vf) vs the experimental value. Error bars correspond to our estimated standard deviation of experimental measurement on different nominally identical samples, taken as $\pm 10\%$.

Except for 2 cases, the predicted Vf was within 15% of the measured Vf. In both cases, the measured Vf was 0%, because the test temperature was higher than the solvus temperature. This model has recognized the correlation between solvus temperature and Vf, as shown in Fig. 6-12, but it does not correctly assign $V_f = 0$ in cases where the solvus temperature is lower than the aging temperature.

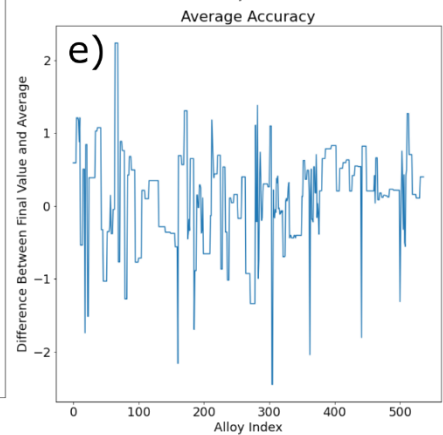
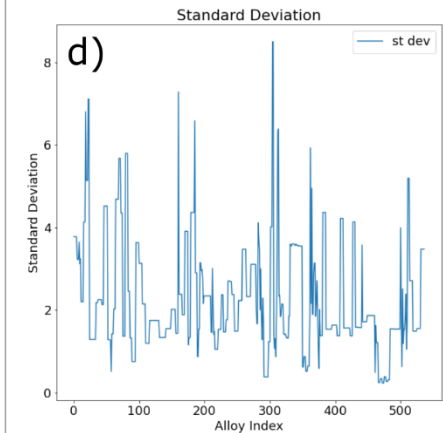
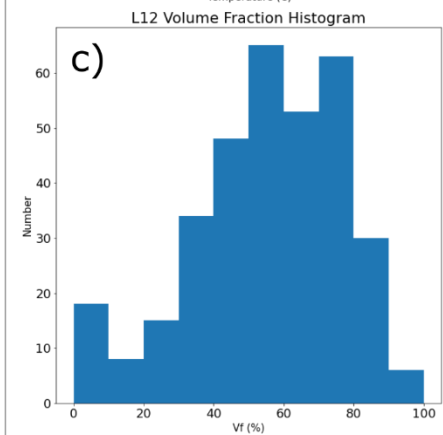
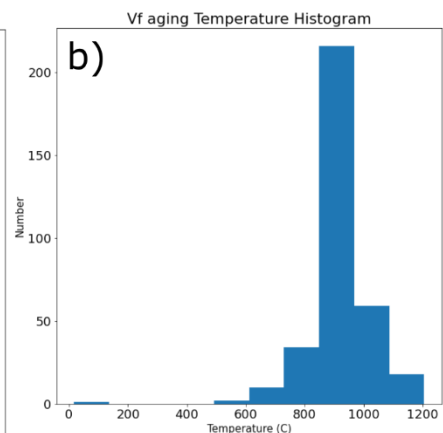


Figure 6-12. Plots for (a) creep feature importance, (b) and (c) histogram of database measurements, (d) standard deviation plot, and (e) average accuracy plot.

Fig. 6-12 shows the feature importance for Vf; as expected, the solvus temperature and aging temperature plays the largest role. Unfortunately, the model has not realized that Vf should go to zero when the aging temperature is higher than the solvus temperature, likely because this scenario only exists in a few instances in the database. However, by definition there cannot be γ' above the solvus temperature, so in the future we could automatically add many datapoints for each alloy which have Vf = 0% at temperatures higher than the solvus. This addition may help the model recognize the physical connection between these values.

6.5.6 ML Prediction of Hardness

The model for peak hardness was trained on alloy composition and magpie descriptors. Fig. 6-13 shows the predicted hardness values after training this model. This set of test data shows one major outlier, and many points that fall outside the estimated experimental error (± 50 HV), but still correlate with their experimental measurement. The hardness experimental data are the least reliable in our database, because hardness is physically influenced by various uncaptured variables such as grain size and texture.

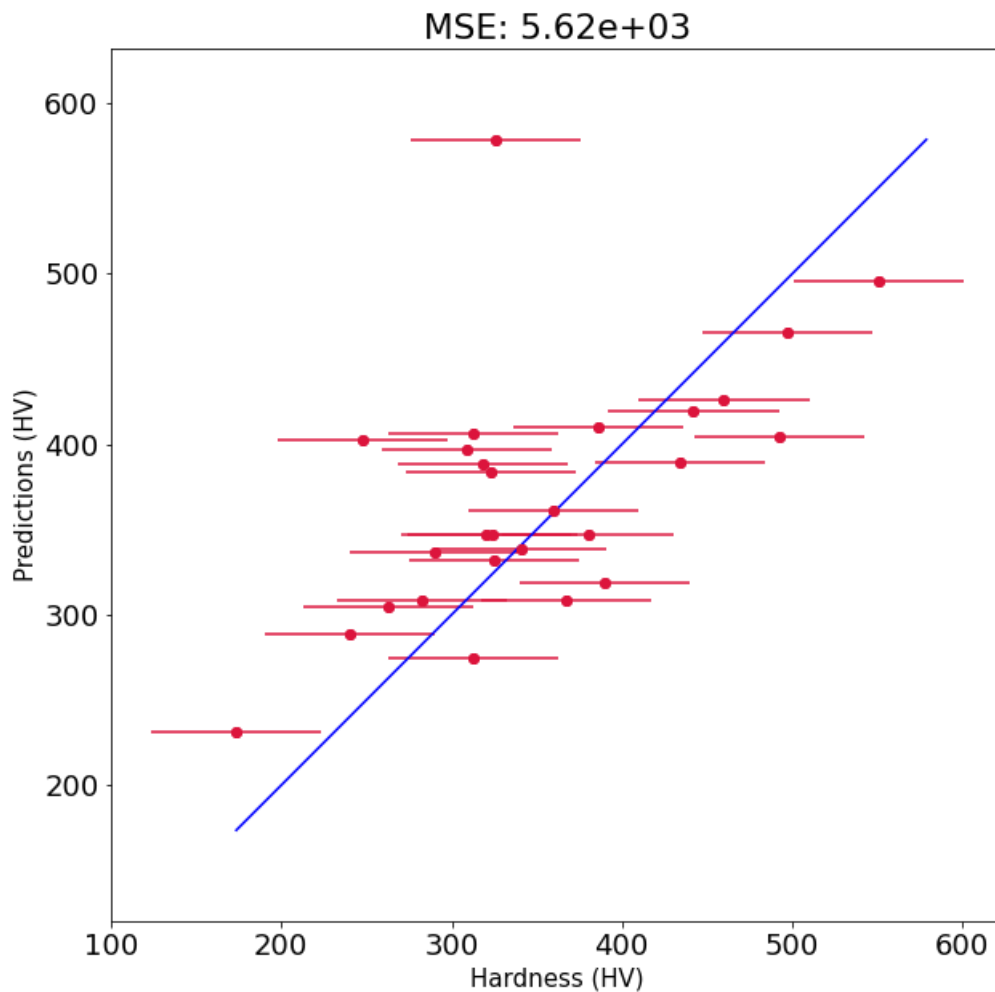


Figure 6-13. Test fitting of the predicted peak hardness vs the experimental value. Error bars correspond to our estimated reproducibility of this experimental measurement, taken as ± 50 HV.

In Fig. 6-13 a), it is apparent that none of the features are especially important. Co, Al, and W slightly lead the other features, reflecting the fact that the database mostly includes alloys in the Co-Al-W family. Likely, this model recognizes that these elements are more influential because it is indirectly capturing the effect these elements have on the volume fraction of γ' .

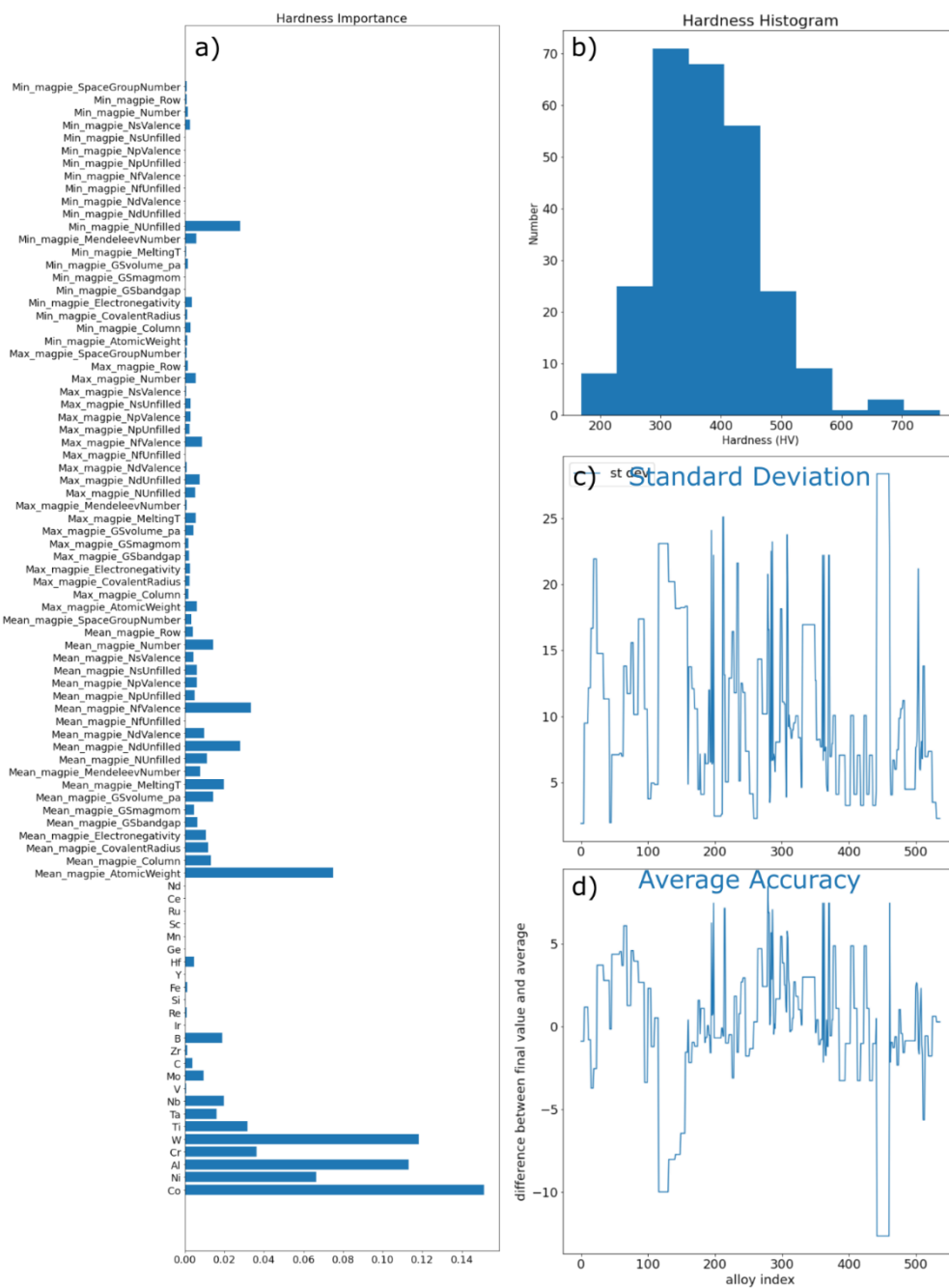


Figure 6-14. Plots for (a) hardness feature importance, (b) histogram of database measurements, (c) standard deviation plot, and (d) average accuracy plot

Fig. 6-14 b) and c) show a variance and standard deviation that, while high, is on par with experimental variation on samples with different processing histories. However, this variance is

still higher than the variation expected from measuring hardness on different grains of the same sample.

The hardness model does not perform well enough to directly predict an alloy's peak hardness, but it may still provide a useful feature for the ultimate target, creep rate prediction. If the data generated by this model are not useful for predicting creep, the hardness will be assigned a low importance. Indeed, as shown in Fig. 6-19, hardness is the least important of all the intermediary models; however, it is still more important than most of the chemical descriptors.

6.5.7 ML Prediction of Yield Strength (at Various Temperatures)

The model for yield strength was trained on alloy composition, magpie descriptors, test temperature, lattice misfit, and solvus, solidus, and liquidus. Fig. 6-15 shows the predicted yield strength values after training this model. While there are several points with predictions very far (>100 MPa) from the experimental measurement, most data fits closely.

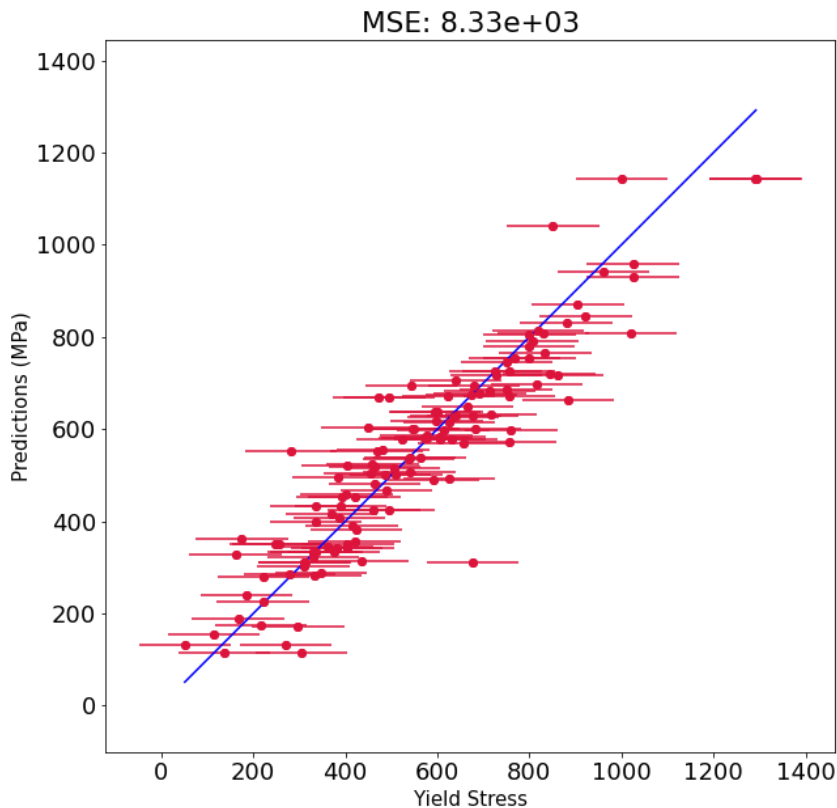


Figure 6-15. Test fitting of the predicted yield strength vs the experimental value. Error bars correspond to our estimated reproducibility of this experimental measurement on different nominally identical samples, taken as ± 100 MPa.

As shown in Fig. 6-16a, temperature at which the yield stress is measured has by far the largest importance, as expected physically. The magpie “minimum electronegativity” also showed surprisingly large importance; our hypothesis for this is that the minimum electronegativity corresponds with the likelihood of the alloy to be “designed for mechanical properties.” This value is the smallest electronegativity of any element, divided by the sum of all elements’ electronegativities. Thus, this value will be very low for alloys which have certain elements (C, B, or Si have low electronegativities and are known to strengthen grain boundaries even in very small

concentrations) and alloys with many different elements (solid solution strengthening). Solvus temperature is about as important as solidus and liquidus temperature, and lattice misfit.

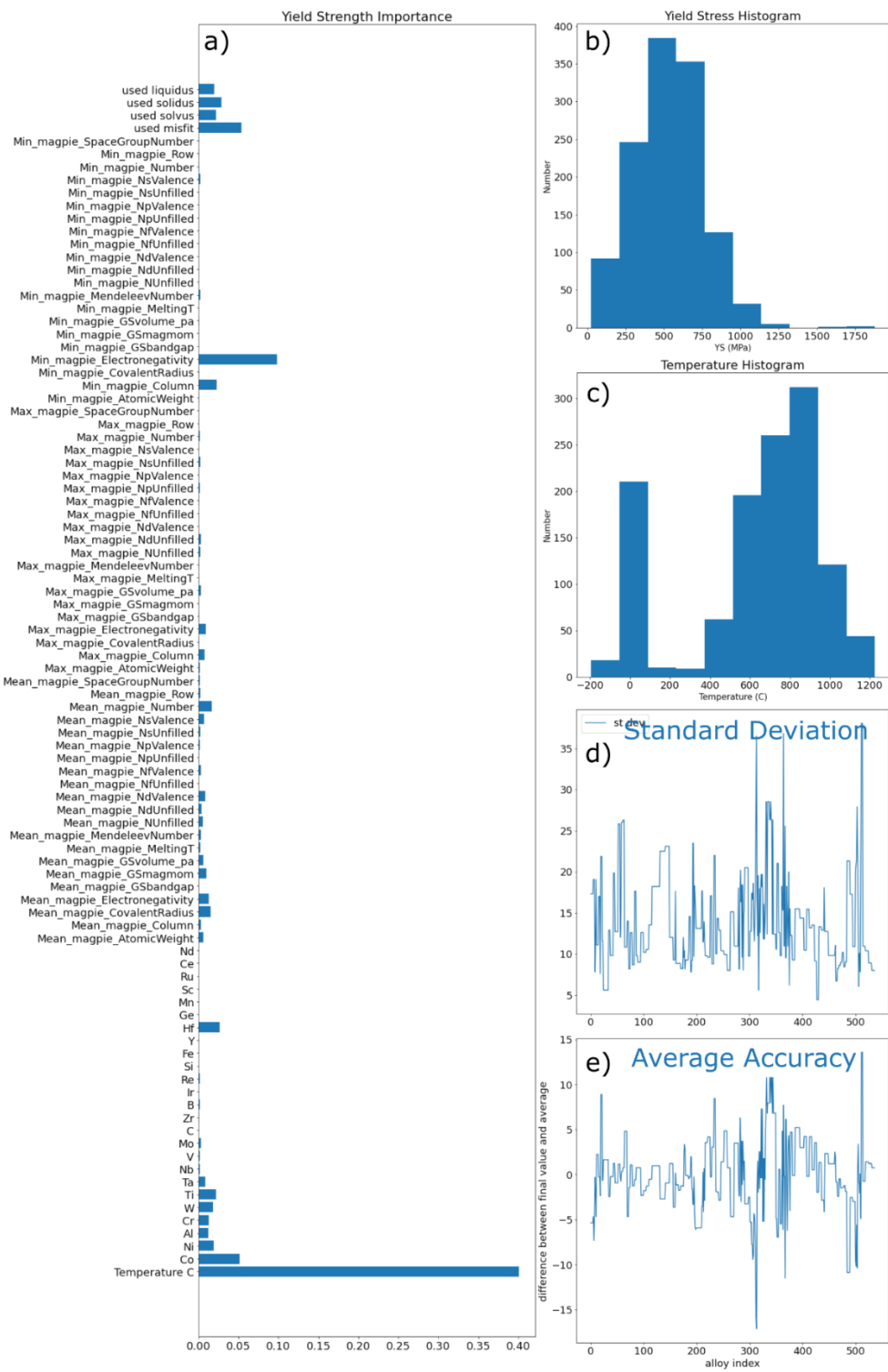


Figure 6-16. Plots for (a) creep feature importance, (b) and (c) histogram of database measurements, (d) standard deviation plot, and (e) average accuracy plot

The accuracy and standard deviation for the yield strength prediction is mostly on par with expected sample-to-sample experimental variation.

6.5.8 Effect of K-means Clustering

The K-means clustering algorithm used alloy composition, magpie descriptors, processing parameters (i.e., solutionization temperature and time, 1st step aging temperature and time, 2nd step aging temperature and time), test conditions (i.e., temperature, compression/tension), microstructure (i.e., polycrystal/single crystal, and γ' volume fraction), misfit, solvus, solidus, liquidus, peak hardness and yield strength (and associated test temperature).

We display three types of “elbow plot,” which are visual indicators of the cluster quality. The Within Cluster Sum of Squares measures the n-dimensional distance between each point and the cluster centroid. The closer points are, the better they fit in a group. Necessarily, the more clusters exist, the closer together each point and corresponding centroid must be. Data which are easily clustered typically shows an “elbow” or plateau, beyond which the sum of squared distance doesn’t significantly improve.

Another measure of cluster quality uses the Silhouette score which ranges from -1 to +1 and considers the distance between points in a cluster and the distance between other clusters. Good clustering has points that are close to other points in the same cluster, and far from points in other clusters, which would correspond to a silhouette score closer to 1.

A third measure of cluster quality, the Calinski-Harabasz Index [180], also measures how close each point is to its own cluster compared to other clusters. A higher CH index indicates more distinct clusters, and there is no maximum value.

The three cluster metrics are shown in Fig. 6-17.

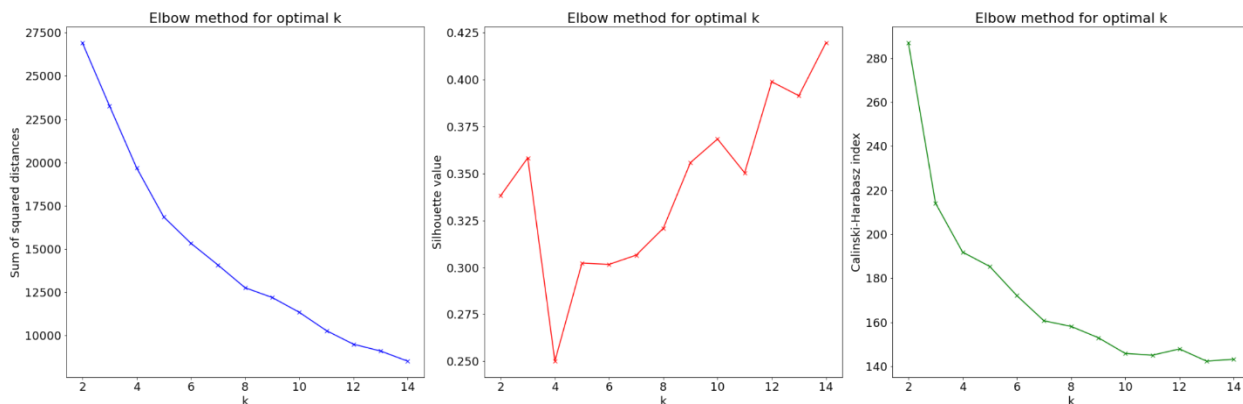


Figure 6-17. Plots of cluster quality vs k value. (left) sum of squared distances (lower is better); (middle) Silhouette value (closer to 1 is better); (right) Calinski-Harabasz index (higher is better).

There is no clear elbow, so there is no obvious number of groups to cluster into. Thus, we have run the program 100 times each, varying the cluster from 1 to 7 groups. As discussed previously, the training data is used to decide clustering parameters. Each group is trained on its own regressor. Test and validation data are assigned a cluster based on the same parameters, then predicted using the corresponding regressor. Having more groups allows regressors to capture different behaviors from the different subfamilies of Co-based superalloys, but each group is then trained on less data, resulting in a less accurate regressor.

6.5.9 ML Prediction of Steady-State Creep Rate

The model for creep time was trained on alloy composition, magpie descriptors, test temperature, lattice misfit, and solvus, solidus, and liquidus. Fig. 6-18 shows the test fit for creep with 5 clusters, which had the lowest MSE on the first random seed.

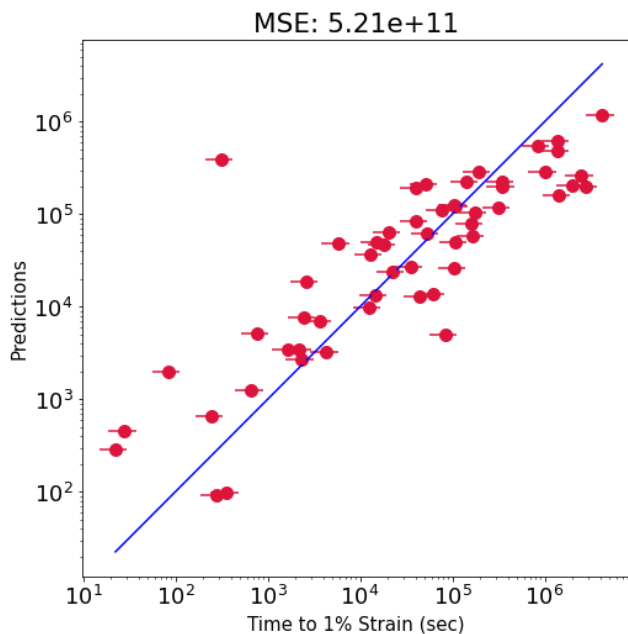


Figure 6-18. Double logarithmic plot of time to 1% steady-state creep strain (which is inversely proportional to a strain rate) vs the experimental value. Error bars correspond to our estimated reproducibility of this experimental measurement, taken as $\pm 33\%$ of the value.

However, the number of clusters actually made almost no difference to the final prediction fitness. Fig. 6-19 shows the variation in MSE over 100 different test/training splits, for clusters between 1 and 7.

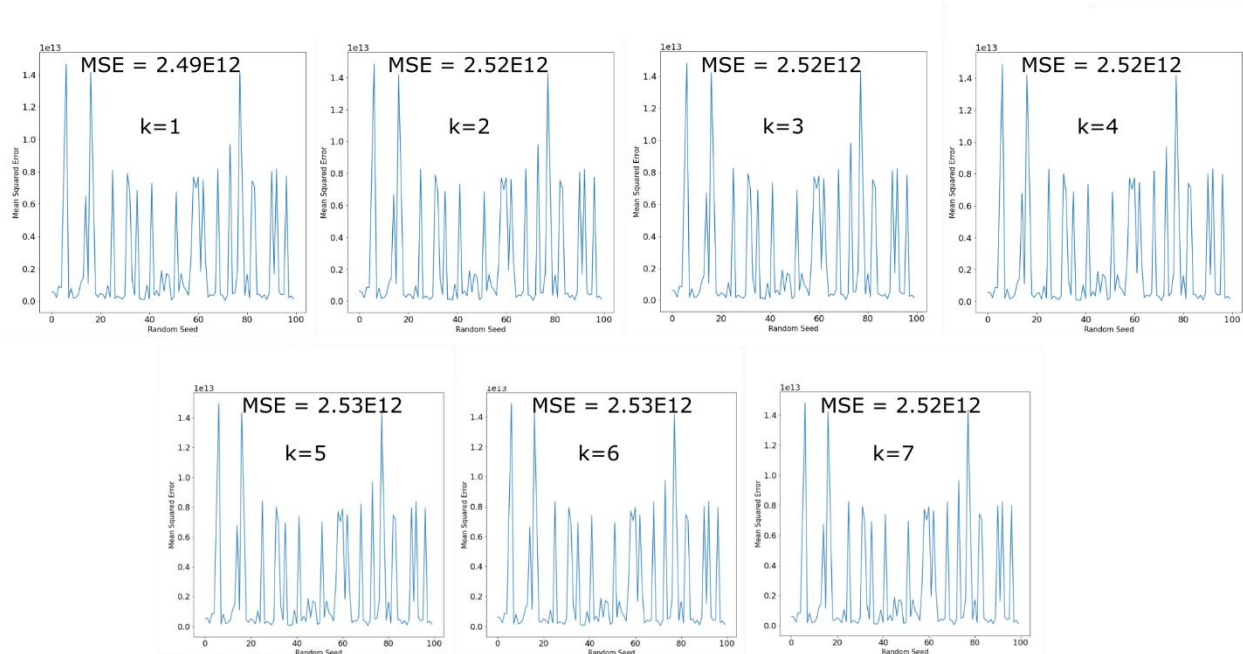


Figure 6-19. Plots of mean-squared error (MSE) vs seed number for 100 seeds randomly creating test/training data splits.

The average MSE varied by $<2\%$ between the models with different cluster sizes. The model with a single cluster has the lowest MSE; more importantly, it has the largest dataset. The fact that k -clustering does not improve the fit suggests that the various families of Co-based superalloys creep under identical mechanisms, expected to be dislocation motion (power-law creep). We have continued with the non-clustered model because clustering brings no improvement, and a single model with the largest dataset gives the best chance to extract a relationship between elements which are present in the intermediary model dataset, but not the creep model dataset.

6.5.10 Data Validation

To test the robustness of the model, we predicted creep values for 16 recent Co-based superalloys investigated at Northwestern University by us and our collaborators. Specifically, we

chose superalloys with high amounts of Fe, which we recently studied in unpublished work. Iron appears sparsely in the database and no creep data were previously reported on any Fe-containing L1₂-strengthened Co-based superalloy. Thus, if the model is able to accurately predict properties for these alloys, it indicates that the addition of intermediary models and chemical descriptors allows the model to predict properties for alloys *far outside* the known composition space. Experimentally, researchers would still need to verify the γ' volume fraction, but microstructure high-throughput studies are much more feasible than creep high-throughput studies. Creep predictions could be improved if we let the model know experimental values for the intermediary properties, but we want to simulate a situation where a researcher only knows the composition and volume fraction.

The 16 alloys have compositions given in Table 6-1.

Table 6-1. Compositions of 16 alloys used for validation data, and not included in the database.

Label	Nominal Composition, at.%											
	Co	Fe	Ni	Al	Cr	V	Ti	Nb	Ta	B	W	Vf (%)
Fe-containing, W-free												
12Fe4Cr [175]	52.9	12	18	5	4	3	2	1.5	1.5	0.08	0	48
14Fe4Cr [175]	"	14	16	"	"	"	"	"	"	"	"	41
18Fe4Cr [175]	"	18	12	"	"	"	"	"	"	"	"	33
12Fe8Cr [175]	48.9	12	18	"	8	"	"	"	"	"	"	42
14Fe8Cr [175]	"	14	16	"	"	"	"	"	"	"	"	44
18Fe8Cr [175]	"	18	12	"	"	"	"	"	"	"	"	21
Fe-free, W-free												
10Ni4Cr [152]	72.9	0	10	5	4	3	2	1.5	1.5	0.08	0	32
10Ni8Cr [152]	68.9	"	"	"	8	"	"	"	"	"	"	44
20Ni4Cr [152]	62.9	"	20	"	4	"	"	"	"	"	"	37
20Ni8Cr [152]	58.9	"	"	"	8	"	"	"	"	"	"	45
0Fe4Cr [152]	52.9	"	30	"	4	"	"	"	"	"	"	49
0Fe8Cr [152]	48.9	"	"	"	8	"	"	"	"	"	"	45

Fe-containing, W-containing												
0Fe-W [181]	49.9	0	30	10	4	0	0	0	0	0.1	6	41
4Fe-W [181]	45.9	4	"	"	"	"	"	"	"	"	"	40
8Fe-W [181]	41.9	8	"	"	"	"	"	"	"	"	"	30
12Fe-W [181]	37.9	12	"	"	"	"	"	"	"	"	"	25

Fig. 6-20 shows the validation prediction of creep time for 120 combinations of temperatures (all 850 °C) and stress (200-500 MPa) on these 16 different alloys, which belong in a subfamily absent in the existing database. Creep validation was tested for the 16 alloys with inputs of (i) only composition, (ii) composition and volume fraction, and (iii) all intermediary quantities measured. Mean squared error of seconds to 1% steady-state creep decreased from 2.06×10^{10} to 1.69×10^{10} to 1.65×10^{10} , respectively. Thus, having real experimental volume fraction is especially important to obtain accurate results.

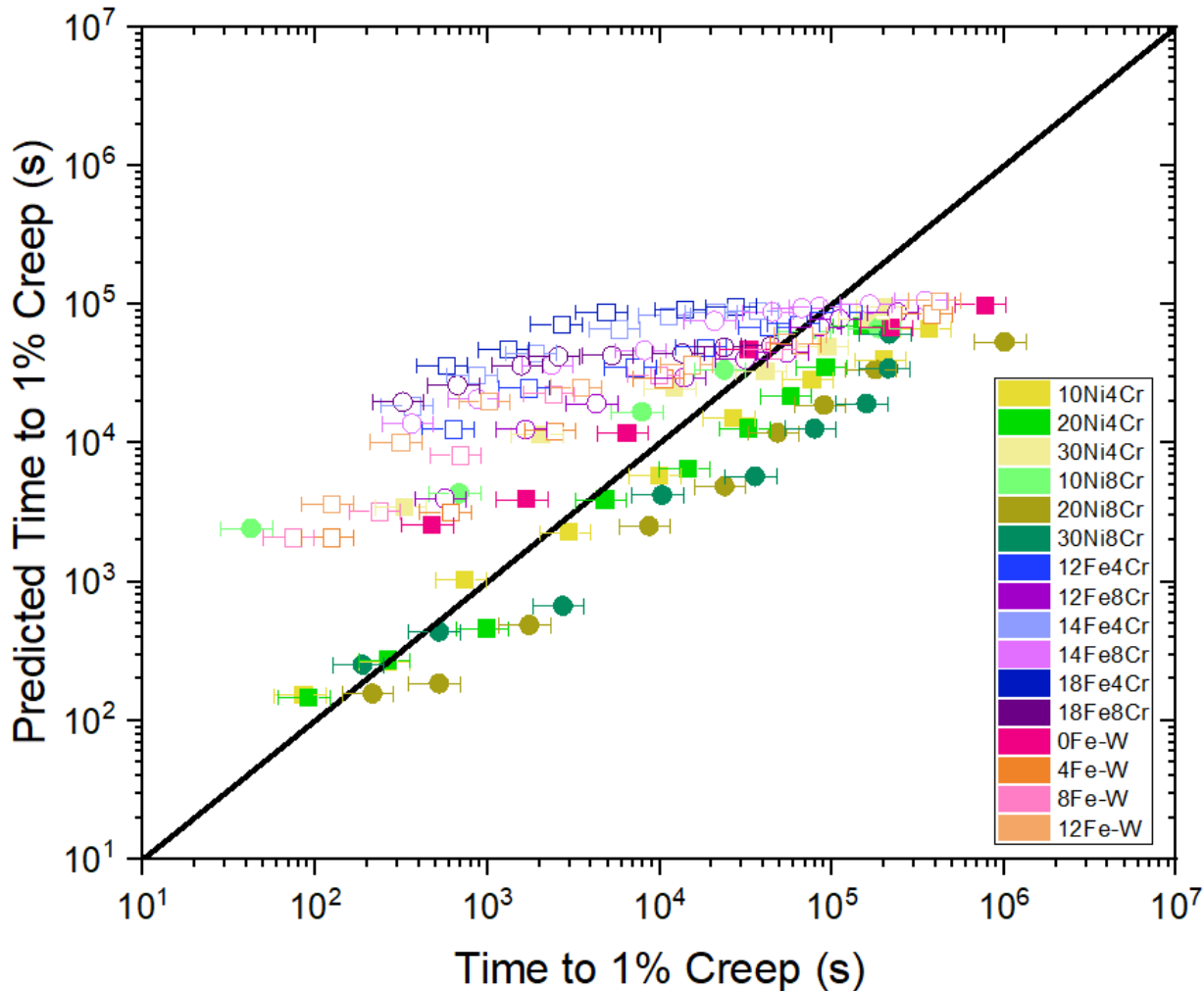


Figure 6-20. Double logarithmic plot of predicted time to 1% steady-state creep (which is inversely proportional to a strain rate) vs the experimental value. Error bars correspond to our estimated reproducibility of this experimental measurement, taken as $\pm 33\%$ of the value. Validation MSE = $8.00E10$. Colors represent the family (green-yellow: W-free, Fe-free; blue-purple: W-free, Fe-containing; red-orange: W-containing, Fe-containing). Hollow symbols represent elements with Fe, and solid symbols represent Fe-free alloys. Squares indicate alloys with 4% Cr, and circles indicate alloys with 8%Cr.

78% of the alloys were predicted within 1 order of magnitude, and the MSE for the data validation was 1.65×10^{10} , even lower than the test fitting (averaging 2.4×10^{12} over 100 seeds, or 5.2×10^{11} for seed 0). This improvement could be due to these alloys having a slightly lower average creep life than the test fitting, or it could be that these data are consistent with standard practices and includes no outliers. However, while the fit is impressive, as shown by the key, the

model systematically overpredicts the creep life for the Fe-bearing alloys. This error decreases with longer creep time, becoming quite tolerable above $\sim 5 \times 10^4$ s. These longer tests are the most valuable to predict. Fast creep rates are comparable yield strength tests, which are typically conducted at a strain rate of 10^{-4} s^{-1} ; we know (but the model may not) that Fe produces a weakening effect on yield strength; thus it is not unexpected that the Fe-containing alloys are consistently overestimated.



Figure 6-21. Feature importance for predicting creep on the 16-alloy validation set.

As shown in Fig. 6-21, while stress and temperature predicably have the highest importance to predict creep behavior, yield strength, solvus, and volume fraction also have a high importance. Physically, it is expected that yield strength correlate with creep resistance, as these are two measures of strength, especially since much of the yield stress data are measured at elevated temperature. W and Al are the most important elements for the same reason as discussed previously, i.e. almost all training data has compositions based on the Co-Al-W system. Fig. 6-22 shows a few selected plots of steady-state creep rate vs compressive stress, for experimental data and ML predictions.

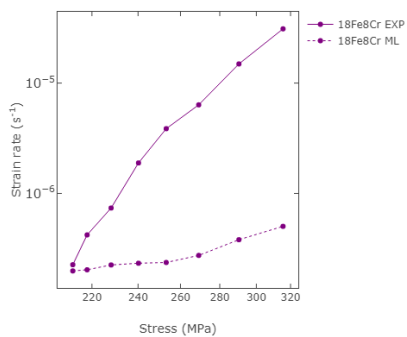
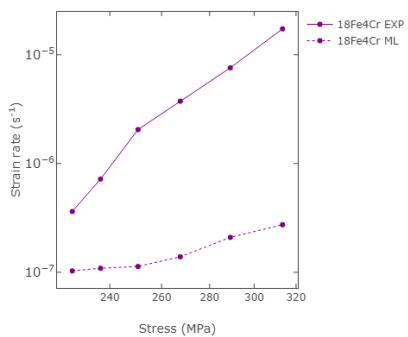
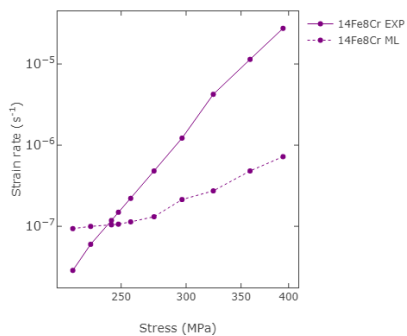
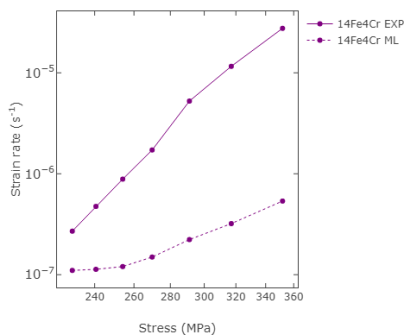
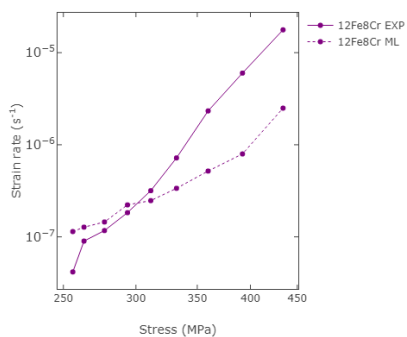
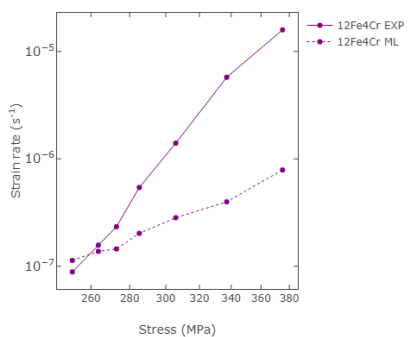
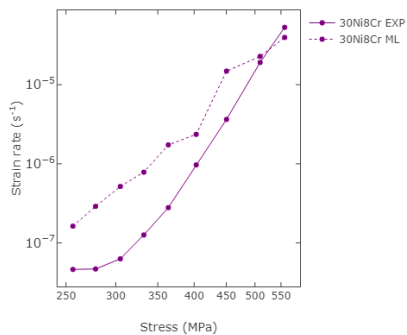
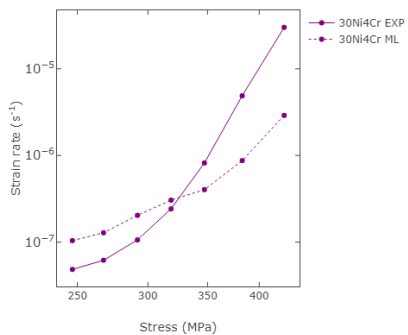


Figure 6-22. Experimental data compared with machine learning predictions for 8 selected validation creep curves.

While the model can predict creep life for most points to within one order of magnitude (about three times our estimated experimental error, and comparable to experimental variation between different samples with the same nominal composition), the chemical descriptors and intermediary models are not sufficient to be correctly identify the effect of a new element (Fe).

6.6 Future Work

A future step for this model is to integrate it into the materials design pipeline. With a method for accurate volume fraction (such as diffusion couples or CALPHAD using a database optimized for the composition space), we can generate millions of potential alloy compositions, while staying within the known composition space. Creep could be predicted before the alloy is ever cast.

This tool may also assist in prioritizing creep experiments for already-known alloys. Considering that ~85% of alloys in the database have no measured creep data, using this database can prioritize which of those alloys should be subjected first to creep experiments.

6.7 Conclusions

Using data collected from the literature on Co-based superalloys with γ/γ' microstructure, we have built seven “intermediary” machine-learning models, which predict (i) lattice misfit according to temperature, (ii) solvus temperature, (iii) solidus temperature, (iv) liquidus temperature, (v) peak hardness, (vi) γ' volume fraction according to temperature, and (vii) yield strength according to temperature. Using these models to fill missing data in the measured property list, we predict time

to 1% creep (which is inversely proportional to an average strain rate) in the steady-state creep regime.

We have additionally attempted the “divide and conquer” approach, using k-means clustering to train several independent models. We have concluded that, despite their large composition range, all Co-based alloys are equally-well predicted with the same regressor, so no improvement was made with this technique.

Finally, we validated the model using 16 new Co-based superalloys: (i) six alloys which are free of W but contain Fe, (ii) six alloys which are free of both W and Fe, and (iii) four alloys which contain W but no Fe. This data validation stretched into the unknown composition space, which the model was able to reasonably capture due to the intermediary models and elemental descriptors; however, the model did not accurately predict the specific change due to the addition of a new element, Fe.

6.8 Acknowledgements

This study was supported by the U.S. Department of Commerce, National Institute of Standards and Technology, as part of the Center for Hierarchical Materials Design (CHiMaD) at Northwestern University via award 70NANB14H012. B. Ohl acknowledges coding assistance from Haroon Nawaz, Jesse Ji, Kamal Choudhary, Marty Ohl, and especially Ren Lopez. Thanks to Fei Xue for providing experimental creep data ahead of publication.

6.9 Competing Interests Statement

Declarations of interests: DCD discloses a financial interest in Amatrium Inc., a company involved in machine learning for alloys.

6.10 Supplementary Information

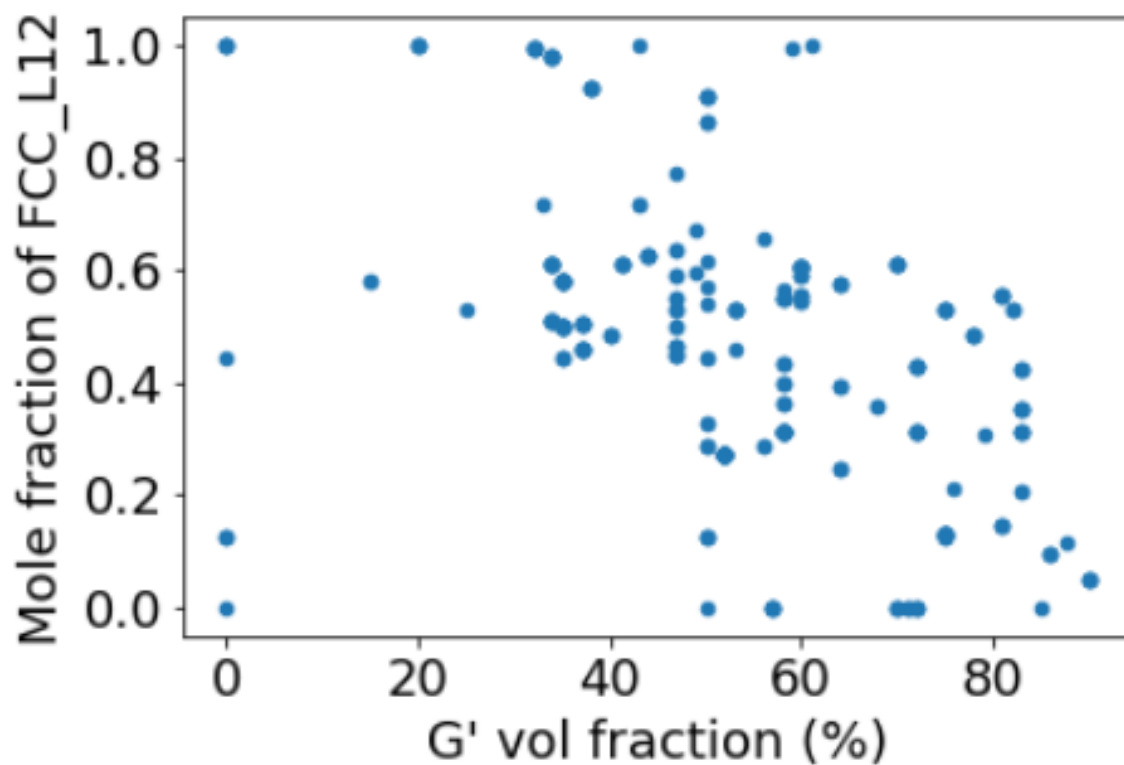


Figure S 6-1. Calphad prediction of γ' volume fraction using TCNI-11 database (y-axis), vs. experimental volume fraction (x-axis).

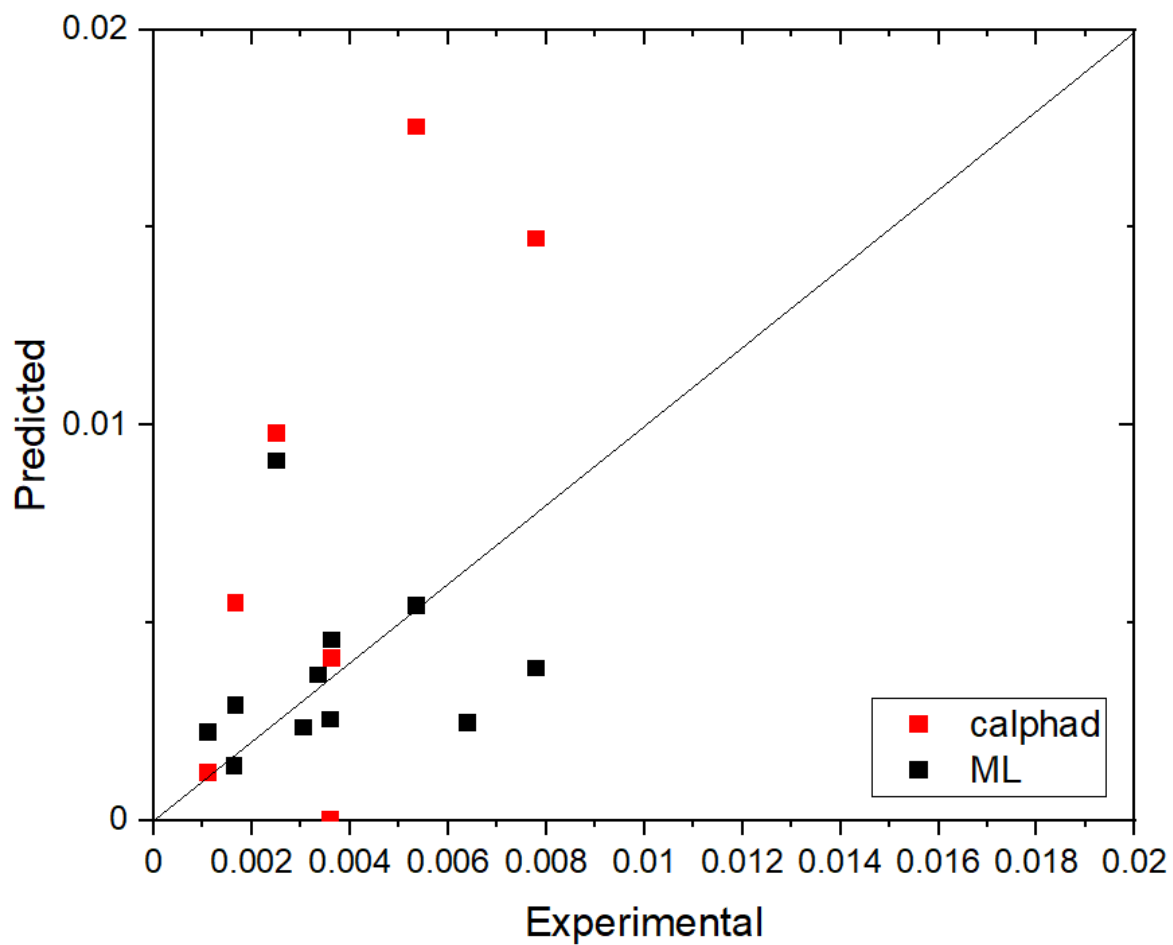


Figure S 6-2. Calphad (TCNI-11) predictions of lattice misfit (dimensionless) and an early version of our ML predictions of lattice misfit, compared to experimental prediction of lattice misfit.

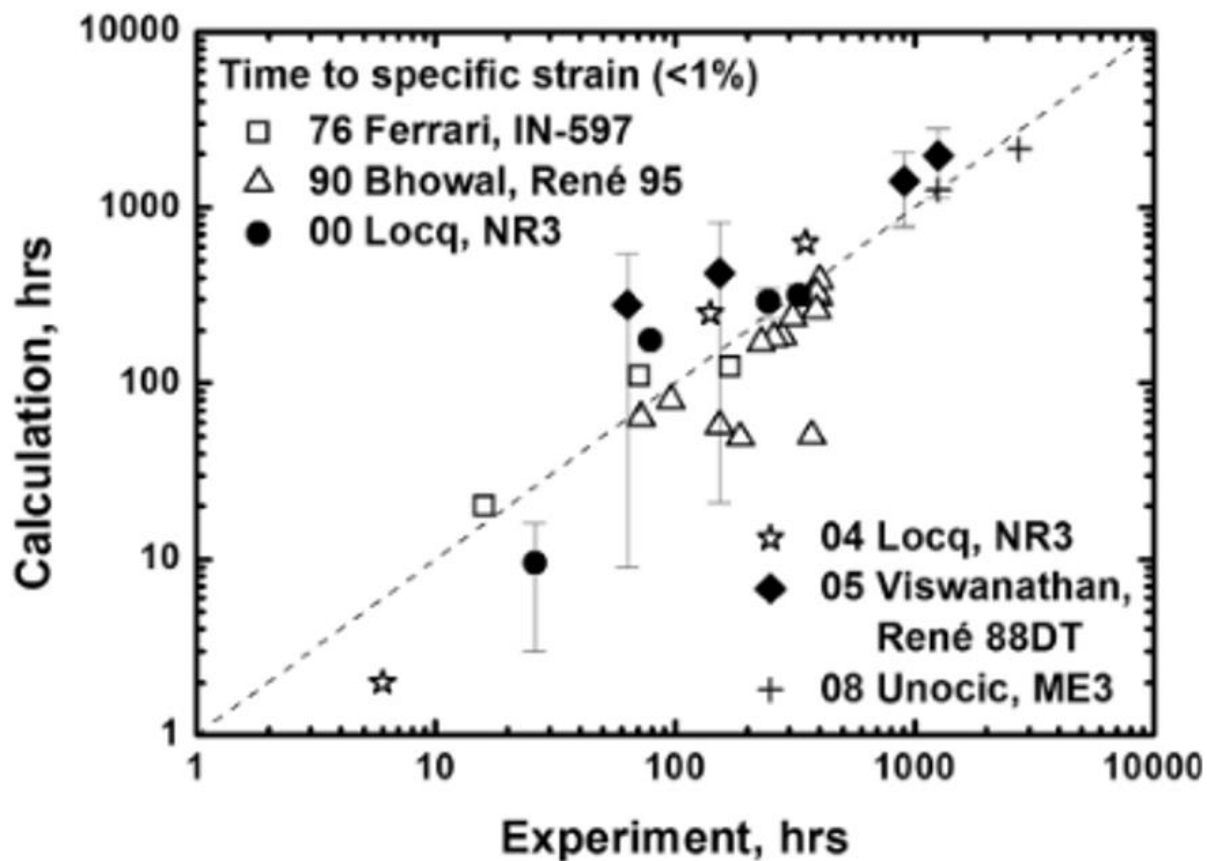


Figure S 6-3. Kim et al's result upon predicting time to 1% strain in Ni-based superalloys. Reproduced from [167].

Kim et al's result upon predicting time to 1% strain in Ni-based superalloys, for comparison, which we seem to predict similarly well.

7. Development of a W-free CoFeNi-based High-Entropy Superalloy with High γ' Volume Fraction

7.1 Abstract

Six multi-principal-element (“high-entropy”) CoFeNi-based superalloys were produced with (i) various ratios of Co, Fe, and Ni, (ii) a constant concentration (13 at%) of γ' formers (V, Al, Ti, Nb, and/or Ta, without W), and (iii) up to 8% Cr. The role of different ratios of γ' - to γ -formers on phase stability is investigated via calorimetry and microstructural studies after aging up to 1000 h at 850 °C, culminating in a novel W-free γ' -strengthened superalloy with equiatomic γ - and γ' -forming elements, $(\text{Co,Fe,Ni})_{87}(\text{V,Ti,Al})_{13}$. We find a stable, continuous $\gamma+\gamma'$ phase field when transitioning from W-free Co-based superalloys to the equiatomic $(\text{CoFeNi})_{87}(\text{V,Ti,Al})_{13}$ composition, which display a γ/γ' microstructure with γ' volume fraction of $\sim 40\%$ and without additional phases.

7.2 Introduction

Gas turbine blades and disks, which operate at high temperature, stress, and in corrosive environments, have long relied on superalloys based on nickel, iron, and/or cobalt [1] to provide necessary creep resistance. Ni-based superalloys have seen much wider use than Co- or Fe-based superalloys because their γ/γ' microstructure (fcc matrix with coherent $L1_2$ precipitates) impedes dislocation motion—especially at high temperature—due to dislocation interactions such as Kear-Wilsdorf locking [2–5]. However, Co and Fe have superior melting points than Ni, so if Co- or Fe-based superalloys could be developed with a γ/γ' microstructure, these alloys may surpass Ni-based

superalloys. 2006 marked the first breakthrough in achieving the γ/γ' microstructure in a Co-based superalloy, starting a new class of materials [6,7]. In these alloys, the γ' phase is based on variations of the following L1₂ phases: Co₃(Al,W), Co₃Ti, Co₃(Nb,Mo), Co₃(Al,V), Co₃(Ti,V), Co₃(Nb,V), or Co₃(Ta,V) [8–12,14,121]. Although these γ' compositions have largely been considered distinct subfamilies of Co-based superalloy, our results here suggest that these subfamilies, and L1₂-strengthened high entropy alloys[182,183], all belong to the same larger family.

The development of an Fe-based γ' -strengthened superalloy would be even more significant, as Fe has an even higher melting point than Co and is significantly cheaper than Co or Ni. However, Fe is known to destabilize the γ/γ' phase field. Commercial Ni-based superalloys may have high Fe concentrations, most notably IN718 which contains 18.5 wt% Fe and is strengthened by γ' and γ'' precipitates [113–115]; however, these alloys have lower γ' volume fractions because Fe partitions strongly to the matrix. In most Co-based superalloys, Fe has even more detrimental effects, reducing solvus temperature and frequently destabilizing the microstructure [61,128–131,184,185]. Even most so-called “high entropy superalloys” typically limit Fe concentration to <12 at.% [186–188]. Nevertheless, in our recent work we were able to add 18 at.% Fe to an existing W-free Co-based superalloy [152,175]. While the γ/γ' microstructure was maintained after aging for 1000h at 850 °C, additional deleterious phases also emerged, indicating that the alloy system would require further modification to compete with modern superalloys.

Following the discovery that W-free Co-based superalloys can maintain stable γ/γ' microstructures with much higher Fe content than in W-containing Co-based superalloys, we have developed 6 new alloys, designed to further explore this new phase space. We start with a “base”

alloy from our previous work Co-18Fe-12Ni-5Al-3V-2Ti-1.5Nb-1.5Ta (all compositions are given in at%) which maintained ~20% γ' volume fraction after aging 850 °C for 1000h, but also developed additional intermetallic phases with associated γ' depletion zones (hence the low γ' volume fraction). By modifying this alloy, we can identify the effects of (i) adjusting Fe/Ni ratios, and (ii) adjusting γ' -former ratios. It will become clear whether the additional phases disappear (becoming less stable than in the base alloy) or whether the γ' phase disappears. In particular, the base alloy's deleterious phases were rich in Ta and especially Nb, so we replace the 3 at.% (Nb + Ta) with additional amounts of the other γ' -formers, namely V, Ti, and Al. Alloy VVV has +3 at.% V (for a total of 4 at.%), alloy VTiAl has +1% V, +1% Ti, +1% Al, and alloy VTiTa has +1% V, +1% Ti, and re-adds +1% Ta.

We also create three alloys to test variations in γ -former concentrations. In our previous studies, we started with 30% (Ni + Fe) and substituted Fe for Ni, arriving at a maximum Fe concentration of 18% with a minimum 12% Ni concentration. Conventional alloy design takes it for granted that Ni improves the γ' phase stability; however, a series of 100% $L1_2$ alloys with compositions in the (Co, Fe, Ni)₃V space showed that Ni was not necessarily stabilizing this phase [189]. We now adjust our base alloy to keep Ni at its initial 30% value (alloy name: 30Ni), substituting 18% Fe for Co and allowing us to see the effect of substituting Fe for Co, compared to substituting Fe for Ni. Since alloy 30Ni has near-equiatomic amounts of Co and Ni, we also developed two alloys with completely equiatomic amounts of the three γ -formers (Co, Fe, and Ni). Alloy CCA has the same concentrations of Cr and γ' -formers as alloy VTiAl, but with equiatomic Co, Fe, and Ni concentrations. Alloy HEA has equiatomic concentrations for both γ -formers (Co, Fe, Ni) and γ' -

formers (V, Ti, Al). This is the only alloy of the series where we have reduced Cr and B to zero, since high Cr is known to reduce phase stability, especially when interacting with Fe [88,131,175,184,185]. All six alloys have γ' -formers totaling 13%, which is expected to yield γ' volume fractions of ~50% assuming γ composition (Co, Fe, Ni) and γ' composition (Co, Fe, Ni)₃(V, Ti, Al, Ta, Nb). Nominal compositions for these six new alloys are given in Table 7-1.

7.3 Experimental Methods

Six high-entropy superalloys (HESAs) were produced with 13 at% γ' formers (V, Al, Ti, Nb, and/or Ta) up to 8% Cr, and various ratios of Co, Fe, and Ni culminating in an equiatomic composition, as shown in Table 7-1. Compositions were verified by Energy Dispersive Spectroscopy (EDS) using polished cross-sections of homogenized specimens in a FEI Quanta 65 Scanning Electron Microscope (SEM). Also depicted are related alloys from previous studies, including the “base” alloy for this work, 18Fe8Cr. All composition, unless specified otherwise, are in at.%.

Table 7-1. Nominal compositions (at.%) of present study and four literature alloys.

Alloy	Nominal Composition, at.%									
	γ -formers			Oxide former	γ' -formers					GB modifier
	Co	Fe	Ni	Cr	Al	V	Ti	Nb	Ta	B
Present study										
30Ni	30.9	18	30	8	5	3	2	1.5	1.5	0.08
VVV	48.9	18	12	“	“	6	“	0	0	“
VTiAl	“	“	“	“	6	4	3	“	“	“
VTiTa	“	“	“	“	5	“	“	“	1	“

CCA	26.3	26.3	26.3	"	6	"	"	"	0	"
HEA	29	29	29	0	4.3	4.3	4.3	"	"	0
Related Alloys										
0Fe4Cr [152]	52.9	0	30	4	5	3	2	1.5	1.5	0.08
0Fe8Cr [152]	48.9	"	"	8	"	"	"	"	"	"
18Fe4Cr [175]	52.9	12	18	4	"	"	"	"	"	"
18Fe8Cr [175]	48.9	"	"	8	"	"	"	"	"	"

The six alloys were arc-melted in Ar as button-shaped ingots (~15 g) using pure elements - Co (99.9+%), Ni (99.95%), Al (99.5%), Cr (99.995%), V (99.7%), Ti (99.95%), Nb (99.8%), Ta (99.95%), and B (95-97%), purchased from Alfa Aesar (Tewksbury, MA), with a flip between each of the six re-meltings. Samples were encapsulated in evacuated fused silica tubes, homogenized for 24 h at 1200 °C, and water quenched. Sections of the ingots were aged in evacuated fused silica tubes at 850°C for durations between 24 and 1000 h, followed by water quenching.

Alloy compositions were verified by Energy Dispersive Spectroscopy (EDS) using polished cross-sections of homogenized specimens in a FEI Quanta 65 Scanning Electron Microscope (SEM). All aged specimens were investigated with secondary-electron- and backscatter-electron detectors. Specimens for SEM were mounted in epoxy, polished down to 1µm diamond suspension, and etched with Carapella's reagent.

The γ' area fraction was determined in ImageJ [190], by a combination of thresholding, Weka segmentation [191], and hand-tracing of precipitates from at least five micrographs. Here, the γ' volume fraction is assumed to be equal to the area fraction [20,63]. In an ordered cubic structure, this approximation may be an overestimate [16]. For some of the alloys, automatic image analysis is especially difficult because the misfit is so small that the transition from γ to γ' is almost

continuous. Furthermore, the elements have similar atomic weights, so the BSE contrast between γ and γ' is low. In these cases, the precipitates were traced by hand.

Differential Scanning Calorimetry (DSC) was performed using a Mettler Toledo TGA/DSC 3+ instrument operating with an alumina pan and 60 mL/min N₂ cover gas, with heating and cooling rates of 10 °C/min. Homogenized samples were cycled twice in the solvus-liquidus range to collect solvus, solidus, and liquidus temperatures upon heating and cooling (no solvus associated with 1st heat).

7.4 Results and Discussion

7.4.1 Transformation Temperatures

Solvus, solidus, and liquidus values for the six alloys are shown in Fig. 7-1.

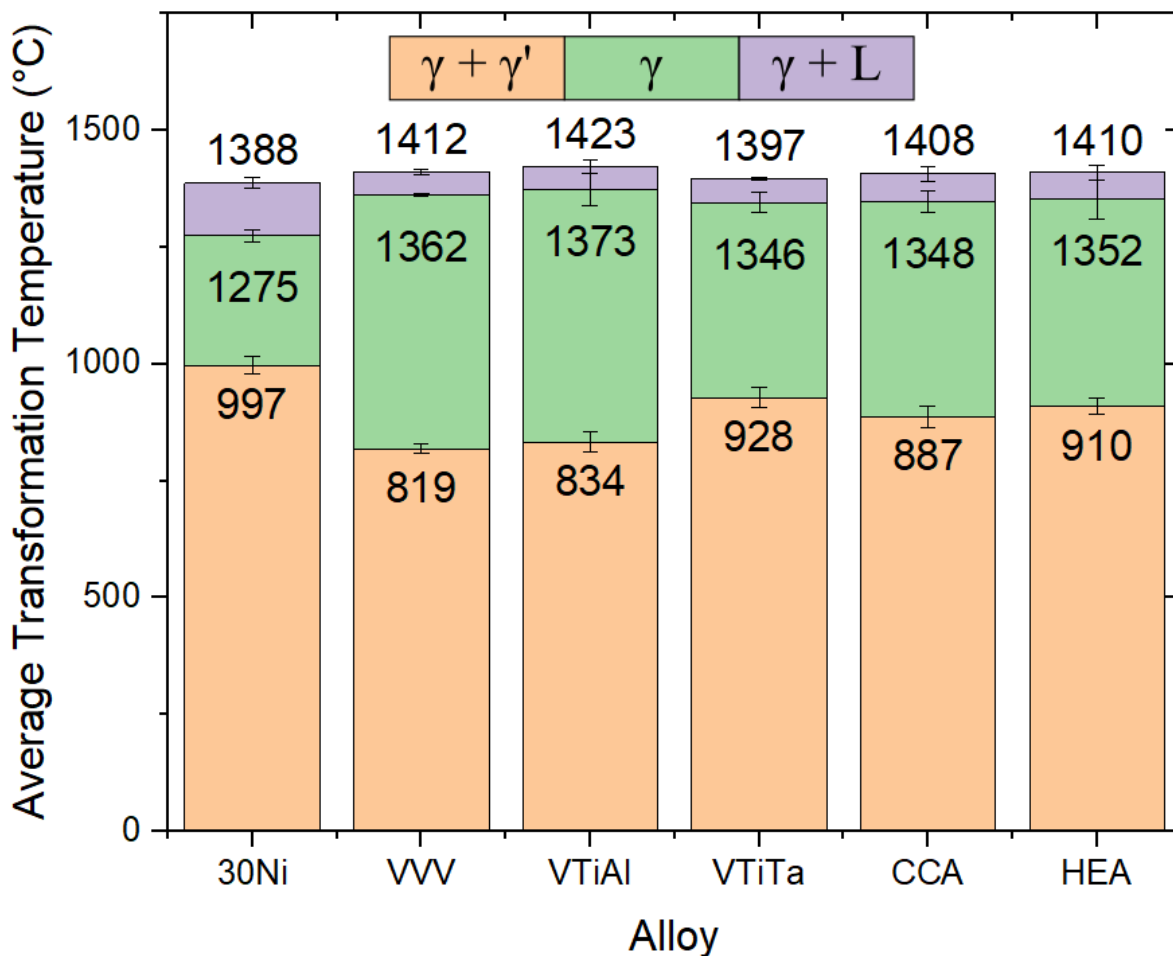


Figure 7-1. DSC measurements for solvus, solidus, and liquidus of all 6 alloys. Reported measurement averages heating and cooling cycles, and error bars correspond to the standard deviation.

As shown in Fig. 7-1, the solvus temperature varies significantly, although the liquidus is nearly the same for all alloys, ranging from 1388-1423 °C. The alloy with the highest solvus is 30Ni, which fits with this alloy having the highest amount of refractory elements (1.5% Nb + 1.5% Ta).

The alloy with the next-highest solvus is VTiTa, consistent with its 2nd-highest concentration of refractory elements (1% Ta). Alloy VVV and VTiAl both had solvus values below 850 °C,

which means they do not produce γ' with the standard 850 °C heat treatment. However, going from VTiAl to CCA, which changes γ' -forming ratios from 49.8Co-18Fe-12Ni to 26.3Co-26.3Fe-26.3Ni, improves solvus by ~50 °C, allowing CCA to be heat-treatable at 850 °C. Going from CCA to HEA, which involves rebalancing γ' -formers from 4V-3Ti-6Al to 4.33V-4.33Ti-4.33Al increases solvus by another ~20 °C. Again, as long as the microstructure is not destabilized, this is expected that reducing the lowest-melting element (Al) would increase solvus.

Fig. 7-2 shows the solvus plot of these alloys, and literature alloys, as a function of Fe concentration.

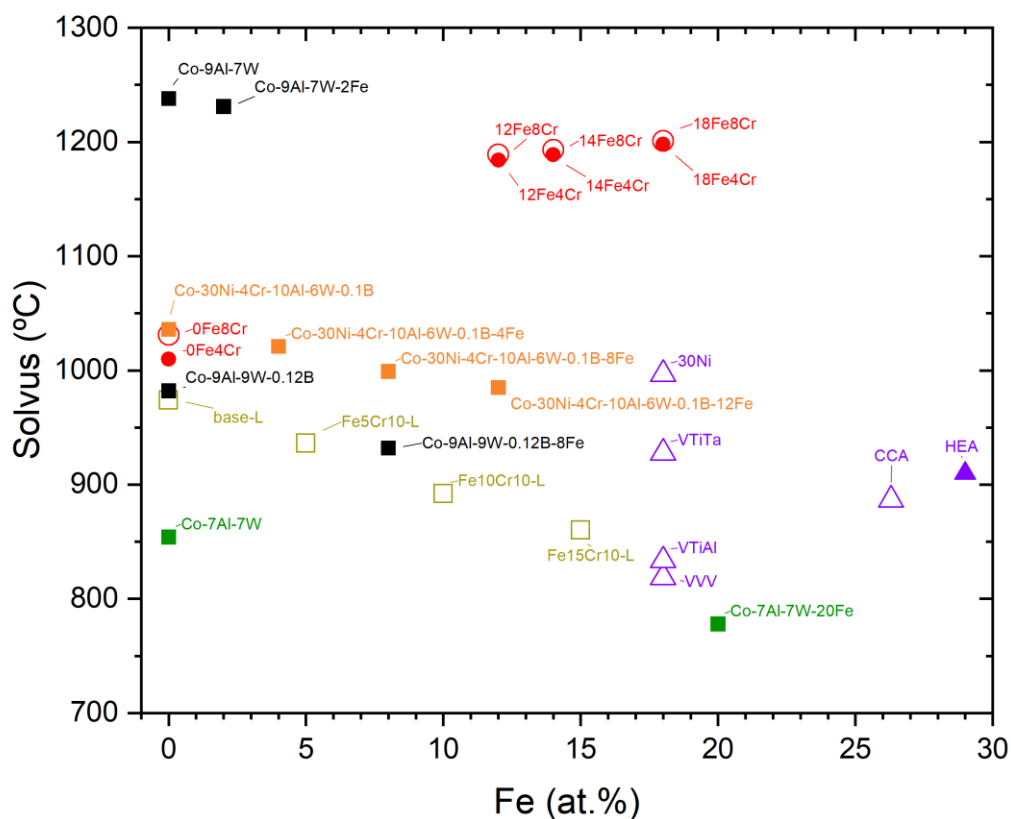


Figure 7-2. Plot of solvus vs Fe at.%. Hollow symbols represent Cr = 8 at.%, solid symbols have less Cr. Present work is shown in purple triangles. Prior work of related alloys is shown in circles [152,175]. Additional literature data shows Co-9Al-7W-xFe (black)[129], Co-9Al-9W-0.12B-xFe (black)[61], Co-7Al-7W-xFe (green)[184], Co-20Ni-10Cr-10Al-7W-0.1B-xFe (mustard) [131] and Co-30Ni-4Cr-10Al-6W-0.1B-xFe (orange) [181].

For W-containing alloys in the literature, there is a clear trend that substituting Fe for Co reduces solvus. For our W-free alloys, the trend is not as clear. Comparing our 30Ni to previous 0Fe8Cr (Co-30Ni-8Cr-5Al-3V-2Ti-1.5Nb-1.5Ta) [152] which had solvus 1031 °C, it is apparent that substituting 18%Fe for Co drops the solvus by ~30 °C. However, comparing 30Ni to Co-12Ni-18Fe-8Cr-5Al-3V-2Ti-1.5Nb-1.5Ta [175] shows that the change from 12% Ni to 30% Ni,

substituting for Co, reduces solvus by over 200 °C. Thus, the effect of increasing Fe seems to depend on whether Fe substitutes for Ni or Co. Fig. 7-3 plots solvus as a function of Fe/(Fe+Co).

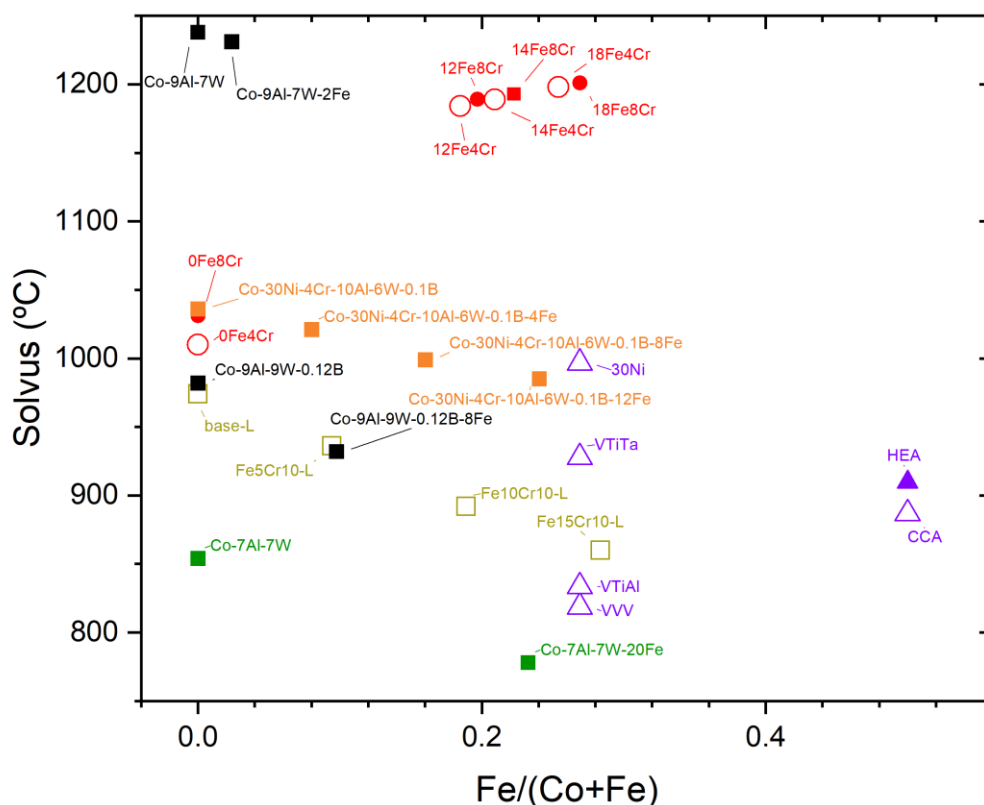


Figure 7-3. Plot of solvus vs Fe/(Co+Fe) at.%. Hollow symbols represent Cr = 8 at.%, solid symbols have less Cr. Present work is shown in purple triangles. Prior work of related alloys is shown in circles [152,175]. Additional literature data shows Co-9Al-7W-xFe (black)[129], Co-9Al-9W-0.12B-xFe (black)[61], Co-7Al-7W-xFe (green)[184], Co-20Ni-10Cr-10Al-7W-0.1B-xFe (mustard) [131] and Co-30Ni-4Cr-10Al-6W-0.1B-xFe (orange) [181].

As shown in Fig. 7-3, solvus stays approximately the same from 0Fe4Cr to 30Ni, as the Fe:Co ratio increases, and more dramatically drops from 30Ni to HEA and CCA. However, HEA and CCA have different γ' -formers than 30Ni, so this drop is unlikely to be caused by the Fe:Co ratio

alone. In our previous alloys with red circle symbols in Fig. 7-3 [3], a consistent increase in solvus is apparent with increasing $Fe/(Co+Fe)$. We previously claimed that the addition of 4Cr to 8Cr (substituting for Co), led to a small increase in solvus temperature due to Cr's higher melting point. However, graphed in this way, the solvus for these alloys appears to linearly increase with $Fe/(Co+Fe)$.

In Fig. 7-4, we plot solvus against $Fe/(Ni+Fe)$.

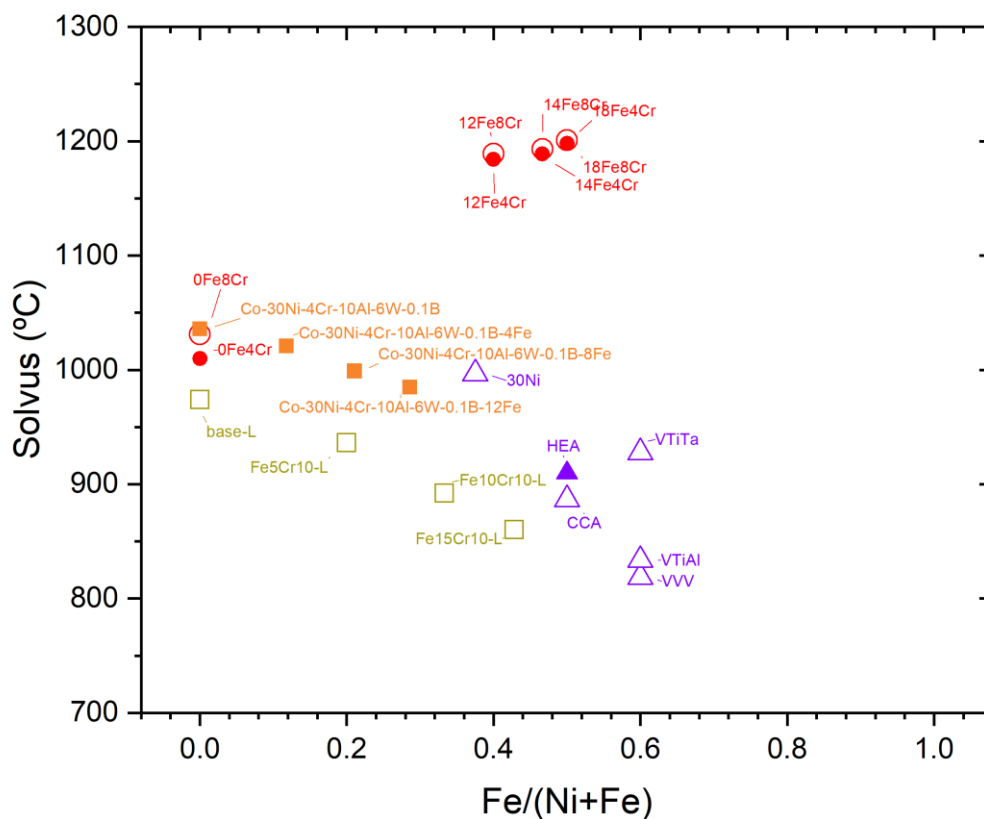


Figure 7-4. Plot of solvus vs $Fe/(Ni+Fe)$ at.%. Hollow symbols represent $Cr = 8$ at.%, solid symbols have less Cr. Present work is shown in purple triangles. Prior work of related alloys is shown in circles [152,175]. Additional literature data shows Co-9Al-7W-xFe (black)[129], Co-9Al-9W-0.12B-xFe (black)[61], Co-7Al-7W-xFe (green)[184], Co-20Ni-10Cr-10Al-7W-0.1B-xFe (mustard) [131] and Co-30Ni-4Cr-10Al-6W-0.1B-xFe (orange) [181].

Fig. 7-4 shows how solvus changes with Fe/(Ni+Fe) ratio. This does not show as clear a trend as the previous figure. Moving from 0Fe8Cr to 30Ni results in the small solvus drop, as mentioned previously. HEA and CCA decreases from 30Ni due to the changing γ' -formers, but VTiAl (which has the same γ' -formers as CCA) further drops. As before, the series with both Nb and Ta increases in solvus.

Finally, Fig 7-5 shows how solvus changes with Ni/(Ni+Co) ratio.

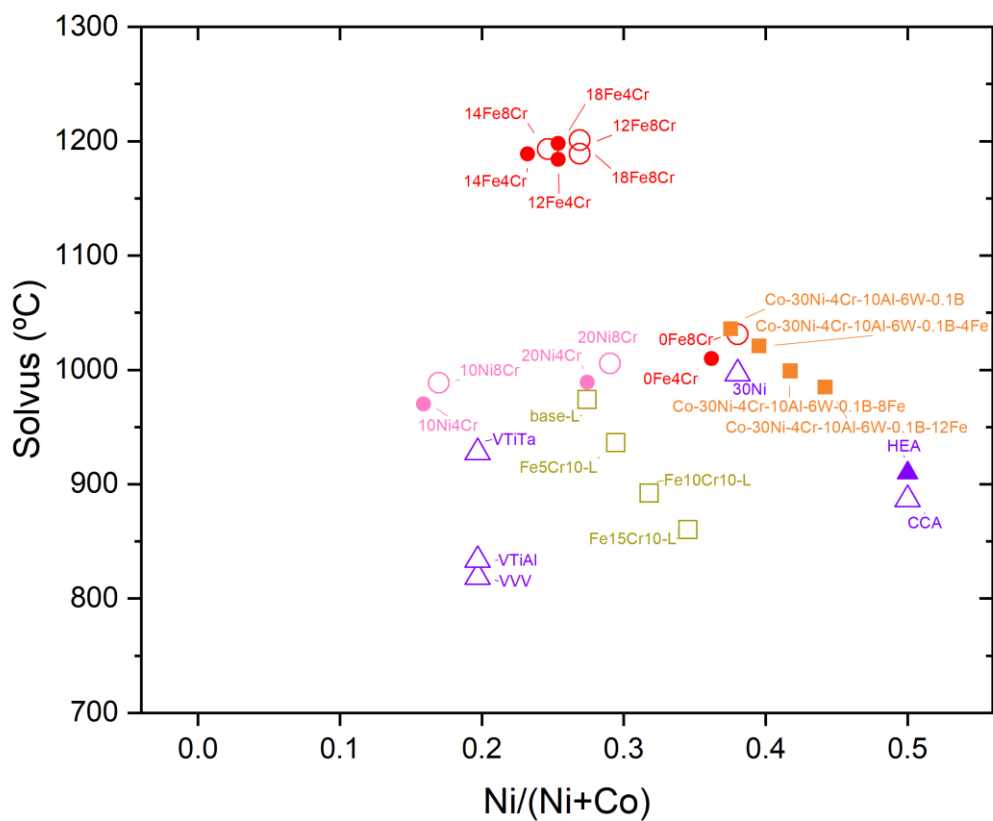


Figure 7-5. Plot of solvus vs Ni/(Ni+Co) at.%. Hollow symbols represent Cr = 8 at.%, solid symbols have less Cr. Present work is shown in purple triangles. Prior work of related alloys is shown in circles [152,175]. Additional literature data shows Co-9Al-7W-xFe (black)[129], Co-9Al-9W-0.12B-xFe (black)[61], Co-7Al-7W-xFe (green)[184], Co-20Ni-10Cr-10Al-7W-0.1B-xFe (mustard) [131] and Co-30Ni-4Cr-10Al-6W-0.1B-xFe (orange) [181].

The W-containing alloys [131,132] show a clear picture—decreasing in solvus as Ni:Co ratio increases. Our previous W- and Fe-free alloys[152] slightly increase in solvus, and our previous Fe-containing alloys [175] appears uncorrelated with Ni:Co ratio. Moving from VTiAl to CCA shows improvement in the solvus temperature.

7.4.2 Microstructure

The microstructure of alloys HEA, CCA, 30Ni, and VTiTa after 1000h aging at 850 °C are shown in Figs. 7-6 to 7-9. Alloys VVV and VTiAl are not depicted, as these have a single phase γ at 850 °C.

Fig. 7-6 shows the bulk- and grain-boundary microstructures of HEA after 1000h aging. The γ' volume fraction is ~40%. The alloy is free of additional precipitates, even at the grain boundaries. Based on the “rounded cuboidal” morphology of the precipitates, we estimate lattice misfit to be between 0.25 and 0.5%. This small misfit is difficult to detect in laboratory XRD, so it should be measured with synchrotron X-rays or neutron diffraction. The latter technique would be preferable, as Co high absorption of neutrons typically allows for superlattice peak visibility, which is often below the noise level of X-rays in similar alloys. Superlattice peak identification is necessary for verifying whether the misfit is positive or negative; given that Ni-based superalloys typically have negative misfit, while Co-based superalloys typically have positive misfit, the misfit sign of HEA is not obvious. Alternatively, the orientation of γ' -precipitates rafted under uniaxial stress (compression or tension) can reveal the sign of the misfit.

HEA aged 850 °C 1000h

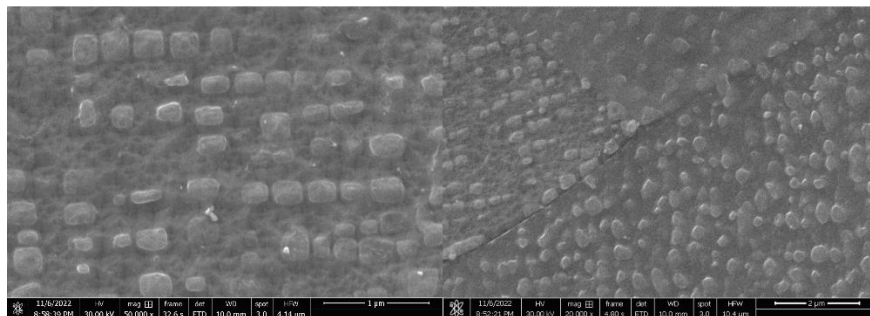


Figure 7-6. SE micrograph of alloy HEA aged 850 °C for 1000h, (left) bulk $\gamma+\gamma'$ region, (right) grain boundaries at triple point, which are free of additional phases.

Fig 7-7 shows, in alloy CCA aged for 1000h, that γ' precipitates are spherical, and not aligned in any crystallographic direction. This is indicative of either a very high misfit (to the point of incoherency) or a very low misfit. The latter hypothesis is more likely, as the γ' precipitates have coarsened slowly and not fused. We expect the misfit to be between -0.2% and 0.2%, given the known trend of Fe reducing misfit when substituted for Co, and the morphological similarity between these γ' precipitates and those of other low-misfit alloys [132].

CCA aged 850 °C 1000h

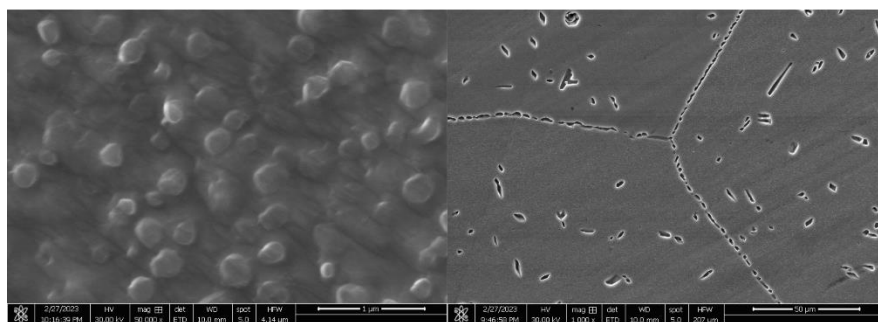


Figure 7-7. SE micrograph of alloy CCA aged 850 °C for 1000h, (left) bulk $\gamma+\gamma'$ region, (right) grain boundaries at triple point, both of which contain an additional intermetallic phase in moderate ~10% volume fraction.

Additionally, alloy CCA shows an intermetallic phase (with a volume fraction $\sim 10\%$) on the grain boundaries and within the bulk grain. This phase appears to be aggressively targeted by our etchant, but upon re-polishing and investigating with EDS (without etching), this phase appears rich in Ti and Al. It is unclear whether CCA's reduced γ' phase stability, compared to HEA, is due to the additional Cr, or to the high Al and Ti concentrations. Given that the microstructure of 30Ni, shown in Fig. 7-8, suggests that these alloys can be stable even with Ta and Nb, a future alloy in the family $(\text{CoFeNi})_{87}(\text{AlVTiTaNb})_{13}$ would benefit by (i) reducing Al and Ti to remove this intermetallic phase, and (ii) increasing solvus temperature via Ta and Nb refractory content.

30Ni aged 850 °C 1000h

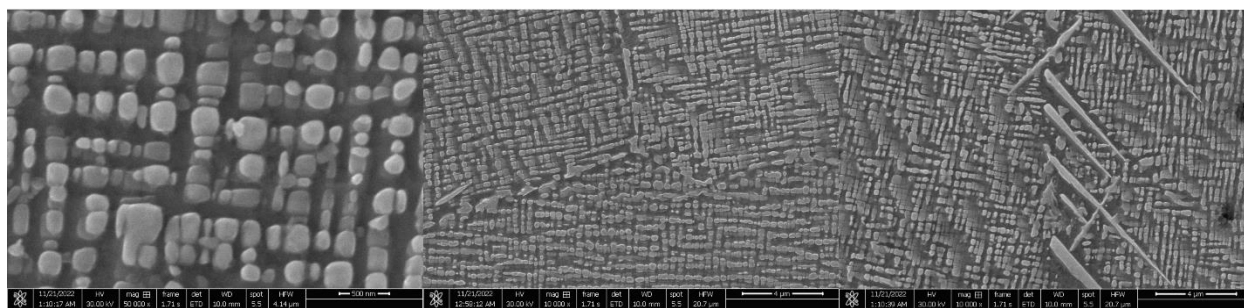


Figure 7-8. SE micrograph of alloy 30Ni aged 850 °C for 1000h, (left) bulk $\gamma+\gamma'$ region, (center) grain boundaries at triple point, which are free of additional phases, (right) grain boundary with needlelike precipitate, possibly due to oxygen diffusing through grain boundaries.

Alloy 30Ni has rounded cuboidal γ' precipitates with volume fraction $\sim 50\%$. Based on the morphology of the precipitates and the misfit of similar alloys [175], we estimate the misfit to be 0.3 to 0.5%. As shown in Fig 7-8, the typical grain boundaries have coalesced γ' with neither additional phases nor depletion zone. However, some grain boundaries exhibit a needle-like phase, possibly due to oxygen diffusing through the grain boundary and disrupting the local stoichiometry. Nonetheless, 30Ni displays a *significantly* more stable microstructure than 18Fe8Cr

[175], showing that the substitution of Co to Ni (becoming a CoNi alloy, rather than Co-based alloy) indeed improves stability in this system.

Fig. 7-9 shows the microstructure of alloy VTiTa after 1000h aging. The γ' volume fraction of this alloy is extremely low, likely due to the precipitation of an additional phase on the grain boundaries and ubiquitously through the bulk grain. Unlike 18Fe8Cr which precipitated Nb- and Ta-rich phases, this alloy precipitates a Ti- and Al-rich phase. Notably, VTiTa has the highest fraction of this phase (also present in CCA and VTiAl when aged at a lower temperature); it also has the highest Ti/Al ratio. In some HEAs [192–194], having a high Ti/Al ratio is known to destabilize the γ' phase. We expect that an alloy of composition $(\text{CoFeNi})_{87}(\text{Al}_{0.4}\text{V}_{0.4}\text{Ti}_{0.2})_{13}$, with lower Ti/Al ratio, would show improved stability. The γ' precipitates visible in Fig. 7-9 show sharp corners, indicative of a high lattice misfit. This makes sense—assuming that Al and Ti are sequestered in the deleterious intermetallic phase, the γ' becomes enriched in Ta, an element with high atomic radius that increases the lattice parameter of the γ' phase, thus increasing misfit to an estimated value of 0.5-1%.

VTiTa aged 850 °C 1000h

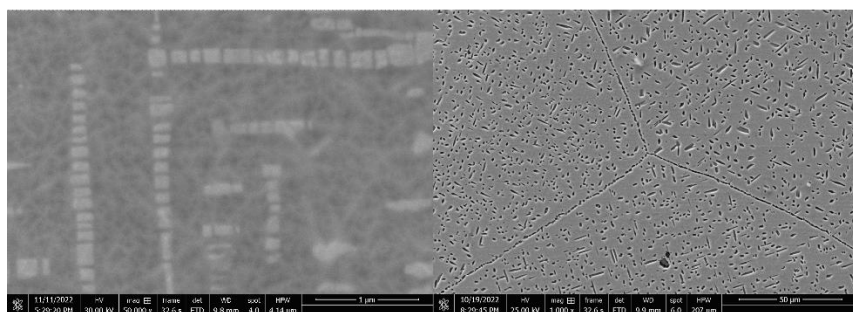


Figure 7-9. SE micrograph of alloy HEA aged 850 °C for 1000h, (left) bulk $\gamma+\gamma'$ region, (right) grain boundaries at triple point, which are free of additional phases.

7.4.3 Volume Fraction of γ' phase

Fig. 7-10 shows the γ' volume fraction of these alloys and literature alloys as a function of Fe concentration. In addition to Co-based superalloys, we include a $L1_2$ -strengthened high-entropy alloy [195], although this alloy was only aged 1 h at a lower temperature, so its long-term stability is uncertain.

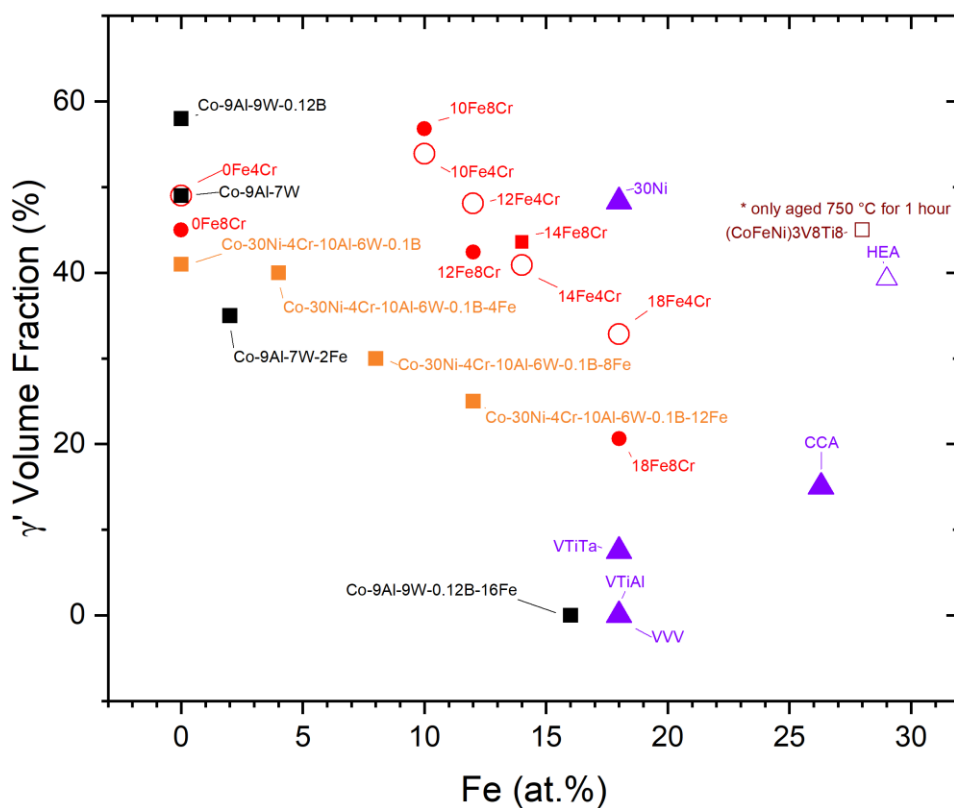


Figure 7-10. Plot of γ' volume fraction vs Fe concentration. Hollow symbols represent Cr = 8 at.%, solid symbols have less Cr. Present work is shown in purple triangles. Prior work of related alloys is shown in circles [152,175]. Additional literature data shows Co-9Al-7W-xFe (black)[129], Co-9Al-9W-0.12B-xFe (black)[61], and Co-30Ni-4Cr-10Al-6W-0.1B-xFe (orange) [181]. Additionally, we plot the high entropy alloy (CoFeNi)₃V₈Ti₈ [195].

As shown in Fig. 7-10, there is a clear correlation between increasing Fe content and decreasing γ' volume fraction; however, a few exceptions to this trend do exist. Moving from 0Fe4/8Cr to 10Fe4/8Cr [175] slightly increases γ' volume fraction, before it drops again. In the current alloys, we see γ' volume fraction slightly increases when going from 12% Fe VVV (0%), VTiAl (0%), and VTiTa (11%) to CCA with 26% Fe (16%). Volume fraction of γ' then dramatically improves from CCA to HEA, although this is likely due to the removal of Cr and the rebalancing of γ' -formers, suppressing the γ' -sequestering phase in the prior alloys.

Fig. 7-11 shows γ' volume fraction as a function of Fe/(Fe+Co) atomic ratio.

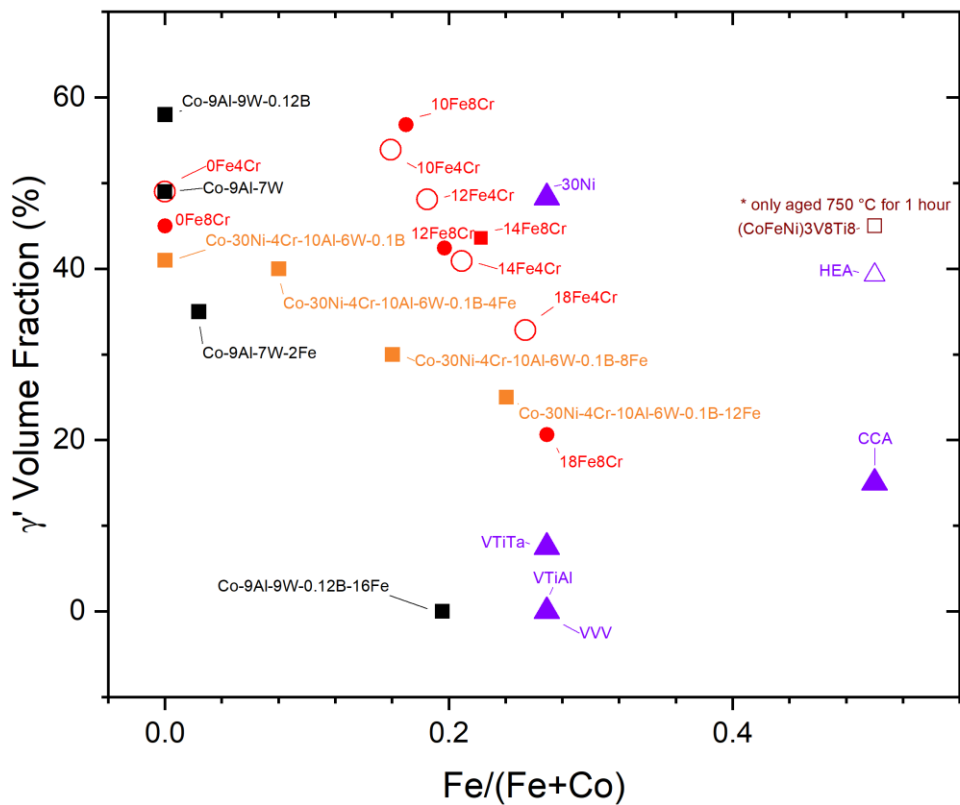


Figure 7-11. Plot of γ' volume fraction vs Fe/(Fe+Co) atomic ratio. Hollow symbols represent $Cr = 8$ at.%, solid symbols have less Cr. Present work is shown in purple triangles. Prior work of related alloys is shown in circles [152,175]. Additional literature data shows Co-9Al-7W-xFe (black)[129], Co-9Al-9W-0.12B-xFe (black)[61], and Co-30Ni-4Cr-10Al-6W-0.1B-xFe (orange) [181]. Additionally, we plot the high entropy alloy $(CoFeNi)_3V_8Ti_8$ in maroon [195].

As the Fe/(Fe+Co) atomic ratio increases, the γ' volume fraction decreases for all but a few elements, as discussed in the plot where Fe concentration is shown (Fig. 7-10).

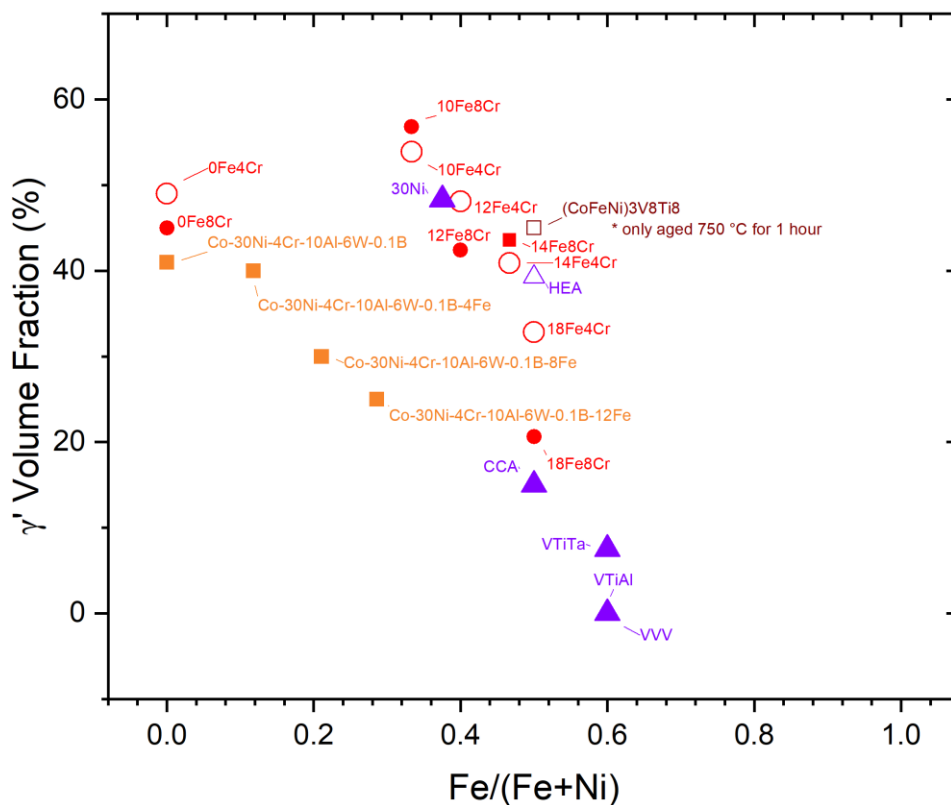


Figure 7-12. Plot of γ' volume fraction vs $Fe/(Fe+Ni)$ atomic ratio. Hollow symbols represent $Cr = 8$ at.%, solid symbols have less Cr . Present work is shown in purple triangles. Prior work of related alloys is shown in circles [152,175]. $Co-30Ni-4Cr-10Al-6W-0.1B-xFe$ (orange) [181] and the high entropy alloy $(CoFeNi)_3V_8Ti_8$ in maroon [195].

Fig. 7-12 shows the γ' volume fraction as a function of $Fe/(Fe+Ni)$. Except for the region between $0Fe_4/8Cr$ and $10Fe_4/8Cr$, each alloy series shows monotonically decreasing γ' volume fraction with increasing $Fe/(Fe+Ni)$. This suggests that Fe-rich alloys are unfavorable, and that Fe and Ni should be increased synchronously in Co-based superalloys.

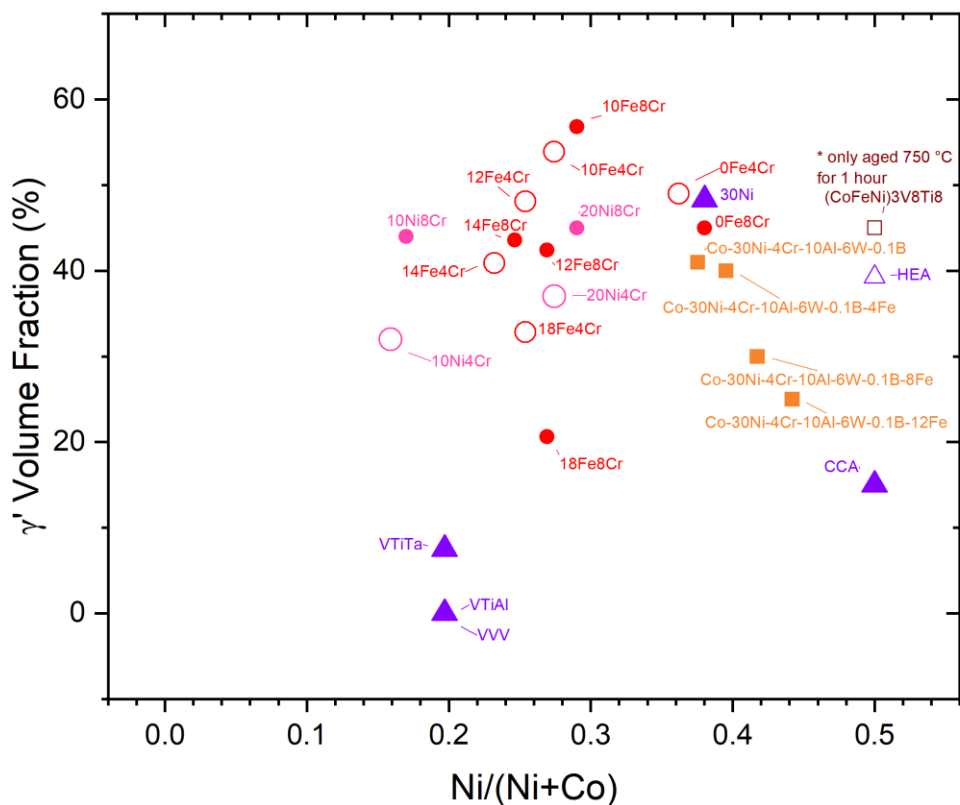


Figure 7-13. Plot of γ' volume fraction vs Ni/(Ni+Co) atomic ratio. Hollow symbols represent Cr = 8 at.%, solid symbols have less Cr. Present work is shown in purple triangles. Prior work of related alloys is shown in circles [152,175]. Co-30Ni-4Cr-10Al-6W-0.1B-xFe (orange) [181] and the high entropy alloy (CoFeNi)₃V₈Ti₈ in maroon [195].

Finally, Fig. 7-13 shows the plot of γ' volume fraction as a function of Ni/(Ni+Co) atomic ratio. In the W-containing alloy [132] increasing Ni:Co ratio actually decreases γ' volume fraction; however, this is likely because Fe is being substituted for Co (rather than Ni), so this reflects the known behavior of Fe reducing γ' volume fraction in these alloys. In our alloys, in this study and previously, there appears to be an optimal Ni/(Ni+Co) atomic ratio near 0.3, in terms of γ' volume fraction. However, the data scatter is high, so this may simply be an artifact from uncorrelated results.

7.5 Conclusions

We conclude that there is a continuous γ/γ' phase region extending from W-free Co-based superalloys (e.g. Co-10Ni-8Cr-5Al-3V-2Ti-1.5Nb-1.5Ta [152]) to alloys with high Fe (Co-30Ni-18Fe-8Cr-5Al-3V-2Ti-1.5Nb-1.5Ta), to high-entropy (multi-principal-element) alloys with completely equiatomic γ - and γ' -formers (i.e. (Co,Fe,Ni)₈₇(V,Ti,Al)₁₃). We note that the Co-rich alloy with equiatomic γ' -formers and 8Cr does not display a two-phase region: future work must be performed to determine if this is due to extra Cr destabilizing the microstructure, or the “high entropy effect” stabilizing the microstructure. We also found that higher Ni:Co ratios improves phase stability, so future alloys may be able to tolerate small additions of refractory Nb and Ta, which should improve solvus temperature.

7.6 Acknowledgements

This study was supported by the U.S. Department of Commerce, National Institute of Standards and Technology, as part of the Center for Hierarchical Materials Design (CHiMaD) at Northwestern University via award 70NANB14H012. This work made use of the MatCI Facility which receives support from the MRSEC Program (NSF DMR-1720139) of the Materials Research Center at Northwestern University; and the IMSERC X-RAY and the EPIC facility of Northwestern University’s NUANCE Center, which received support from the Soft and Hybrid Nanotechnology Experimental (SHyNE) Resource (NSF ECCS-1542205).

The authors gratefully acknowledge Dr. Carla Shute (NU) for experimental assistance in the MatCI facility. The following NU colleagues are acknowledged for helpful discussions: Dr. Amir Farkoosh, Dr. Yoshiki Kumagai, Dr. Hyeji Im.

7.7 Competing Interests Statement

Declarations of interests: none

8. References

- [1] C.T. Sims, A History of Superalloy Metallurgy for Superalloy Metallurgists, in: Superalloys 1984, 1984: pp. 399–419.
- [2] R.C. Reed, The Superalloys : Fundamentals and Applications, Cambridge University Press, 2006.
- [3] B.H. Kear, H.G.F. Wilsdorf, H. Kear, Volume 224 - Institute of Metals Division - Dislocation Configurations in Plastically Deformed Polycrystalline Cu₃Au Alloys, Transactions of the Metallurgical Society of AIME. 224 (1962) 382–386.
- [4] M.J. Donachie, S.J. Donachie, Superalloys: A Technical Guide, 2nd Edition, 2002.
- [5] R.C. Reed, C.M.F. Rae, Physical Metallurgy of the Nickel-Based Superalloys, in: Physical Metallurgy: Fifth Edition, Elsevier Inc., 2014: pp. 2215–2290. <https://doi.org/10.1016/B978-0-444-53770-6.00022-8>.
- [6] C.S. Lee, Precipitation-hardening Characteristics of Ternary Cobalt-Aluminum-X Alloys, PhD Dissertation, University of Arizona, 1971. <http://hdl.handle.net/10150/287709>.
- [7] J. Sato, T. Omori, K. Oikawa, I. Ohnuma, R. Kainuma, K. Ishida, Cobalt-base high-temperature alloys, Science (1979). 312 (2006) 90–91. <https://doi.org/10.1126/science.1121738>.
- [8] P.J. Bocchini, Microstructure and Mechanical Properties in Gamma(face-centered cubic) + Gamma Prime(L12) Precipitation-Strengthened Cobalt-based Superalloys, PhD Dissertation, Northwestern University, 2015.
- [9] S.K. Makineni, B. Nithin, K. Chattopadhyay, A new tungsten-free γ - γ' Co-Al-Mo-Nb-based superalloy, Scr Mater. 98 (2015) 36–39. <https://doi.org/10.1016/j.scriptamat.2014.11.009>.

- [10] C.H. Zenk, I. Povstugar, R. Li, F. Rinaldi, S. Neumeier, D. Raabe, M. Göken, A novel type of Co–Ti–Cr-base γ/γ' superalloys with low mass density, *Acta Mater.* 135 (2017) 244–251. <https://doi.org/10.1016/j.actamat.2017.06.024>.
- [11] F.L. Reyes Tirado, J. Perrin Toinin, D.C. Dunand, $\gamma+\gamma'$ microstructures in the Co-Ta-V and Co-Nb-V ternary systems, *Acta Mater.* 151 (2018) 137–148. <https://doi.org/10.1016/j.actamat.2018.03.057>.
- [12] T. Takasugi, HIGH TEMPERATURE STRENGTH AND DUCTILITY OF POLYCRYSTALLINE Co,Ti, 1985.
- [13] Y. Chen, C. Wang, J. Ruan, T. Omori, R. Kainuma, K. Ishida, X. Liu, High-strength Co–Al–V-base superalloys strengthened by γ' -Co₃(Al,V) with high solvus temperature, *Acta Mater.* 170 (2019) 62–74. <https://doi.org/10.1016/j.actamat.2019.03.013>.
- [14] J.J. Ruan, X.J. Liu, S.Y. Yang, W.W. Xu, T. Omori, T. Yang, B. Deng, H.X. Jiang, C.P. Wang, R. Kainuma, K. Ishida, Novel Co-Ti-V-base superalloys reinforced by L12-ordered γ' phase, *Intermetallics (Barking)*. 92 (2018) 126–132. <https://doi.org/10.1016/j.intermet.2017.09.015>.
- [15] N. Volz, C.H. Zenk, R. Cherukuri, T. Kalfhaus, M. Weiser, S.K. Makineni, C. Betzing, M. Lenz, B. Gault, S.G. Fries, J. Schreuer, R. Vaßen, S. Virtanen, D. Raabe, E. Spiecker, S. Neumeier, M. Göken, Thermophysical and Mechanical Properties of Advanced Single Crystalline Co-base Superalloys, *Metall Mater Trans A Phys Metall Mater Sci.* 49 (2018) 4099–4109. <https://doi.org/10.1007/s11661-018-4705-1>.

- [16] M. Kolb, C.H. Zenk, A. Kirzinger, I. Povstugar, D. Raabe, S. Neumeier, M. Göken, Influence of rhenium on γ' -strengthened cobalt-base superalloys, *J Mater Res.* 32 (2017) 2551–2559. <https://doi.org/10.1557/jmr.2017.242>.
- [17] S. Neumeier, L.P. Freund, M. Göken, Novel wrought γ/γ' cobalt base superalloys with high strength and improved oxidation resistance, *Scr Mater.* 109 (2015) 104–107. <https://doi.org/10.1016/j.scriptamat.2015.07.030>.
- [18] A. Suzuki, T.M. Pollock, High-temperature strength and deformation of γ/γ' two-phase Co-Al-W-base alloys, *Acta Mater.* 56 (2008) 1288–1297. <https://doi.org/10.1016/j.actamat.2007.11.014>.
- [19] F. Xue, H.J. Zhou, Q. Feng, Improved High-Temperature Microstructural Stability and Creep Property of Novel Co-Base Single-Crystal Alloys Containing Ta and Ti, *JOM.* 66 (2014) 2486–2494. <https://doi.org/10.1007/s11837-014-1181-y>.
- [20] H.Y. Yan, V.A. Vorontsov, D. Dye, Alloying effects in polycrystalline γ' strengthened Co-Al-W base alloys, *Intermetallics (Barking).* 48 (2014) 44–53. <https://doi.org/10.1016/j.intermet.2013.10.022>.
- [21] C.H. Zenk, S. Neumeier, H.J. Stone, M. Göken, Mechanical properties and lattice misfit of γ/γ' strengthened Co-base superalloys in the Co-W-Al-Ti quaternary system, *Intermetallics (Barking).* 55 (2014) 28–39. <https://doi.org/10.1016/j.intermet.2014.07.006>.
- [22] A.M. Jokisaari, S.S. Naghavi, C. Wolverton, P.W. Voorhees, O.G. Heinonen, Predicting the morphologies of γ' precipitates in cobalt-based superalloys, *Acta Mater.* 141 (2017) 273–284. <https://doi.org/10.1016/j.actamat.2017.09.003>.

- [23] J. Coakley, E.A. Lass, D. Ma, M. Frost, D.N. Seidman, D.C. Dunand, H.J. Stone, Rafting and elastoplastic deformation of superalloys studied by neutron diffraction, *Scr Mater.* 134 (2017) 110–114. <https://doi.org/10.1016/j.scriptamat.2017.03.007>.
- [24] L. Wang, X. Wu, H. Su, B. Deng, G. Liu, Z. Han, Y. Su, Y. Huang, Y. Zhang, J. Shen, G. Zhang, Microstructure and mechanical property of novel L12 nanoparticles-strengthened CoFeNi-based medium entropy alloys, *Materials Science and Engineering: A.* 840 (2022) 142917. <https://doi.org/10.1016/j.msea.2022.142917>.
- [25] R. Reed, *Physical Metallurgy and Microstructure of Superalloys*, The Institute of Materials, Minerals and Mining. (2007) 1–5.
- [26] F.L. Reyes Tirado, S. v. Taylor, D.C. Dunand, Low-density, W-free Co–Nb–V–Al-based superalloys with γ/γ' microstructure, *Materials Science and Engineering A.* 796 (2020). <https://doi.org/10.1016/j.msea.2020.139977>.
- [27] P. Zhou, D. Zhai, Y. Guo, J. Yu, X. Sun, H. Guan, Z. Hu, The Role of Ti on Reducing the Misfit of a Co-Al-W Alloy, in: TMS (Ed.), TMS 2014 143rd Annual Meeting and Exhibition, Elsevier, San Diego, n.d.
- [28] S.K. Makineni, M.P. Singh, K. Chattopadhyay, Low-Density, High-Temperature Co Base Superalloys, (2021). <https://doi.org/10.1146/annurev-matsci-080619>.
- [29] R.J. Barbera, D.L. Bodde, E.M. Ehrlich, *Cobalt: Policy Options for a Strategic Mineral*, 1982.
- [30] J.D. Donaldson, D. Beyersmann, Cobalt and Cobalt Compounds, in: *Ullmann's Encyclopedia of Industrial Chemistry*, Wiley-VCH Verlag GmbH & Co. KGaA, Weinheim, Germany, 2005. https://doi.org/10.1002/14356007.a07_281.pub2.

- [31] A.F. Giamei, Development of Single Crystal Superalloys: A Brief History, *Advanced Materials and Processes*. (2013) 26–30.
- [32] C. Nyshadham, C. Oses, J.E. Hansen, I. Takeuchi, S. Curtarolo, G.L.W. Hart, A computational high-throughput search for new ternary superalloys, *Acta Mater.* 122 (2017) 438–447. <https://doi.org/10.1016/j.actamat.2016.09.017>.
- [33] F.L. Reyes Tirado, Tungsten-free Cobalt-based Superalloys with Gamma Prime Precipitates, Northwestern University, 2019.
- [34] F.L. Reyes Tirado, S. Taylor, D.C. Dunand, Effect of Al, Ti and Cr additions on the γ - γ' microstructure of W-free Co-Ta-V-Based superalloys, *Acta Mater.* 172 (2019) 44–54. <https://doi.org/10.1016/j.actamat.2019.04.031>.
- [35] C.T.T. Liu, H. Inouye, Control of Ordered Structure and Ductility of (Fe, Co, Ni)₃V Alloys, 1979.
- [36] E. Arzt, Size Effects in Materials Due to Microstructural and Dimensional Constraints: A Comparative Review, *Acta Mater.* 46 (1998) 5611–5626. [https://doi.org/10.1016/s0957-5820\(99\)70836-0](https://doi.org/10.1016/s0957-5820(99)70836-0).
- [37] F.R.N. Nabarro, H.L. de Villiers, *The Physics Of Creep: Creep And Creep-Resistant Alloys*, 2018. <https://doi.org/10.1201/9780203979846>.
- [38] A.K. Mukherjee, J.E. Bird, J.E. Dorn, E. Org, EXPERIMENTAL CORRELATIONS FOR HIGH-TEMPERATURE CREEP, 1968.
- [39] F.R.N. Nabarro, The 1995 Institute of Metals Lecture and Robert Franklin Mehl Award Rafting in Superalloys, *Metallurgical and Materials Transactions A*. 27A (1996) 513–530. <https://link.springer.com/content/pdf/10.1007/BF02648942.pdf>.

- [40] S. Sulzer, R. Reed, Critical assessment 31: on the modelling of tertiary creep in single-crystal superalloys, *Materials Science and Technology (United Kingdom)*. 34 (2018) 2174–2201. <https://doi.org/10.1080/02670836.2018.1528733>.
- [41] H. Mughrabi, Microstructural aspects of high temperature deformation of monocrystalline nickel base superalloys: Some open problems, *Materials Science and Technology*. 25 (2009) 191–204. <https://doi.org/10.1179/174328408X361436>.
- [42] J. Svoboda, P. Luka, MODEL OF CREEP IN h001i-ORIENTED SUPERALLOY SINGLE CRYSTALS, n.d.
- [43] H. Mughrabi, The importance of sign and magnitude of γ/γ' lattice misfit in superalloys - With special reference to the new γ' -hardened cobalt-base superalloys, *Acta Mater*. 81 (2014) 21–29. <https://doi.org/10.1016/j.actamat.2014.08.005>.
- [44] N. Matan, D.C. Cox, M.A. Rist, C.M.F. Rae, CREEP OF CMSX-4 SUPERALLOY SINGLE CRYSTALS: EFFECTS OF RAFTING AT HIGH TEMPERATURE R., *Acta Mater*. 47 (1999) 3367–3381. <https://doi.org/10.5860/choice.39-2861>.
- [45] R.C. Reed, T. Tao, N. Warnken, Alloys-By-Design: Application to nickel-based single crystal superalloys, *Acta Mater*. (2009). <https://doi.org/10.1016/j.actamat.2009.08.018>.
- [46] B. Cao, Y. Zhao, T. Yang, C.T. Liu, L12-Strengthened Co-Rich Alloys for High-Temperature Structural Applications: A Critical Review, *Adv Eng Mater*. 23 (2021). <https://doi.org/10.1002/adem.202100453>.
- [47] A. Suzuki, H. Inui, T.M. Pollock, L1 2 -Strengthened Cobalt-Base Superalloys, *Annu Rev Mater Res*. 45 (2015) 345–368. <https://doi.org/10.1146/annurev-matsci-070214-021043>.

- [48] D. Coutsouradis, A. Davin, M. Lamberigts, Cobalt-based Superalloys for Applications in Gas Turbines, 1987. [https://doi.org/10.1016/0025-5416\(87\)90061-9](https://doi.org/10.1016/0025-5416(87)90061-9).
- [49] D.L. Klarstrom, Wrought Cobalt-Base Superalloys, *J Mater Eng Perform.* 2 (1993) 523–530. <https://doi.org/10.1007/BF02661736>.
- [50] C.T. Sims, A Contemporary View of Cobalt-base Alloys, *Journal of Metals.* (1969) 27–42.
- [51] S.K. Makineni, B. Nithin, D. Palanisamy, K. Chattopadhyay, Phase evolution and crystallography of precipitates during decomposition of new “tungsten-free” Co(Ni)–Mo–Al–Nb γ - γ' superalloys at elevated temperatures, *J Mater Sci.* 51 (2016) 7843–7860. <https://doi.org/10.1007/s10853-016-0026-1>.
- [52] S.K. Makineni, A. Samanta, T. Rojhirunsakool, T. Alam, B. Nithin, A.K. Singh, R. Banerjee, K. Chattopadhyay, A new class of high strength high temperature Cobalt based γ - γ' Co-Mo-Al alloys stabilized with Ta addition, *Acta Mater.* 97 (2015) 29–40. <https://doi.org/10.1016/j.actamat.2015.06.034>.
- [53] S.K. Makineni, B. Nithin, K. Chattopadhyay, Synthesis of a new tungsten-free γ - γ' Cobalt-based superalloy by tuning alloying additions, *Acta Mater.* 85 (2015) 85–94. <https://doi.org/10.1016/j.actamat.2014.11.016>.
- [54] B. Yoo, H.J. Im, J.B. Seol, P.P. Choi, On the microstructural evolution and partitioning behavior of L12-structured γ' -based Co-Ti-W alloys upon Cr and Al alloying, *Intermetallics (Barking)*. 104 (2019) 97–102. <https://doi.org/10.1016/j.intermet.2018.10.027>.

- [55] J.P. Minshull, S. Neumeier, M.G. Tucker, H.J. Stone, Al-L12 structures in the Al-Co-Ni-Ti quaternary phase system, in: *Adv Mat Res*, 2011: pp. 399–404. <https://doi.org/10.4028/www.scientific.net/AMR.278.399>.
- [56] C.H. Zenk, N. Volz, A. Bezold, L.-K. Huber, Y.M. Eggeler, E. Spiecker, M. Göken, S. Neumeier, The Effect of Alloying on the Thermophysical and Mechanical Properties of Co–Ti–Cr-Based Superalloys, in: *Superalloys 2020*, 2020: pp. 909–919. https://doi.org/10.1007/978-3-030-51834-9_89.
- [57] K.A. Christofidou, N.G. Jones, E.J. Pickering, R. Flacau, M.C. Hardy, H.J. Stone, The microstructure and hardness of Ni-Co-Al-Ti-Cr quinary alloys, *J Alloys Compd.* (2016). <https://doi.org/10.1016/j.jallcom.2016.07.159>.
- [58] J. Yu, S. Guo, Y. Chen, J. Han, Y. Lu, Q. Jiang, C. Wang, X. Liu, A two-stage predicting model for γ' solvus temperature of L12-strengthened Co-base superalloys based on machine learning, *Intermetallics (Barking)*. 110 (2019) 106466. <https://doi.org/10.1016/j.intermet.2019.04.009>.
- [59] Y. Chen, C. Wang, J. Ruan, T. Omori, R. Kainuma, K. Ishida, X. Liu, High-strength Co–Al–V-base superalloys strengthened by γ' -Co₃(Al,V) with high solvus temperature, *Acta Mater.* 170 (2019) 62–74. <https://doi.org/10.1016/j.actamat.2019.03.013>.
- [60] X. Liu, W. Cai, Z. Chen, Y. Chen, X. Chen, S. Yang, Y. Lu, J. Han, C. Wang, Effects of alloying additions on the microstructure, lattice misfit, and solvus temperature of a novel Co–Ni-based superalloy, *Intermetallics (Barking)*. 141 (2022). <https://doi.org/10.1016/j.intermet.2021.107431>.

- [61] A. Bauer, S. Neumeier, F. Pyczak, M. Göken, Creep Strength and Microstructure of Polycrystalline γ' - Strengthened Cobalt-Base Superalloys, in: Superalloys 2012, 2012: pp. 695–703. <https://doi.org/10.1002/9781118516430.ch77>.
- [62] K. Shinagawa, T. Omori, J. Sato, K. Oikawa, I. Ohnuma, R. Kainuma, K. Ishida, Phase equilibria and microstructure on γ' phase in Co-Ni-Al-W system, Mater Trans. 49 (2008) 1474–1479. <https://doi.org/10.2320/matertrans.MER2008073>.
- [63] J.C. Russ, R.T. Dehoff, Practical Stereology, Springer US, 2000. <https://doi.org/10.1007/978-1-4615-1233-2>.
- [64] J. Müller, A Study on Microstructures and Extended Defects in Ni-and Co-Base Superalloys- Development and Application of Advanced TEM Techniques, n.d.
- [65] Y. Chen, C. Wang, J. Ruan, S. Yang, T. Omori, R. Kainuma, K. Ishida, J. Han, Y. Lu, X. Liu, Development of low-density γ/γ' Co–Al–Ta-based superalloys with high solvus temperature, Acta Mater. 188 (2020) 652–664. <https://doi.org/10.1016/j.actamat.2020.02.049>.
- [66] C.H. Zenk, N. Volz, C. Zenk, P.J. Felfer, S. Neumeier, Impact of the Co/Ni-ratio on microstructure, thermophysical properties and creep performance of multi-component γ' -strengthened superalloys, Crystals (Basel). 10 (2020) 1–12. <https://doi.org/10.3390/cryst10111058>.
- [67] P. Zhou, X. Gao, D. Song, Y. Liu, J. Cheng, Effect of Ni on Microstructure and Mechanical Property of a Co-Ti-V-Based Superalloy, Scanning. 2021 (2021). <https://doi.org/10.1155/2021/6678085>.
- [68] P. Fratzl, O. Paris, W.C. Johnson, INFLUENCE OF COHERENCY STRESS ON MICROSTRUCTURAL EVOLUTION IN MODEL Ni-Al-Mo ALLOYS, 1995.

- [69] S. Meher, L.J. Carroll, T.M. Pollock, M.C. Carroll, Solute partitioning in multi-component γ/γ' Co-Ni-base superalloys with near-zero lattice misfit, *Scr Mater.* 113 (2016) 185–189. <https://doi.org/10.1016/j.scriptamat.2015.10.039>.
- [70] F.R.N.N. Nabarro, Rafting in superalloys, *Metall Mater Trans A Phys Metall Mater Sci.* 27 (1996) 513–530. <https://doi.org/10.1007/BF02648942>.
- [71] I. Povstugar, C.H. Zenk, R. Li, P.P. Choi, S. Neumeier, O. Dolotko, M. Hoelzel, M. Göken, D. Raabe, Elemental partitioning, lattice misfit and creep behaviour of Cr containing gamma prime strengthened Co base superalloys, *Materials Science and Technology (United Kingdom)*. 32 (2016) 220–225. <https://doi.org/10.1179/1743284715Y.0000000112>.
- [72] B. Nithin, A. Samanta, S.K. Makineni, T. Alam, P. Pandey, A.K. Singh, R. Banerjee, K. Chattopadhyay, Effect of Cr addition on $\gamma-\gamma'$ cobalt-based Co–Mo–Al–Ta class of superalloys: a combined experimental and computational study, *J Mater Sci.* 52 (2017) 11036–11047. <https://doi.org/10.1007/s10853-017-1159-6>.
- [73] P. Pandey, S.K. Makineni, A. Samanta, A. Sharma, S.M. Das, B. Nithin, C. Srivastava, A.K. Singh, D. Raabe, B. Gault, K. Chattopadhyay, Elemental site occupancy in the L12 A3B ordered intermetallic phase in Co-based superalloys and its influence on the microstructure, *Acta Mater.* 163 (2019) 140–153. <https://doi.org/10.1016/j.actamat.2018.09.049>.
- [74] X. Zhuang, S. Antonov, L. Li, Q. Feng, Effect of alloying elements on the coarsening rate of γ' precipitates in multi-component CoNi-based superalloys with high Cr content, *Scr Mater.* 202 (2021). <https://doi.org/10.1016/j.scriptamat.2021.114004>.

- [75] C. Chu, Q. Guo, Y. Guan, Z. Qiao, Y. Liu, Deformation mechanisms of a γ' phase strengthened CoNi-based superalloy at high temperatures, *Materials Science and Engineering A*. 833 (2022). <https://doi.org/10.1016/j.msea.2021.142587>.
- [76] Y. Li, F. Pyczak, A. Stark, L. Wang, M. Oehring, J. Paul, U. Lorenz, Temperature dependence of misfit in different Co–Al–W ternary alloys measured by synchrotron X-ray diffraction, *J Alloys Compd*. 819 (2020). <https://doi.org/10.1016/j.jallcom.2019.152940>.
- [77] H.Y. Yan, J. Coakley, V.A. Vorontsov, N.G. Jones, H.J. Stone, D. Dye, Alloying and the micromechanics of Co-Al-W-X quaternary alloys, *Materials Science and Engineering A*. 613 (2014) 201–208. <https://doi.org/10.1016/j.msea.2014.05.044>.
- [78] J. Coakley, E.A. Lass, D. Ma, M. Frost, H.J. Stone, D.N. Seidman, D.C. Dunand, Lattice parameter misfit evolution during creep of a cobalt-based superalloy single crystal with cuboidal and rafted gamma-prime microstructures, *Acta Mater*. 136 (2017) 118–125. <https://doi.org/10.1016/j.actamat.2017.06.025>.
- [79] Q. Gao, Y. Jiang, Z. Liu, H. Zhang, C. Jiang, X. Zhang, H. Li, Effects of alloying elements on microstructure and mechanical properties of Co–Ni–Al–Ti superalloy, *Materials Science and Engineering A*. 779 (2020). <https://doi.org/10.1016/j.msea.2020.139139>.
- [80] B. Chattopadhyay, G.C. Wood, The Transient Oxidation of Alloys, *Oxidation of Metals*. 2 (1970) 373–399. <https://link.springer.com/content/pdf/10.1007/BF00604477.pdf>.
- [81] S. Mrowec, A. Stoklosa, Calculations of Parabolic Rate Constants for Metal Oxidation, *Oxidation of Metals*. 8 (1974) 379–391.

- [82] D. Monceau, B. Pieraggi, Determination of Parabolic Rate Constants from a Local Analysis of Mass-Gain Curves, *Oxidation of Metals*. 50 (1998) 477–493.
- [83] M. Weiser, M.C. Galetz, H.E. Zschau, C.H. Zenk, S. Neumeier, M. Göken, S. Virtanen, Influence of Co to Ni ratio in γ' -strengthened model alloys on oxidation resistance and the efficacy of the halogen effect at 900 °C, *Corros Sci*. 156 (2019) 84–95. <https://doi.org/10.1016/j.corsci.2019.05.007>.
- [84] C.H. Zenk, S. Neumeier, N.M. Engl, S.G. Fries, O. Dolotko, M. Weiser, S. Virtanen, M. Göken, Intermediate Co/Ni-base model superalloys - Thermophysical properties, creep and oxidation, *Scr Mater*. 112 (2016) 83–86. <https://doi.org/10.1016/j.scriptamat.2015.09.018>.
- [85] M.E. Kassner, *Fundamentals of Creep in Metals and Alloys*, 2nd ed., Elsevier Science, 2009.
- [86] A. Bauer, S. Neumeier, F. Pyczak, R.F. Singer, M. Göken, Creep properties of different γ' -strengthened Co-base superalloys, *Materials Science and Engineering A*. 550 (2012) 333–341. <https://doi.org/10.1016/j.msea.2012.04.083>.
- [87] A. Bauer, S. Neumeier, F. Pyczak, M. Göken, Influence of iridium on the properties of γ' -strengthened co-base superalloys, *Adv Eng Mater*. 17 (2015) 748–754. <https://doi.org/10.1002/adem.201400266>.
- [88] D.-W. Chung, J.P. Toinin, E.A. Lass, D.N. Seidman, D.C. Dunand, Effects of Cr on the properties of multicomponent cobalt-based superalloys with ultra high γ' volume fraction, *J Alloys Compd*. 832 (2020) 1–10. <https://doi.org/10.1016/j.jallcom.2020.154790>.

- [89] D.J. Sauza, D.C. Dunand, D.N. Seidman, Microstructural evolution and high-temperature strength of a γ (f.c.c.)/ γ' (L12) Co–Al–W–Ti–B superalloy, *Acta Mater.* 174 (2019) 427–438. <https://doi.org/10.1016/j.actamat.2019.05.058>.
- [90] D.S. Ng, D.W. Chung, J.P. Toinin, D.N. Seidman, D.C. Dunand, E.A. Lass, Effect of Cr additions on a γ - γ' microstructure and creep behavior of a Co-based superalloy with low W content, *Materials Science and Engineering A.* 832 (2020) 154790. <https://doi.org/10.1016/j.msea.2020.139108>.
- [91] P.J. Bocchini, C.K. Sudbrack, R.D. Noebe, D.C. Dunand, D.N. Seidman, Microstructural and creep properties of boron- and zirconium-containing cobalt-based superalloys, *Materials Science and Engineering A.* 682 (2017) 260–269. <https://doi.org/10.1016/j.msea.2016.10.124>.
- [92] E.A. Lass, D.J. Sauza, D.C. Dunand, D.N. Seidman, Multicomponent γ' -strengthened Co-based superalloys with increased solvus temperatures and reduced mass densities, *Acta Mater.* 147 (2018) 284–295. <https://doi.org/10.1016/j.actamat.2018.01.034>.
- [93] H. Okamoto, Al-Ni (Aluminum-Nickel), *J Phase Equilibria Diffus.* 25 (2004) 394–394. <https://doi.org/10.1361/15477030420232>.
- [94] Y.F. Gu, C. Cui, D. Ping, H. Harada, T. Fukuda, J. Fujioka, Creep behavior of new kinds of Ni-Co-base superalloys, *Materials Science and Engineering A.* 510–511 (2009) 250–255. <https://doi.org/10.1016/j.msea.2008.04.128>.
- [95] R.D. Dragsdorf, W.D. Forgeng, *The Intermetallic Phases in the Cobalt-Tantalum System*, 1962.

- [96] K. Shinagawa, H. Chinen, T. Omori, K. Oikawa, I. Ohnuma, K. Ishida, R. Kainuma, Phase equilibria and thermodynamic calculation of the Co-Ta binary system, *Intermetallics* (Barking). 49 (2014) 87–97. <https://doi.org/10.1016/j.intermet.2014.01.015>.
- [97] H. Okamoto, Co-Ta (Cobalt-Tantalum), *J Phase Equilibria Diffus.* 25 (2005) 571–572. <https://doi.org/10.1361/15477020421115>.
- [98] C.Y. Cui, Y.F. Gu, D.H. Ping, H. Harada, Phase constituents in Ni-Al-Co-Ti quaternary alloys, *Intermetallics* (Barking). 16 (2008) 910–916. <https://doi.org/10.1016/j.intermet.2008.04.006>.
- [99] B.H. Toby, R.B. Von Dreele, *GSAS-II: the genesis of a modern open-source all purpose crystallography software package*, 2013. <https://doi.org/10.1107/S0021889813003531>.
- [100] A. Royer, P. Bastie, Misfit and Lattice Parameters of Single Crystal AM1 Superalloy: Effects of Temperature, Precipitate Morphology and γ' Interfacial Stresses, in: *The Minerals, Metals and Materials Society*, 2012: pp. 221–228. https://doi.org/10.7449/1996/superalloys_1996_221_228.
- [101] S. Neumeier, F. Pyczak, M. Göken, The temperature dependent lattice misfit of rhenium and ruthenium containing nickel-base superalloys – Experiment and modelling, *Mater Des.* 198 (2021). <https://doi.org/10.1016/j.matdes.2020.109362>.
- [102] H.-A. Kuhn, H. Biermann I, AN X-RAY STUDY OF CREEP-DEFORMATION INDUCED CHANGES OF THE LATTICE MISMATCH IN THE γ' -HARDENED MONOCRYSTALLINE NICKEL-BASE SUPERALLOY SRR 99, 1991.
- [103] W.F. Gale, T.C. Totemeier, eds., Elastic properties, damping capacity and shape memory alloys, in: *Smithells Metals Reference Book*, 8th ed., ASM international, Elsevier, 2004: pp. 1–45.

- [104] Nickel (Ni) - Properties, Applications, AZOM. (2001).
- [105] An Introduction to Cobalt, AZOM. (2001).
- [106] J. Minshull, Al-L1 2 Alloys Based on the Al-Co-Ni-Ti Quaternary System, University of Cambridge, 2009.
- [107] H. Okamoto, Co-Ta (Cobalt-Tantalum), *J Phase Equilibria Diffus.* 25 (2005) 571–572.
<https://doi.org/10.1361/15477020421115>.
- [108] D.A. Porter, K.E. Easterling, M.Y. Sherif, *Phase Transformations in Metals and Alloys*, 3rd ed., CRC Press, 2009.
- [109] A. Bhowmik, K.M. Knowles, H.J. Stone, Discontinuous precipitation of Co 3V in a complex Co-based alloy, *Philosophical Magazine.* 94 (2014) 752–763.
<https://doi.org/10.1080/14786435.2013.861946>.
- [110] P.E. Kueser, K. Detert, J.W. Toth, R.J. Towner, *HIGH TEMPERATURE (800" TO 1600" F) MAGNETIC MATERIALS*, n.d.
- [111] P. Wang, W. Xiong, U.R. Kattner, C.E. Campbell, E.A. Lass, O.Y. Kontsevoi, G.B. Olson, Thermodynamic re-assessment of the Al-Co-W system, *CALPHAD.* 59 (2017) 112–130.
<https://doi.org/10.1016/j.calphad.2017.09.007>.
- [112] W.W. Xu, Q. Yu, F. Xia, G. Yin, Y. Huang, L. Chen, Exploration of crystal structure and the origin of unexpected intrinsic ductility of χ Co₇Ta₂, *J Alloys Compd.* 797 (2019) 1198–1204.
<https://doi.org/10.1016/j.jallcom.2019.05.223>.
- [113] Alessio Malandrucolo, Stefano Gialanella, *Topics in Mining, Metallurgy and Materials Engineering Series Editor: Aerospace Alloys*, 2020. <http://www.springer.com/series/11054>.

- [114] E. Akca, A. Gürsel, A Review on Superalloys and IN718 Nickel-Based INCONEL Superalloy, *Periodicals of Engineering and Natural Sciences (PEN)*. 3 (2015). <https://doi.org/10.21533/pen.v3i1.43>.
- [115] C.K. Yong, G.J. Gibbons, C.C. Wong, G. West, A critical review of the material characteristics of additive manufactured in718 for high-temperature application, *Metals (Basel)*. 10 (2020) 1–22. <https://doi.org/10.3390/met10121576>.
- [116] A.K. Roy, A. Venkatesh, Evaluation of yield strength anomaly of Alloy 718 at 700-800 °C, *J Alloys Compd.* 496 (2010) 393–398. <https://doi.org/10.1016/j.jallcom.2010.02.023>.
- [117] J.F. Barker, The Initial Years of Alloy 718 - A G.E. Perspective, *Superalloy 718--Metallurgy and Applications*. (1989) 269–277.
- [118] Y. Wu, C. Li, X. Xia, H. Liang, Q. Qi, Y. Liu, Precipitate coarsening and its effects on the hot deformation behavior of the recently developed γ' -strengthened superalloys, *J Mater Sci Technol.* 67 (2021) 95–104. <https://doi.org/10.1016/j.jmst.2020.06.025>.
- [119] H. de Cicco, M.I. Lупpo, L.M. Gribaudo, J. Ovejero-García, Microstructural development and creep behavior in A286 superalloy, *Mater Charact.* 52 (2004) 85–92. <https://doi.org/10.1016/j.matchar.2004.03.007>.
- [120] T. Sugahara, A.A. Couto, M.J.R. Barboza, F.P. Neto, R.J. Takahashi, D.A.P. Reis, Creep and mechanical behavior study of Inconel 718 Superalloy, *Materials Research*. 25 (2022). <https://doi.org/10.1590/1980-5373-MR-2021-0280>.

- [121] Y. Chen, C. Wang, J. Ruan, T. Omori, R. Kainuma, K. Ishida, X. Liu, High-strength Co–Al–V-base superalloys strengthened by γ' -Co₃ (Al,V) with high solvus temperature, *Acta Mater.* 170 (2019) 62–74. <https://doi.org/10.1016/j.actamat.2019.03.013>.
- [122] H.Y. Yan, V.A. Vorontsov, D. Dye, Alloying effects in polycrystalline γ' strengthened Co-Al-W base alloys, *Intermetallics* (Barking). 48 (2014) 44–53. <https://doi.org/10.1016/j.intermet.2013.10.022>.
- [123] C.H. Zenk, S. Neumeier, H.J. Stone, M. Göken, Mechanical properties and lattice misfit of γ/γ' strengthened Co-base superalloys in the Co-W-Al-Ti quaternary system, *Intermetallics* (Barking). 55 (2014) 28–39. <https://doi.org/10.1016/j.intermet.2014.07.006>.
- [124] A.M. Jokisaari, S.S. Naghavi, C. Wolverton, P.W. Voorhees, O.G. Heinonen, Predicting the morphologies of γ' precipitates in cobalt-based superalloys, *Acta Mater.* 141 (2017) 273–284. <https://doi.org/10.1016/j.actamat.2017.09.003>.
- [125] K. Shinagawa, T. Omori, J. Sato, K. Oikawa, I. Ohnuma, R. Kainuma, K. Ishida, Phase equilibria and microstructure on γ' phase in Co-Ni-Al-W system, *Mater Trans.* 49 (2008) 1474–1479. <https://doi.org/10.2320/matertrans.MER2008073>.
- [126] C. Chu, Q. Guo, Y. Guan, Z. Qiao, Y. Liu, Deformation mechanisms of a γ' phase strengthened CoNi-based superalloy at high temperatures, *Materials Science and Engineering A.* 833 (2022). <https://doi.org/10.1016/j.msea.2021.142587>.
- [127] B. Ohl, J. Minshull, L. Owen, D. Dunand, H. Stone, Lattice misfit and aging of quaternary (Co,Ni)-12.5 at.%(Ta,Al) alloys with $\gamma + \gamma'$ microstructure, (n.d.).

- [128] T. Omori, K. Oikawa, J. Sato, I. Ohnuma, U.R. Kattner, R. Kainuma, K. Ishida, Partition behavior of alloying elements and phase transformation temperatures in Co-Al-W-base quaternary systems, *Intermetallics (Barking)*. 32 (2013) 274–283. <https://doi.org/10.1016/j.intermet.2012.07.033>.
- [129] M. Ooshima, K. Tanaka, N.L. Okamoto, K. Kishida, H. Inui, Effects of quaternary alloying elements on the γ' solvus temperature of Co-Al-W based alloys with fcc/L12 two-phase microstructures, *J Alloys Compd.* 508 (2010) 71–78. <https://doi.org/10.1016/j.jallcom.2010.08.050>.
- [130] M. Cartón-Cordero, B. Srinivasarao, M. Campos, A. García-Junceda, J.M. Torralba, On the role of processing parameters in sintered new Co-based (W,Al) alloys, *J Alloys Compd.* 674 (2016) 406–412. <https://doi.org/10.1016/j.jallcom.2016.03.077>.
- [131] E.A. Lass, The effects of Fe and Si on the phase equilibria in a γ' -strengthened Co–Al–W-based superalloy, *J Alloys Compd.* 825 (2020). <https://doi.org/10.1016/j.jallcom.2020.154158>.
- [132] F. Xue, D.W. Chung, S.I. Baik, E.A. Lass, D.C. Dunand, D.N. Seidman, Effects of Fe additions on phase stability, creep properties and oxidation resistance of a CoNi-base superalloy, In *Preparation*. (n.d.).
- [133] L.J. Nagel, B. Fultz, J.L. Robertson, Phase Equilibria of Co₃V, *Journal of Phase Equilibria*. 18 (1997) 21–23.
- [134] S. Saito, The Crystal Structure of VCo₃, *500 Acta Cryst.* 12 (1959) 500.
- [135] J. Xu, A.J. Freeman, Electronic structure, cohesive properties, and phase stability of Ni₃V, Co₃V, and Fe₃V, *Phys Rev B*. 45 (1992) 10863–10871.

- [136] A.K. Sinha, Close-Packed Ordered AB₃ Structures in Ternary Alloys of Certain Transition Metals, *Transactions of the Metallurgical Society of AIME*. 245 (1969) 911–917.
- [137] C.T. Liu, Physical metallurgy and mechanical properties of ductile ordered alloys (Fe, Co, Ni)₃V, *International Metals Reviews*. 29 (1984) 168–194. <https://doi.org/10.1179/imtr.1984.29.1.168>.
- [138] R.E. Hanneman, A.N. Mariano, Lattice-Parameter and Volumetric Data of the Iron-Vanadium System, *Transactions of the Metallurgical Society of AIME*. 230 (1964) 937–939.
- [139] H.P. Stüwe, Description of the Sigma Phase as a Structure with Sphere Packing, *Transactions of the Metallurgical Society of AIME*. 215 (1959) 408–411.
- [140] C.T. Liu, H. Inouye, Control of Ordered Structure and Ductility of (Fe, Co, Ni)₃V Alloys, *Metallurgical Transactions A*. 10A (1979) 1515–1525.
- [141] C.T. Liu, Development of Ductile Long-Range Ordered Alloys for Fusion Reactor Systems, *Journal of Nuclear Materials*. 85 (1979) 907–911.
- [142] T.T. Liu, DEVELOPMENT OF IRON-BASE LONG-RANGE ORDERED (LRO) ALLOYS FOR FUSION REACTOR FIRST WALL AND BLANKET APPLICATIONS, *Journal of Nuclear Materials*. 103 (1981) 1205–1210.
- [143] C.T. Liu, E.M. Schulson, The Fracture of Ordered (Fe, Co)₃V, *Metallurgical Transactions A*. 15A (1984) 701–706.
- [144] C.T. Liu, Atomic Ordering and Structural Transformation in the V-Co-Ni Ternary Alloys, *Metallurgical Transactions*. 4 (1973) 1743–1753.
- [145] Y. Umakoshi, J.R. Boland, D.P. Pope, V. Vitek, The Temperature and Orientation Dependence of the Flow Stress of Ordered and Disordered (Fe, Co)₃V Single Crystals, 1984.

- [146] K.R. Finney, L.W. Lherbier, Long Range Ordered (LRO) Superalloys, n.d.
- [147] J. Chen, X. Zhou, W. Wang, B. Liu, Y. Lv, W. Yang, D. Xu, Y. Liu, A review on fundamental of high entropy alloys with promising high-temperature properties, *J Alloys Compd.* 760 (2018) 15–30. <https://doi.org/10.1016/j.jallcom.2018.05.067>.
- [148] M. Joele, W.R. Matizamhuka, A review on the high temperature strengthening mechanisms of high entropy superalloys (Hesa), *Materials.* 14 (2021). <https://doi.org/10.3390/ma14195835>.
- [149] L. Wang, X. Wu, H. Su, B. Deng, G. Liu, Z. Han, Y. Su, Y. Huang, Y. Zhang, J. Shen, G. Zhang, Microstructure and mechanical property of novel L12 nanoparticles-strengthened CoFeNi-based medium entropy alloys, *Materials Science and Engineering: A.* 840 (2022) 142917. <https://doi.org/10.1016/j.msea.2022.142917>.
- [150] Z.G. Wang, W. Zhou, L.M. Fu, J.F. Wang, R.C. Luo, X.C. Han, B. Chen, X.D. Wang, Effect of coherent L12 nanoprecipitates on the tensile behavior of a fcc-based high-entropy alloy, *Materials Science and Engineering A.* 696 (2017) 503–510. <https://doi.org/10.1016/j.msea.2017.04.111>.
- [151] F.L. Reyes Tirado, D.C. Dunand, Increasing γ' volume fraction in Co–Nb–V- and Co–Ta–V-based superalloys, *Journal of Materials Research and Technology.* 11 (2021) 2305–2313. <https://doi.org/10.1016/j.jmrt.2021.02.028>.
- [152] B. Ohl, D.C. Dunand, Effects of Ni and Cr additions on $\gamma + \gamma'$ Microstructure and Mechanical Properties of W-free Co-Al-V-Nb-Ta-based Superalloys, *Materials Science & Engineering A.* 849 (2022). <https://doi.org/https://doi.org/10.1016/j.msea.2022.143401>.
- [153] B. Ohl, D.C. Dunand, Design of W-free Co-based Superalloys with γ - γ' -Microstructure, (2019).

- [154] B.H. Toby, R.B. von Dreele, *GSAS-II*: the genesis of a modern open-source all purpose crystallography software package, 2013. <https://doi.org/10.1107/S0021889813003531>.
- [155] K. Shinagawa, T. Omori, J. Sato, K. Oikawa, I. Ohnuma, R. Kainuma, K. Ishida, Phase equilibria and microstructure on γ' phase in Co-Ni-Al-W system, *Mater Trans.* 49 (2008) 1474–1479. <https://doi.org/10.2320/matertrans.MER2008073>.
- [156] J. Zhu, M.S. Titus, T.M. Pollock, Experimental Investigation and Thermodynamic Modeling of the Co-Rich Region in the Co-Al-Ni-W Quaternary System, *J Phase Equilibria Diffus.* 35 (2014) 595–611. <https://doi.org/10.1007/s11669-014-0327-5>.
- [157] A. Suzuki, G.C. DeNolf, T.M. Pollock, Flow stress anomalies in γ/γ' two-phase Co-Al-W-base alloys, *Scr Mater.* 56 (2007) 385–388. <https://doi.org/10.1016/j.scriptamat.2006.10.039>.
- [158] T.P. Gabb, R.L. Dreshfield, Superalloy data, in: C.T. Sims, N.S. Stoloff, W.C. Hagel (Eds.), *Superalloys II*, Wiley-Interscience, New York, 1987: pp. 575–579.
- [159] Engineering Properties of ALLOY 713C, n.d. https://nickelinstitute.org/media/2487/alloys-713c_337.pdf (accessed April 2, 2022).
- [160] INCONEL ® alloy 718, n.d. <https://www.specialmetals.com/documents/technical-bulletins/inconel/inconel-alloy-718.pdf> (accessed April 2, 2022).
- [161] Blaine. Geddes, *Superalloys : alloying and performance.*, ASM International, 2010.
- [162] A.J. Knowles, D. Dye, R.J. Dodds, A. Watson, C.D. Hardie, S.A. Humphry-Baker, Tungsten-based bcc-superalloys, *Appl Mater Today.* 23 (2021). <https://doi.org/10.1016/j.apmt.2021.101014>.

- [163] C. Helbig, A.M. Bradshaw, A. Thorenz, A. Tuma, Supply Risk Considerations for the Elements in Nickel-Based Superalloys, *Resources*. 9 (2020) 1–16. <https://doi.org/10.3390/resources9090106>.
- [164] D.W. Maclachlan, D.M. Knowles, Modelling and prediction of the stress rupture behaviour of single crystal superalloys, 2001. www.elsevier.com/locate/msea.
- [165] I.N. Vladimirov, S. Reese, G. Eggeler, Constitutive modelling of the anisotropic creep behaviour of nickel-base single crystal superalloys, *Int J Mech Sci*. 51 (2009) 305–313. <https://doi.org/10.1016/j.ijmecsci.2009.02.004>.
- [166] B. Fedelich, A. Epishin, T. Link, H. Klingelhöffer, G. Künecke, P.D. Portella, Experimental characterization and mechanical modeling of creep induced rafting in superalloys, in: *Comput Mater Sci*, 2012: pp. 2–6. <https://doi.org/10.1016/j.commatsci.2012.05.071>.
- [167] Y.K. Kim, D. Kim, H.K. Kim, C.S. Oh, B.J. Lee, An intermediate temperature creep model for Ni-based superalloys, *Int J Plast*. 79 (2016) 153–175. <https://doi.org/10.1016/j.ijplas.2015.12.008>.
- [168] S. Sulzer, R. Reed, Critical assessment 31: on the modelling of tertiary creep in single-crystal superalloys, *Materials Science and Technology (United Kingdom)*. 34 (2018) 2174–2201. <https://doi.org/10.1080/02670836.2018.1528733>.
- [169] V. Venkatesh, H.J. Rack, A neural network approach to elevated temperature creep-fatigue life prediction, 1999.
- [170] Y.S. Yoo, C.Y. Jo, C.N. Jones, Compositional prediction of creep rupture life of single crystal Ni base superalloy by Bayesian neural network, 2002. www.elsevier.com/locate/msea.

- [171] J.J. He, R. Sandström, Creep rupture prediction using constrained neural networks with error estimates, *Materials at High Temperatures*. 39 (2022) 239–251. <https://doi.org/10.1080/09603409.2022.2078147>.
- [172] A. Rohatgi, WebPlotDigitizer, (2020). <https://automeris.io/WebPlotDigitizer/>.
- [173] B.H. Toby, R.B. von Dreele, GSAS-II: the genesis of a modern open-source all purpose crystallography software package, 2013. <https://doi.org/10.1107/S0021889813003531>.
- [174] C.H. Zenk, S. Neumeier, H.J. Stone, M. Göken, Mechanical properties and lattice misfit of γ/γ' strengthened Co-base superalloys in the Co-W-Al-Ti quaternary system, *Intermetallics (Barking)*. 55 (2014) 28–39. <https://doi.org/10.1016/j.intermet.2014.07.006>.
- [175] B. Ohl, L. Owen, H. Stone, D.C. Dunand, Microstructure and Mechanical Properties of L1 2-strengthened Co-Ni-Fe-based Superalloys, n.d. <https://ssrn.com/abstract=4349977>.
- [176] K. Choudhary, K.F. Garrity, A.C.E. Reid, B. DeCost, A.J. Biacchi, A.R. Hight Walker, Z. Trautt, J. Hattrick-Simpers, A.G. Kusne, A. Centrone, A. Davydov, J. Jiang, R. Pachter, G. Cheon, E. Reed, A. Agrawal, X. Qian, V. Sharma, H. Zhuang, S. v. Kalinin, B.G. Sumpter, G. Pilania, P. Acar, S. Mandal, K. Haule, D. Vanderbilt, K. Rabe, F. Tavazza, The joint automated repository for various integrated simulations (JARVIS) for data-driven materials design, *NPJ Comput Mater*. 6 (2020). <https://doi.org/10.1038/s41524-020-00440-1>.
- [177] L. Ward, A. Agrawal, A. Choudhary, C. Wolverton, A general-purpose machine learning framework for predicting properties of inorganic materials, *NPJ Comput Mater*. 2 (2016) 1–7. <https://doi.org/10.1038/npjcompumats.2016.28>.

- [178] K. Choudhary, B. Decost, F. Tavazza, Machine learning with force-field-inspired descriptors for materials: Fast screening and mapping energy landscape, *Phys Rev Mater.* 2 (2018). <https://doi.org/10.1103/PhysRevMaterials.2.083801>.
- [179] G. Lindwall, K.W. Moon, M. Williams, W. Tso, C. Campbell, Development of a Diffusion Mobility Database for Co-Based Superalloys, *J Phase Equilibria Diffus.* 43 (2022) 931–952. <https://doi.org/10.1007/s11669-022-01011-1>.
- [180] T. Caliński, J. Harabasz, A Dendrite Method For Cluster Analysis, *Communications in Statistics.* 3 (1974) 1–27. <https://doi.org/10.1080/03610927408827101>.
- [181] F. Xue, D.W. Chung, S.I. Baik, D.T. Keane, W.E.J. Guise, E.A. Lass, D.N. Seidman, D.C. Dunand, Effects of Fe additions on phase stability, creep properties and oxidation resistance of a Co-Ni-base superalloy, In Preparation. (2023).
- [182] A.M. Manzoni, S. Singh, H.M. Daoud, R. Popp, R. Völkl, U. Glatzel, N. Wanderka, On the path to optimizing the Al-Co-Cr-Cu-Fe-Ni-Ti high entropy alloy family for high temperature applications, *Entropy.* 18 (2016). <https://doi.org/10.3390/e18040104>.
- [183] T. Yang, Y.L. Zhao, Y. Tong, Z.B. Jiao, J. Wei, J.X. Cai, X.D. Han, D. Chen, A. Hu, J.J. Kai, K. Lu, Y. Liu, C.T. Liu, Multicomponent intermetallic nanoparticles and superb mechanical behaviors of complex alloys, *Science* (1979). 362 (2018) 933–937. <https://doi.org/10.1126/science.aas8815>.
- [184] H.Y. Yan, V.A. Vorontsov, D. Dye, Alloying effects in polycrystalline γ' strengthened Co-Al-W base alloys, *Intermetallics* (Barking). 48 (2014) 44–53. <https://doi.org/10.1016/j.intermet.2013.10.022>.

- [185] F. Xue, D.W. Chung, S.I. Baik, D.T. Keane, W.E.J. Guise, E.A. Lass, D.N. Seidman, D.C. Dunand, D.N. Seidman, Effects of Fe additions on phase stability, creep properties and oxidation resistance of a CoNi-base superalloy, In Preparation. (2023).
- [186] Y.T. Chen, Y.J. Chang, H. Murakami, S. Gorsse, A.C. Yeh, Designing high entropy superalloys for elevated temperature application, *Scr Mater.* 187 (2020) 177–182. <https://doi.org/10.1016/j.scriptamat.2020.06.002>.
- [187] A. Yeh, T. Tsao, Y. Chang, K. Chang, J. Yeh, M. Chiou, S. Jian, C. Kuo, W. Wang, H. Murakami, Developing New Type of High Temperature Alloys–High Entropy Superalloys, *International Journal of Metallurgical & Materials Engineering.* 1 (2015). <https://doi.org/10.15344/2455-2372/2015/107>.
- [188] S. Antonov, M. Detrois, S. Tin, Design of Novel Precipitate-Strengthened Al-Co-Cr-Fe-Nb-Ni High-Entropy Superalloys, *Metall Mater Trans A Phys Metall Mater Sci.* 49 (2018) 305–320. <https://doi.org/10.1007/s11661-017-4399-9>.
- [189] C.T. Liu, Physical metallurgy and mechanical properties of ductile ordered alloys (Fe, Co, Ni)₃V, *International Metals Reviews.* 29 (1984) 168–194. <https://doi.org/10.1179/imtr.1984.29.1.168>.
- [190] J. Schindelin, I. Arganda-Carreras, E. Frise, V. Kaynig, M. Longair, T. Pietzsch, S. Preibisch, C. Rueden, S. Saalfeld, B. Schmid, J.Y. Tinevez, D.J. White, V. Hartenstein, K. Eliceiri, P. Tomancak, A. Cardona, Fiji: An open-source platform for biological-image analysis, *Nat Methods.* 9 (2012) 676–682. <https://doi.org/10.1038/nmeth.2019>.

- [191] I. Arganda-Carreras, V. Kaynig, C. Rueden, K.W. Eliceiri, J. Schindelin, A. Cardona, H.S. Seung, Trainable Weka Segmentation: A machine learning tool for microscopy pixel classification, *Bioinformatics*. 33 (2017) 2424–2426. <https://doi.org/10.1093/bioinformatics/btx180>.
- [192] Y.J. Chang, A.C. Yeh, The evolution of microstructures and high temperature properties of $\text{Al}_x\text{Co}_{1.5}\text{CrFeNi}_{1.5}\text{Ti}_y$ high entropy alloys, *J Alloys Compd.* 653 (2015) 379–385. <https://doi.org/10.1016/j.jallcom.2015.09.042>.
- [193] D. Chen, F. He, B. Han, Q. Wu, Y. Tong, Y. Zhao, Z. Wang, J. Wang, J. jung Kai, Synergistic effect of Ti and Al on L12-phase design in CoCrFeNi-based high entropy alloys, *Intermetallics (Barking)*. 110 (2019). <https://doi.org/10.1016/j.intermet.2019.106476>.
- [194] J. Joseph, M. Senadeera, Q. Chao, K.F. Shamlaye, S. Rana, S. Gupta, S. Venkatesh, P. Hodgson, M. Barnett, D. Fabijanic, Computational design of thermally stable and precipitation-hardened Al-Co-Cr-Fe-Ni-Ti high entropy alloys, *J Alloys Compd.* 888 (2021). <https://doi.org/10.1016/j.jallcom.2021.161496>.
- [195] L. Wang, X. Wu, H. Su, B. Deng, G. Liu, Z. Han, Y. Su, Y. Huang, Y. Zhang, J. Shen, G. Zhang, Microstructure and mechanical property of novel L12 nanoparticles-strengthened CoFeNi-based medium entropy alloys, *Materials Science and Engineering: A*. 840 (2022) 142917. <https://doi.org/10.1016/j.msea.2022.142917>.

9. Summary and Future Work

The 20 W-free superalloys designed in this work have culminated in high-Fe, high-Ni, Co-based compositions with stable γ/γ' microstructure after aging at 850 °C. This work has demonstrated that Co-based superalloys and L1₂-strengthened high entropy superalloys (HESAs) are part of the same W-free family, demonstrating promise in a new unexplored phase space. Fig. 9-1 illustrates the alloying considerations taken when trying to improve upon the base alloy, Co-18Fe-12Ni-5Al-8Cr-3V-2Ti-1.5Nb-1.5Ta-0.08B (18Fe8Cr).

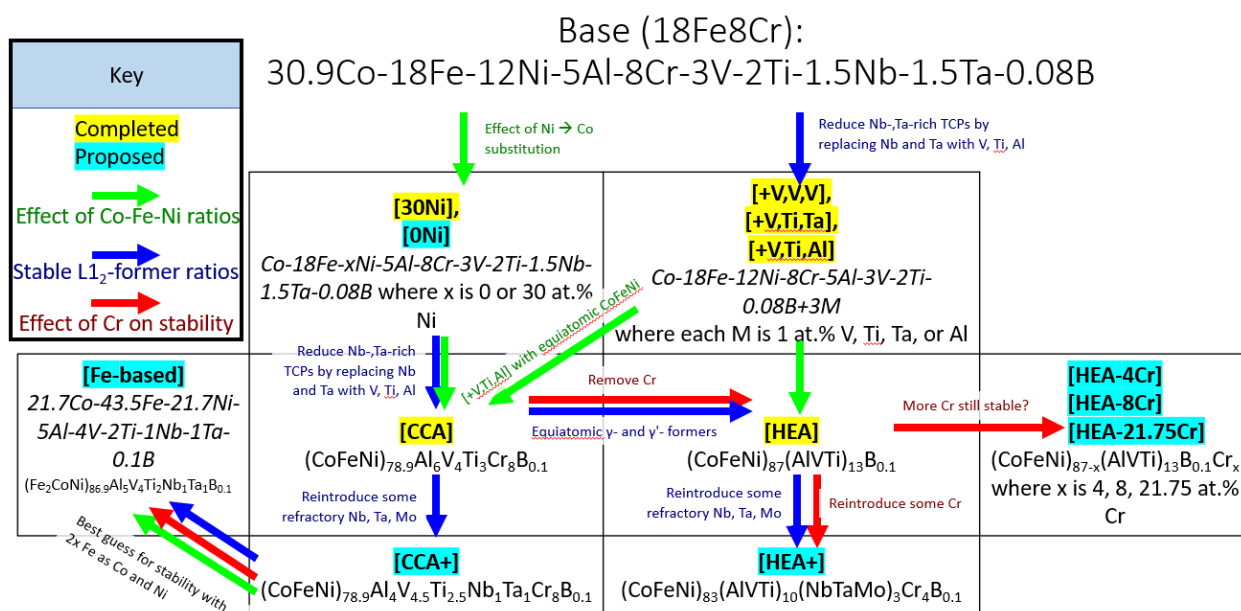


Figure 9-1. Chart showing the completed (yellow) and proposed future (teal) W-free Co-based superalloy compositions, with design considerations for what effect each alloy would clarify.

From the base 18Fe8Cr alloy, which displays both desirable $\gamma + \gamma'$ regions and undesirable intermetallic + depletion zone regions, we have investigated the effect upon phase stability of changing (i) Co:Fe:Ni ratios, (ii) γ' -former ratios (Al, V, Ti, Nb, Ta), and (iii) various levels of Cr: the latter element is beneficial for oxidation and mechanical properties but often destabilizes the γ

+ γ' microstructure. We have extended these Co-based superalloys directly into the equiatomic high-entropy alloy space—now with the understanding that HEA “rules of thumb” may apply to these alloys and vice versa, we propose several new alloys:

As we have tested Co-18Fe-12Ni-5Al-8Cr-3V-2Ti-1.5Nb-1.5Ta-0.08B and Co-18Fe-30Ni-5Al-8Cr-3V-2Ti-1.5Nb-1.5Ta-0.08B, the trend appears that increasing Ni:Co ratio improves $\gamma + \gamma'$ stability. To confirm this, we suggest an alloy with a highly destabilized microstructure **(1) Co-18Fe-0Ni-5Al-8Cr-3V-2Ti-1.5Nb-1.5Ta-0.08B**. This is the only alloy which intentionally lacks γ' , as we seek to find the relationship between γ -forming ratios and phase stability. Furthermore, if the Ni’s stabilizing effect continues, it means that we may be able to further increase Fe even while maintaining 8% Cr, by using equiatomic γ' -formers. This alloy would be **(2) (CoFeNi)_{78.9}Cr₈Al₄V₃Ti₂(NbTa)₃B_{0.1}**. Unlike current dual-phase HEAs in the literature, the refractory (Nb+Ta) content here should increase solvus temperature, enabling the alloy for high temperature creep. We also suggest a slightly modified version of this second alloy, with lower refractory content, in case alloy (2) precipitates similar amounts of refractory-rich phase as the base 18Fe8Cr. This composition is **(3) (CoFeNi)_{78.9}Cr₈Al₅V_{4.5}Ti_{2.5}(NbTa)₂B_{0.08}**.

We next suggest an “HEA+”, which has 3 groups of equiatomic elements, splitting γ' -formers into “lightweight” (Al, Ti, V) and “refractory” (Mo, Nb, Ta) elements, for composition: **(4) (CoFeNi)_{82.9}(AlTiV)₁₀(MoNbTa)₃Cr₄B_{0.1}**. This is the only alloy proposed here which contains Mo. To test whether our current most-stable alloy (CoFeNi)₈₇(AlTiV)₁₃ was only stable due to lack of Cr, we suggest modifying this alloy with 4- and 8 at.% Cr, for alloys **(5-6): (CoFeNi)₈₃(AlTiV)₁₃Cr₄ and (CoFeNi)₇₉(AlTiV)₁₃Cr₈**. Furthermore, in traditional high entropy

alloys, Cr is treated as another bulk γ former, so we suggest the alloy **(7) (CoCrFeNi)₈₃(AlTiV)₁₃**, which truly tests the “high entropy effect” with 20.75 at.% Cr, more than double the highest Cr concentration in any of our stable $\gamma + \gamma'$ alloys.

Furthermore, as we saw some instability in our alloys with high Ti:Al ratios (which is often an important balancing point in the high entropy alloy literature), we suggest adjusting the Ti:Al ratio in our currently stable (CoFeNi)₈₇(AlTiV)₁₃ HESA, with compositions: **(8-9) (CoFeNi)₈₇(Al₂TiV_{1.5})₁₃ and (CoFeNi)₈₇(AlTi₂V_{1.5})₁₃**. Finally, with the goal of producing a γ' -strengthened superalloy which can truly be considered “Fe-based” with at least as much Fe as Co and Ni combined, we suggest: **(10) (CoFe₂Ni)₈₇Al₅V₄Ti₂NbTaB_{0.1}**.

These alloys are listed, alongside the other alloys studied in this work, in Fig. 9-2.

Source		Co	Fe	Ni	Al	Cr	V	Ti	Nb	Ta	B	Mo	Calc Density (g/cm ³)	Solvus (°C)	Vol fraction of γ' aged 850 C, 1000h
Chapter 3	10Ni4Cr	72.92	0	10	5	4	3	2	1.5	1.5	0.08	0	8.46	970	32
Chapter 3	20Ni4Cr	62.92	0	20	5	4	3	2	1.5	1.5	0.08	0	8.46	989	37
Chapter 3	10Ni8Cr	68.92	0	10	5	8	3	2	1.5	1.5	0.08	0	8.39	989	44
Chapter 3	20Ni8Cr	58.92	0	20	5	8	3	2	1.5	1.5	0.08	0	8.39	1006	45
Chapter 3/5	0Fe4Cr	52.92	0	30	5	4	3	2	1.5	1.5	0.08	0	8.46	1010	49
Chapter 5	10Fe4Cr	52.92	10	20	5	4	3	2	1.5	1.5	0.08	0	8.35		53.9
Chapter 5	12Fe4Cr	52.92	12	18	5	4	3	2	1.5	1.5	0.08	0	8.33	1184	48.1
Chapter 5	14Fe4Cr	52.92	14	16	5	4	3	2	1.5	1.5	0.08	0	8.31	1189	40.9
Chapter 5	18Fe4Cr	52.92	18	12	5	4	3	2	1.5	1.5	0.08	0	8.27	1198	32.8
Chapter 3/5	0Fe8Cr	48.92	0	30	5	8	3	2	1.5	1.5	0.08	0	8.39	1031	45
Chapter 5	10Fe8Cr	48.92	10	20	5	8	3	2	1.5	1.5	0.08	0	8.28		56.8
Chapter 5	12Fe8Cr	48.92	12	18	5	8	3	2	1.5	1.5	0.08	0	8.26	1189	42.4
Chapter 5	14Fe8Cr	48.92	14	16	5	8	3	2	1.5	1.5	0.08	0	8.24	1193	43.6
Chapter 5	18Fe8Cr	48.92	18	12	5	8	3	2	1.5	1.5	0.08	0	8.20	1201	20.6
Chapter 7	VVV	48.92	18	12	5	8	6	2	0	0	0.08	0	8.01	808.1	0
Chapter 7	30Ni	30.92	18	30	5	8	3	2	1.5	1.5	0.08	0	8.20	978.25	48.3
Chapter 7	VTiTa	48.92	18	12	5	8	4	3	0	1	0.08	0	8.10	905.75	11
Chapter 7	VTiAl	48.92	18	12	6	8	4	3	0	0	0.08	0	7.96	813.3	0
Chapter 7	CCA	26.3	26.3	26.3	6	8	4	3	0	0	0.1	0	7.87	863	15.3
Chapter 7	HEA	29.01	29	29	4.33	0	4.33	4.33	0	0	0	0	8.02	891.45	39.3
Proposed	[1] ONi	60.9	18	0	5	8	3	2	1.5	1.5	0.08	0			
Proposed	[2] equi-base	26.3	26.3	26.3	5	8	3	2	1.5	1.5	0.08	0			
Proposed	[3] CCA+	26.3	26.3	26.3	4	8	4.5	2.5	1	1	0.1	0			
Proposed	[4] HEA+	27.7	27.7	27.7	3.3	4	3.3	3.3	1	1	0.1	1			
Proposed	[5] HEA-4Cr	27.7	27.7	27.7	4.3	4	4.3	4.3	0	0	0.1	0			
Proposed	[6] HEA-8Cr	26.3	26.3	26.3	4.3	8	4.3	4.3	0	0	0.1	0			
Proposed	[7] HEA-equiCr	21.75	21.75	21.75	4.3	21.75	4.3	4.3	0	0	0.1	0			
Proposed	[8] HEA-2AlTi	29.01	29	29	5.77	0	4.33	2.89	0	0	0	0			
Proposed	[9] HEA-2TiAl	29.01	29	29	2.89	0	4.33	5.77	0	0	0	0			
Proposed	[9] HEA-2TiAl	29.01	29	29	2.89	0	4.33	5.77	0	0	0	0			
Proposed	[10] Fe-based	21.7	43.5	21.7	5	0	4	2	1	1	0.1	0			

Figure 9-2. Table of compositions, calculated density, solvus temperature, and γ' volume fraction for alloys studied in this work and proposed new alloys (1-10) with their short names (teal colors). Cells are color-coded such that green applies to the maximum value in a given range, and red applies to the minimum value.

10. Appendix

10.1 Scanning Electron Microscopy

Island of silver,
What secret can you tell me?
Wait, you are just dust!